

**THE MECHANICAL PROPERTIES AND MICROSTRUCTURES OF VANADIUM BEARING
HIGH STRENGTH DUAL PHASE STEELS PROCESSED WITH CONTINUOUS
GALVANIZING LINE SIMULATIONS**

by

Yu Gong

B.S. in Materials Science and Engineering, Zhejiang University, 2009

Submitted to the Graduate Faculty of
Swanson School of Engineering in partial fulfillment
of the requirements for the degree of
Doctor of Philosophy

University of Pittsburgh

2015

UNIVERSITY OF PITTSBURGH
SWANSON SCHOOL OF ENGINEERING

This dissertation was presented

by

Yu Gong

It was defended on

October 30th, 2015

and approved by

Albert Chi Fu To, Ph.D., Associate Professor, Mechanical Engineering and Materials Science

Scott X. Mao, Ph.D., Professor, Mechanical Engineering and Materials Science

John A. Barnard, Ph.D., Professor, Mechanical Engineering and Materials Science

Ian Nettleship, Ph.D., Associate Professor, Mechanical Engineering and Materials Science

Dennis Haezebrouck, Ph.D., Sr. Research Consulting Manager, USS Company

Luis E. Vallejo, Professor, Ph.D., Civil and Environmental Engineering

Dissertation Director: Anthony J. DeArdo, Ph.D., Professor, Mechanical Engineering and Materials
Science

Copyright © by Yu Gong

2015

**THE MECHANICAL PROPERTIES AND MICROSTRUCTURES OF VANADIUM
BEARING HIGH STRENGTH DUAL PHASE STEELS PROCESSED WITH CONTINUOUS
GALVANIZING LINE SIMULATIONS**

Yu Gong, PhD

University of Pittsburgh, 2015

For galvanized or galvanized steels to be commercially successful, they must exhibit several attributes: (i) easy and inexpensive processing in the hot mill, cold mill and on the coating line, (ii) high strength with good formability and spot weldability, and (iii) good corrosion resistance. At the beginning of this thesis, compositions with a common base but containing various additions of V or Nb with or without high N were designed and subjected to Gleeble simulations of different galvanizing(GI), galvannealing(GA) and supercooling processing. The results revealed the phase balance was strongly influenced by the different microalloying additions, while the strengths of each phase were somewhat less affected. Our research revealed that the amount of austenite formed during intercritical annealing can be strongly influenced by the annealing temperature and the pre-annealing conditions of the hot band (coiling temperature) and cold band (% cold reduction). In the late part of this thesis, the base composition was a low carbon steel which would exhibit good spot weldability. To this steel were added two levels of Cr and Mo for strengthening the ferrite and increasing the hardenability of intercritically formed austenite. Also, these steels were produced with and without the addition of vanadium in an effort to further increase the strength. Since earlier studies revealed a relationship between the nature of the starting cold rolled microstructure and the response to CGL processing, the variables of hot band coiling temperature and level of cold reduction prior to annealing were also studied. Finally, in an effort to increase strength and ductility of both the final sheet (general formability) and the sheared edges of cold punched holes (local formability), a new thermal path was developed that replaced the conventional GI ferrite-martensite microstructure with a new ferrite-martensite-tempered martensite and retained austenite

microstructure. The new microstructure exhibited a somewhat lower strength but much high general and local formabilities. In this thesis, both the physical and mechanical metallurgy of these steels and processes will be discussed. This research has shown that simple compositions and processes can result in DP steels with so-called Generation III properties.

TABLE OF CONTENTS

ACKNOWLEDGEMENTS	XXV
1.0 INTRODUCTION	1
2.0 BACKGROUND	6
2.1 GENERAL DESCRIPTION OF DUAL-PHASE STEELS	6
2.2 MECHANICAL PROPERTIES OF DUAL-PHASE STEELS	10
2.2.1 Tensile strength and yield strength	11
2.2.2 Work hardening	13
2.2.3 Ductility	16
2.2.4 Yielding behavior	17
2.3 ALLOYING ELEMENTS.....	18
2.3.1 Manganese	18
2.3.2 Vanadium	19
2.3.3 Niobium	20
2.3.4 Chromium and molybdenum.....	21
2.4 FORMATION OF AUSTENITE.....	22
2.5 TEMPERING OF DUAL-PHASE STEELS	29
2.6 BANDING IN DUAL-PHASE STEELS	31
3.0 STATEMENT OF OBJECTIVE.....	36
4.0 EXPERIMENTAL PROCEDURE.....	39
4.1 MICROSTRUCTURAL ANALYSIS.....	39

4.1.1	Optical microscopy (OM).....	39
4.1.2	Scanning electron microscope (SEM) and EBSD.....	40
4.1.3	Transmission electron microscopy (TEM)	40
4.2	MECHANICAL PROPERTIES.....	41
4.2.1	Tensile testing.....	41
4.2.2	Micro hardness and nano hardness.....	41
4.2.3	Hole expansion tests.....	42
4.3	HEAT TREATMENTS	42
4.4	MEASUREMENT OF RETAINED AUSTENITE.....	43
4.5	STORED ENERGY	44
4.5.1	Calculation of stored energy from EBSD scanning	44
4.5.2	Other methods to get stored energy	45
5.0	RESULTS AND DISCUSSION	47
5.1	MECHANICAL PROPERTIES OF DUAL PHASE STEELS WITH VANADIUM OR NIOBIUM ADDITIONS	47
5.1.1	Chemical compositions and thermomechanical processing.....	47
5.1.2	Results of hot rolled and cold rolled sheets.....	50
5.1.3	Mechanical properties	52
5.1.4	Work hardening behavior	63
5.1.5	Microstructures of dual phase steels with full processing.....	67
5.1.6	Micro hardness.....	77
5.1.7	Results of dual phase steels with partial processing: study of austenite formation, dissolution behavior of cementite and recrystallization behavior of cold rolled ferrite.....	80
5.1.7.1	Effects of alloying elements on the austenite formation during intercritical annealing.....	80
5.1.7.2	Dissolution behavior of cementite.....	84
5.1.7.3	Recrystallization behavior of cold rolled ferrite	87
5.2	EFFECTS OF INTERCRITICAL ANNEALING TEMPERATURE AND COOLING RATE ON THE PROPERTIES OF DP STEELS.....	94

5.3	EFFECTS OF V OR VN ON THE SOFTENING RESISTANCE OF DUAL PHASE STEELS WITH EXTENDING HOLDING AT ZINC POT TEMPERATURE.....	102
5.4	INFLUENCE OF STORED ENERGY IN COLD ROLLED SHEET ON THE FORMATION OF AUSTENITE DURING THE SUBSEQUENT INTERCRITICAL ANNEALING OF V-BEARING DUAL-PHASE STEELS.....	114
5.4.1	Austenite formation during intercritical annealing.....	114
5.4.2	Effects of stored energy on the formation of austenite during intercritical annealing.....	117
5.5	EFFECTS OF THERMOMECHANICAL AND VANADIUM ADDITIONS ON THE MICROSTRUCTURE AND MECHANICAL PROPERTIES OF DUAL PHASE STEELS WITH HIGH CR, MO CONTENTS.....	127
5.5.1	Chemical compositions and thermomechanical processing.....	127
5.5.2	Mechanical properties of dual phase steels with high Cr, Mo contents.....	130
5.5.3	Effects of coiling temperature on the strength of vanadium bearing steels.....	155
5.5.4	Effects of coiling temperature and cold rolling reduction on ferrite grain size	160
5.5.5	Fracture study	165
5.5.6	Sheared edge formability-hole expansion ratio.....	168
5.6	EFFECTS OF THERMOMECHANICAL AND VANADIUM ADDITIONS ON THE MICROSTRUCTURE AND MECHANICAL PROPERTIES OF DUAL PHASE STEELS WITH LOW CR, MO CONTENTS.....	178
5.6.1	Mechanical properties of dual phase steels with low Cr, Mo contents	178
5.6.2	Microstructures of low alloyed DP steels and the discussions of the roles of Cr, Mo.....	186
5.6.3	Sheared-edge formability of low alloyed DP steels	192
5.7	OVERALL DISCUSSIONS: IMPROVING THE STRENGTH-DUCTILITY BALANCE IN HIGH STRENGTH DUAL PHASE STEELS THROUGH THE ADDITION OF VANADIUM.....	197
5.7.1	Stored energy of initial cold rolled sheets.....	197
5.7.2	Mechanical properties of dual phase steels with various conditions.....	206
5.7.3	Retained austenite and supercool temperatures	216
5.7.4	Precipitation hardening from the benefits of vanadium additions.....	220
5.7.5	Work hardening of vanadium bearing dual phase steels.....	230
6.0	CONCLUSIONS	241

7.0 FUTURE WORK	246
APPENDIX A	248
BIBLIOGRAPHY	255

LIST OF TABLES

Table 5.1.1. Chemical compositions of the five steels used in this study, Wt.%, The chemical composition of the commercial steel is also included.....	47
Table 5.1.2 Predicted Critical temperatures of the five steels used in this study, and the volume fractions of austenite at different IAT are also shown.....	50
Table 5.1.3 Mechanical properties of the DP steels for the 7 full processing in this current study.....	59
Table 5.1.4. Hole expansion ratios (HE %) and reduction in area (RA%), which was measured from OM images of the fracture surfaces after tensile testing, of the DP steels with different alloying elements. A1 is the standard galvanizing processing and C1 is the supercool processing with supercool temperature 250°C.....	63
Table 5.1.5. $n(\epsilon) = \frac{d(\ln\sigma)}{d(\ln\epsilon)}$, ϵ is true strain, σ is true stress. The values of n in the table are the averaged ones in the specific true strain range as shown in the table.....	64
Table 5.1.6. Strain-hardening exponent (m) from modified C-J analysis and the transition strains between the two stages of work hardening behavior	64
Table 5.1.7. Volume fractions (%) of MA, and TM in the DP steels with five different compositions and A1,A 3, B1 and C1 processing.....	71
Table 5.1.8 values of VHN in soft region and hard region for DP_V	78
Table 5.1.9. VHN values of soft region and hard region for DP_VN, 10g, Gleeble1 at USS	78
Table 5.1.10 values of VHN in soft region and hard region for DP_NbV.....	78
Table 5.1.11 Volume fractions of MA of the five steels with processing group M.....	81
Table 5.1.12. Volume fractions (%) of non-recrystallized ferrite at different intercritical annealing temperatures and holding times for DPV and DPVN.....	91
Table 5.2.1. Heating rate to IAT (T) is 5°C/s, the numbers are the tensile strength (MPa).....	95
Table 5.2.2. Heating rate to IAT (T) is 5°C/s, the numbers are the yield strength (MPa).	95

Table 5.2.3 Volume fraction of MA, a, 800°C, 1min; b, 800°C, 2min; c, 800°C, 5min; and d, 820°C, 2min (water quenched).....	97
Table 5.3.1. Analyzed chemical compositions (wt.%) of DPV and DPVN. DPU is the commercial dual phase steels supplied by USS.....	103
Table 5.3.2. Tensile strength (UTS) and yield strength (YS) of dual phase steels with V or VN addition and commercial DPs without micro alloying elements. Each number is the average of two tests.	103
Table 5.3.3. Uniform elongation (UE, converted to 2 inch gauge length), total elongation (TE, converted to 2 inch gauge length), and work hardening ratios (between 4% and 6% engineering strain) of dual phase steels with V or VN addition and commercial DPs without micro alloying elements. Each number is the average of two tests.	103
Table 5.3.4. Volume fractions (%) of MA and bainite in DPV with different holding time at zinc pot temperature	106
Table 5.3.5. Volume fractions (%) of MA and bainite in DPVN with different holding time at zinc pot temperature	106
Table 5.4.1. Austenite amount (%) after intercritical annealing and water quench (or air cooling AC) for cold rolled (60% vs 72%) DPV, DPVN and DPNbV steels. The number in the parentheses is the heating rate from room temperature to IAT.....	117
Table 5.4.2. Averaged stored energy calculated using different methods (J/cm ³) and the VHN values. .	121
Table 5.4.3. Volume fraction of stored energy greater than 5, 10 or 14 J/cm ³ for cold rolled (CR) samples	124
Table 5.4.4. Different Gleeble processing applied to DPV (60%CR and 72%CR) and DPVN (60%CR)	126
Table 5.5.1. Chemical composition (wt. %) of the four steels used in this section and section 5.6	128
Table 5.5.2. Conditions (addition of microalloying elements, coiling temperatures (CT) and cold rolling reduction) of initial cold rolled (CR) sheets with sample IDs used in this paper.	128
Table 5.5.3. Critical temperatures of austenite formed at 790°C of steels 2A and 2B, estimated from JMatPro commercial software.	128
Table 5.5.4. Increase in the tensile strength due to the addition of 0.06% wt.% vanadium. UTS-A is the tensile strength of dual phase steels without vanadium addition in the first column, and UTS-B is the tensile strength of DPs with vanadium addition in the second column. ΔUTS is the increase in UTS.....	135
Table 5.5.5. Increase in the yield strength due to the addition of 0.06% wt.% vanadium. YS-A is the yield strength of dual phase steels without vanadium addition in the first column, and YS-B is the yield strength of DPs with vanadium addition in the second column. ΔYS is the increase in YS.	135
Table 5.5.6. UTS, reduction in area (%RA) and estimated hole expansion ratios (HER) from reduction in area.....	139

Table 5.5.7. Work hardening exponents (n-values between engineering strain 4% and 6%) of dual phase steels with high Cr, Mo contents.....	140
Table 5.5.8. Volume fractions of martensite, bainite and tempered martensite in high alloyed DPs with 80% cold reduction.	152
Table 5.5.9. Volume fractions of martensite, bainite and tempered martensite in high alloyed DPs with 50% cold reduction.	153
Table 5.5.10. Mechanical properties (UTS, YS, TE and HE) of the dual phase steels with 50% cold rolling reduction, the Gleeble heat treatment E1: 790°C/60s, 15°C/s, 250°C/20s, 42°C/s, 460°C/30s, 10°C/s to RT.....	156
Table 5.5.11. Tensile strength (UTS) of hot band steels with high Cr, Mo and with or without V addition. Each number is the average of two tests.	157
Table 5.5.12. Ferrite grain size of high alloyed DPs with E1 processing.	165
Table 5.5.13. Measured hole expansion ratios (HER).	175
Table 5.5.14. Comparison of hole expansion ratios of vanadium free DPs and vanadium bearing DPs at the same UTS level, TE were converted to 2 inch specimens	177
Table 5.6.1. Increase in the tensile strength due to the addition of 0.06% wt.% vanadium. UTS-A is the tensile strength of dual phase steels without vanadium addition in the first column, and UTS-B is the tensile strength of DPs with vanadium addition in the second column. Δ UTS is the increase in UTS.....	183
Table 5.6.2. Increase in the yield strength due to the addition of 0.06% wt.% vanadium. YS-A is the yield strength of dual phase steels without vanadium addition in the first column, and YS-B is the yield strength of DPs with vanadium addition in the second column. Δ YS is the increase in YS.	183
Table 5.6.3. Work hardening exponents (n-values between engineering strain 4% and 6%) of dual phase steels with low Cr, Mo contents.....	186
Table 5.6.4. Volume fractions of martensite, bainite and tempered martensite in low alloyed DPs with 80% cold reduction, 2%-6% bainite can be found for E1 processing.....	191
Table 5.6.5. Volume fractions of martensite, bainite and tempered martensite in low alloyed DPs with 50% cold reduction, 2%-6% bainite can be found for E1 processing.....	191
Table 5.6.6. Hole expansion ratios of DPs with low Cr, Mo and various heat treatments. Top holder 6mm radius flat	193
Table 5.6.7. hole expansion ratios of USS commercial DP590 and DP780 tested at BAMPRI using the same procedure as for the tests in Table 5.6.6 i.e. Bottom holder 40mm hole, top holder 40mm hole and 6mm radius flat, and continuous die moving speed 0.5mm/s. The hole expansion ratios of USS commercial DP980 were tested in USS lab.....	193
Table 5.7.1. Stored energy (J/cm ³) of cold rolled sheets with low Cr, Mo contents.....	197
Table 5.7.2. Stored energy (J/cm ³) of cold rolled sheets with high Cr, Mo contents.....	198

Table 5.7.3. VHN (300g) of cold rolled (50%CR and 80%CR) initial steel sheets with low Cr, Mo contents, and the increase in VHN (Δ VHN) due to the addition of 0.06% w.t.% vanadium.	198
Table 5.7.4. VHN (300g) of cold rolled (50%CR and 80%CR) initial steel sheets with high Cr, Mo contents, and the increase in VHN (Δ VHN) due to the addition of 0.06% w.t.% vanadium.	198
Table 5.7.5. Retained austenite calculated from magnetic properties.....	217
Table 5.7.6. Amount of retained austenite from magnetic measurements.....	220
Table 5.7.7. Strain hardening exponents n-values (4%-6% engineering strain) and uniform elongations of DPs with high Cr, Mo contents.....	231
Table 5.7.8. Strain hardening exponents n-values (4%-6% engineering strain) and uniform elongations of DPs with low Cr, Mo contents.....	232
Table 5.7.9. Work hardening exponent n-values between engineering strain 0.2% and 0.5%.....	234
Table 5.7.10. Work hardening exponent n-values between engineering strain 0.2% and 0.5%.....	234
Table A1. Volume fractions of RA, polygonal ferrite and martensite from IQ peak fitting for DPV, GI (A3).....	253
Table A2. Volume fractions of RA, polygonal ferrite and martensite from IQ peak fitting for DPNbV, GI (A3).....	254
Table A3. Volume fractions of RA, polygonal ferrite and martensite from IQ peak fitting for DPVN, GI (A3).....	254

LIST OF FIGURES

Figure 1.1. Comparison of tensile strength and total elongation for different types of steels	2
Figure 2.1.1. Schematic representation of basic two-phase microstructure species	7
Figure 2.1.2 Schematic stress-strain curves for plain carbon, HSLA, and dual phase steels. SAE 950X and 980X are Society of Automotive Engineers designations for HSLA steels of different strength levels. GM 980X is a General Motors developed dual phase steel. GM 980 ^[9]	8
Figure 2.1.3 Schematic representation of intercritical annealing and water quenching (WQ) for developing dual phase structure, IAT means intercritical annealing temperature.....	9
Figure 2.2.1 The 0.2 pct flow stress and the tensile strength as a function of percent martensite for the Fe-Mn-C alloys ^[21]	11
Figure. 2.2.2 Uniform elongation as a function of tensile strength for standard HSLA steels and Fe-Mn-C dual phase steels ^[21]	11
Figure 2.4.1 (a) Schematic view of the microstructure, (b) variation of the carbon content across the cementite-austenite-ferrite boundaries, F=ferrite, A=austenite, and P=pearlite ^[80]	24
Figure 2.4.2 Carbon concentration profile around the carbide spheroid during dissolution ^[88]	26
Figure 2.4.3 Initial conditions. A ferrite-pearlite mixture is heated into the intercritical range to produce austenite particles of width, 2L, separated by distance, 2W, as illustrated schematically in (a). The austenite is initially of eutectoid composition C_E^E , with a carbon concentration profile as in (b). The manganese concentration is uniform as shown in (c)	27
Figure 2.6.1 An illustration of the common mechanism of banding	32
Figure 2.6.2 Schematization of Mn segregation and microstructures expected to depend on the austenite grain size and the density of ferrite nuclei	34
Figure 5.1.1. Schematic diagram of hot rolling and cold rolling used for each type of steel in the current study, RT means room temperature	48
Figure 5.1.2. Schematic representation of heat-treatment schedules for Gleeble processes. GI: A1, x=15,y=10,t=30s; A2, x=30,y=10,t=30s; A3, x=15,y=30,t=30s; A4, x=30,y=30,t=30s; A5, x=15,y=10,t=60s; A6, x=15,y=10,t=120s; GA: B1, t=30s; B2, t=60s; B3, t=120s; and Supercool: C1, x=15; C2, x=30.....	49

Figure 5.1.3. 2% Nital etched microstructures of hot rolled samples (a) DP_V, (b) DP_Nb, (c) DP_V higher magnification, and (d) DP_V SEM microstructure.	51
Figure 5.1.4 (a) optical microstructure of DP_Nb, Nital etched, (b) optical microstructure of DP_VN, Nital etched, (c) optical microstructure of DP_VN, LePera etched, and (d) SEM microstructure of DP_VN.....	52
Figure 5.1.5 Engineering strain versus stress curves of DP_V and DP_NbV with full processing GI (A1-A4), GA (B1) and Supercool (C1-C2).....	53
Figure 5.1.6 True strain versus stress curves of DP_V and DP_NbV with full processing GI (A1-A4), GA (B1) and Supercool (C1-C2).....	53
Figure 5.1.7 Tensile strength and 0.2% yield strength of DP steels in this work, and the corresponding values of commercial DP steels are also included	54
Figure 5.1.8 Values of work hardening exponent n (4%-6%) and yield strength to tensile strength ratios of DP steels in this work, and the corresponding values of commercial DP steels are also included	55
Figure 5.1.9 Total elongation and uniform elongation of DP steels in this work, and the corresponding values of commercial DP steels are also included	56
Figure 5.1.10 Values of $UTS \times TE$ and $YS \times UE$ of DP steels in this work, and the corresponding values of commercial DP steels are also included.....	57
Figure 5.1.11 (a) Comparison of MA volume fraction versus UTS with the corresponding values obtained by Davies ^[21] , the data of DPV, DPVN and DPNbV with A1, A3 and B1 processing were plotted in this figure, (b) comparison of UTS versus UE with the corresponding values obtained by Davies ^[21] . The values of commercial steels are also included.....	58
Figure 5.1.12. The relationship between the volume fractions of retained austenite obtained by magnetometry and the total elongations of the DPNbV steels	60
Figure 5.1.13 . Relationship among hole expansion ratio (HE%), tensile strength (UTS), n -values, YS/UTS ratios and reduction in area (RA%).....	62
Figure 5.1.14 Instantaneous n -values versus true strain curves for the 7 full processing of DP_NbV	65
Figure 5.1.15 $\ln(d\sigma/d\epsilon)$ versus $\ln\sigma$ curves of the five steels with GI (A3) processing, the transition strains and the slopes of the two parts of the curves are also shown in the figure	67
Figure 5.1.16 SEM microstructures of DP_V, DP_VN and DP_NbV, 2% Nital etched.....	69
Figure 5.1.17. SEM microstructures of (a) DPV, A3, (b) DPNbV, A3 and (c) DPVN, A3 processing	70
Figure 5.1.18. SEM microstructures of (a) DPVN, C1, (b) DPNbVN, C1, (c) DPNbV, C1, and (d) DPNb, C1.....	71
Figure 5.1.19 SEM microstructures of DP_V with full processing B1 (a) and B2 (c), (b) is the microstructure with higher magnification of the area enclosed with dashed red square in (a), (d) are the enlarged microstructures of the area enclosed with dashed red lines in (c). The bright white particles enclosed with dashed blue lines are the cementite	73

Figure 5.1.20 SEM microstructures of DP_V with full processing GA (B3) (a) and C2 (b), (c) is the microstructure with higher magnification of the area enclosed by dashed red circle in (a), (d) is the enlarged microstructures of the area enclosed with dashed red square in (c). The bright white particles enclosed with dashed blue lines are the cementite	74
Figure 5.1.21 SEM microstructures of DP_VN with full processing GA (B2), (b) and (c) are the magnified microstructures of (a) at the central region.....	75
Figure 5.1.22 Optical microstructures of DP_NbV, GI(A3). (a) and (b) Nital etched, (c) LePera etched.	76
Figure 5.1.23 Optical microstructures of DP_NbV. (a) GI(A4), LePera etched, (b) GA(B1) LePera etched, (c) Supercool (C2), Nital etched.	76
Figure 5.1.24 SEM microstructures of DP_NbV with full processing GI (A1 and A3), GA (B1) and Supercool (C2).....	77
Figure 5.1.25. VHN (10g) of DP_V, DP_VN and DP_NbV at ferrite bands (soft region) and MA bands (hard region) respectively	79
Figure 5.1.26. Micro-hardness indents (VHN 10g) in DP_NbV, GI (A3), LePera etched.....	79
Figure 5.1.27 partial processing conducted in MTS system, (a) M1 1min, M2 2min, and M3 5min. (b) T1 0s, T2 30s and T3 8min. Air cooling (AC), water quenching (WQ)	80
Figure 5.1.28. microstructures of DP_V with processing M1 (a) LePera etched, (b) Nital etched, (c) and (d) SEM microstructures of different magnifications.....	82
Figure 5.1.29. DPV, 60% cold rolled (a) 780°C, 1min, WQ, (b) 780°C, 2min, WQ and (c) 780°C, 5min, WQ. (LePera Etched, White MA, Brown Ferrite)	82
Figure 5.1.30 Volume fractions of the five steels with different holding time at IAT 780°C.....	83
Figure 5.1.31 LePera etched microstructures (a) DP_VN, M1 (b) DP_Nb, M1(c) DP_NbV, M2.....	83
Figure 5.1.32 SEM microstructures of DP_VN, (a) M1, 780°C, 1min, (b) M2, 780°C, 2min, (c) M3, 780°C, 5min and (d) DP_NbVN, M2, 780°C, 2min.....	84
Figure 5.1.33. OM images (above 3 images) of DPVN, DPNbV and DPV (from left to right) and SEM microstructures of the corresponding steels (bottom, from left to right DPVN, DPNbV and DPV, respectively), the heat treatment is 650°C/5min, WQ, heating rate from RT to IAT 650°C is 5°C/s.	85
Figure 5.1.34. SEM microstructures of DPV (60%CR) (a) 700°C for 5minutes, (b) 720°C for 5 minutes, (c) 740°C for 5minutes, (d) 760°C for 1minute, (e) 760°C for 2minutes, (f) 780°C for 0s, and (g) 780°C for 1minute, water quenched.....	86
Figure 5.1.35 Microstructures of DP_NbV, (a) cold rolled, LePera etched, (b) cold rolled, SEM, (c) 680°C, for 5minutes, water quenched, LePera etched, and (d) 680°C for 5minutes, water quenched, SEM.....	89
Figure 5.1.36 Optical microstructures of DP_V, DP_Nb, DP_VN, and DP_NbVN with processing at 680°C for 5 minutes, WQ.....	90

Figure 5.1.37. SEM microstructures of (a) DPVN, (b) DPV and (c) DPNb after holding at 680°C for 5 minutes and then water quenched.	91
Figure 5.1.38. OM microstructures of (a) DPV, 780°C 0s WQ, and (b) DPVN, 780°C, 0s, WQ.....	92
Figure 5.1.39 SEM microstructures of DP_V with partial processing T2 (460°C, 30s), ACRT	93
Figure 5.1.40 SEM microstructures of DP_VN with partial processing T3 (460°C, 8min), ACRT.....	93
Figure 5.1.41 SEM microstructures (a) DP_V with partial processing T3 (460°C, 8min), ACRT (b) DP_VN, with partial processing T2 (460°C, 30s), ACRT	94
Figure 5.2.1. Tensile strength and yield strength of DPV and DPVN with IAT 790°C and 820°C, as listed in Tables 5.2.1 and 5.2.2. The first number in the horizontal axis is the cooling rate (°C/s) from IAT to zinc pot temperature, and the second is the cooling rate from zinc pot temperature to room temperature.	96
Figure 5.2.2. Optical microstructures (LePera etched) of DP_V, (a) 800°C, 1min, (b) 800°C, 2min, (c) 800°C, 5min, (d) 820°C, 2min (water quenched). MA white, ferrite brown.....	97
Figure 5.2.3. (a) DPV, 820°C/1min, 30°C/s, 460°C/30s, 10°C/s to RT, 35% bainite, 12% MA, (b) DPV, 820°C/1min, 30°C/s, 460°C/30s, 30°C/s to RT, 31% bainite, 15% MA.....	98
Figure 5.2.4. Illustration of the effects of different alloying elements on the transformation of austenite to bainite for galvanizing processing ^[80]	98
Figure 5.2.5. Predicted Bs and Ms temperatures using JMatPro of DPV at different intercritical annealing temperatures.....	99
Figure 5.2.6. SEM microstructures of (a) DPVN, 820°C/(60°C/s)460°C/(10°C/s)RT, (b) DPVN, 820°C/(30°C/s)460°C/(30°C/s)RT, (c) DPVN, 820°C/(60°C/s)460°C/(30°C/s)RT (d) DPVN, 790°C/(30°C/s)460°C/(30°C/s)RT. For higher IAT 820°C, bainite microstructures can be clearly observed and all the ferrite are recrystallized, while for lower IAT 790°C, little bainite was found and some non-recrystallized ferrite still existed.	100
Figure 5.2.7. SEM microstructures of (a) DPVN, 820°C-30°C/s-460°C-30°C/s-RT, (b) DPVN, 820°C-60°C/s-460°C-30°C/s-RT	102
Figure 5.3.1. Tensile strength (UTS) of dual phase steels with V or VN addition and commercial DPs without micro alloying elements.....	104
Figure 5.3.2. Yield strength (YS) of dual phase steels with V or VN addition and commercial DPs without micro alloying elements.....	104
Figure 5.3.3. SEM micrographs of (a) DPV, A5 (460°C, 60s), (b) DPV, A6 (460C, 120°C), (c) DPVN, A5 (460°C, 60s), and (d) DPVN, A6 (460C, 120°C)	105
Figure 5.3.4. Bright field image (a) and Dark field image (b) of twined martensite, SADP of twined martensite TM (c), and retained austenite (RA) (d) in DPV, A5	107
Figure 5.3.5. HRTEM images of VCx precipitates in DPV, A5 (460°C/60s)	108

Figure 5.3.6. HRTEM and FFT of a larger VC in extracted replica. Note the quality of the lattice image of the particle edge is much better than that in the center, in DPV, A5.....	109
Figure 5.3.7. Typical and conventional electron diffraction pattern (EDP) from thin foil specimen, showing VC forms in α ferrite with Baker-Nutting orientation relationship in DPV, A5.....	109
Figure 5.3.8. HRTEM images of VCx particle embedded in ferrite matrix in the foil of DPV, A5, the FFT patterns of VCx and ferrite confirmed the relationship between particle and ferrite matrix, i.e. Baker-Nutting orientation relationship.	110
Figure 5.3.9. HRTEM images of VCx or V(CN)x precipitates in DPVN, A5 (460°C/60s).....	112
Figure 5.3.10. AlN found in DPVN, A5, replica	113
Figure 5.4.1. DPV, 72% cold rolled (a) 780°C, 0s, WQ, (b) 780°C, 1min, WQ and (c) 790°C, 1min, WQ and (d) 820°C, 1min, WQ (SEM micros, 2% Nital Etched)	116
Figure 5.4.2. X-ray diffraction profiles of as cold rolled DPV(60%CR and 72%CR), DPVN(60%CR) and DPNb(60%CR), hot band steels of DPV and DPNbV, as well as annealed DPV(60%CR, 720°C for 1minute and then water quenched).....	117
Figure 5.4.3. Image Quality (IQ) images of (a) DPV, HB, quarter, (b) DPNbV, HB, quarter. Blue lines for 15°-180° grain boundaries, green lines 5°-15° grain boundaries and red lines for 2°-5° grain boundaries. Stored Energy (SE) distribution maps of (c) DPV, HB, quarter, and (d) DPNbV, HB, quarter.	119
Figure 5.4.4. Stored Energy (SE) distribution maps of (a) DPV, 60% CR, (b) DPNbV, 60% CR, (c) DPV, 72% CR. The size of each image is 60 μ m \times 60 μ m.	121
Figure 5.4.5. Stored Energy (SE) distribution maps of (a) DPV, 60% CR, 740°C, 0s WQ, (b) DPVN, 60% CR, 740°C, 0s WQ, (c) DPNbV, 60% CR, 740°C, 0s WQ, and (d) DPV, 72% CR, 740°C, 0s, WQ. The size of each image is 60 μ m \times 60 μ m.	123
Figure 5.4.6. The positive relationship between SE from sub-grain method and SE from IQ data (left); the positive relationship between SE from sub-grain method and VHN (300g) hardness (right)	124
Figure 5.4.7. (a) shows the local volumes with SE higher than 8 J/cm ³ in the microstructure of initial 72% cold rolled steel, the size is 60x60 μ m, and (b) illustrates the austenite found after heating to 760°C and water quenching immediately with no holding time. (c) and (d) are the SEM microstructures of DPVN with Galvannealing processing with nucleation of austenite at sub-grain boundaries in non-recrystallized ferrite	125
Figure 5.4.8. Tensile strengths (UTS) of DPV (60%CR and 72%CR) and DPVN with different Gleeble processing, the steel IDs are the same as those listed in Table 5.4.4.....	127
Figure 5.5.1 (a). Schematic diagram of hot rolling and cold rolling used for each type of steel in the current study, RT means room temperature. (b). Simulated CGL heat treatments used in this study. Anneal D1 was the standard GI anneal while E1 (T=250°C), E2 (T=320°C) & E3 (T=390°C) were the anneals incorporating the new supercooled feature. Note: For Process D1: Heating Rate: +5 °C/s and Cooling Rates: - 15 °C/s or -10 °C/s. For Processes E: Heating Rates: + 5 °C/s and + 42 °C/s and Cooling Rates: - 15 °C/s or - 10 °C/s	129

Figure 5.5.2. Engineering stress-strain curves of DP steels with high Cr, Mo contents and standard galvanizing and supercool processing.....	131
Figure 5.5.3. True stress-strain curves of DP steels with high Cr, Mo contents and standard galvanizing and supercool processing	132
Figure 5.5.4. Tensile strength (UTS) of dual phase steels with standard galvanizing (D1) and supercool processing, X=A is vanadium free, X=B is vanadium bearing, 1 represents high CT 650°C and 3 represents low CT 500°C.	134
Figure 5.5.5. Yield strength (YS) of dual phase steels with standard galvanizing (D1) and supercool processing.	136
Figure 5.5.6. Total elongations (TE) of dual phase steels with standard galvanizing (D1) and supercool processing. TEs were converted to 50mm (2 inch) standard gage length specimen.....	137
Figure 5.5.7. YS/UTS ratios of dual phase steels with standard galvanizing (D1) and supercool processing.	138
Figure 5.5.8. Comparison of SEM microstructures of dual phase steels with and without vanadium addition, (a) 2A3A (vanadium free), (b)2B3A (with vanadium addition). The heat treatment is D1 (standard galvanizing processing).....	142
Figure 5.5.9. Comparison of SEM microstructures of dual phase steels with high and low coiling temperatures (CT), (a) 2A1E (CT=650°C, vanadium free), (b)2A3E (CT=500°C, vanadium free). The heat treatment is D1 (standard galvanizing processing)	142
Figure 5.5.10. Comparison of SEM microstructures of dual phase steels with high and low coiling temperatures (CT), (a) 2B1E (CT=650°C, with vanadium), (b)2B3E (CT=500°C, with vanadium). The heat treatment is D1 (standard galvanizing processing)	143
Figure 5.5.11. Comparison of SEM microstructures of dual phase steels with and without vanadium addition, (a) 2A3A (vanadium free), (b)2B3A (with vanadium addition). The heat treatment is E3 (supercool processing, supercool temperature 390°C).....	143
Figure 5.5.12. Comparison of SEM microstructures of dual phase steels with high and low coiling temperatures (CT), (a) 2B1A (CT=650°C, with vanadium addition, UTS=904MPa), (b)2B3A (CT=500°C, with vanadium addition, UTS=967MPa). The heat treatment is E1 (supercool processing, supercool temperature 250°C).....	144
Figure 5.5.13. Comparison of SEM microstructures of dual phase steels with high and low coiling temperatures (CT), high magnification showing fresh MA and tempered martensite, (a) 2B1A (CT=650°C, with vanadium addition), (b)2B3A (CT=500°C, with vanadium addition). The heat treatment is E1 (supercool processing, supercool temperature 250°C).....	144
Figure 5.5.14. Comparison of SEM microstructures of dual phase steels with and without vanadium addition, (a) 2A3A (vanadium free, UTS=919MPa), (b)2B3A (with vanadium addition, UTS=967MPa). The heat treatment is E1 (supercool processing, supercool temperature 250°C)	145

Figure 5.5.15. Comparison of SEM microstructures of dual phase steels with and with different cold rolling reductions, (a) 2A1E (50%CR, vanadium free, UTS=853MPa), (b)2A1A (80%CR, vanadium free, UTS=894MPa). The heat treatment is E1 (supercool processing, supercool temperature 250°C).....	145
Figure 5.5.16. Steels with high Cr, Mo contents, vanadium free, high coiling temperature 650°C and different cold rolling reductions; inverse pole figures (IPF) (a) 2A1C, hot band, (b) 2A1E, 50%CR, and (c) 2A1A, 80%CR; stored energy distribution mappings (d) 2A1C, hot band, average SE 0.90J/cm ³ , (e) 2A1E, 50%CR, average SE 2.86J/cm ³ , and (f) 2A1A, 80%CR, average SE 3.66J/cm ³ . The horizontal direction is the normal direction and the vertical direction is the transverse direction.....	146
Figure 5.5.17. SEM microstructures of dual phase steels with high Cr, Mo contents, (a) (b) 2A1A, E2; (c) (d) 2A1E, E2; (e) (f) 2B1A, E2; (g) (h) 2B1E, E2.....	148
Figure 5.5.18. SEM microstructures of dual phase steels with high Cr, Mo contents, (a) (b) 2A3E, E2, (c) (d) 2B3A, E2, (e) (f) 2B3E, E2.....	149
Figure 5.5.19. SEM microstructures of (a) 2A1A, E3 (b) 2A1E, E3 (c) 2B1A, E3 and (d) 2B1E, E3, Low magnification 2000x	150
Figure 5.5.20. SEM microstructures of (a) 2A1A, E3 (b) 2A1E, E3 (c) 2B1A, E3 and (d) 2B1E, E3, High magnification 8000x	151
Figure 5.5.21. SEM microstructures of (a) 2A3A, E3 (b) 2A3E, E3 (c) 2B3A, E3 (d) 2B3E, E3, low magnification 2000x	153
Figure 5.5.22. SEM microstructures of (a) 2A3A, E3 (b) 2A3E, E3 (c) 2B3A, E3 (d) 2B3E, E3, high magnification 8000x	154
Figure 5.5.23. Volume fraction of martensite of high alloyed DPs with different Gleeble full processings.	154
Figure 5.5.24. Volume fraction of tempered martensite (TM) of high alloyed DPs with different Gleeble full processings.	155
Figure 5.5.25. Inverse pole figures of hot band steels, vertical direction is RD, horizontal direction is ND. (a) 2A1C, (b) 2A2C, (c) 2A3C, (d) 2B1C, (e) 2B2C and (f) 2B3C. black lines are the high angle (15°) grain boundaries. The IPF triangle describes the relationship between colors and orientations.....	157
Figure 5.5.26. VHN of hot band steels with high Cr, Mo contents and different coiling temperatures ...	158
Figure 5.5.27. Nanohardness of ferrite and tempered martensite (TM) in 2A1E, 2A3E, 2B1E and 2B3E with E1 processing.....	160
Figure 5.5.28. Distribution of ferrite grain size in 2A1E, 2A3E, 2B1E and 2B3E with E1 processing ...	162
Figure 5.5.29. Distribution of ferrite grain size in 2A1A, 2A3A, 2B1A and 2B3A with E1 processing .	164

Figure 5.5.30. Optical microstructures of (a) 2B1C, HB steel with coiling temperature 650°C, VHN(300g) 210±3 (b) 2B3C, HB steel with coiling temperature 500°C, VHN (300g) 278±6, 2% Nital etched	165
Figure 5.5.31. SEM micrographs near fracture surfaces, (a) 2B1A, D1, (b) 2B3A, D1	166
Figure 5.5.32. SEM micrographs near fracture surfaces, (a) 2B1E, D1, (b) 2B3E, D1	166
Figure 5.5.33. Fractured surfaces after tensile tests of (a) 2B3A, D1, (b) 2B3E, D1	168
Figure 5.5.34. Fractured surfaces after tensile tests of (a) 2B1E, E1, (b) 2B3E, E1	168
Figure 5.5.35. Hole expansion tested samples (a) 2A3A, D1, (b) 2A3E, D1, (c) high magnification image of the region inside the dashed square in (b), (d) 2B3A, D1, (e) 2B3E, D1, (f) high magnification image of the region inside the dashed square in (e). Vertical direction is the rolling direction...	169
Figure 5.5.36. Microstructures near the hole edge punched or sheared of 2B3E, D1, before hole expansion test, (a) 350x, (b) 2000x, and (c) 8000x	172
Figure 5.5.37. Microstructures near the hole edge punched or sheared of 2B3A, E1, before hole expansion test, (a) low magnification and (b) higher magnification	173
Figure 5.5.38. Hole expansion tested samples (a) 2A1E, E1, (b) 2A3E, E1, (c) high magnification image of the region inside the dashed square in (b), (d) 2B1E, E1, (e) 2B3E, E1, (f) high magnification image of the region inside the dashed square in (e). Vertical direction is the rolling direction...	173
Figure 5.5.39. Reduction in area (%RA) of dual phase steels with standard galvanizing (D1) and supercool processing (E1, E2 and E3)	174
Figure 5.5.40. Hole expansion ratios (HE%) of dual phase steels with standard galvanizing (D1) and supercool processing (E1, E2 and E3)	175
Figure 5.5.41. The data points were in Table 5.5.14 were plotted in 3D form.	177
Figure 5.5.42. (a) data points (UTS-HE) of high alloyed DPs, (b) averaged UTS values at three hole expansion ratio levels, 20-30%, 30-40% and 40-50%	178
Figure 5.6.1. Engineering strain and stress curves of DP steels with low Cr, Mo contents and standard galvanizing and supercool processing	179
Figure 5.6.2. True strain-stress curves of DP steels with low Cr, Mo contents and standard galvanizing and supercool processing	180
Figure 5.6.3. Tensile strength (UTS) of dual phase steels with standard galvanizing (D1) and supercool processing.	182
Figure 5.6.4. Yield strength (YS) of dual phase steels with standard galvanizing (D1) and supercool processing.	183
Figure 5.6.5. Total elongations (TE) of dual phase steels with standard galvanizing (D1) and supercool processing. TEs were converted to 2 inch standard specimen	184

Figure 5.6.6. YS/UTS ratios of dual phase steels with standard galvanizing (D1) and supercool processing.	185
Figure 5.6.7. SEM microstructures of DP steels with low Cr, Mo contents, (a) 4A1A, D1, (b) 4A1E, D1, (c) 4B1A, D1, (d) 4B1E, D1.	187
Figure 5.6.8. SEM microstructures of DP steels with low Cr, Mo and without vanadium addition, (a) (b): 4A1A, E1, (c) (d): 4A3A, E1, (e) (f): 4A1E, E1, (g) (h): 4A3E, E1.	188
Figure 5.6.9. (a) 4A3A, E3, (b) 4A3E, E3, (c) 4B3A, E3, (d) 4B3E, E3. Low magnification 2000x.	189
Figure 5.6.10. (a) 4A3A, E3, (b) 4A3E, E3, (c) 4B3A, E3, (d) 4B3E, E3. High magnification 8000x.	189
Figure 5.6.11. Volume fractions of martensite in low alloyed DPs with different Gleeble processings. .	192
Figure 5.6.12. The relationship between hole expansion ratio and heat treatments.	194
Figure 5.6.13. Hole expansion tested samples (a) 4A3A, D1, (b) 4B3A, D1, (c) high magnification image of the region inside the dashed square in (b), (d) 4A3A, E1, (e) 4B3A, E1, (f) high magnification image of the region inside the dashed square in (e). Vertical direction is the rolling direction.	195
Figure 5.6.14. (a) data points (UTS-HE) of low alloyed DPs, (b) averaged UTS values at four hole expansion ratio levels, 35-40%, 40-45%, 45-50% and 50-55%.	196
Figure 5.7.1. IPFs (a) 2A1E, (c) 2A1A, (e) 2B1E, (g) 2B1A; SE mappings (b) 2A1E, (d) 2A1A, (f) 2B1E, and (h) 2B1A. The IPF triangle describes the relationship between colors and orientations, and this triangle can be applied to all the IPFs in the following part of this thesis.	200
Figure 5.7.2. Inverse pole figures of (a) 2A3E, (b) 2B3E, (c) 2A3A and (d) 2B3A.	200
Figure 5.7.3. Stored energy mapping of (a) 2A3E, (b) 2B3E, (c) 2A3A and (d) 2B3A. The size of each image is 60 μ m \times 60 μ m.	201
Figure 5.7.4. Inverse pole figures of (a) 4A1E, (b) 4B1E, (c) 4A1A and (d) 4B1A.	203
Figure 5.7.5. Stored energy mappings of (a) 4A1E, (b) 4B1E, (c) 4A1A and (d) 4B1A, the size is 60 μ m \times 60 μ m.	204
Figure 5.7.6. Inverse pole figures of (a) 4A3E, (b) 4B3E, (c) 4A3A, and (d) 4B3A.	205
Figure 5.7.7. Stored energy mappings of (a) 4A3E, (b) 4B3E, (c) 4A3A, and (d) 4B3A, the size of each image is 60 μ m \times 60 μ m.	206
Figure 5.7.8. Tensile strength (UTS) of dual phase steels with standard galvanizing (D1) and supercool processing.	209
Figure 5.7.9. Tensile strength (UTS) of dual phase steels with standard galvanizing (D1) and supercool processing (E1, E2, and E3). The DPs with 80%CR are stronger than corresponding DPs with 50%CR.	210
Figure 5.7.10. relationship between total elongations and tensile strength of DP steels with vanadium addition and without vanadium addition. (a) red line is fitted for DPs with vanadium and black	

line is fitted for DPs without vanadium using exponential function ($TE\% \propto \exp(-UTS)$). (b) red line is linearly fitted for DPs with vanadium and black line is linearly fitted for DPs without vanadium. (c), (d) red solid, red dashed, black solid and black dashed lines are for 26000, 22000, 18000, 10000 UTSxTE (MPa x %) respectively. 211

Figure 5.7.11. Comparison of MA volume fraction vs UTS with the corresponding values obtained by Davies. Only dual phase steels with high Cr, Mo and galvanizing (D1) processing are shown in the figure. 212

Figure 5.7.12. Comparison of UTS vs UE with the corresponding values obtained by Davies. . Only dual phase steels with high Cr, Mo and galvanizing (D1) processing are shown in the figure. 212

Figure 5.7.13. Relationship between hole expansion ratios (HE%) and tensile strength (UTS), all the data of 64 DP steels were included..... 213

Figure 5.7.14. Relationship between hole expansion ratios (HE%) and heat treatment processing. 213

Figure 5.7.15. Post UE-HE data points for low alloyed and high alloyed steels with various conditions. The black line is fitted by linear equation, $PUE\%=0.13xHE\%+5.85$, the coefficient of determination R^2 is 0.24, and the Pearson's linear correlation coefficient ρ is 0.49..... 215

Figure 5.7.16. Reduction in area (RA)-HE data points for low and high alloyed steels with various conditions. The black lines were fitted by linear equations, (a) $HE\%=0.99xRA\%-17.6$, the coefficient of determination R^2 is 0.6, and the Pearson's linear correlation coefficient ρ is 0.76, the steels are with vanadium additions, (b) $HE\%=1.48xRA\%-41.2$, the coefficient of determination R^2 is 0.52, and the Pearson's linear correlation coefficient ρ is 0.76, the steels with and without vanadium additions are all included..... 215

Figure 5.7.17. Magnetic Field (in G) vs Moment/Mass (emu/g) curves of DPV, 72%CR supercooled steels..... 218

Figure 5.7.18. HRTEM images of DP 2B1E, E1 (50%CR, high CT 650°C), showing fine and dense VCx precipitates in ferrite matrix..... 223

Figure 5.7.19. (a) example showing the precipitation of nitrides, nitrogen-rich carbonitrides and carbides in 0.10%V steels at various nitrogen contents, (b) chemical driving force, $\Delta G_m/RT$, for precipitation of VC and VN in 0.12% V steel^[150]. 226

Figure 5.7.20. HRTEM images of VCx particles (a-c) in 2B1E (50%CR) cold rolled sheets (without heat treatments), (d) is the EDX from the particles indicated by the arrow in (c)..... 227

Figure 5.7.21. Predicted results from JMatPro4.0 of 2B (vanadium bearing steel), (a) amount of precipitates (M(C,N), M is alloying elements, AlN and MnS), (b) weight percent of different elements in M(C,N) and (c) contents of nitrogen in different phases (Austenite, ferrite, M(C,N) and AlN) at different temperatures at equilibrium states. 230

Figure 5.7.22. UE-n-value data points for low alloyed and high alloyed steels with various conditions (all the data of the 64 steels in Tables 5.7. and 5.7. were included). The black line is fitted by linear equation, $UE=63xn+0.13$, the coefficient of determination R^2 is 0.71, and the Pearson's linear correlation coefficient ρ is 0.84. 233

Figure 5.7.23. Work hardening ratios between engineering strain 0.2% and 0.5%, i.e. just after yielding of the steels, of the steels with high coiling temperatures 650°C, the sample IDs are listed in Tables 5.7.9 and 5.7.10.....	235
Figure 5.7.24. $\ln\sigma$ - $\ln\epsilon$ curves of DPs with E1 processing.	237
Figure 5.7.25. $\ln\sigma$ - $\ln\epsilon$ curves of DPs with D1 and E1 processing.	240
Figure A1. LePera etched microstructures of DPV annealed at 780°C for (a) 1 minute (18±1%MA), (b) 2 minutes (37±2%MA), and (c) 5 minutes (39±3%MA) and then water quenched.	249
Figure A2. LePera etched microstructures of DPNbV annealed at 780°C for (a) 1 minute (47±2%MA), (b) 2 minutes (54±1%MA), and (c) 5 minutes (85±1%MA) and then water quenched.	250
Figure A3. LePera etched microstructures of DPVN annealed at 780°C for (a) 1 minute (34±2%MA), (b) 2 minutes (38±2%MA), and (c) 5 minutes (39±3%MA) and then water quenched.	250
Figure A4. LePera etched microstructures of DPNb annealed at 780°C for (a) 1 minute (51±2%MA), (b) 2 minutes (54±3%MA), and (c) 5 minutes (64±3%MA) and then water quenched.	250
Figure A5. DPV, Gleeble A3 (standard galvanizing processing), IQ image (up left) (red lines 2°-5°, green lines 5°-15°, and blue lines 15°-180°), IPF mapping (up right), and IQ peak fitting curves (below).	251
Figure A6. DPNbV, Gleeble A3 (standard galvanizing processing), IQ image (up left) (red lines 2°-5°, green lines 5°-15°, and blue lines 15°-180°), IPF mapping (up right), and IQ peak fitting curves (below).....	252
Figure A7. DPVN, Gleeble A3 (standard galvanizing processing), IQ image (up left) (red lines 2°-5°, green lines 5°-15°, and blue lines 15°-180°), IPF mapping (up right), and IQ peak fitting curves (below).....	253
Figure A8. AlN found at the ferrite grain boundary for DP_NbV, GI (A3) standard galvanizing processing, carbon replica sample.	254

ACKNOWLEDGEMENTS

The completion of this thesis would have never been possible without the help, support and assistance from so many kind persons. Here, I would like to give my most sincere thanks to them.

First and foremost, I would like to thank my advisor, Professor Anthony J. DeArdo for his great guidance and generous support throughout my research. His invaluable advices and suggestions make the whole research so well organized and directed. Secondly, I would like to thank my academic advisor Albert Chi Fu To for the help on courses.

I would like to thank Dr. Ken Goldman. He is a very kind and generous man and a great teacher in both research and language. His help makes so many things much easier.

Special thanks are due to Dr. Xiaojun Liang and Professor Mingjian Hua for their great help in the research, helpful discussions and suggestions. Special thanks are also extended to Victoria Wang, Juha Uusitalo, Bing Ma, Brendan Connolly, Junyu Duan, Petch Janbanjong, Cole Van Ormer, and Dr. Susheng Tan, for their generous and constant help on my experiments.

I would like to thank the Basic Metals Processing Research Institute (BAMPRI) and the Mechanical Engineering and Materials Science Department, University of Pittsburgh for providing the facilities to conduct this work. I would also like to thank Vanitec Ltd., London (The Vanadium International Technical Committee) for financially sponsoring this work, and the United States Steel Research and Technology Center for in-kind assistance. Their generous support is greatly appreciated. Special thanks are also due for helpful discussions to Dennis Haezebrouck, Research and Technology Center of United States Steel Corp. and Robert Glodowski of Everaz, PLC.

I would also like to thank the undergraduate group members of BAMPRI, e.g. Patrick Andrew Soloski, Michael O'Donnell, Mitchell Stephen Hrapchak, Katia Santos, Joseph J Hartle, Nicholas J Thimons, Joshua Taylor Barron, and Anthony E Analo for their help on my experiments.

Last but not least, I would like to thank my parents for their love, support and courage.

Thank you all very much!

1.0 INTRODUCTION

Considering the increasing pressure from energy-saving and ecological responsibility, the automobile industry has to find promising steels to produce fuel-efficient vehicles by reducing the weight of vehicles. The application of advanced high strength sheet steels is a good choice, since they show both high strength and good ductility, as well as they can also reduce the weight, optimize environmental performance and improve passenger safety, but still at affordable cost.

Today various types of steels are used in automotive industry. The comparison of some of these steels is depicted in Figure 1.1^[1]. Interstitial-free (IF)^[2] steels with carbon content less than 0.01wt.% are extensively used in automotive industries for making car outer panels because of the high formability that they possess. However the tensile strength level of IF steels is relatively low. In recent years, efforts have been made to improve the strength of IF steels, using solid solution hardening, precipitation hardening or by means of grain refinement through SPD (severe plastic deformation) procedures. Bake-hardening (BH)^[3] steels are another class of forming steels with both good formability and high dent resistance used in automotive industry for outer panels. After forming and paint baking, they can offer high yield strength due to strain aging, which is the interaction between solute carbon and dislocations (formation of Cottrell atmospheres). However, as can be seen in Figure 1.1, both IF steels and BH steels have low tensile strength level compared with the other classes of steels.

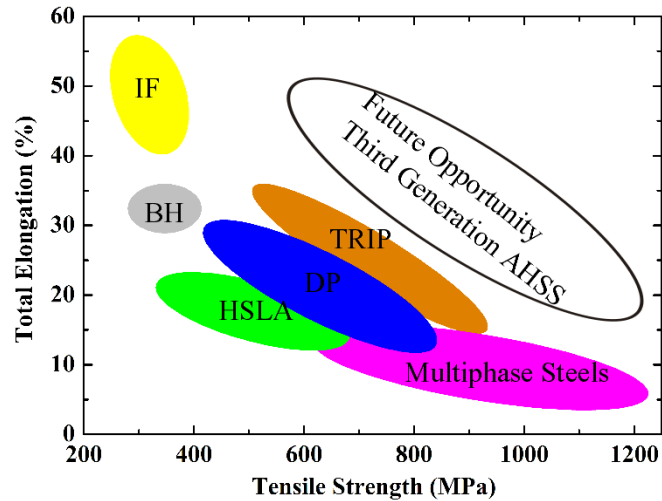


Figure 1.1. Comparison of tensile strength and total elongation for different types of steels

Efforts between the global steel and automobile industries have developed the “Advanced High Strength Steels” (AHSS). AHSS steels are multi-phase steels, whose microstructure may contain a defined content of martensite, bainite and/or austenite. Compared with conventional high strength steels (HSS or HSLA steels) which are hardened by solid solution, precipitation or grain refinement, the AHSS steels are hardened principally by phase transformation. The AHSS include dual phase (DP) steels, transformation induced plasticity (TRIP) and complex multiphase (CPS) steels. Due to their superiority in strength and ductility combination as compared with conventional HSS, AHSS enable higher energy absorption during impact and ensure safety when reducing weight. The TRIP^[4] steels with microstructure of ferrite, bainite and 5%~15% retained austenite possess high elongation and excellent sustainable work hardening ratio. The high ductility of this steel is the result of martensite formation from the retained austenite during deformation. High strength low-alloy (HSLA) steels are also used in automotive industries^[5, 6], which usually contain 0.05~0.25% carbon content to retain formability and weldability. Compared with conventional HSLA, dual-phase steels (DP) exhibit better ductility as shown in Figure 1.1.

The successful development of Ultra Light Steel Auto Body (ULSAB) in 1998 and the ULSAB-Advanced Vehicle Concepts (AVC) program^[7] have inspired researchers to do further research on the

Advanced High Strength Steels (AHSS). The AHSS (Dual-Phase and TRIP) used in automobile is expected to reduce fuel consumption, improve safety, and increase recyclability, all at reasonable prices.

Since most forming operations in automobiles involve plane strain bending or stretch-forming, the ideal steels must have moderate yield strength to improve die life and good work hardening. In addition, candidate steels must also have good sheared edge ductility and an acceptable bake hardening response. The modern dual-phase steels (DP) satisfy these requirements. Due to its particular advantage in mechanical properties, dual-phase steels are promising candidate for bumper beams, motor compartment-longitudinal rails, rocker inners, and door inners, and so on.

Today, DP590 (590MPa, UTS) and DP780 (780MPa, UTS) are commercial realities, while DP980 (980MPa, UTS) and DP1180 (1180MPa, UTS) are still being investigated. Firstly, in this thesis, the DP steels at the 980 MPa level that have been microalloyed with Nb, V and V-N and have been processed using a Continuous Galvanizing Line (CGL) simulation on a Gleeble 3500 unit will be studied in detail. After final CGL processing, these steels exhibited UTS values between 900 and 1100 MPa, and total elongations (corrected for sub-sized gauge length) between 8 and 17%. Some factors, e.g., the dissolution of cementite, recrystallization behavior of cold rolled ferrite, intercritical annealing temperature, and cooling rates will be studied and discussed. Then the effects of vanadium on the softening resistance during extended holding at zinc pot temperature and the precipitation hardening of vanadium carbonitrides will be investigated.

Most steel companies producing DP steels usually cool the strip from the intercritical annealing temperature (IAT) to zinc-pot temperature (460°C), and then either cool the strip to RT or reheat it to 520°C and then cool to RT. The tensile strength is closely related to the amount of martensite in the final microstructure which is controlled by the amount of the austenite formed during intercritical annealing, which is a common first step in producing the DP steels. So understanding the formation of austenite during intercritical annealing is very important in optimizing the processing schedules and compositions of steels. The formation of austenite can be affected by many factors, e.g. micro alloying elements, IAT,

heating rate or reduction of cold rolling. Secondly, in this thesis, the effect of cold rolling will be emphasized, which is related to the stored energy.

The stored energy is associated with the lattice defects and can reflect the extent of the deformation of grains. It is thought to provide the initial driving force for recovery and recrystallization during the annealing process. In this work, it was also found that increasing the stored energy in the initial cold rolled samples can make the formation of austenite during intercritical annealing faster, resulting in more austenite after only 1 minute annealing at different IATs. The stored energy was estimated using sub-grain method from EBSD data, and cross checked with IQ data and hardness values in order to get reasonable stored energy values. 60% and 72% cold reductions were applied in order to get different initial conditions, and, therefore, with different starting stored energy we can study how the stored energy can affect the formation of austenite. The effects of higher stored energy of the cold band with higher cold reductions on the final properties after full CGL process simulation will be shown.

Finally, in the late part of this thesis, research will be conducted on aluminum killed, low carbon (0.1%) steels containing Mn, Cr, and Mo. The steels were produced with and without V and at high and low levels of Cr and Mo. The four steels were processed using four CGL simulations, one a conventional GA simulation and three others where the steels were supercooled to various temperatures below the zinc pot temperature prior to being heated to the galvanizing temperature of 460°C.

However, before different CGL processing paths can be discussed, it is very important that the cold rolled condition going into the CGL anneal be fully understood. This cold rolled condition is comprised of two factors: (i) the stored energy in the hot rolled coil and (ii) the increase in this stored energy due to cold rolling. Together, these two factors have a large influence on both the amount of austenite formed at 790°C, and the amount of fresh martensite found in the final microstructure. Higher stored energy means more and finer austenite formed in the anneal at 790°C, therefore lower coiling temperatures and higher cold reductions together promote higher amounts of intercritically formed austenite. These also refine the ferrite grain size, as well. Two levels of cold reductions (50% and 80%) will be applied to study the influence of cold reductions on the final properties of dual phase steels.

Moreover, high and low coiling temperatures will be used to investigate the effects of coiling temperatures on the precipitation hardening from vanadium carbonitrides.

After final CGL processing, these steels exhibited UTS values between 800 and 1050 MPa, and total elongations (corrected for sub-sized gauge length) between 15 and 35%. The microstructural observations and processing-microstructure-property relations will be presented, described and discussed.

2.0 BACKGROUND

2.1 GENERAL DESCRIPTION OF DUAL-PHASE STEELS

Dual phase steels are characterized by a microstructure consisting of a dispersion of hard martensite particles in a soft, ductile ferrite matrix. There are two main phases, i.e., ferrite and martensite, in the microstructure essentially, although small amounts of bainite or retained austenite may also be present. According to some early researchers, it was postulated that the general dual-phase microstructure can be characterized as follows (Figure 2.1.1)^[8]:

- As in a duplex structure, the number of ferrite and martensite grains per unit volume is equal.
- As in a dispersion structure, the second phase martensite forms isolated zones surrounded by ferrite.
- As in a network structure, the martensite zones are all connected by ferrite grain boundaries.

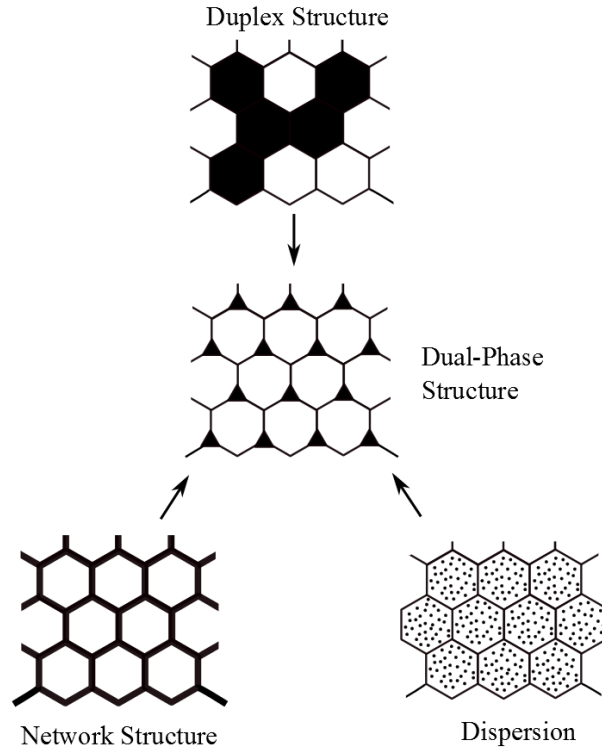


Figure 2.1.1. Schematic representation of basic two-phase microstructure species

Due to this typical microstructure, dual phase steels possess a number of unique properties compared with ferrite-pearlite steels such as plain carbon steels or the HSLA steels, Figure 2.1.2^[9]. The ferrite-pearlite steels have yield point elongation, and a high yield strength to ultimate tensile strength (YS/UTS) ratio. The dual phase steels have higher work hardening rates than conventional steels, a low 0.2 percent offset yield strength, high tensile strength, low yield strength to tensile strength ratio, continuous yielding behavior (no yield point) and high uniform and total elongation. The low yield strength combined with the good uniform elongation of these steels gives them good formability, suitable for forming both outer panels and body-in-white components used in the automotive industries. Due to the high tensile strength, together with the high work hardening rates which provide high strength after forming, they have the potential for significantly improved crash performance. As a result, these steels are an attractive material for weight-saving applications in automotive industries.

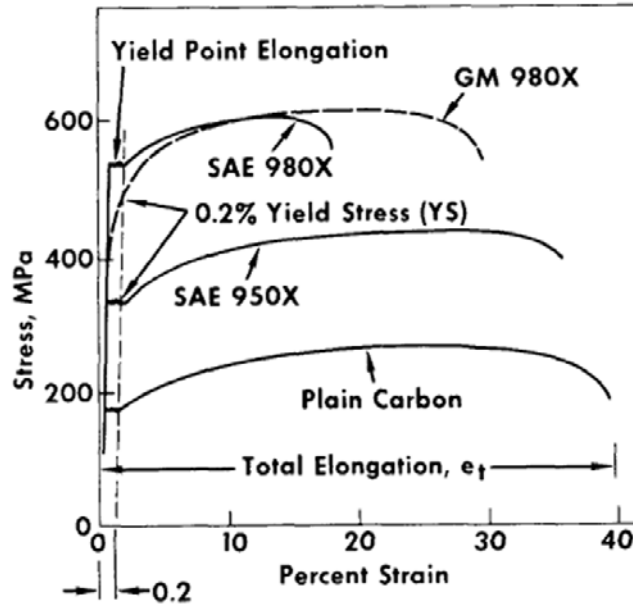


Figure 2.1.2 Schematic stress-strain curves for plain carbon, HSLA, and dual phase steels. SAE 950X and 980X are Society of Automotive Engineers designations for HSLA steels of different strength levels. GM 980X is a General Motors developed dual phase steel. GM 980^[9]

There are mainly two ways to produce the dual-phase steels. The first method develops the dual phase microstructure in the hot band^[10, 11]. The hardenability of the steel and the cooling rate are matched such that the ferrite forms during the cooling period between hot rolling and coiling while the martensite forms during coiling.

However, using the first method to produce dual-phase steels, it is difficult to get an optimum ratio of ferrite and martensite volume fraction since the transformation starts from a fully austenitic structure after hot rolling. Compared with the first method, the intercritical annealing method^[12, 13] makes it much easier to control the volume fraction of martensite, since the transformation starts from a two phase ($\alpha+\gamma$) region as shown in Figure 2.1.3.

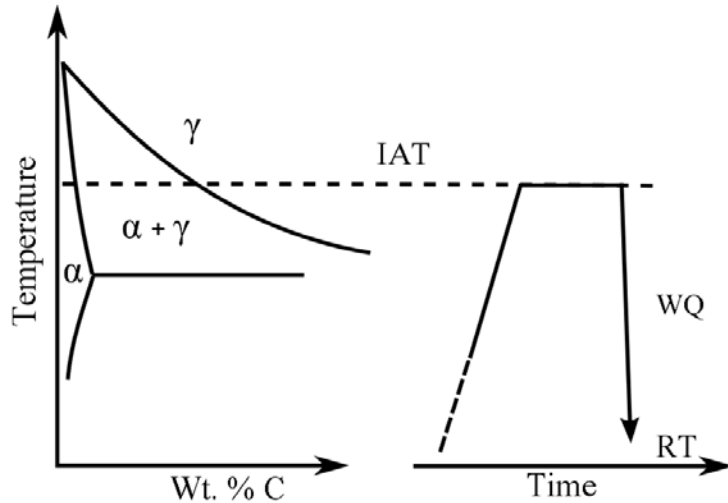


Figure 2.1.3 Schematic representation of intercritical annealing and water quenching (WQ) for developing dual phase structure, IAT means intercritical annealing temperature

From the Fe-C phase diagram, it is clear that at a low intercritical temperature, the carbon content in austenite is high, and the stability of austenite is high, but the volume fraction of austenite is low, while at a high intercritical temperature, the carbon content in austenite is low, and the stability of austenite is low, but the volume fraction of austenite is high according to the lever rule. Similarly, the carbon content in ferrite is higher at low intercritical temperature than that at high intercritical temperature. So the general idea to control the volume fraction of martensite in DP steel is to control the intercritical annealing temperature and the carbon content in the original steel. Usually, the volume fraction of martensite will be controlled around 20% to get a best combination of the mechanical properties^[14], because earlier research found that the ductility and impact toughness degrade rapidly with increasing martensite amount above 25%. By reheating the material into the two phase region ($\alpha+\gamma$) at some intercritical temperature and holding for some time, we can get proper amounts of ferrite and austenite. The austenite will be transformed into martensite during the subsequent cooling if the cooling rate is fast, e.g., water quenching. The cooling rate depends on the composition of the steel. It was found that the critical cooling rate (CR) to produce a dual-phase microstructure after cooling from the ($\alpha+\gamma$) region can be expressed in terms of a manganese equivalent (Mn_{eq}) as follows^[15]:

$$\text{Log CR(C/sec)} = -1.73\text{Mn}_{\text{eq}}(\%) + 3.95 \quad (2.1)$$

$$\text{Mn}_{\text{eq}}(\%) = \text{Mn}(\%) + 1.3\text{Cr}(\%) + 2.7\text{Mo}(\%) \quad (2.2)$$

2.2 MECHANICAL PROPERTIES OF DUAL-PHASE STEELS

The important factors that can influence the mechanical properties of dual-phase steels include the volume fraction of martensite, size and distribution of martensite, ferrite grain size, fine precipitates in the ferrite matrix, the morphology of ferrite and martensite, retained austenite, and so on^[16-33]. Much research has been done in order to understand the effects of these factors on the mechanical properties of dual phase steels. Obviously, it is extremely complex and difficult to completely understand the microstructure-mechanical properties relationships in dual-phase steels.

R.G. Davies^[21] investigated the relationship between flow stress (tensile strength and yield strength) and amount of martensite. In his research, the flow stresses were found to be mainly linearly related to percent martensite as shown in Figure 2.2.1. He also plotted the uniform elongation as a function of tensile strength as shown in Figure 2.2.2. As we can see, at a given strength level dual phase steels have superior ductility to standard HSLA steels, and the uniform elongation decreases with increasing tensile strength as can be expected.

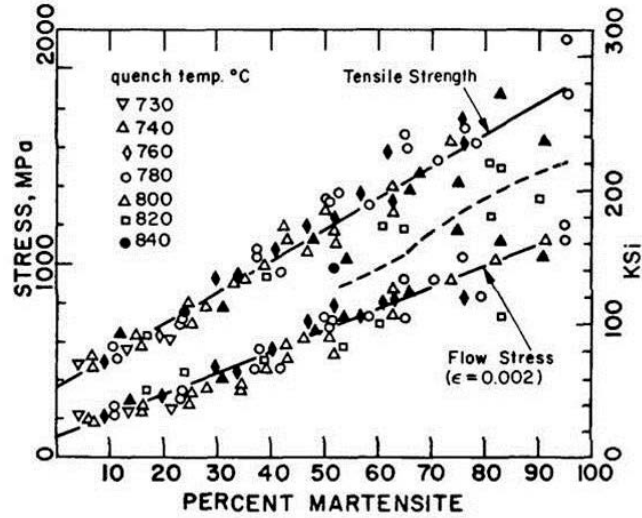


Figure 2.2.1 The 0.2 pct flow stress and the tensile strength as a function of percent martensite for the Fe-Mn-C alloys^[21]

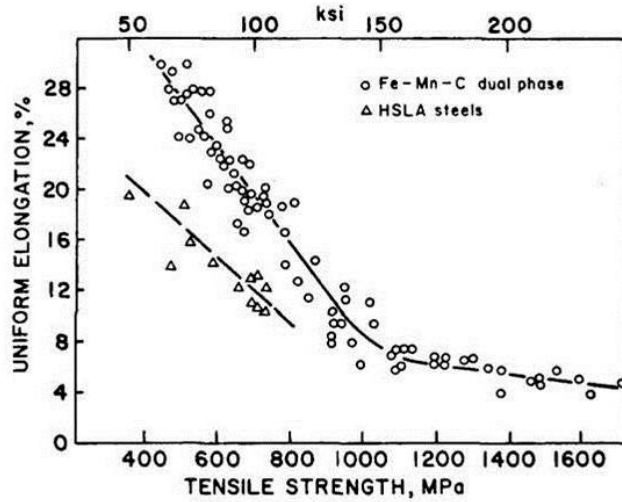


Figure. 2.2.2 Uniform elongation as a function of tensile strength for standard HSLA steels and Fe-Mn-C dual phase steels^[21]

2.2.1 Tensile strength and yield strength

If we assume the dual-phase microstructure is a mixture of two phases of equal density and applying the law of mixtures^[12, 14, 34], the relationship of carbon content between these two phases can be expressed as follows:

$$[C]_{\text{tot}}=[C]_{\text{m}} \cdot x_{\text{m}}+[C]_{\text{f}} \cdot (1-x_{\text{m}}) \quad (2.3)$$

where x_{m} is the volume fraction of martensite, $[C]_{\text{m}}, [C]_{\text{f}}, [C]_{\text{tot}}$ are carbon content (wt.%) in the martensite, ferrite and in the steel, respectively.

The same law of mixtures can be applied to ultimate tensile strength (UTS) and yield strength (YS) for simplicity:

$$(\text{UTS})_{\text{tot}}=(\text{UTS})_{\text{m}} \cdot x_{\text{m}}+(\text{UTS})_{\text{f}} \cdot (1-x_{\text{m}}) \quad (2.4)$$

$$(\text{YS})_{\text{tot}}=(\text{YS})_{\text{m}} \cdot x_{\text{m}}+(\text{YS})_{\text{f}} \cdot (1-x_{\text{m}}) \quad (2.5)$$

where $(\text{UTS})_{\text{m}}$ and $(\text{UTS})_{\text{f}}$ are the ultimate tensile strengths of the 100% martensite and ferrite phases respectively, while $(\text{YS})_{\text{m}}$ and $(\text{YS})_{\text{f}}$ are the yield strengths of the 100% martensite and ferrite phases, respectively.

However, the variation of ultimate tensile strength and yield strength with volume fraction of martensite is much more complex. Tamura et al.^[35], found that equation (2.5) was obeyed only when the values of the yield strength of the martensite $(\text{YS})_{\text{m}}$ and ferrite $(\text{YS})_{\text{f}}$ were nearly the same, as in tempered dual-phase steels. They introduced another parameter called C, which is $(\text{YS})_{\text{m}}/(\text{YS})_{\text{f}}$. If C is less than 3, the law of mixtures was nearly obeyed, while if C is more than 3, the value of yield strength first increased linearly with the volume fraction of martensite and then deviated strongly from this linear relationship at some value of x_{m} .

Speich and Miller^[36] suggested that the $(\text{YS})_{\text{m}}$ and $(\text{UTS})_{\text{m}}$ in (2.4) and (2.5) may be replaced by $(\text{YS})_{\text{m}'}$ and $(\text{UTS})_{\text{m}'}$, where

$$(\text{YS})_{\text{m}'}=(\text{YS})_{\text{f}}+(1/3(\text{YS})_{\text{m}}-(\text{YS})_{\text{f}})x_{\text{m}}/100 \quad (2.6)$$

$$(\text{UTS})_{\text{m}'}=(\text{UTS})_{\text{f}}+((\text{YS})_{\text{m}}-(\text{UTS})_{\text{f}})x_{\text{m}}/100 \quad (2.7)$$

Equations 2.6 and 2.7 are a “modified law of mixtures”. The yield strength of martensite is related to the carbon content of the martensite phase, as follows^[37]

$$(\text{YS})_{\text{m}}(\text{MPa})=620+2585C_{\text{m}} \quad (2.8)$$

where C_{m} is the carbon content of the martensite phase in weight percent.

$$C_{\text{m}}=C_{\text{o}}+\rho_{\text{f}}/\rho_{\text{m}}(100/x_{\text{m}}-1)(C_{\text{o}}-C_{\text{f}}) \quad (2.9)$$

where ρ_f is the density of the ferrite, ρ_m is the density of martensite, C_f is the carbon content of the ferrite and C_o is the carbon content of the steel. ρ_f/ρ_m is approximately 1.025, or simply 1. If $C_o \gg C_f$, then we can simply use^[14, 36]

$$C_m = 100(C_o/x_m). \quad (2.10)$$

2.2.2 Work hardening

The work-hardening behavior of dual-phase steels can be simply described by the Hollomon equation^[38], which is commonly used to analyze the work-hardening behavior of metallic materials,

$$\sigma = K\varepsilon^n \quad (2.11)$$

where σ and ε are the true stress and true strain, respectively, n is the work-hardening exponent and K is the strength coefficient. From the Considere' condition^[14, 39]

$$(d\sigma/d\varepsilon) = \sigma \quad (2.12)$$

and assume this power law (2.11) is obeyed, it can be shown that

$$n = \varepsilon_{u, \sigma} \quad (2.13)$$

where $\varepsilon_{u, \sigma}$ is the true uniform strain. The work of Davies^[21] indicates that the uniform elongation (n value) decreased in a nonlinear manner with increasing percent martensite. Speich and Miller^[36] in addition, found that the uniform elongation increased slightly when the carbon content of the martensite phase was decreased. The empirical equation is

$$\frac{\varepsilon_{u, \sigma}}{\varepsilon_{u, \sigma}^0} = 1 - 2.2C_m \left(\frac{P_m}{100} \right)^{1/2} \quad (2.14)$$

where $\varepsilon_{u, \sigma}$ and $\varepsilon_{u, \sigma}^0$ are the uniform elongation for the composite and for 100 percent ferrite, respectively.

P_m is the volume fraction of martensite. Similarly, the total elongation was found to depend not only on the volume fraction of martensite but also the carbon content of the martensite. The empirical equation is

$$\frac{e_t}{e_{t,\alpha}^0} = 1 - 2.2C_m \left(\frac{P_m}{100} \right)^{1/2} \quad (2.15)$$

where e_t and $e_{t,\alpha}^0$ are the total elongation for the composite and for 100 percent ferrite, respectively.

The value of n can be obtained using a ln-ln plot of true stress and true strain, since equation (2.11) can be expressed as

$$\ln \sigma = \ln K + n \ln \epsilon \quad (2.16)$$

However, a nonlinear variation of $\ln \sigma$ with $\ln \epsilon$ can usually be observed, which may be due to different stages of work hardening.

Some researchers suggested that work-hardening behavior in dual-phase steels occurred in three different stages^[14, 36, 40, 41], which could be revealed by the Jaoul-Crussard(J-C) analyses^[42-46]. The J-C analyses are based on the following equation:

$$\sigma = \sigma_0 + K\epsilon^n \quad (2.17)$$

where σ_0 and ϵ_0 are reference true stress and true strain, respectively. The equation (2.17) can be expressed as

$$\ln\left(\frac{d\sigma}{d\epsilon}\right) = \ln K + \ln n + (n-1) \ln \epsilon \quad (2.18)$$

Analysis of the true stress-strain using equation (2.18) is referred to the J-C analysis, by using which several researchers have been able to reveal the three stages of work hardening in dual-phase steels. These stages of work hardening may be explained by the following deformation mechanisms^[14, 36, 40, 41]:

(1) Stage I consists of homogeneous deformation of the ferrite matrix by the glide of mobile dislocations present near the martensitic regions.

(2) Stage II covers a diminished work hardening with constrained ferrite deformation and with possible transformation of retained austenite to martensite.

(3) Stage III consists of ferrite deformation with attendant cross-slip and dynamic recovery together with martensitic deformation.

However, some researchers, e.g., Jiang et al.^[47], observed only two stages of work-hardening behavior in dual-phase steels containing a volume fraction of martensite larger than 0.3 using the modified J-C analysis.

The modified Crussard-Jaoult (C-J) analysis^[48, 49] based on the Swift equation^[50], which is known to best describe the work hardening behavior of dual phase steels, was used in this study. The Swift stress-strain relationship is expressed as

$$\varepsilon = \varepsilon_0 + k\sigma^m, \quad (2.19)$$

where ε and σ are the true strain and true stress, respectively, m is the strain hardening exponent, and ε_0 and k are the material constants. When we differentiate the logarithmic form of Eq. (2.19) with respect to ε , we get

$$\ln\left(\frac{d\sigma}{d\varepsilon}\right) = (1 - m) \ln(\sigma) - \ln(km). \quad (2.20)$$

The values of m can be obtained from the slope, $(1-m)$ of the $\ln(d\sigma/d\varepsilon)$ versus $\ln\sigma$ curves. From the $\ln(d\sigma/d\varepsilon)$ versus $\ln\sigma$ curves we can clearly see the different stages of work hardening behavior .

The instantaneous n -value can be defined as the slope of the stress-strain curve in its logarithmic form.

$$n(\varepsilon) = \frac{d(\ln\sigma)}{d(\ln\varepsilon)} \quad (2.21)$$

where ε is true strain, σ is true stress. The so defined differential n -value is independent of strain hardening laws.

2.2.3 Ductility

Most of the previous results on the ductility of dual-phase steels indicate that both uniform elongation and total elongation decrease with the volume fraction of martensite (V_m)^[21]. Many investigators suggest that the type of martensite dictates the ductility of dual-phase steels (twinned or lath) and conclude that a finer microstructure shows higher ductility. Great efforts have been made to develop an expression for uniform or total elongation in terms of the volume fraction of martensite. But no single expression can explain all the situations.

It is suggested that the lower values of the carbon content of the martensite phase favor higher ductility. Speich and Miller^[36] argued that the lower carbon content of the martensite increased ductility because cracking of the martensite particle or decohesion of the martensite/ferrite interface then became more difficult. Rashid^[51] argued that the improved ductility of ferrite-martensite steels in contrast to ferrite-pearlite steels was caused by the higher plasticity of the martensite phase. The distribution of the martensite must also influence ductility. Chains of martensite particles that are linked up may be detrimental to ductility because this may offer an easy crack propagation path through the ferrite matrix. So the uniformly dispersed, small martensite particles are desired in order to get high ductility.

Lowering the carbon content of the ferrite, as well as increasing the amount of epitaxial (“new”) ferrite can improve the ductility of dual phase steels. The retained austenite can also improve the ductility of the dual phase steels due to the transformation induced plasticity (TRIP) mechanism. Speich and Miller^[36] argued that when large amounts of retained austenite were present and when the stability of the austenite is sufficient that transformation of retained austenite occurs late in the plastic deformation, then large effects on uniform elongation can be expected. However, small amounts of retained austenite and early transformation of the retained austenite can affect the ductility negligibly.

2.2.4 Yielding behavior

Dual phase steels usually exhibit continuous yielding and low yield strength to tensile strength ratio. In order to explain the continuous yielding and low yield strength of dual phase steels, several models have been proposed. It has been suggested that the internal stresses play an important role in the yielding behavior and that the mobile dislocations nucleated at martensite particles due to transformation stresses can significantly lower the yield strength. Internal residual stresses arise as a result of differential thermal contraction of the terminal phases, as well as the transformation strains due to volume increase from the austenite-martensite phase transformation. Speich et al.^[52], suggested that the residual stress pattern around the martensite particles is similar to that in the case of a spherical hole in an infinite matrix when the hole is expanded by a uniform internal pressure. There is a plastic zone immediately adjacent to the particles in which the yield stress of the ferrite matrix is exceeded due to transformation stresses. Out of this plastic zone the stresses are in an elastic state and decay rapidly with increasing distance from the martensite particle. As a result, even when the applied stresses are below the normal yield stress, the plastic deformation will occur due to the combined effects of the applied stresses and the residual elastic stresses.

If we further consider the dislocations around martensite particles, which can be observed in TEM microstructures, a mobile-dislocation-density model can be used to explain the initial yielding behavior of dual-phase steels^[52]. Since the existence of a bundle of mobile dislocations about martensite particles, low applied stresses are needed to promote the motion of the existing dislocations and so the plastic deformation occurs. These suggestions can be supported by the tempering results of dual phase steels. After tempering at high temperatures, discontinuous yielding returns due to the absence of residual stresses and that the overall dislocation density has been significantly lowered.

However, some researchers proposed that the major effect of the transformation stress on the mechanical properties of the dual phase steel is the generation of mobile dislocations around the martensite particles and that the internal stresses at the ferrite-martensite interfaces should have little

effect on the yield strength. Crawley et al.^[13], argued that the transformation strain generates stresses in the ferrite matrix which decrease as $1/r^3$ from a maximum shear stress of

$$\tau_{\max} = \sim 0.012\mu \quad (2.22)$$

which is large enough to cause motion of existing dislocations to nucleate fresh dislocations. Here, μ is the shear modulus of the matrix. However, the only average stress in the matrix is an image stress which is a hydrostatic tension

$$\sigma_m = \sim 0.002\mu \quad (2.23)$$

This hydrostatic stress is supposed to have no effect on the yield strength. Their tensile results from the dual phase steel and the ferrite phase also show no decrease in the yield strength due to the internal residual stresses at the ferrite-martensite interface.

2.3 ALLOYING ELEMENTS

The addition of alloy elements, e.g., V, Nb, Mn, Mo, N, in a dual-phase steel can increase hardenability, refine grain size, and affect the martensite formation during heat treatment. A secondary effect would be to strengthen the ferrite phase by solid solution strengthening or by precipitation hardening, which may lower the ductility.

2.3.1 Manganese

Manganese plays at least three roles in carbon steels, i.e. as deoxidizer, desulphurizer, and as a hardening element. Manganese and iron are completely isomorphous and can form continuous solid solution. Mn also reacts with carbon to form carbide. The double effects which are the solution of Mn in ferrite and the presence of manganese carbide, undoubtedly have a significant effect on the mechanical properties of the steel^[53]. Manganese is one of the major austenite stabilizers. It is reported that the stabilization of

austenite as a single phase at room temperature requires adding 18 to 30% Mn^[54-57]. High-strength steels with reasonable plasticity needs some amount of retained austenite because of the TRIP phenomenon. Mn content ranging between 3 and 13% is thought to be enough for retention from 15 to 30% of retained austenite^[53, 58-61]. However the Mn content normally will be controlled to be less than 2%.

The addition of Mn can also lower the critical temperatures such as Ar1 of steel. The research done by Matsushita^[62] indicated that the magnitude of this effect on the Ar1 transformation temperature in iron-carbon alloys is slightly less than 20°C for each percent of Mn, provided the total amount is less than 9.8 percent. Another effect of Mn is the left shift of the eutectoid ratio, i.e. to a lower percentage of carbon^[63].

The effect of Mn on the grain size of steel also was investigated. Howe^[64] pointed out that the effect of Mn on the mechanical properties of the steel is due primarily to its retarding action on the transformations and on the coalescence of the microconstituents into progressively coarser masses. The retarding effect on the structural changes shows itself by leading in general to finer structure, finer ferrite masses, finer network structure, and finer pearlite. Moreover the segregation of manganese^[65, 66] is thought to be the main reason for the formation of banded structures in steels, which will be discussed in the following section.

2.3.2 Vanadium

The main metallurgical properties of vanadium in steel are the high solubility of the carbonitrides of vanadium in austenite, the low solute drag coefficient of vanadium and the positive interaction of vanadium with nitrogen which provides an effective use of the residual nitrogen in steel^[67]. The high solubility of V(C,N) has a number of benefits including excellent castability with minimal cracking, reduced reheat temperature requirements and predictable strengthening over a large alloy range. The high solubility of the V reduced the tendency to precipitate in the grain boundaries, thereby reducing the cracking sensitivity. The precipitation of V(C,N) or VC will start when the ferrite has formed. It is

deduced that the vanadium segregation on migrating austenite/ferrite interphase boundary is quite important to understand the interphase boundary precipitation behavior of vanadium carbide during isothermal ferrite transformation^[68]. Vanadium has a relative low solute drag coefficient relative to other microalloys, e.g., Nb, Ti. So the austenite recrystallization will not be retarded, and it is easier to get complete recrystallization of the austenite through the thickness of the slab during rolling. Vanadium is the only microalloy element that effectively strengthens steel as a nitride precipitate. The VC is much more soluble than VN, resulting in the driving force for V precipitation to be much stronger with N present. Controlling the nitrogen level maximizes the strengthening of the vanadium containing steels and the preferred precipitation of V(C,N) minimizes the risks of nitrogen strain aging.

Besides the above three main properties of vanadium in steels, a large amount of research reveals other effects of vanadium, the mechanism of precipitation, and so on. The addition of vanadium can promote the formation of acicular ferrite^[69-71]. It is also suggested that the intragranular vanadium segregation to form clusters or regions rich in vanadium may facilitate the intragranular ferrite nucleation. The vanadium segregation in the microstructure may be related to the effect of vanadium in encouraging the formation of acicular ferrite. The segregation of vanadium to the austenite grain boundaries may cause suppression of the grain boundary reaction to produce coarse grains^[69].

2.3.3 Niobium

The precipitation of niobium carbide or nitride can strengthen the steels^[72-74]. The NbC carbides have the NaCl structure. The NaCl-type carbides adopt the Baker-Nutting orientation relation in ferrite, i.e., (100)bcc//(100)fcc, and [011]bcc//[010]fcc^[75, 76]. The lattice parameters of the bcc ferrite and the fcc NbC (NaCl type) phase are 0.286 and 0.447 nm, respectively. The misfit is around 40% in the direction perpendicular to the (001) habit plane and is around 10% in the direction parallel to the habit plane. The precipitation of NbC in the ferrite matrix can strengthen the ferrite due to the distortion of the ferrite lattice and by acting as Orowan barriers to dislocation motion.

It was reported that Nb decreases the transformation start temperature, A_{r1} , of austenite to ferrite^[77]. Nb in solution in austenite and segregated to the austenite grain boundaries retards the recovery and recrystallization of deformed austenite^[77, 78], where defects stored in the austenite provide intragranular nucleation sites for ferritic phases. The Nb segregated at the austenite grain boundaries can promote the formation of bainite or acicular ferrite, and suppress the formation of polygonal ferrite^[77]. Since the dislocation density in bainite or acicular ferrite is higher than polygonal ferrite, as well as the grain size of bainite or acicular ferrite is smaller, the Nb-microalloyed steels will be further strengthened^[77]. It was also observed that Nb atoms are distributed in ferrite non-randomly, resulting in clusters together with N atoms. The clusters may have a cluster strengthening effect^[79], along with the solid solution strengthening effect from individual Nb solute atoms throughout the ferrite matrix.

2.3.4 Chromium and molybdenum

One challenging for producing high strength dual phase steels using hot-dip galvanizing line is the risk of bainite formation during holding at zinc pot temperature (460°C). The formation of bainite can decrease the amount of martensite, reduce the tensile strength and increase the yield strength, and thus the yield to tensile strength ratios and work hardening exponents (n-values) increased. To avoid the bainite transformation at zinc pot temperature, the additions of alloying elements, such as Mo, Cr and Mn, will usually be used. Mo has the largest effect on shifting the bainite start curve towards longer time (to right on TTT or CCT diagrams), followed by Cr, Mn, Cu, Ni and Si^[80-82]. Moreover, extensive research has shown that the additions of Mo and Cr can decrease the B_s temperature. In order to increase the hardenability and stability of intercritically formed austenite, and thus reduce the possibility of bainite transformation, the additions of Mo and Cr are helpful to produce low carbon DP steels of higher strength levels (DP780-DP1180).

Davies^[83] investigated the effects of Mo on the properties of DP steels. In his study, he found that a lack of hardenability (without Mo additions) allows the formation of nonmartensitic products and the

strength decreased rapidly. When increasing the intercritical annealing temperature, the increase in the amount of austenite decreased the carbon content and hardness of austenite, and the additions of elements Mn, Mo and or V can increase the hardenability of the austenite with lower carbon content. He found that the DP steels with Mo addition had essentially constant strength with increasing annealing temperature, while for leaner alloys higher cooling rate should be applied in order to prevent the decrease in strength. These findings suggested that the element Mo can effectively increase the hardenability of the intercritically formed austenite.

Beside the fact that Mo and Cr can make the bainite transformation sluggish during galvanizing operation, the additions of Mo and Cr can increase the tensile strength due to solid solution strengthening in general. Mo can retard the growth of austenite during intercritical annealing and impede the growth of ferrite and thus can refine the microstructure^[84]. However, Davies^[83] found that Mo did not appear to exert any influence on the ferrite grain size. Cr and Mo are both carbide-forming elements and can decrease the carbon diffusivity by attracting carbon atoms and raising the diffusion activation energy of carbon^[85].

The effects of Cr, Mo contents on the properties of dual phase steels will be carefully investigated in this thesis.

2.4 FORMATION OF AUSTENITE

With the development of dual phase steels, the interest in studying the formation of austenite has been increased. During the last 3 decades, a lot of work has been done to understand the formation of austenite during heat treatments. The formation of austenitic phase can occur in pearlite as well as in ferrite regions^[86].

For hypoeutectoid steel consisting of ferrite and pearlite, upon heating the steel from room temperature (RT) to some temperature between A1 and A3 temperatures, the transformation of austenite

in pearlite and in ferrite-ferrite grain boundaries can be schematically described in Figure 2.4.1 (a)^[80]. The first situation related to the formation of austenite within the pearlite phase at the ferrite-cementite interface can be schematically represented in Figure 2.4.1 (b)^[80] which shows the variation of carbon content across cementite-austenite-ferrite interfaces. In this situation, the interface movement is controlled by the carbon diffusion through the austenite phase. The second situation is related to the austenite formation on ferrite-ferrite grain boundaries. Due to the difference in carbon concentration at the ferrite/cementite ($C^{\alpha/\theta}$) and ferrite/austenite ($C^{\alpha/\gamma}$) grain boundaries, a concentration gradient within the ferrite phase is present, creating the driving force for carbon to diffuse toward the ferrite-austenite grain boundary. The subsequent growth of the austenite nuclei requires the diffusion of carbon from cementite into the not-transformed ferrite. The velocity of the austenite growth in this stage depends on how fast the carbon is supplied to it. So the formation of austenite in pearlite is much faster than that in the ferrite-ferrite grain boundaries due to the shorter diffusion distances and the higher carbon concentration.

In addition, the research done by Garcia and DeArdo^[87], as well as many others^[88-92], found that austenite was preferentially formed on the ferrite-ferrite grain boundaries with carbide particles. In the case where alloy carbides, e.g., vanadium carbides, are present, it has been suggested that the vanadium carbide also has the role of cementite particles to help the nucleation of austenite at the ferrite grain boundaries^[93].

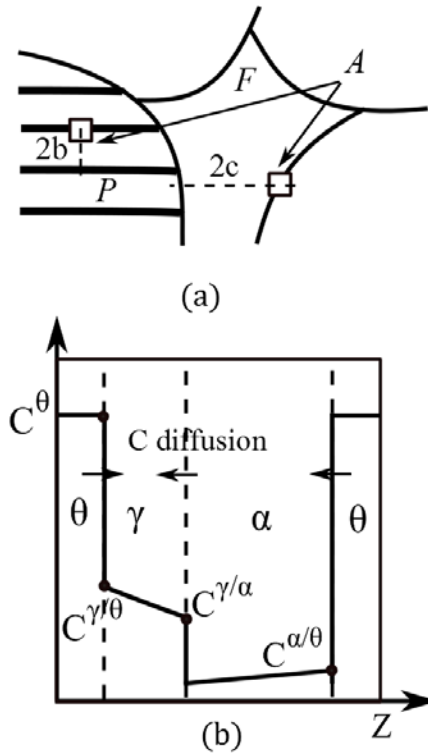


Figure 2.4.1 (a) Schematic view of the microstructure, (b) variation of the carbon content across the cementite-austenite-ferrite boundaries, F=ferrite, A=austenite, and P=pearlite^[80]

According to the research done by Speich et al., who studied the intercritical annealing of DP steels, the ferrite-to-austenite transformation begins with the nucleation of austenite at the ferrite-pearlite interfaces and growth of austenite into pearlite. It is assumed that the nucleation of austenite is instantaneous and with nearly no nucleation barrier. The rate of growth in this first stage is controlled primarily by carbon diffusion in austenite. The second step of the transformation is the growth of austenite into ferrite which is controlled by the carbon diffusion in austenite and the manganese diffusion in ferrite. In the final step, the equilibrium between ferrite and austenite is achieved by manganese diffusion through austenite.

The formation of austenite can be affected by heating rate, the amount of cold rolling, etc. Cold rolling increases dislocation density, reduces the interlamellar spacing in pearlite as well as the pearlite

band spacing if pearlite banding exists in the initial microstructure. So the dissolution of cementite and the growth of austenite are accelerated.

There are several models to describe the formation of austenite. The first one, proposed by Judd and Paxton^[94] who considered the binary Fe-C system, assumed that: (1) local equilibrium at all interfaces exists, (2) during the growth of austenite, carbon diffusion in ferrite is negligible, (3) capillarity effects on the dissolution rate of the cementite particles were negligible. Fig.2.4.2 shows the carbon concentration profile crossing the cementite-austenite-ferrite interfaces. From the flux balance at the ferrite/austenite interface, we can obtain:

$$(c^{\gamma/\alpha} - c^{\alpha}) \frac{dr_1}{dt} = -(D_c^{\gamma})_{r_1} \left(\frac{dc}{dr} \right)_{r_1} \quad (2.24)$$

where $c^{\gamma/\alpha}$ and c^{α} are carbon concentration at the interface in austenite and ferrite, respectively, r_1 is the outer radius of the austenite, $(D_c^{\gamma})_{r_1}$ is the diffusion coefficient of carbon in austenite, and t is the time. The positions of the Fe_3C/γ interface, r_2 , and γ/α interface, r_1 , as a function of time can be determined using the following equation proposed by Judd and Paxton^[94],

$$t = \frac{1}{2(D_c^{\gamma})_{r_1}} \left(\frac{c^{\gamma/\alpha} - c^{\alpha}}{c^{Fe_3C/\gamma} - c^{\gamma/\alpha}} \right) \left\{ r_o^2 \left(1 + \frac{1}{K} \right) - r_1^2 - \frac{1}{K} \left[r_o^3 \left(1 + \frac{1}{K} \right) - r_1^3 K \right]^{2/3} \right\} \quad (2.25)$$

where r_o is the radius at $t = 0$, and

$$K = \frac{(D_c^{\gamma})_{r_2}}{(D_c^{\gamma})_{r_1}} \left(\frac{c^{\gamma/\alpha} - c^{\alpha}}{c_c - c^{Fe_3C/\gamma}} \right) \quad (2.26)$$

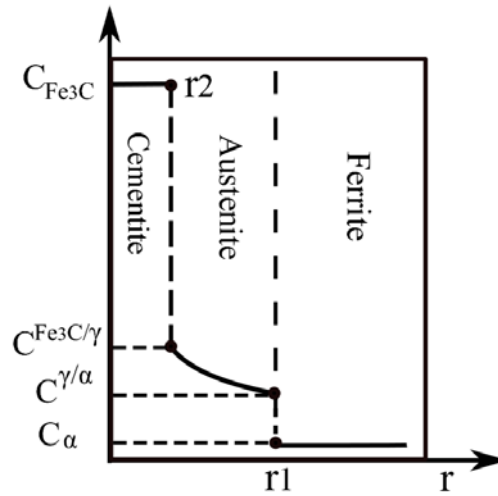


Figure 2.4.2 Carbon concentration profile around the carbide spheroid during dissolution^[88]

However, this model only applied to situations of low volume fraction of austenite, where the carbon needed for austenite growth can come from the adjacent cementite particle. Wycliffe et al.^[95], considered both ternary Fe-C-Mn and quaternary Fe-C-Mn-Si steels with ferrite-pearlite mixtures. In their calculations, for the initial conditions, the carbon content in ferrite was assumed to be negligible and the carbon content of austenite was assumed uniform and of eutectoid composition, C_e^E . The time for the nucleation of austenite from pearlite was neglected. The initial concentration of manganese was also assumed to be uniform as C_{Mn}^0 . The initial structure is schematically depicted in Figure 2.4.3 (a) and the initial concentration profiles are illustrated in Figures 2.4.3 (b) and (c).

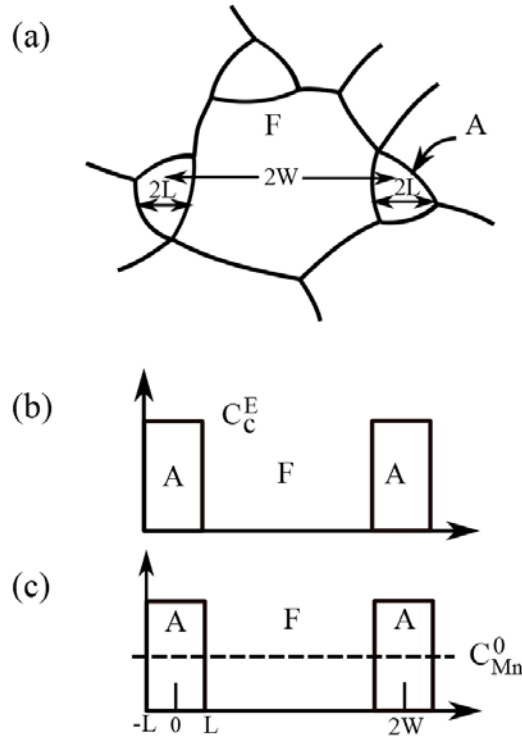


Figure 2.4.3 Initial conditions. A ferrite-pearlite mixture is heated into the intercritical range to produce austenite particles of width, $2L$, separated by distance, $2W$, as illustrated schematically in (a). The austenite is initially of eutectoid composition C_C^E , with a carbon concentration profile as in (b). The manganese concentration is uniform as shown in (c)

For the initial growth controlled by carbon diffusion, the austenite-ferrite interface velocity, $\frac{dX_0}{dt}$,

is related to the flux, J , of carbon and manganese, and the concentration difference, ΔC , as:

$$\left| \frac{dX_0}{dt} \right| = \left| \frac{J_{Mn}}{\Delta C_{Mn}} \right| = \left| \frac{J_c}{\Delta C_c} \right| \quad (2.27)$$

the flux is determined by Fick's first law:

$$J = D \frac{dC}{dX} \quad (2.28)$$

Further growth after carbon has reached uniform activity throughout the material will proceed under manganese diffusion control in the ternary Fe-C-Mn system.

The net interface velocity, $\frac{dX_0}{dt}$, is then the sum of the component due to flux in α and flux in γ :

$$\frac{dX_0}{dt} = \left(\frac{dX_0}{dt}\right)^\alpha + \left(\frac{dX_0}{dt}\right)^\gamma \quad (2.29)$$

$\left(\frac{dX_0}{dt}\right)^\alpha$ can be calculated as :

$$D_{Mn}^\alpha \frac{c_{Mn}^0 - c_{Mn}^\alpha}{f} = (C_{Mn}^\gamma - C_{Mn}^\alpha) \left(\frac{dX_0}{dt}\right)^\alpha \quad (2.30)$$

where f is used to determine the magnitude of the concentration gradient in the ferrite. f can be calculated using mass balance of Mn.

$\left(\frac{dX_0}{dt}\right)^\gamma$ can be calculate as:

$$\left(\frac{dX_0}{dt}\right)^\gamma = \frac{J^\gamma}{c_{Mn}^\gamma - c_{Mn}^\alpha} \quad (2.31)$$

J^γ is derived using Fick's first law:

$$J^\gamma = D_{Mn}^\gamma \left(\frac{dc_{Mn}^\gamma[x]}{dx}\right)_{x=X_0} \quad (2.32)$$

Austenite growth ends when the flux of manganese in the austenite equals that in the ferrite:

$$|J^\gamma| = |J^\alpha| \quad (2.33)$$

Using the similar analysis as in the ternary situation, Wycliffe et al, also considered the Fe-C-Mn-Si quaternary case. The net interface velocity can be expressed as:

$$\left(\frac{dX_0}{dt}\right)_{Mn} = \left(\frac{dX_0}{dt}\right)_{Mn}^\alpha + \left(\frac{dX_0}{dt}\right)_{Mn}^\gamma \quad (2.34)$$

$$\left(\frac{dX_0}{dt}\right)_{Si} = \left(\frac{dX_0}{dt}\right)_{Si}^{\alpha} + \left(\frac{dX_0}{dt}\right)_{Si}^{\gamma} \quad (2.35)$$

In the quaternary case, $C_{Mn}^{\gamma}[X]$ and $C_{Si}^{\gamma}[X]$ may not be expressed analytically. At each interface position $C_{Mn}^{\gamma}[X]$ and $C_{Si}^{\gamma}[X]$ are determined iteratively such that the interface velocity based on the flux of Mn equals that based on the flux of Si, i.e. :

$$\left(\frac{dX_0}{dt}\right)_{Mn} = \left(\frac{dX_0}{dt}\right)_{Si} \quad (2.36)$$

2.5 TEMPERING OF DUAL-PHASE STEELS

In the use of dual phase steels as automobile materials, galvanizing for corrosion protection will be carried out prior to forming any components, while finished components are usually paint baked. So the tempering step, i.e. galvanizing around 460°C or paint baking around 170°C, is often applied for the usage of dual phase steels. Moreover tempering produces various microstructural changes and hence complex mechanical property changes in dual phase steels, and can be used as a post-continuous annealing step to improve the strength-ductility combination^[9, 14, 52, 96-104]. So the knowledge of any mechanical property changes resulting from tempering is desirable.

Rashid et al.^[9, 96] investigated the mechanical property changes in a vanadium bearing dual phase steel upon tempering below 500°C. Though they found that the mechanical properties cannot be improved further by tempering below 500°C, the mechanical property changes can be well explained on the basis of microstructural changes observed in the ferrite, martensite and retained austenite. In their study, tempering at low temperatures resulted in an increase in yield strength, which can be explained by the observed relaxation of residual stress in the ferrite-martensite interfaces and the rearrangement of dislocations in the ferrite, as well as the fine cementite precipitates in both ferrite and retained austenite,

and a decrease in tensile strength, which is related to the precipitation of cementite particles in the martensite. When tempering at higher temperatures, the large decrease in ductility seemed to be related primarily to the decomposition of the retained austenite to upper bainite, and hence no contribution from the transformation induced plasticity or TRIP phenomenon.

Speich et al.^[14, 52, 98] also investigated the effect of tempering at different temperatures on the strength, yield behavior and ductility of ferrite-martensite dual phase steels. They found that the tensile strength decreased after tempering at both low and high temperatures in a manner that can be explained from the volume fraction and change in hardness of the martensite phase using a simple composite-strengthening model. However, the yield behavior was complex since it can be affected by residual stresses, carbon segregation to dislocations, mobile dislocation density, transformation of retained austenite and plastic incompatibility of the hard and soft phases. When tempering at low temperatures, e.g., 200°C, in their study, at low percentages of martensite the residual stresses in the ferrite are low and can be relieved by tempering, resulting in the return of discontinuous yielding and the large increase in yield strength. Increasing the amount of martensite, the residual stresses in the ferrite are larger and can be only partly relieved by tempering, so the continuous yielding behavior is maintained and the increase in yield strength is small. In addition, tempering at low temperatures would cause carbon to segregate to dislocations in the ferrite and lower the mobile dislocation density, which can also explain the return of the discontinuous yielding in those steels with lower volume fractions of martensite. On the other hand, if the volume fraction of martensite is higher, the dislocation density in the ferrite is so high that only part of the dislocations are pinned by the available carbide particles; then, the discontinuous yielding behavior wouldn't return. When tempering at high temperatures, the residual stresses are relieved and the dislocation density is greatly lowered, resulting in the return of discontinuous yielding.

A. Kamp et al.^[105] found that tempering at temperatures between 200°C and 450°C can noticeably increase the yield strength and the UTS remains essentially the same, while tensile elongation decreased. However, the elongation was recovered by further increasing tempering time and temperature, accompanied with a drop of the yield strength and ultimate tensile strength. Moreover, the formation of

carbide within both ferrite and martensite was observed, resulting in the property changes due to pinning of dislocations in ferrite and a reduction in carbon supersaturation in martensite. S. Gunduz^[106] investigated the effect of tempering on mechanical properties of dual phase steels with and without micro alloying elements (V and Nb) and found that the decrease in UTS and YS after tempering at temperatures of 100 to 600°C can be minimized for microalloyed dual phase steels. That is due to the tempering of the martensite and precipitation in the ferrite. H.S.Lee et al.,^[107] pointed out that with increasing tempering temperature, ductile fracture tended to increase. As the ferrite/martensite interfacial strength increased due to martensite softening and carbon diffusion after tempering, fewer voids were formed at ferrite/martensite interfaces than at the untempered specimen. Therefore the ductility increased.

A large amount of research done on understanding the effects of tempering on the mechanical properties of dual phase steels shows that the tempering effects are really quite complex and need to be further investigated.

2.6 BANDING IN DUAL-PHASE STEELS

The banded structures, which can be described as alternating parallel bands of ferrite and martensite phases, can usually be found in hot rolled dual phase steels with high manganese levels. Though the formation mechanisms of banded structures in steels have been intensively investigated, the fundamental mechanisms are still not clear.

As we know, microstructural banding of ferrite and pearlite^[108-112] is usually observed in hot-rolled low-alloy steel, which is primarily due to segregation of solutes during the cooling of steel from the molten state. During the solidification from liquid to δ -ferrite, elements such as manganese, silicon, are partitioned into the interdendritic regions. Subsequent deformation, e.g., hot rolling, causes these regions to spread out as bands. Manganese is thought to be the most important element which segregates in the banding form^[112-115]. Carbon also segregates during solidification, but it diffuses rapidly as the steel cools

through the δ and austenite region, resulting in that the carbon maintains a uniform chemical potential in the austenite. In addition, manganese lowers the activity of carbon and hence the carbon concentration is somewhat higher in the Mn-rich regions.

The solute-depleted regions tend to decompose into ferrite, and as a result, carbon is partitioned into the adjacent solute-rich austenite, which transforms to pearlite during subsequent slow cooling, Figure 2.6.1^[109]. For the ferrite-martensite banding, ferrite forms first in the manganese-depleted regions, and the carbon partitioned into the manganese-rich regions of austenite, which further enhances the hardenability of the manganese-rich regions, which transform into bands of hard microstructure such as martensite during subsequent fast cooling.

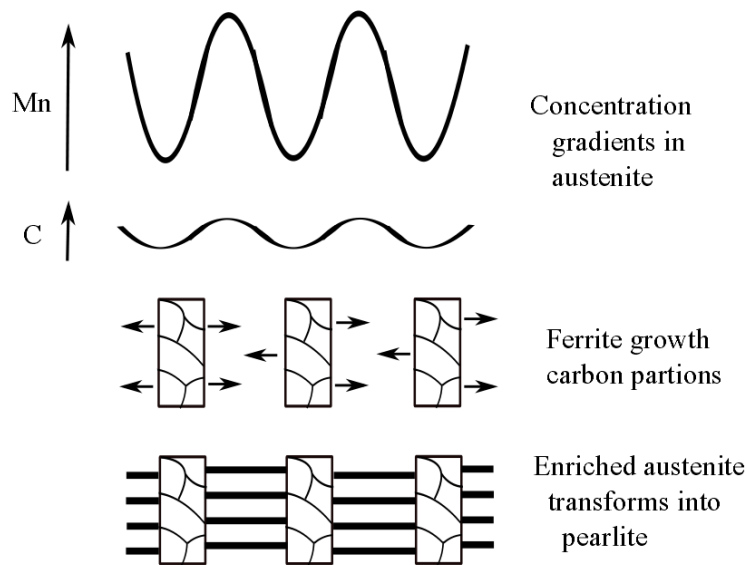


Figure 2.6.1 An illustration of the common mechanism of banding

Starting from hot rolled steels with a banded structure, e.g., ferrite-pearlite banded structure, after cold rolling and intercritical annealing, the banded structure remains. During intercritical annealing, austenite formation occurs in the carbon-rich regions, i.e., pearlite bands, while the low-carbon regions,

i.e., ferrite bands, remain ferritic. After rapid cooling, martensite will form in the regions previously occupied by pearlite. As a result, the ferrite-martensite banded structure appears.

Park et al.,^[116] also related the martensite bands formation to the segregation of alloying element of manganese. According to their research, when there was little manganese segregation, no martensite bands were found in the as-rolled dual phase steels.

Some researchers take the nucleation of ferrite as an important factor on the formation of banding^[112, 115, 117, 118]. If we suppose that the banding structure is mainly controlled by the difference in nucleation rates at different regions with high and low carbon content, the banding structures can be controlled using different cooling rates which are related to the ferrite nucleation rates. If the cooling rate is fast enough for ferrite to be formed at solute rich and poor regions simultaneously, the banding microstructure formation can be prevented.

Krebs et al.,^[113] pointed out that the ferrite transformation from the austenite region is also important to understand the mechanism of banding structure formation. The austenitization temperature, different types of ferrite, i.e., allotriomorphic and acicular, cooling rate and initial austenite grain size can all affect the final banding structure. Two types of ferrite, i.e., allotriomorphic ferrite and acicular ferrite, have different effects on the formation of banding structure. Allotriomorphic ferrite grows preferentially in the Mn poor regions and promotes the formation of banding structure, while acicular ferrite grows in some specific directions imposed by the crystallography rather than by the distribution of Mn composition, resulting in less pronounced banding structure.

One interesting result obtained by them^[113] is that the distance between the segregated bands is reduced with decreasing the austenite grain size and the ferritization temperature (in their study, they cooled the samples from some austenitization temperature to some temperature T_α , which they called ferritization temperature, promoting isothermal austenite-to-ferrite transformation), which may be explained by considering the initial Mn segregation with less and more deep fluctuations as shown in Figure 2.6.2^[113]. At higher ferrite transformation temperature which gives low transformation driving forces, ferrite nucleation can take place only at deeper Mn valleys, resulting in a coarser banding

structure, while at lower ferritization temperatures corresponding to higher driving forces, nucleation can occur at both shallow and deep Mn valleys, and so the nucleation density is high, leading to finer banding structures. For large austenite grain size, the austenite grain boundary may reach at least one Mn rich region, and since ferrite nucleates and grows easily along grain boundaries than in the grain, as a result, the intensity of banding structure can be reduced because ferrite can grow within the Mn rich regions through the austenite grain boundaries, as well as Mn poor region. However, a coarser banded structure can then be obtained.

Indeed, banding structures impact the resistance to hydrogen cracking, toughness and damage resistance^[119]. One way to avoid banding microstructure is to use accelerated cooling. As stated above, during fast cooling from the austenite region to the dual phase (ferrite plus austenite) region, transformation, e.g., ferrite transformation, occurs everywhere, even in the manganese-rich regions, resulting in a more homogeneous microstructure.

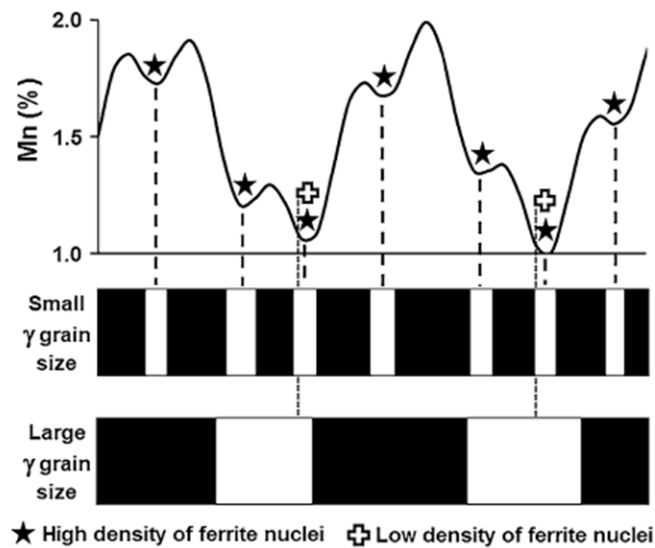


Figure 2.6.2 Schematization of Mn segregation and microstructures expected to depend on the austenite grain size and the density of ferrite nuclei

Francisca et al.,^[120] investigated the evolution of microstructural banding during the manufacturing process of dual phase steels. They used different initial hot rolled specimens with or

without banding structures. Cold rolling of the hot rolled specimens does not affect the banding structures. They found that the banding eliminated by fast cooling after hot rolling will appear after intercritical annealing at 800°C. However increasing the cooling rate during hot rolling and using low intercritical annealing temperatures (750°C) and longer soaking time is a possible way to permanently eliminate microstructural banding in cold rolled dual phase steels according to their study.

3.0 STATEMENT OF OBJECTIVE

Developing high strength and good ductility dual phase steels is very attractive to the automotive industry. Today, DP590, DP780 and DP980 are commercial realities, while DP1180 is still being investigated. A lot of work has been done to investigate the high strength dual phase steels and our previous results by BAMPRI indicate that it is possible to develop high strength and good ductility dual phase steels (980 grade) with the addition of certain microalloying elements.

The main purpose of Sections 5.1 and 5.2 is to conduct a study of additions of the microalloying elements Nb, V and V-N to a low carbon, high-strength (980 grade) Dual-Phase steel that was processed using a CGL simulation. In this study, compositions with a common base but containing various additions of V or Nb with or without high N were designed and subjected to Gleeble simulation of different Galvanizing (GI), galvannealing (GA) and supercooling processing. These experiments were supplemented with additional heat treatments performed using a quartz filament furnace. The effects of different microalloying additions on the phase balance (martensite-bainite-ferrite) and the strengths of each phase will be studied. UTS levels of 1100MPa, along with good levels of ductility and work hardening, were measured in steels containing less than 0.1%C and 1.75%Mn. Some important factors for the productions of dual phase steels (e.g., dissolution of cementite, recrystallization of cold rolled ferrite, the formation of austenite during intercritical annealing, intercritical annealing temperatures and cooling rate) will be carefully investigated.

The main purpose of Section 5.3 is to study the effects of vanadium on softening resistance during extended holding at zinc pot temperature and the precipitation hardening from vanadium contained precipitates.

Section 5.4 is to study an important relationship between the stored energy of the hot band, the increase in stored energy in cold rolling and the formation of austenite during intercritical annealing of V-bearing DP 980 steels. The stored energy is measured by combining SEM/FEG/EBSD with newly developed software that sums the sub-grain boundary energy in the steel. The higher amounts of austenite found in cold band of higher stored energy leads to higher strength in the fully CGL processed steels. Current research is studying whether the observed effect is based on thermodynamics, kinetics or both. The effect of higher stored energy of the cold band on the final properties after full CGL process simulation will be shown.

The purpose of Sections 5.5-5.7 is to present research whose goal was to improve the substrate in galvanized or galvanized sheet steel, such that high strength can be obtained while maintaining good global formability (tensile ductility), local formability (sheared-edge ductility), and good spot weldability. It is well-known that the strength of DP steels is controlled by several factors, including the amount of fresh (untempered) martensite found in the final microstructure. However, the factors that control the amount of martensite in the final microstructure are not all together clear, and their identification represents a large portion of the research conducted in this program. The amount of fresh martensite found in the final microstructure can be considered equal to the amount of austenite formed in the intercritical anneal less the amount of austenite lost to various transformation products as the steel undergoes cooling from the intercritical annealing temperature (IAT) to 460°C, isothermal holding at 460°C, final cooling to RT and any remaining austenite retained at RT. Recent research has revealed that the amount of austenite formed during intercritical annealing of a given steel can be strongly influenced by the annealing temperature and the pre-annealing conditions of the hot band (coiling temperature) and cold band (% cold reduction). Current experiments have explored the combination of pre-annealing conditions and four annealing practices to help define the best thermal path needed to optimize the strength-formability balance in these higher strength DP steels. The steels used in these experiments contained (i) low carbon content for good spot weldability, (ii) the hardenability additions Mo and Cr for strength, and (iii) V for grain refinement and precipitation hardening. When processed correctly, these

steels exhibited UTS levels up to 1000MPa, total elongation to 25%, reduction in area to 45%, and Hole Expansion Ratios to 50%. The results of this program will be presented and discussed.

4.0 EXPERIMENTAL PROCEDURE

4.1 MICROSTRUCTURAL ANALYSIS

4.1.1 Optical microscopy (OM)

The optical microscope was used for the microstructural investigations of the heat treated specimens. The magnifications from 50 to 1000 were commonly used. Samples were cut and mounted in Bakelite or copper, and then were ground with 240, 400, 600, 800 and 1200 grit silicon carbide abrasive papers, and finally were polished with 0.05 μm alumina powder. In order to reveal the microstructures of the specimens, different etching methods were applied. 2% Nital, based on the etching of grain boundaries of ferrite, was used to reveal ferritic microstructures, shown as white grains. The LePera's etchant, which is a mixture of 1% sodium metabisulfite in distilled water and 4% picric acid in ethanol in a 1:1 volume ratio, was also used to reveal the ferrite-martensite microstructure. This tint etching technique can color ferrite and bainite brown, and color martensite and retained austenite white.

The quantitative analysis of microstructures such as grain size and volume fraction of microconstituents was conducted using Bioquant image analysis software attached to the optical microscope. The volume fraction of martensite was also measured using the image processing function of Matlab, considering ferrite as the dominating matrix phase and martensite or retained austenite (MA) as a second phase.

4.1.2 Scanning electron microscope (SEM) and EBSD

For the identification of any third phase present (like bainite), or for the investigation of other detailed microstructures of the constituents present, Scanning Electron Microscopy (SEM) was used. In this study, Philips XL-30 field emission scanning electron microscope was used. Samples used in the SEM were mounted in conducting powder and/or conducting tapes to increase conductivity of the samples, and were 2% Nital etched.

Electron Backscattered Diffraction (EBSD) is also used in this study. For EBSD observation, 15kV voltage and the beam spot size of 5 were applied. The step size varied from 0.1 to 0.2 μm depending on the grain size and the features of interest. The TSL OIM data collector software was used for the collection of all the EBSD data and the general analysis, e.g. texture analysis, grain size analysis, was conducted using the TSL OIM Analysis software. Initially recorded image quality (IQ) of the diffraction pattern and the confidence index (CI) can also be normalized and presented using this software. The “EBSD-IQ” technique developed by BAMPRI was applied to identify and calculate volume fraction of some complex phases, such as different morphologies of ferrite, bainite and low carbon martensite, in the steel.

The samples used for EBSD observation should be well prepared. The specimens were carefully polished by hand, and then were further polished in a vibration machine. The Vibromet 2 Vibratory Polisher was used in this part.

4.1.3 Transmission electron microscopy (TEM)

In order to obtain more detailed information on the microstructures of the steel, such as the distribution of dislocations, precipitates, retained austenite, or the lattice constants of martensite, the TEM is used in this study. The JEOL200CX and JEOL2100F were used. The TEM uses tungsten filaments operated at 200kV, 118 μA . The JEOL TEM can provide a linear resolution of 0.13nm.

Thin foils are prepared for TEM observations. Thin foils are cut from 1.2mm thick sheets of selected samples with a Buehler diamond disk cut off machine and are then ground to around 200 μ m, and further reduced to around 50 μ m by chemical thinning. The solution used for chemical thinning is a mixture of 50ml distilled water, 30ml nitric acid, 15ml hydrochloric acid and 7ml hydrofluoric acid. After chemical thinning, discs of 3mm in diameter are punched and then electrochemically polished at room temperature using a Struers-Tunepol Jet polisher. The final thickness at the center is 50-100nm. The electrolyte solution used in electrochemically polishing is a mixture of 90% ethanol and 10% perchloric acid and the polishing was run at 40V and 70-90 mA. The samples were carefully cleaned using ethanol to remove all residues on the sample.

4.2 MECHANICAL PROPERTIES

4.2.1 Tensile testing

Tensile tests were conducted using the MTS 880 system. The sub-size tensile specimens with gage length 25.4mm (1 inch) were machined according to the ASTM standard E 8M-04. The specimens were sectioned from the sheets subjected to Gleeble simulation. The tensile direction is along the rolling direction for all the specimens in Sections 5.1-5.4 and along transverse direction for those in Sections 5.5-5.7.

4.2.2 Micro hardness and nano hardness

Micro hardness test is more convenient to conduct than tensile tests, and from the hardness value (VHN) we can estimate the ultimate tensile strength (UTS) of the steel. One empirical equation proposed by Davis^[121] is:

$$\text{UTS (MPa)} = 0.0017(\text{VHN})^2 + 2.2494(\text{VHN}) + 123.31 \quad (4.1)$$

The typical loads used for the micro hardness tests are 10gram to 500gram. 10gram is used for measuring the hardness of certain constituent, e.g. martensite bands or ferrite bands.

The nano indentation was also used to measure the hardness of the different microconstituents. The nanohardness measurements were performed on a Hysitron Triboindente system.

4.2.3 Hole expansion tests

The hole expansion ratios of dual phase steels were tested at BAMPRI. Holes with 10mm diameter were punched at USS research lab with very high punching speed which was not recorded. The hole expansion test was then used to estimate the sheared edge formability. For the tests, we used bottom holder with 40mm hole, top holder with 40mm hole and 6mm radius flat and continuous die moving speed 0.5mm/s. The failure of hole expansion tests was determined visually with the aid of a monitor screen, i.e. when the crack goes through the thickness.

The hole expansion ratio (HE%) is defined by the following equation:

$$HE\% = \frac{D_f - D_0}{D_0} \times 100 \quad (4.2)$$

where: D_0 is the original inner hole diameter and D_f is the final inner hole diameter.

4.3 HEAT TREATMENTS

The galvanizing (GI), galvannealing (GA) and supercool processing were conducted on Gleeble 3500 (USS lab) or Gleeble 3800 (University of Oulu, Finland). The Gleeble is a fully integrated digital closed loop control thermal and mechanical testing system. Thermocouples were used to accurately control temperatures of the specimen. The Gleeble system can typically heat samples 3 to 10 times faster than

conventional furnace equipped machines, can fast cool specimens and can also hold specimen at constant temperature with good accuracy.

Heat treatments were also simulated in the MTS system. The MTS system (Model MTS 458) contains a quartz filament furnace with 12×1200 watt halogen quartz infrared bulbs and parabolic reflectors. There are three main parts in this system: (a) heating system; (b) hydraulic system; (c) cooling system. In this work, we don't use the hydraulic system. The cooling rate can be controlled by the cooling system. Compressed air or helium is used for cooling the specimens. The cooling rate can reach 10°C/s if we use the compressed air, and the cooling rate can reach 40°C/s if we use helium. The temperature change with time can be recorded on computer.

4.4 MEASUREMENT OF RETAINED AUSTENITE

Magnetometry is one way to determine the retained austenite. Since austenite is paramagnetic, and ferrite, martensite, cementite are all ferromagnetic, the magnetic techniques can be used to determine the amount of retained austenite. The volume fraction of retained austenite f_{γ} can be expressed as^[122, 123],

$$f_{\gamma} = 1 - \beta \frac{M_s(c)}{M_s(f)} \quad (4.3)$$

where $M_s(c)$ is the saturation magnetization of the austenite-containing sample, $M_s(f)$ is the the saturation magnetization of the austenite-free sample, and β is a factor related to the saturation magnetization of ferrite, martensite, cementite, and the volume fraction of cementite. If we assume that the amount of cementite precipitates is negligible, β can be simply taken as one.

A vibrating specimen magnetometer (VSM) was used to measure the saturation magnetization. The dimension of the samples used is 1mm×3mm×5mm (thickness, width and length).

There are some other methods, e.g. XRD^[124], EBSD, dilatometry, optical microscopy combined with image analysis, to measure the amount of austenite. Among them, XRD is the most frequently used,

but its probed volume is surface layer. Moreover, the XRD method has filter problem, e.g., there is no effective way to remove the $K\alpha_2$ peak from the incident beam. Compared with XRD, the probed volume of magnetometry is the whole bulk of the sample, and magnetometry has higher accuracy and can detect smaller volume fractions.

4.5 STORED ENERGY

4.5.1 Calculation of stored energy from EBSD scanning

The stored energy is associated with the lattice defects and can reflect the extent of the deformation of grains. It is thought to provide the initial driving force for recovery and recrystallization during the annealing process. In this work, it was also found that increasing the stored energy in the initial cold rolled samples can make the formation of austenite during intercritical annealing faster, resulting in more austenite after only 1 minute annealing at different IATs (intercritical annealing temperature).

The stored energy can be estimated from the EBSD data using different methods. The image quality (IQ) is related to the number of defects such as dislocations, so it can reflect the state of deformation and internal stresses. Therefore, it is reasonable to use IQ as a measure of stored energy in the deformed microstructure^[125]. In this work, the stored energy (S_i) for each lattice site is assumed to be proportional to the image quality distribution (H_i) for each lattice site as follows^[126]:

$$S_i \propto H_i = 10 \left[1 - \frac{Q_i - Q_{\min}}{Q_{\max} - Q_{\min}} \right] \quad (4.4)$$

where Q_i is the image quality for the site i , Q_{\min} and Q_{\max} are the minimum and maximum image quality of the scanned area. For simplicity, we assume S_i is equal to H_i to compare the stored energy of our samples with different conditions. The drawback is that the IQ is also affected by the surface conditions and beam conditions, which means the stored energy calculated from IQ data is not the true stored energy from the

dislocation density and internal stress. In order to compare the stored energy from IQ data, the conditions of each sample should be kept the same, which is difficult in practical terms.

The other method is the sub-grain method^[127], which is based on the boundary energy of the subgrain. The stored energy of each lattice site is assumed to be $S_i = \alpha \frac{\gamma}{D}$, where α is the geometric constant ~ 3 ^[128], γ is the boundary energy and D is the diameter of subgrains. And further assume that γ is only dependent on the boundary misorientation ($\Delta\theta$), then the boundary energy can be expressed as^[129]:

$$\gamma(\Delta\theta) = \begin{cases} \gamma_m \frac{\theta'}{\theta^*} \left[1 - \ln \left(\frac{\theta'}{\theta^*} \right) \right], & \theta' < \theta^* \\ \gamma_m, & \theta' \geq \theta^* \end{cases} \quad (4.5)$$

where $\theta' = |\Delta\theta|$ for $0 \leq |\Delta\theta| \leq \pi$ and $\theta' = 2\pi - |\Delta\theta|$ for $\pi \leq |\Delta\theta| \leq 2\pi$, $\Delta\theta$ is the boundary misorientation between two neighboring subgrains, θ^* is the misorientation limit for low angle grain boundaries, which was chosen as 15° , and γ_m is the specific energy of high angle grain boundaries which was set to be 0.756J/m^2 . In the present work, we used the subgrain method to calculate the stored energy using the software developed by Dr. Choi^[126, 130-132]. Before calculating the stored energy, the original EBSD data were cleaned to the best state using TSL OIM data collector software to remove the unresolved data, since the stored energy value from sub-grain method is only reliable when the orientations of each lattice site can be well identified. Due to the limitations of the IQ and sub-grain boundary methods, we also used the Vickers Hardness values to compare the stored energy of our samples, since the hardness is also related to stored energy and is a very simple method compared with the methods depending on EBSD data.

4.5.2 Other methods to get stored energy

Stored energy can be calculated from XRD curves. Stored energy from the Stibitz formula^[133, 134]:

$$W = \frac{3}{2} E \frac{\left(\frac{\Delta d}{d}\right)^2}{1+2\nu^2} \quad (4.6)$$

$$\frac{\Delta d}{d} = \frac{\sqrt{B_r^2 - B_a^2}}{2tg(\theta_B)} \quad (4.7)$$

E is Young's modulus and ν is Poisson's ratio. $\Delta d/d$ is the relative change in lattice spacing which can be obtained from the broadening of the Bragg Peaks. B_r and B_a are the measured values of full width at half maximum of the rolled and a standard annealed sample. θ_B is the Bragg angle.

Stored energy from Vickers hardness^[135, 136]:

$$E = \frac{C}{\mu} \frac{Hv^2}{0.09\alpha^2 M^2} \quad (4.8)$$

E is the stored energy, Hv is Vickers hardness, α and C are material constants, μ is the shear modulus, M is the Taylor factor.

5.0 RESULTS AND DISCUSSION

5.1 MECHANICAL PROPERTIES OF DUAL PHASE STEELS WITH VANADIUM OR NIOBIUM ADDITIONS

5.1.1 Chemical compositions and thermomechanical processing

In order to compare the different effects of micro alloying elements, i.e. V alone, V+N alone, Nb alone, V+Nb alone and V+Nb+N, on the mechanical properties of dual phase steels, five main compositions were designed for this study, as shown in Table 5.1.1. A series of laboratory heats were melted in a vacuum induction furnace in USS steel lab. The materials were then hot rolled, cold rolled and subjected to heat treatment simulations using both Gleeble system and MTS system.

Table 5.1.1. Chemical compositions of the five steels used in this study, Wt.%, The chemical composition of the commercial steel is also included

Element/Steel	DP_V	DP_VN	DP_Nb	DP_NbV	DP_NbVN	Commercial Steel
C	0.10	0.10	0.10	0.10	0.10	0.11
Mn	1.75	1.75	1.75	1.75	1.75	2.4
Si	0.40	0.40	0.40	0.40	0.40	-
P	0.01	0.01	0.01	0.01	0.01	-
Al	0.025	0.025	0.025	0.025	0.025	0.045
V	0.06	0.06	0.00	0.06	0.06	-
Nb	0.00	0.00	0.025	0.025	0.025	-
Cr	0.50	0.50	0.50	0.50	0.50	0.25
Mo	0.30	0.30	0.30	0.30	0.30	0.35
N	0.006	0.014	0.006	0.006	0.014	0.005
S	0.003	0.003	0.003	0.003	0.003	-

Ingots with dimensions 76mm thick x 305mm long x 203mm wide were hot rolled in a pilot plant. The thermomechanical process used for each type of steel is shown in a schematic diagram, Figure 5.1.1. For rough rolling, ingots were reheated at 1250°C and then hot rolled to a final thickness of 25mm. The final cooling of rough rolling is air cooling and the number of passes was as needed. For finish hot rolling, ingots were again reheated to 1250°C, and were hot rolled using 5 passes, and the deformation is 27.5% per pass. The finishing temperature was 921°C. Then the ingots were water sprayed with cooling rate 30°C/s to coiling temperature 600°C and then cooled with cooling rate 30°C/h to room temperature. The materials then were cold rolled 60% to achieve a final thickness of approximately 1.2 mm. The cold rolled sheets were sectioned for Gleeble simulations and MTS heat treatments.

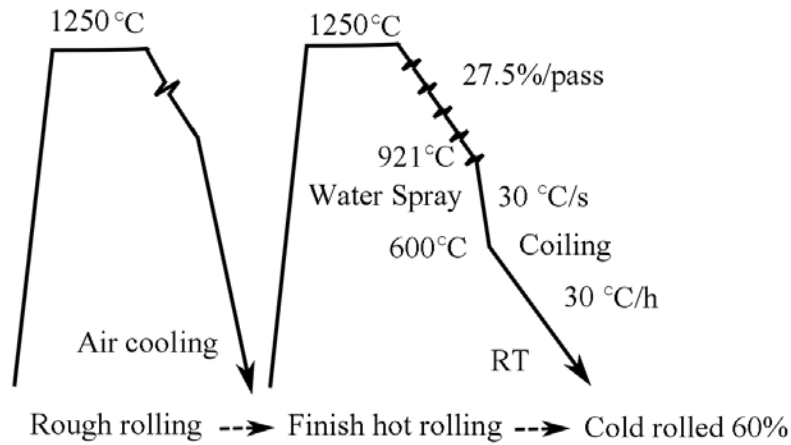


Figure 5.1.1. Schematic diagram of hot rolling and cold rolling used for each type of steel in the current study, RT means room temperature

The cold rolled sheets were then subjected to Gleeble simulations of different galvanizing(GI), galvannealing(GA) and supercooling processing, which are shown in Figure 5.1.2. At all the processing, the samples were heated to 790°C (the reason for the choice of 790°C is related to the austenite formation, dissolution of cementite, recrystallization of cold rolled ferrite and will be discussed in detail in the following sections) with heating rate 5°C/s, and held for 60s. For GI processing, the samples were then cooled to 460°C with different cooling rates (15°C/s for A1, A3, A5 and A6, and 30°C/s for A2, A4), and held at 460°C for 30s, and finally cooled to room temperature with different cooling rates (10°C/s for A1,

A2, A5 and A6, and 30°C/s for A3, A4). For GA processing, the samples were then cooled to 460°C with cooling rate 15°C/s, and held at 460°C for different times (30s for B1, 60s for B2, and 120s for B3), and then up quenched to 520°C with heating rate 20°C/s and held for 20s, and finally cooled to room temperature with cooling rate 10°C/s. For the supercooling processing, the samples were then cooled to 250°C with different cooling rates (15°C/s for C1, and 30°C/s for C2), and held at 250°C for 20s, and then up quenched to 460°C with heating rate 42°C/s and held for 30s, and finally cooled to room temperature with cooling rate 10°C/s.

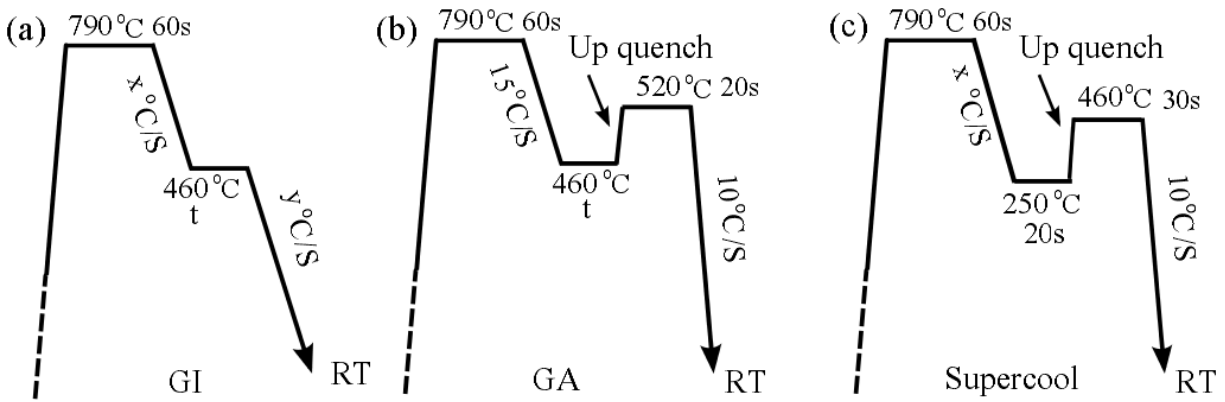


Figure 5.1.2. Schematic representation of heat-treatment schedules for Gleeble processes. GI: A1, $x=15, y=10, t=30s$; A2, $x=30, y=10, t=30s$; A3, $x=15, y=30, t=30s$; A4, $x=30, y=30, t=30s$; A5, $x=15, y=10, t=60s$; A6, $x=15, y=10, t=120s$; GA: B1, $t=30s$; B2, $t=60s$; B3, $t=120s$; and Supercool: C1, $x=15$; C2, $x=30$

As a starting step, we calculated some critical temperatures, e.g. Ar_1 , Ar_3 , M_s , B_s temperatures, and the volume fraction of austenite at different intercritical annealing temperatures (IAT) using JMatPro software. The results are given in Table 5.1.2.

Table 5.1.2 Predicted Critical temperatures of the five steels used in this study, and the volume fractions of austenite at different IAT are also shown

	DP_V	DP_VN	DP_Nb	DP_NbV	DP_NbVN
IAT	Volume fraction of martensite(%)				
780°C	46.7	47.2	47.4	44.9	45.5
790°C	54.1	54.5	54.6	52.1	52.8
	Critical temperatures (°C)				
Ac1	680	680	679	680	680
Ac3	835	834	832	836	834
Ms	403	402	404	404	404
Bs	578	578	578	578	578

5.1.2 Results of hot rolled and cold rolled sheets

The typical optical microstructures of the hot rolled steels are shown in Fig.5.1.3 (a), (b) and (c). There is no obvious difference among these steels. The microstructures of these five steels are also checked using SEM, as shown in Fig.5.1.3 (d). From both of the SEM and optical microstructures of the hot rolled samples, we see that the main constituents are polygonal ferrite, acicular ferrite, bainite, martensite, cementite, and pearlite. From the Nital etched optical microstructures we can see the martensite laths (dark brown) and also can observe the banding structures.

In the Nital etched microstructures, the black spots are the cementite, white grains correspond to ferrite and bainitic ferrite, and the dark brown areas correspond to MA (martensite and retained austenite). After 60% cold rolling, the thickness was reduced and the constituents are not expected to change. From the Nital etched microstructures Figure 5.1.4 (a) and (b), we find that both ferrite and martensite were elongated as expected. We also used LePera etchant to emphasize the martensite in the ferrite matrix. As shown in Fig.5.1.4 (c), the martensite (or MA, white area) was elongated distributed in the brown matrix which corresponds to ferrite or bainite or pearlite. The microstructures of the cold rolled samples were also checked using SEM, Figure 5.1.4 (d).

After checking the hot rolled and cold rolled samples, we find that the starting microstructures of these five steels are quite similar to each other, in view of OM and SEM microstructures.

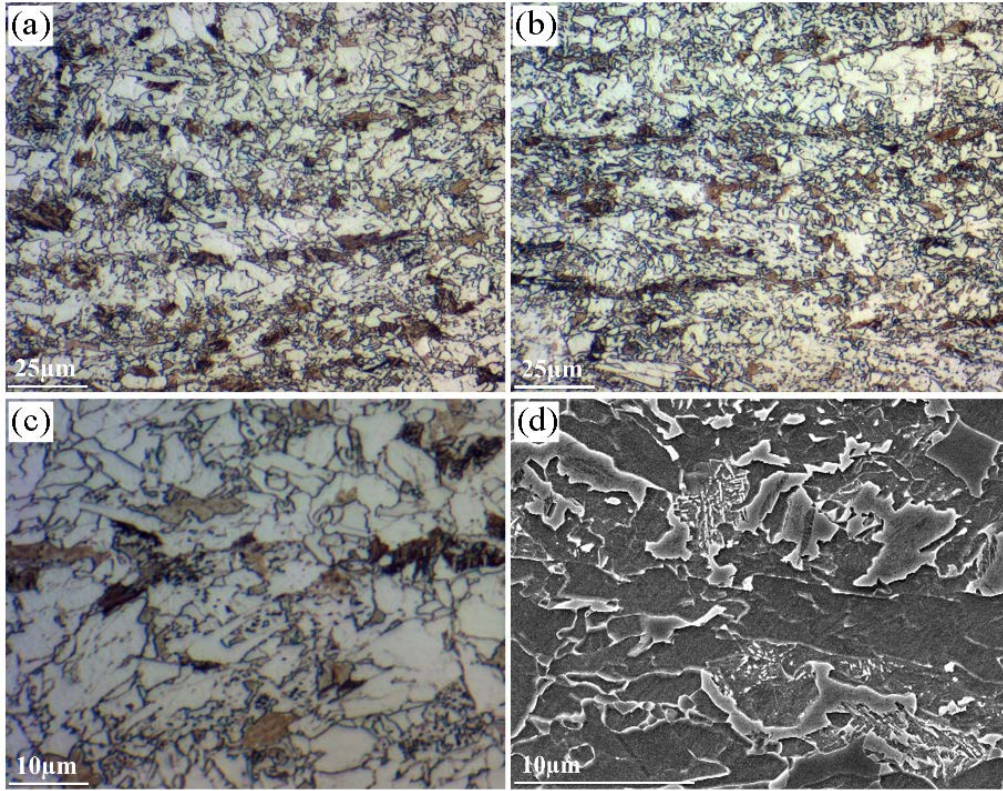


Figure 5.1.3. 2% Nital etched microstructures of hot rolled samples (a) DP_V, (b) DP_Nb, (c) DP_V higher magnification, and (d) DP_V SEM microstructure.

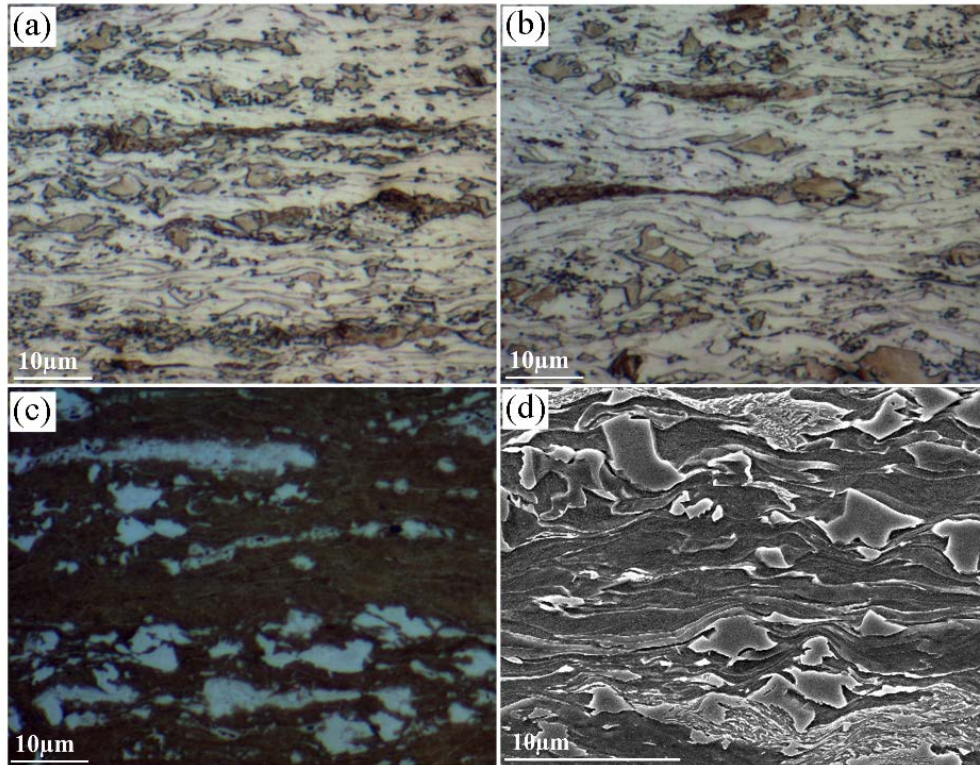


Figure 5.1.4 (a) optical microstructure of DP_Nb, Nital etched, (b) optical microstructure of DP_VN, Nital etched, (c) optical microstructure of DP_VN, LePera etched, and (d) SEM microstructure of DP_VN

5.1.3 Mechanical properties

The typical engineering (true) strain versus stress curves of DP_V, DP_NbV for the 7 full processing are shown in Figure 5.1.5 and Figure 5.1.6. For all the five steels, the engineering strain versus stress curves show continuous yielding under the conditions of GI (A1-A4) and GA (B1) processing. For supercool processing C1 and C2, the cooling rate from intercritical annealing temperature (IAT) 790°C to 250°C can affect the strain-stress curves. When this cooling rate (CR) is 15°C/s, i.e. C1, the yielding point starts to appear though not obviously. As the cooling rate reaches 30°C/s, i.e. C2, there is an obvious yielding point in all the five steels. The appearance of the yielding point is related to the microstructural change under the supercool processing. The tempered martensite is expected when we cool the samples from IAT

to 250°C which is below the Ms temperature and then reheat to 450°C to temper the transformed martensite. The existence of the tempered martensite probably caused the appearance of yielding point.

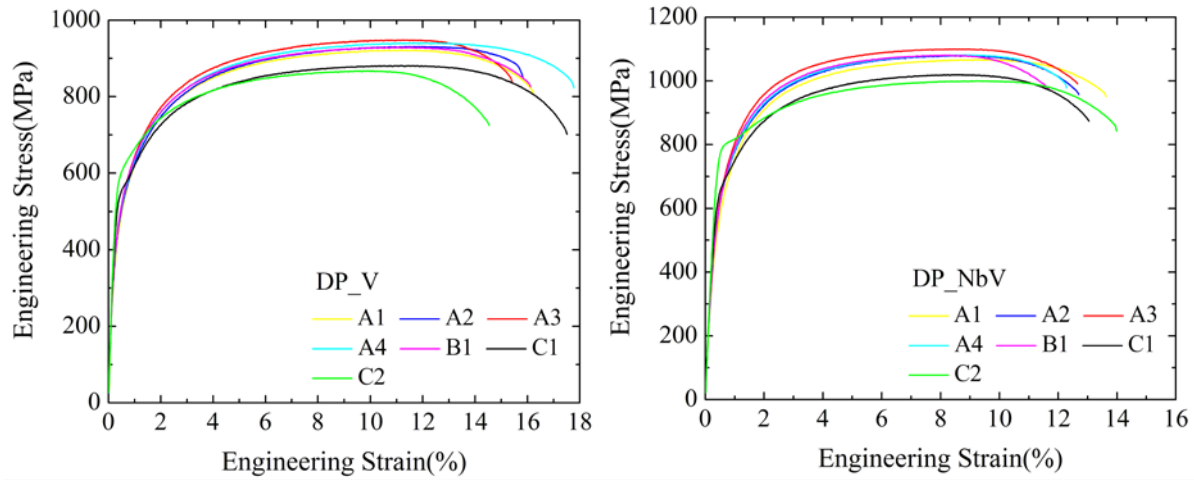


Figure 5.1.5 Engineering strain versus stress curves of DP_V and DP_NbV with full processing GI (A1-A4), GA (B1) and Supercool (C1-C2).

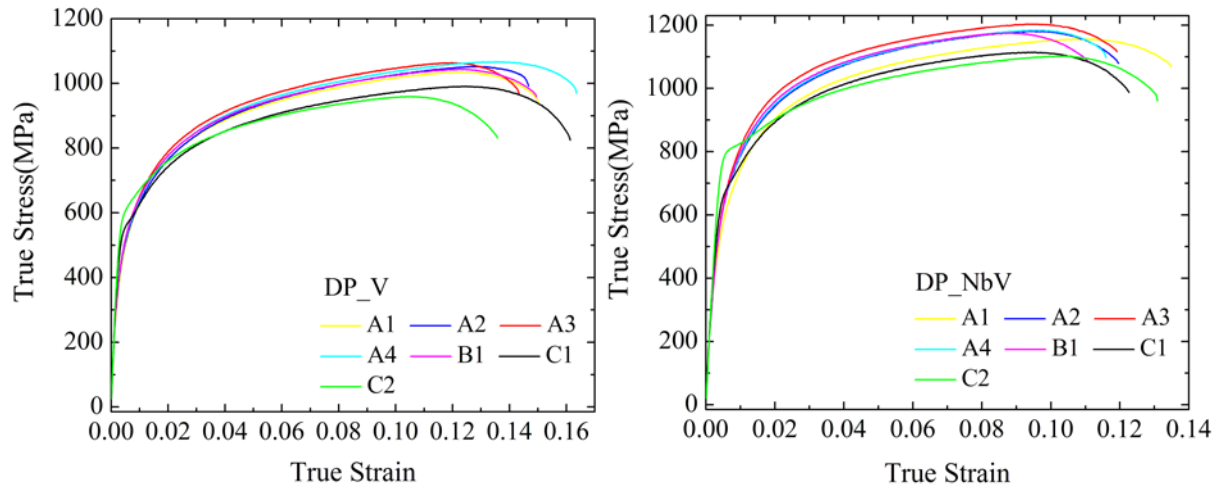


Figure 5.1.6 True strain versus stress curves of DP_V and DP_NbV with full processing GI (A1-A4), GA (B1) and Supercool (C1-C2).

From the engineering strain versus stress curves, we can get the tensile strength, 0.2% yield strength, total elongation (TE), uniform elongation (UE), and the 4%-6% work hardening exponent n values were derived from the true strain and true stress data. The TE and UE obtained from the sub-size specimens were corrected to the values for a 50mm (2") gauge length. Figure 5.1.7 shows the relationship among 11 processing, chemical composition, tensile strength and 0.2% yield strength. The DP_V and commercial steels show the lowest ultimate tensile strength(UTS) around 950MPa, and the DP_NbV and DP_NbVN steels show the highest UTS around 1100MPa, while the DP_VN and DP_Nb steels show the intermediate UTS around 1050 MPa for GI(A1-A6) and GA(B1-B3) processing. Comparing with GI and GA processing, all the steels except the commercial steels with supercool processing (C1 and C2) show lower tensile strength, while the UTS of commercial steels is around 950MPa for all the 11 processing. Similar to UTS, the DP_V steels show lowest YS around 550MPa, and DP_NbV and DP_NbVN show highest YS around 690MPa, while DP_VN, DP_Nb and commercial steels show intermediate YS around 650MPa for GI and GA processing. Comparing with GI and GA processing, all the steels with supercool processing show higher YS, especially for C2 processing. The significant increase in YS for C2 processing is due to the appearing of yield point, which is related to the microstructural change because of tempering at 460°C after supercooling to 250°C.

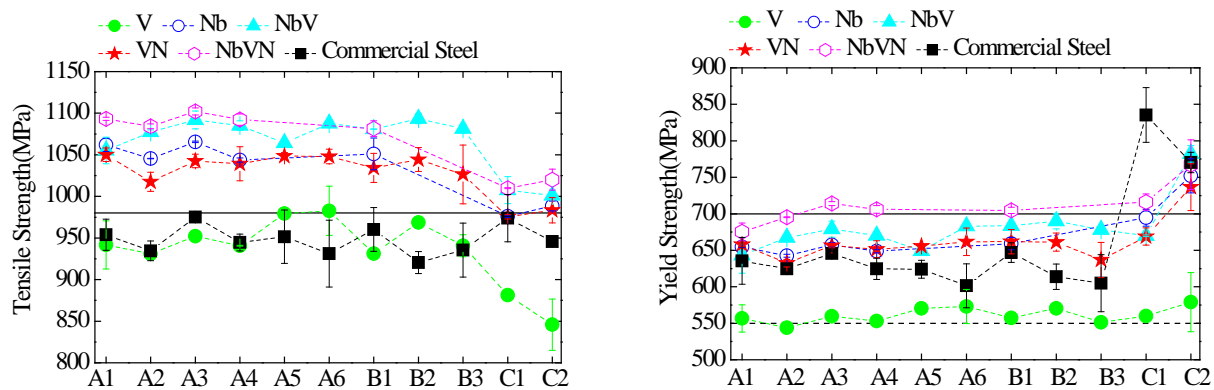


Figure 5.1.7 Tensile strength and 0.2% yield strength of DP steels in this work, and the corresponding values of commercial DP steels are also included

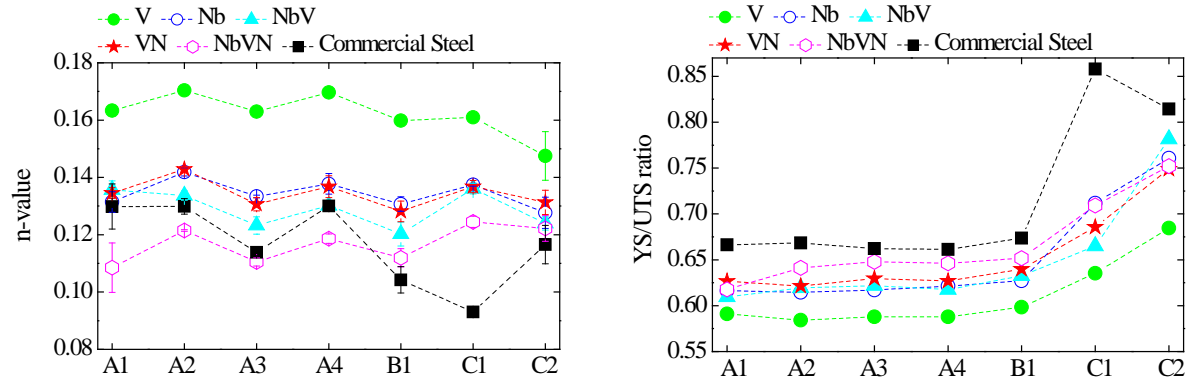


Figure 5.1.8 Values of work hardening exponent n (4%-6%) and yield strength to tensile strength ratios of DP steels in this work, and the corresponding values of commercial DP steels are also included

Figure 5.1.8 shows the relationship among 7 processing (A1-A4, B1 and C1-C2), chemical composition, n -values and yield strength to tensile strength ratios. The DP_V steels have the highest n -value around 0.16, and the DP_NbVN, DP_NbV and commercial steels have lowest n -values around 0.12, while DP_VN and DP_Nb steels exhibit intermediate n -values around 0.14 for all the 7 processing. For commercial steels, the n -values are lower for GA and supercool processing than those with GI (A1-A4) processing. The n -value of DP_V with C2 processing is lower than those with the other 6 processing. For DP_Nb, DP_VN, DP_NbV and DP_NbVN steels, the n -values are nearly the same for all the seven processing.

The yield strength to tensile strength ratios (YS/UTS ratios) of DP_V are the lowest among all the steels, which is consistent with the high n -values. The YS/UTS ratios of commercial steels are the highest, while the YS/UTS ratios of DP_VN, DP_Nb, DP_NbV and DP_NbVN are close to each other. There is an obvious increase in the YS/UTS ratio for the supercool processing, due to the increase of yield strength and decrease of tensile strength.

The relationships among the seven processing (A1-A4, B1, and C1-C2), chemical composition, total elongations and uniform elongations are shown in Figure 5.1.9. The DP_V steels have highest total elongations and uniform elongations, and the DP_NbVN and commercial steels exhibit lowest total and uniform elongations, while the DP_VN, DP_Nb, DP_NbV steels show intermediate similar total and

uniform elongations for all the seven processing. For commercial steels, the total and uniform elongations are lower at B1, C1 and C2 processing when compared with A1-A4 processing. For DP_NbVN steels, the total and uniform elongations are higher at C1 and C2 processing when compared with B1, A1-A4 processing. Such different relationships between processing and total and uniform elongations for commercial and DP_NbVN steels are probably due to the microstructural difference, and should be further investigated.

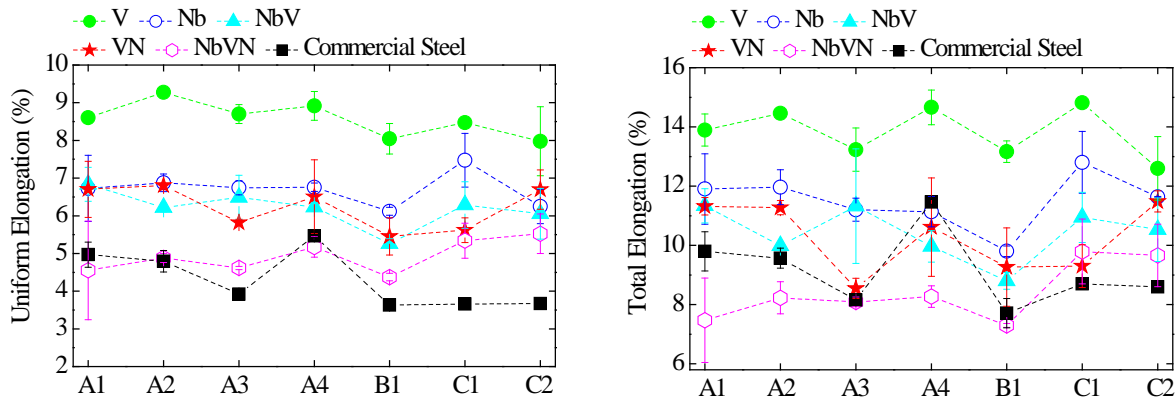


Figure 5.1.9 Total elongation and uniform elongation of DP steels in this work, and the corresponding values of commercial DP steels are also included

The relationships among the seven processing (A1-A4, B1, and C1-C2), chemical composition, $UTS \times TE$, and $YS \times UE$ are shown in Figure 5.1.10. The DP_V steels show highest $UTS \times TE$ and $YS \times UE$, and the DP_NbVN and commercial steels show the lowest $UTS \times TE$ and $YS \times UE$, while the DP_VN, DP_Nb and DP_NbV steels show intermediate $UTS \times TE$ and $YS \times UE$. The detailed relationships between processing and $UTS \times TE$ or $YS \times TE$ are complex for different steels with different compositions. For the commercial steels, both of the $UTS \times TE$ and $YS \times UE$ are lower at processing B1, C1 and C2 when compared with A1-A4 processing. For DP_VN, DP_Nb, DP_NbV and DP_NbVN steels, the values of $YS \times UE$ are close to each other at the processing A1-A4 and B1, and they go up at processing C1 and C2, indicating that the tempered martensite may increase the ductility of these steels. For DP_V steels, the values of $YS \times UE$ are almost at the same level for the seven processing. All the values of the tensile properties are listed in Table 5.1.3.

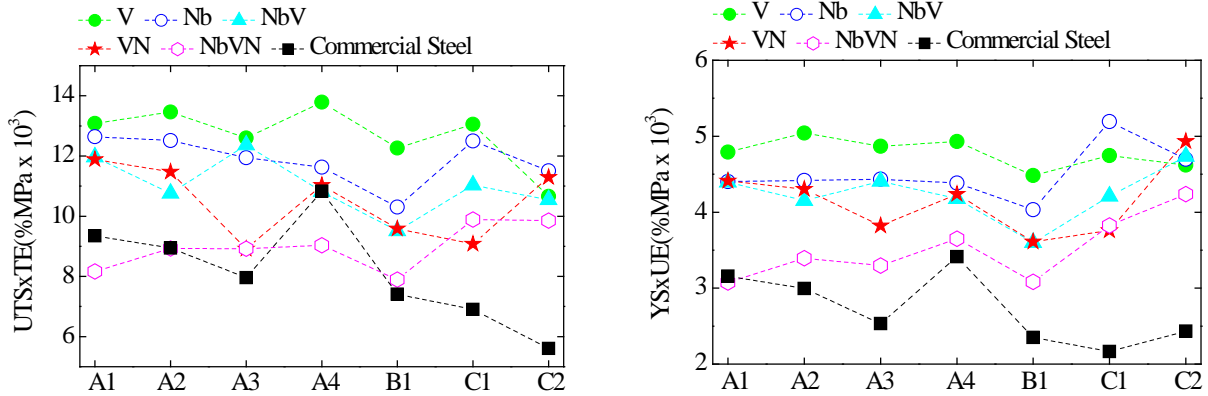


Figure 5.1.10 Values of UTS×TE and YS×UE of DP steels in this work, and the corresponding values of commercial DP steels are also included

A comparison of the tensile properties found in this current study with those from literature is shown in Figure 5.1.11. Figure 5.1.11 (a) shows the relationship between UTS and volume fraction of martensite, and Figure 5.1.11 (b) shows the relationship between uniform elongation and UTS. It is apparent from Figure 5.1.11 (a) that the steels are located above the base line for strength versus volume fraction of martensite in the final structure. However, their ductility values lie somewhat below the Fe-C-Mn trend line, Figure 5.1.11 (b).

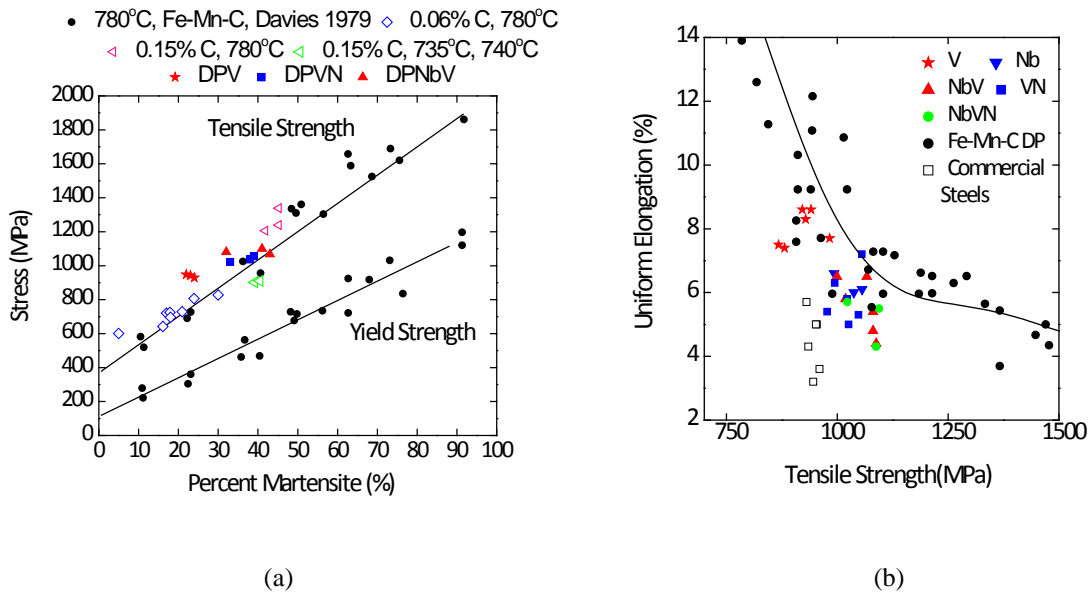


Figure 5.1.11 (a) Comparison of MA volume fraction versus UTS with the corresponding values obtained by Davies^[21], the data of DPV, DPVN and DPNbV with A1, A3 and B1 processing were plotted in this figure, (b) comparison of UTS versus UE with the corresponding values obtained by Davies^[21]. The values of commercial steels are also included

Table 5.1.3 Mechanical properties of the DP steels for the 7 full processing in this current study.

	Yield Strength (YS MPa)						
	A1	A2	A3	A4	B1	C1	C2
DP_V	557	544	558	553	556	560	608
DP_Nb	654	641	660	650	653	687	769
DP_NbV	660	669	687	670	681	671	790
DP_VN	660	636	659	643	650	660	759
DP_NbVN	667	696	712	710	708	724	770
Ultimate Tensile Strength (UTS MPa)							
DP_V	942	931	948	940	929	881	868
DP_Nb	1056	1046	1065	1046	1038	975	993
DP_NbV	1067	1079	1100	1081	1081	1019	1000
DP_VN	1056	1026	1037	1025	1022	977	994
DP_NbVN	1095	1082	1105	1097	1088	1009	1023
YS/UTS ratio							
DP_V	0.5894	0.5844	0.5884	0.5881	0.5986	0.6354	0.7008
DP_Nb	0.6191	0.613	0.6198	0.6217	0.6294	0.7044	0.7747
DP_NbV	0.6188	0.62	0.6248	0.6197	0.6301	0.6586	0.7903
DP_VN	0.6252	0.6201	0.6355	0.6274	0.636	0.6753	0.7634
DP_NbVN	0.6094	0.6431	0.6442	0.6472	0.6507	0.7173	0.7529
Total elongation (TE %) in 2 inch							
DP_V	13.3	14.5	12.7	15.1	13.4	14.8	11.8
DP_Nb	11.1	12.4	10.9	11.5	9.7	12.1	11.6
DP_NbV	10.9	10	10	9.6	9	10.3	11.3
DP_VN	11.5	11.4	8.3	9.4	10.2	8.8	11.2
DP_NbVN	8.5	7.8	8.2	8.5	7.3	10.6	9.3
Uniform elongation (UE %) in 2 inch							
DP_V	8.6	9.3	8.5	9.2	8.3	7.4	7.5
DP_Nb	6.1	6.7	6.9	6.8	6	7	6.6
DP_NbV	6.5	6.1	6.1	6.2	5.4	5.8	6.5
DP_VN	7.2	6.8	5.8	5.8	5.8	5.4	6.3
DP_NbVN	5.5	4.8	4.6	5.4	4.3	5.7	5.7
Strain-hardening exponent (n)							
DP_V	0.16	0.17	0.16	0.17	0.16	0.16	0.14
DP_Nb	0.13	0.14	0.13	0.14	0.13	0.14	0.12
DP_NbV	0.13	0.13	0.12	0.13	0.12	0.13	0.12
DP_VN	0.14	0.14	0.13	0.13	0.13	0.14	0.13
DP_NbVN	0.11	0.12	0.11	0.12	0.11	0.12	0.12

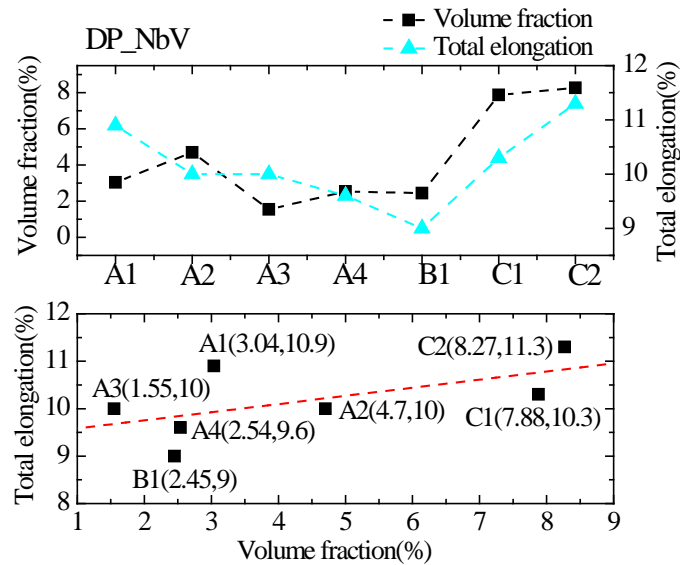


Figure 5.1.12. The relationship between the volume fractions of retained austenite obtained by magnetometry and the total elongations of the DPNbV steels

The retained austenite was measured in DPNbV steel by magnetometry, since it is thought to help improve tensile elongation and n-values. The volume % retained austenite was consistently near 2-5% for the GI(A1-A4) and GA(B) processing, and it reached higher levels of around 8% in the supercooled processing (C1 and C2), as shown in Figure 5.1.12. These data illustrated in Figure 5.1.12 show the positive influence of retained austenite. Combining the strength data, YS/UTS results shown in Table 5.1.3 and the retained austenite measurements given in Figure 5.1.12 describes a steel with a high YS/UTS ratio at high strength levels with good ductility.

Though the tensile strength of DPV is lower than DP steels with other micro alloying elements, the ductility of DPVs is much better (in view of total elongations, uniform elongations, hole expansion ratios and so on). The total elongations and uniform elongations have been discussed in this section. The sheared edge formability was measured as hole expansion ratios. The hole expansion tests were done at USS lab and the data of DPs with A1 and C1 processing were given in Table 5.1.4.

We can see that the DPVs (A1 and C1) possess the best hole expansion (HE%) ratios, as well as reduction in area (RA%) values, compared with other micro alloyed DP steels. When we compare the HE ratios (and reduction in area values) of DPs with A1 and C1 processing, the C1 processed DPs have higher hole expansion ratios. For DPV (C1), the hole expansion ratio even reached 53%, which is very high for DP980 steels. Though the DPV (C1) were not able to reach 980MPa tensile strength, its high hole expansion ratio is still very attractive for industrial applications. Based on this finding, we initiated further studies of the supercool process by using three different supercooling temperatures 250°C, 320°C, and 390°C respectively in Sections 5.5-5.7. The mechanical properties of DPV and vanadium free DPs from tensile tests will also be presented and discussed in Sections 5.5-5.7. The better ductility of DPs with supercool processing derives mainly from the tempered martensite and higher amount of retained austenite compared with galvanizing (A series) and galvannealing processing (B series), which will be discussed in detail in the following sections. Through studying different supercool temperatures, we expected to find the best combination of the amounts of martensite, tempered martensite and retained austenite, so we can get high tensile strength (980MPa grade) and at the same time keep high total elongations and hole expansion ratios. Figure 5.1.13 (a) shows the relationship between hole expansion ratio and tensile strength. We see that the hole expansion ratio decreased with increasing the tensile strength, while Figure 5.1.13 (b) shows that the hole expansion ratio is positively related to the reduction in area values. Since the hole expansion ratio reflects the formability of the sheared steel, it is thought to be related to the post uniform elongation and reduction in area values. As can be seen in Figure 5.1.13 (b), the DP steels with higher reduction in area values possess higher hole expansion ratios. Through simple linear fitting, we get the empirical equation $HER = 1.15 \times RA\% - 19.6$, which may be used to estimate the hole expansion ratios of DPVs with different cold rolling reductions, coiling temperatures and different levels of Cr and Mo contents in Sections 5.5-5.7. Figure 5.1.13 (c) plots the RA% and n-value data, and there is no obvious relationship between hole expansion ratios and n-values. Figure 5.1.13 (d) plots the HE% and YS/UTS ratios data of the six steels, and on obvious relationship between them can be observed.

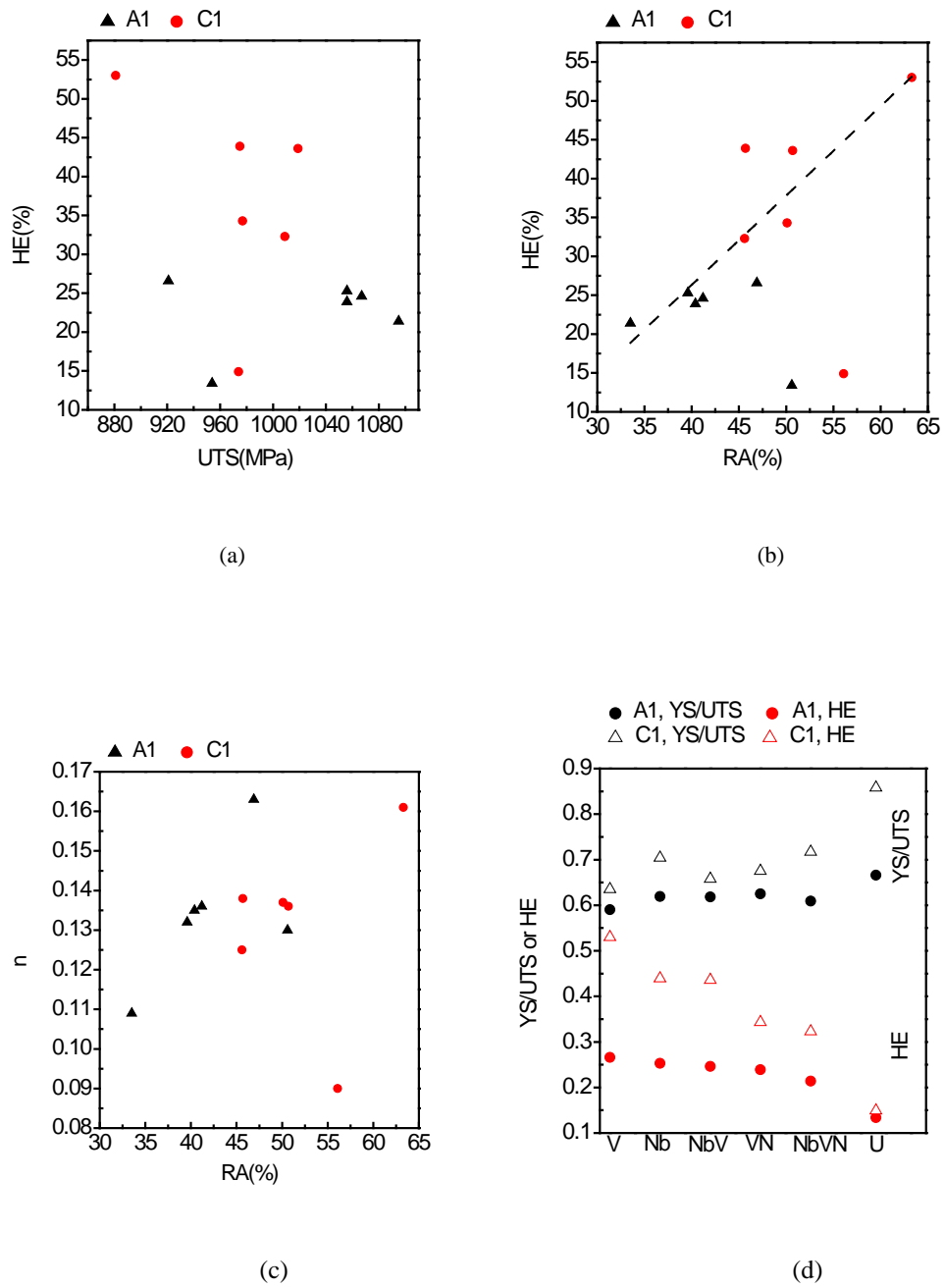


Figure 5.1.13 . Relationship among hole expansion ratio (HE%), tensile strength (UTS), n-values, YS/UTS ratios and reduction in area (RA%)

Table 5.1.4. Hole expansion ratios (HE %) and reduction in area (RA%), which was measured from OM images of the fracture surfaces after tensile testing, of the DP steels with different alloying elements. A1 is the standard galvanizing processing and C1 is the supercool processing with supercool temperature 250°C.

		V	Nb	NbV	VN	NbVN	U
A1	HE%	26.6	25.3	24.6	23.9	21.4	13.4
	RA%	46.9	39.6	41.2	40.4	33.5	50.6
C1	HE%	53.0	43.9	43.6	34.3	32.3	14.9
	RA%	63.3	45.7	50.7	50.1	45.6	56.1

5.1.4 Work hardening behavior

The instantaneous “n values” were also calculated for DP_NbV at the seven processing (A1-A4, B1, C1 and C2). The instantaneous n values were calculated by differentiating $\ln(\sigma)$ with respect to $\ln(\epsilon)$, i.e. $n=d(\ln\sigma)/d(\ln\epsilon)$ without making any prior assumptions about the validity of any strain hardening law. The n versus true strain ϵ curves are shown in Figure 5.1.14, and the values of n in 5 strain ranges are listed in Table 5.1.5. The n values of the 7 processing are similar when ϵ is greater than 4%, and the n values of A1-A4 and B1 are at the same level at the three ranges 0.2%-1%, 1%-2% and 2%-4%, but those of C1 and C2 are lower at these three ranges. This indicates that the steels with mainly ferrite plus tempered martensite microstructures have lower work hardening effect than those with mainly ferrite plus martensite microstructures.

Table 5.1.5. $n(\epsilon) = \frac{d(\ln\sigma)}{d(\ln\epsilon)}$, ϵ is true strain, σ is true stress. The values of n in the table are the averaged ones in the

specific true strain range as shown in the table.

DP_NbV	n				
	$\epsilon=0.002-0.01$	$\epsilon=0.01-0.02$	$\epsilon=0.02-0.04$	$\epsilon=0.04-0.06$	$\epsilon>0.06$
A1	0.42	0.28	0.19	0.14	0.10
A2	0.42	0.26	0.18	0.13	0.09
A3	0.44	0.26	0.17	0.12	0.09
A4	0.43	0.26	0.18	0.13	0.09
B1	0.45	0.26	0.17	0.12	0.09
C1	0.35	0.23	0.18	0.13	0.09
C2	0.38	0.13	0.14	0.12	0.10

Table 5.1.6. Strain-hardening exponent (m) from modified C-J analysis and the transition strains between the two stages of work hardening behavior

	Strain-hardening exponent (m)				
	DP_V	DP_Nb	DP_NbV	DP_VN	DP_NbVN
Stage I	4.5	4.9	4.7	5.3	5.4
Stage II	6.9	7.4	7.5	8.0	8.7
Transition strain (%)	1.8	1.6	1.3	1.6	1.6

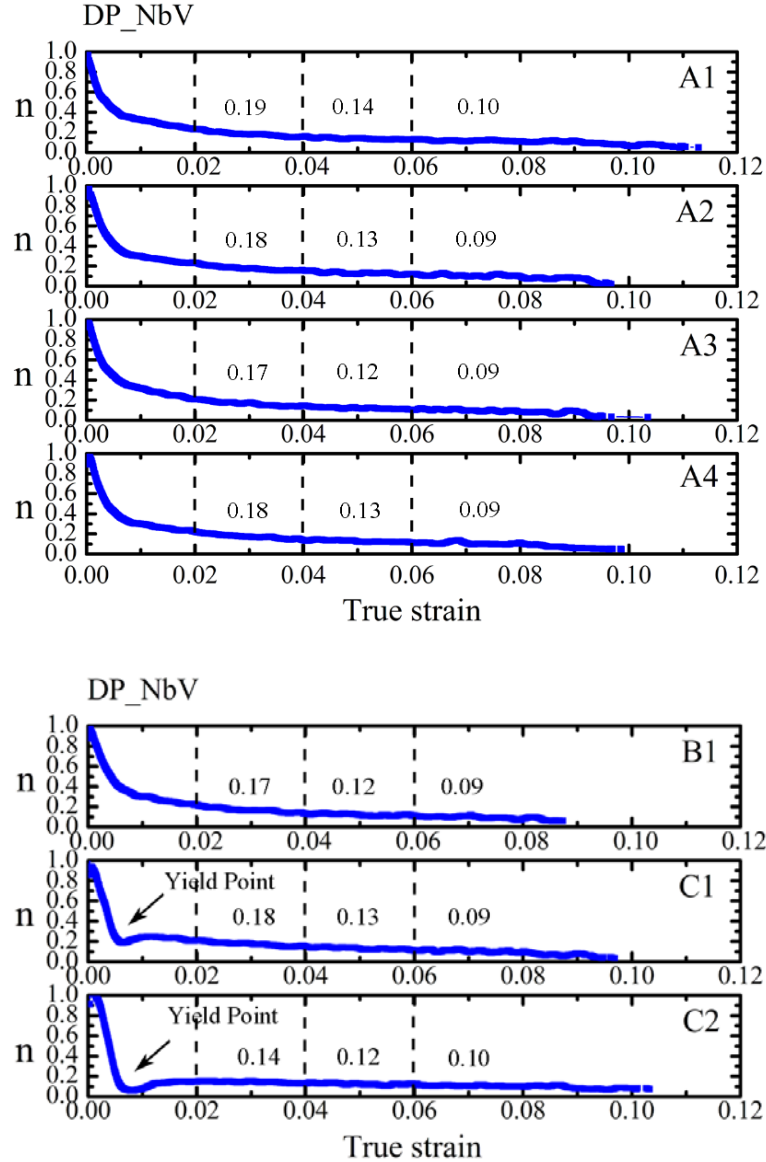


Figure 5.1.14 Instantaneous n-values versus true strain curves for the 7 full processing of DP_NbV

The modified Crussard-Jaoul (C-J) analysis based on the Swift equation, which is known to best describe the work hardening behavior of dual phase steels was used in this study. The Swift stress-strain relationship is expressed as

$$\varepsilon = \varepsilon_0 + k\sigma^m, \quad (5.1.1)$$

where ε and σ are the true strain and true stress, respectively, m is the strain hardening exponent, and ε_0 and k are the material constants. When we differentiate the logarithmic form of Eq. (5.1.1) with respect to ε , we get

$$\ln\left(\frac{d\sigma}{d\varepsilon}\right) = (1 - m) \ln(\sigma) - \ln(km). \quad (5.1.2)$$

The values of m were obtained from the slope, $(1-m)$ of the $\ln(d\sigma/d\varepsilon)$ versus $\ln\sigma$ curves. The $\ln(d\sigma/d\varepsilon)$ versus $\ln\sigma$ curves of the five steels with GI (A3) processing are depicted in Figure 5.1.15 and the m values estimated from the slope of line segments in Figure 5.1.15 are listed in Table 5.1.6.

From Figure 5.1.15, we can see that all of the five steels exhibited the two stage hardening behavior, as similar to conventional dual phase steels. At the first stage with low slope, ferrite matrix deforms plastically but martensite remains elastic. At the second stage with high slope, both ferrite and martensite deform plastically.

The m values of the five steels are close, around 5 at the first stage. At the second stage, the m values of DP_V, DP_Nb and DP_NbV are at the same level and are lower than those of DP_VN and DP_NbVN. Such difference is related to the microstructural difference of the steels and need to be further investigated. The transition strains between the first and second stages are close to each other for DP_V, DP_Nb, DP_VN and DP_NbVN, and the transition strain of DP_NbV is lower, which may be probably due to the existence of the hard dense martensite bands in DP_NbV. The plastic deformation of martensite in DP_NbV with GI (A3) processing started earlier than other steels under the same processing, implying that load transfer from ferrite to martensite was more pronounced due to dense martensite bands.

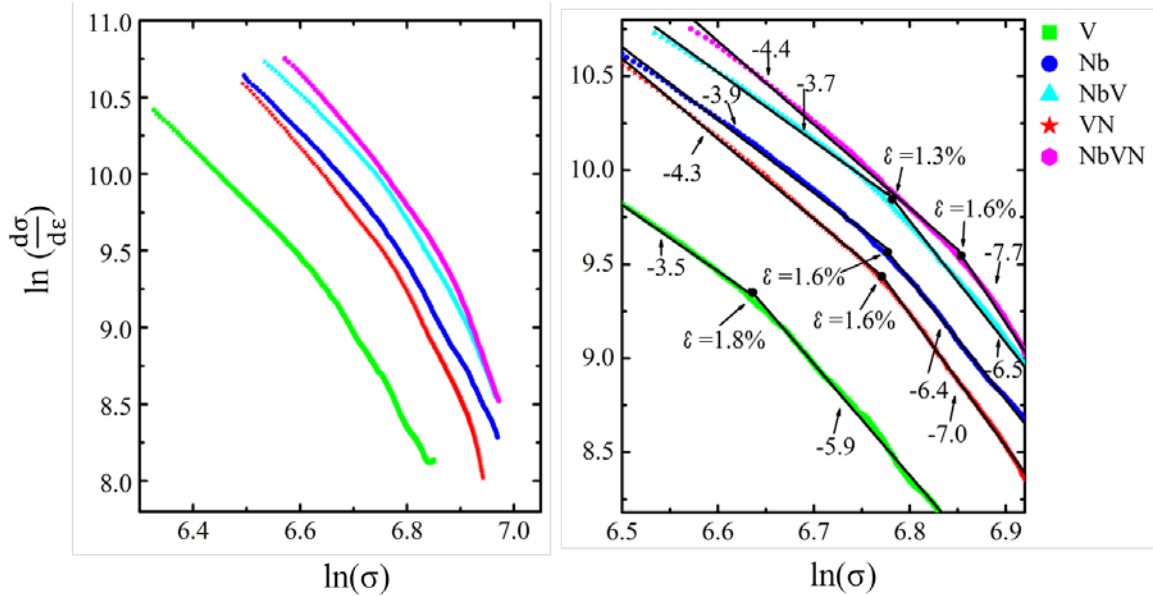


Figure 5.1.15 $\ln(d\sigma/d\varepsilon)$ versus $\ln\sigma$ curves of the five steels with GI (A3) processing, the transition strains and the slopes of the two parts of the curves are also shown in the figure

5.1.5 Microstructures of dual phase steels with full processing

Since the mechanical properties of dual phase steels are closely related to the microstructures, this section will discuss the microstructures of DPs with full Gleeble processing, and some typical microstructures (SEM or OM) will be presented.

Figure 5.1.16 compared the SEM microstructures of DPV, DPVN and DPNbV with standard galvanizing A1 processing, from which it is clear that the amount of martensite in DPV (A1) is much lower than that in DPNbV or DPVN, which is also true for other processings (A2-A4, B1). The microstructures of the five types of DPs (DPV, DPVN, DPNb, DPNbV and DPNbVN) mainly consist of polygonal ferrite and martensite for A1-A4 and B1 processings, while some non-recrystallized ferrite can be found in DPVN and DPNbVN. The comparison of the microstructures of DPV, DPVN and DPNbV with A3 processing can be found in Figure 5.1.17. For supercool processing (C1 and C2), most of the hard phase is tempered martensite and the amount of fresh martensite is less than 10% for all the five types of DPs, while the soft phase is mainly polygonal ferrite for DPV, DPNbV and DPNb, and some

non-recrystallized ferrite existed in DPVN and DPNbVN. The microstructures of DPs (DPV, DPVN, DPNbVN and DPNbV) with C1 processing were shown in Figure 5.1.16 (c) and 5.1.18, from which it can be easily found that the total amount of tempered martensite and martensite is much less in DPV(C1) than that in DPs (C1) with other alloying elements. The volume fractions of martensite, tempered martensite in DP steels with five different compositions and A1, A3, B1 and C1 processings were listed in Table 5.1.7. From the above discussions, we see that the lower strength of DPV compared with DPs with other alloying elements is mainly due to the lower amount of hard phases (martensite or tempered martensite), and the significant improvement of the elongations and hole expansion ratios for supercool C1 processing is due to the tempered martensite which is the main hard phase. The low amount of martensite in the final microstructures of DPV is closely related to the low amount of austenite formed during 1 minute intercritical annealing at 790°C. To explain the low amount of austenite formed at IAT, the austenite formation kinetics and stored energy in the initial cold rolled sheets with different alloying elements will be discussed in detail in the following sections and ways to improve the amount of martensite and thus strengthen the DPV steels will be studied.

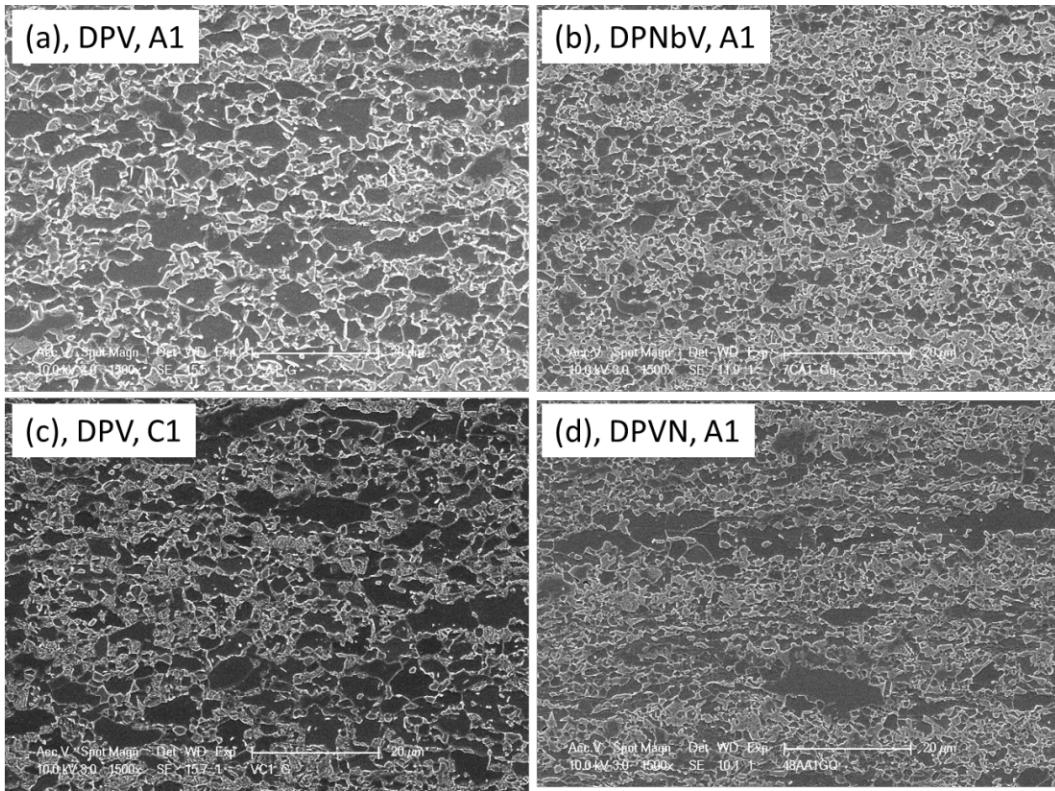
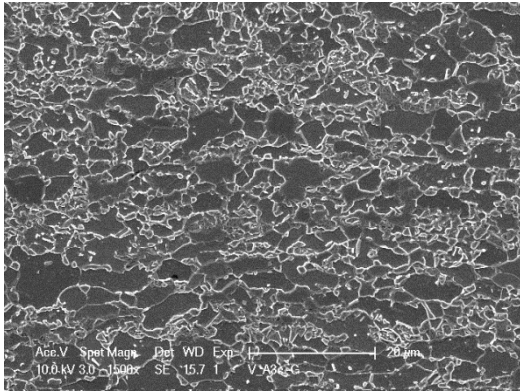
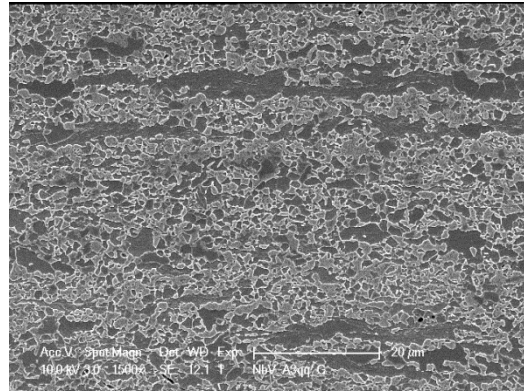


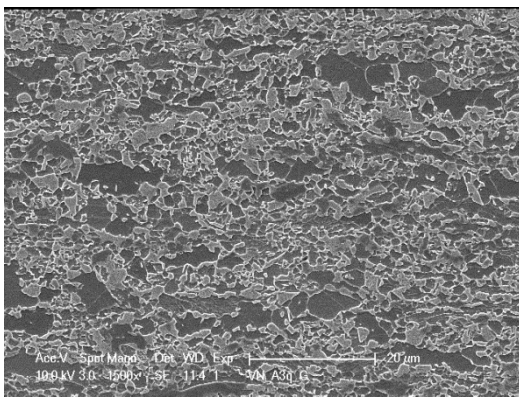
Figure 5.1.16 SEM microstructures of DP_V, DP_VN and DP_NbV, 2% Nital etched



(a)



(b)



(c)

Figure 5.1.17. SEM microstructures of (a) DPV, A3, (b) DPNbV, A3 and (c) DPVN, A3 processing

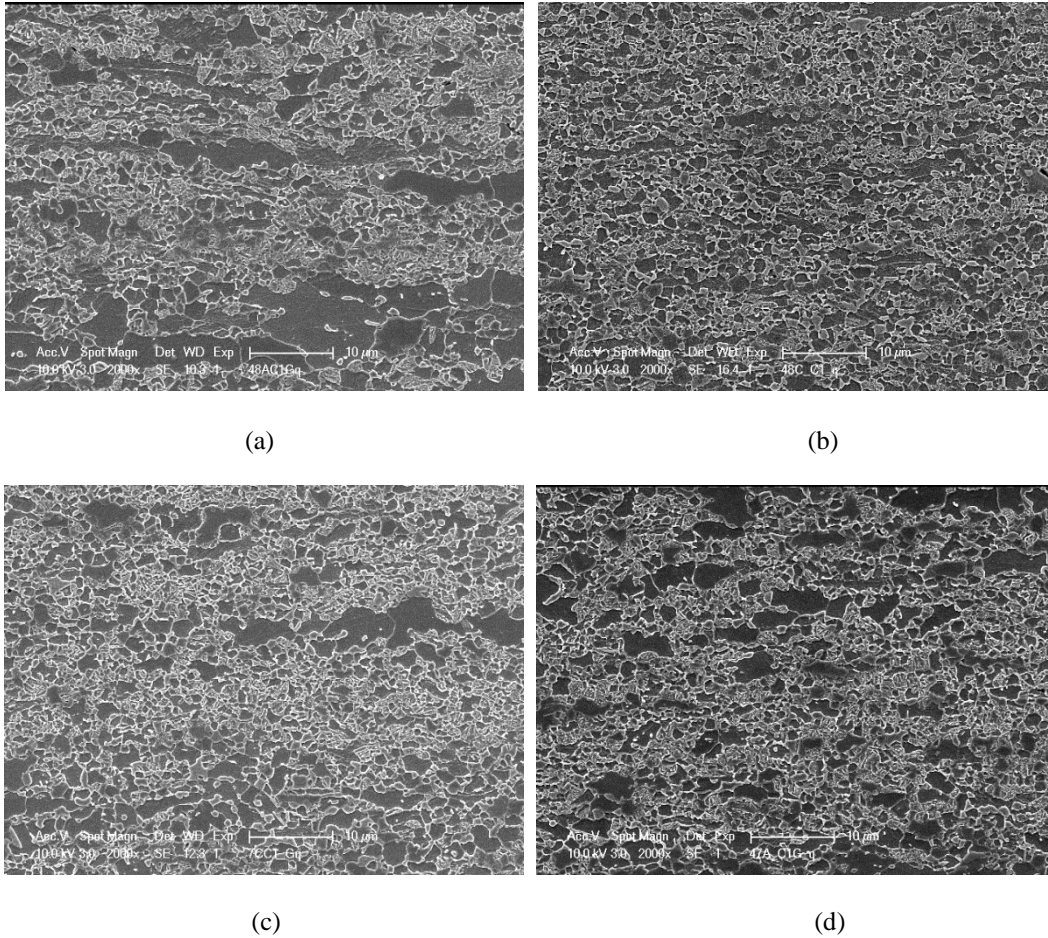


Figure 5.1.18. SEM microstructures of (a) DPVN, C1, (b) DPNbVN, C1, (c) DPNbV, C1, and (d) DPNb, C1

Table 5.1.7. Volume fractions (%) of MA, and TM in the DP steels with five different compositions and A1,A 3, B1 and C1 processing

	DPV	DPVN	DPNb	DPNbV	DPNbVN
A1, MA	23	39	38	43	44
A3, MA	22.5	38	35	41	42
B1, MA	24	33	36	32	35
C1, MA	6.5	10	12	13	8.5
C1, TM	20	34.5	29	33	38

In the remaining part of this section, more microstructures of DPs with full processing will be checked carefully. The microstructures of DPV with full processing, i.e. B1-B3 and C2 were carefully investigated using SEM, Figures 5.1.19 and 5.1.20. The main constituents are ferrite and MA (TM for

C2). As can be seen, all the cementite (except only several cementite particles) was dissolved at the IAT 790°C under all these conditions. In Figures 5.1.19 and 5.1.20, we can see that more bainite can be found in DPV with B2 and B3 processings compared with DPV with B1 processing, which can be expected since for B2 and B3, the holding time at 460°C is longer (B2 60s, B3 120s while B1 only 30s). The longer holding time at 460°C allows more transformation of bainite from austenite. More than one kinds of bainite have been found, mainly lower bainite and upper bainite. The amount of bainite existing in the final state of the DPV may explain the low strength of DP_V with full processing compared with the other four steels. For processing C2 (Figure 5.1.20 (b) (d)), most of the martensite is tempered martensite, which is softer than the normal martensite, contributing to the lower tensile strength for the supercool processing (C1 and C2).

The typical SEM microstructures of DPVN with GA processing are shown in Figure 5.1.21. Figure 5.1.21 (a) is the microstructure of DPVN with GA (B2) processing with low magnification, and (b) and (c) are central region of (a) at higher magnification to see the detailed structures. As we can see, there is a large amount of non-recrystallized ferrite with the morphology of cold-rolled ferrite. Besides the recrystallized polygonal ferrite, non-recrystallized ferrite, MA, several not dissolved carbide is also there, while little bainite can be found. The large amount of non-recrystallized ferrite may be one important reason for the higher strength but lower ductility of DPVN compared with DPV.

Some optical microstructures of DP_NbV with full processing are shown in Figure 5.1.22 and Figure 5.1.23. Figure 5.1.22 (a) and (b) are the Nital etched microstructures of DP_NbV with processing GI (A3), in which the white grains are the ferrite grains and the other color represents MA, and (c) is the LePera etched microstructure of this steel, in which the white area is the MA, while the ferrite exhibits brown color. The obvious banding structure can be observed from Figure 5.1.22. Figure 5.1.23 (a) and (b) are the LePera etched microstructures of DP_NbV with processing GI (A4) and GA (B1) respectively, while (c) is the Nital etched microstructure of DP_NbV with processing C2. The microstructures of DP_NbV with full processing were further checked using SEM as shown in Figure 5.1.24. The various characterization methods (optical (Nital and LePera etched) microstructures and SEM microstructures)

indicate that the final microstructure of DP_NbV with GI and GA processing consists of mainly recrystallized ferrite and MA, sometimes non-crystallized ferrite can also be found, but not much, while little bainite was found. The microstructures of DP_NbV with supercool processing (C1 and C2) consist of mainly recrystallized ferrite, MA and tempered martensite.

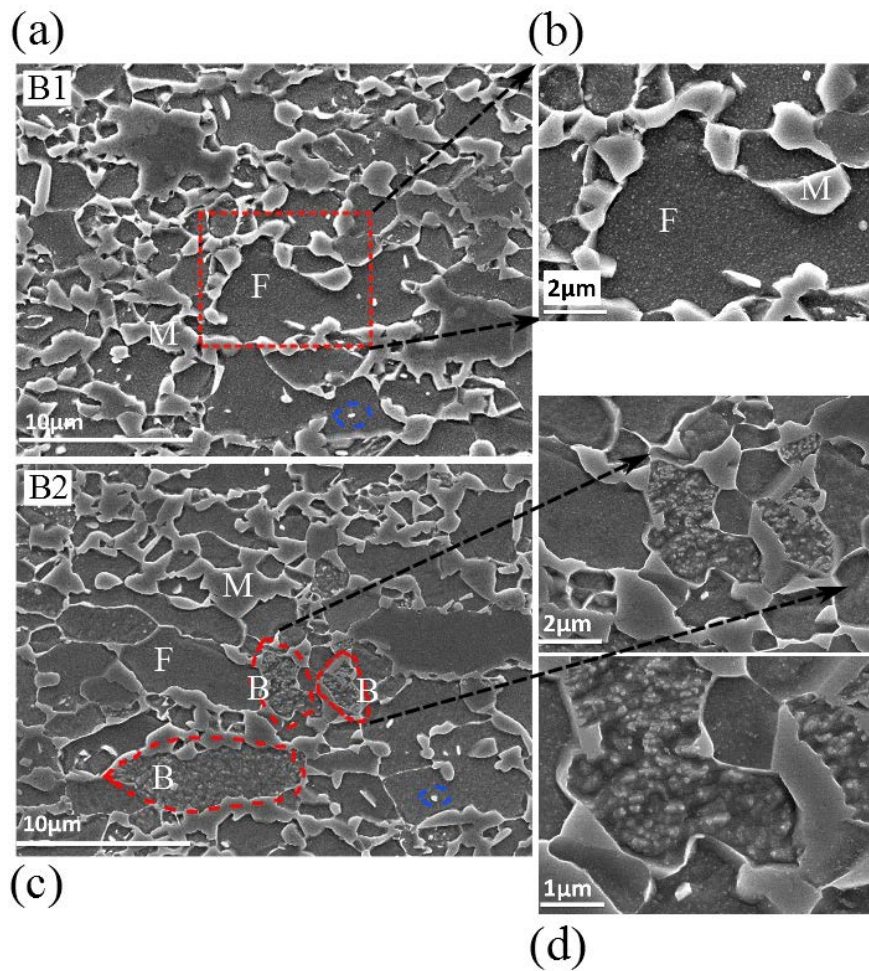


Figure 5.1.19 SEM microstructures of DP_V with full processing B1 (a) and B2 (c), (b) is the microstructure with higher magnification of the area enclosed with dashed red square in (a), (d) are the enlarged microstructures of the area enclosed with dashed red lines in (c). The bright white particles enclosed with dashed blue lines are the cementite

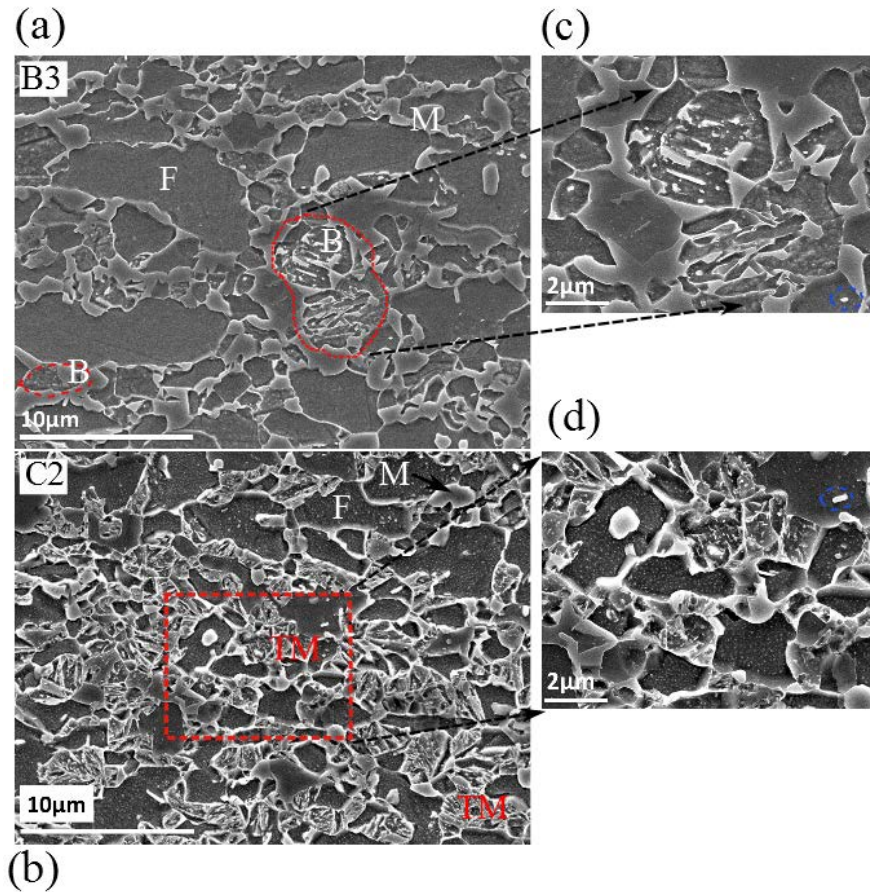


Figure 5.1.20 SEM microstructures of DP_V with full processing GA (B3) (a) and C2 (b), (c) is the microstructure with higher magnification of the area enclosed by dashed red circle in (a), (d) is the enlarged microstructures of the area enclosed with dashed red square in (c). The bright white particles enclosed with dashed blue lines are the cementite

One interesting thing is that very little non-recrystallized ferrite was found in DP_NbV with full processing, while we found much non-recrystallized ferrite in DP_VN with full processing. From the discussions in Section 5.1.7.3, it can be deduced that the addition of Nb and V can effectively retard the recrystallization of ferrite, the reason for the little non-recrystallized ferrite found in DP_NbV with full processing is probably that the non-recrystallized ferrite was transformed to austenite during intercritical annealing which further decomposed to MA. This assumption can be supported by the frequently found MA in the non-recrystallized ferrite matrix (Figure 5.1.21). Since there are more defects like distortions of crystal lattice, dislocations in the non-recrystallized deformed ferrite, carbides can be easily dissolved at

the significantly deformed sites in these “old” recovered ferrite. Due to the high stored energy in the non-recrystallized ferrite, the driving force for dissolving the carbides is lower and so the austenite tends to form more easily at the non-recrystallized ferrite matrix. Some non-dissolved carbides can frequently be found in the recrystallized polygonal ferrite, further indicating that the driving force for dissolving the carbides in the recrystallized ferrite is high compared with that in the non-recrystallized ferrite. In this case of DP_NbV, the more amount of martensite in the final microstructure is probably one important factor causing the DP_NbV much stronger than DP_V. The more amount of martensite in DP_NbV is related to the effects of addition of Nb and V on suppressing the recrystallization of ferrite and promoting the formation of austenite during intercritical annealing, and it is expected that austenite can easily form in the non-recrystallized ferrite matrix than in the recrystallized ferrite.

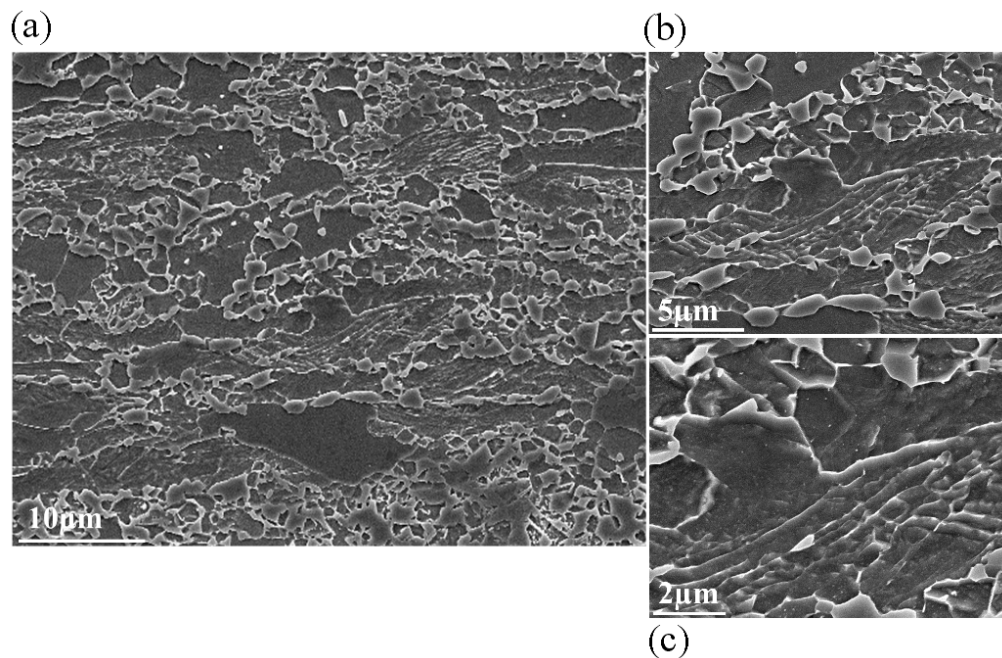


Figure 5.1.21 SEM microstructures of DP_VN with full processing GA (B2), (b) and (c) are the magnified microstructures of (a) at the central region

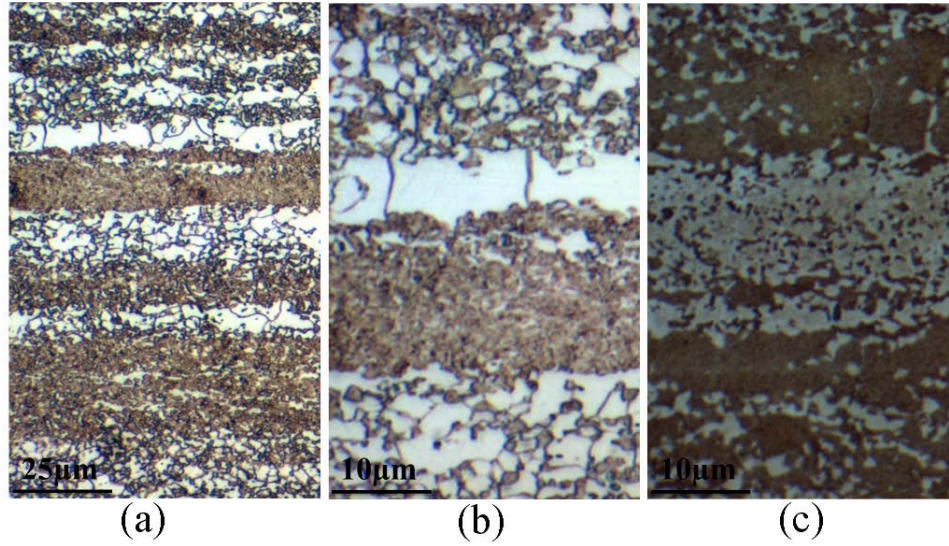


Figure 5.1.22 Optical microstructures of DP_NbV, GI(A3). (a) and (b) Nital etched, (c) LePera etched.

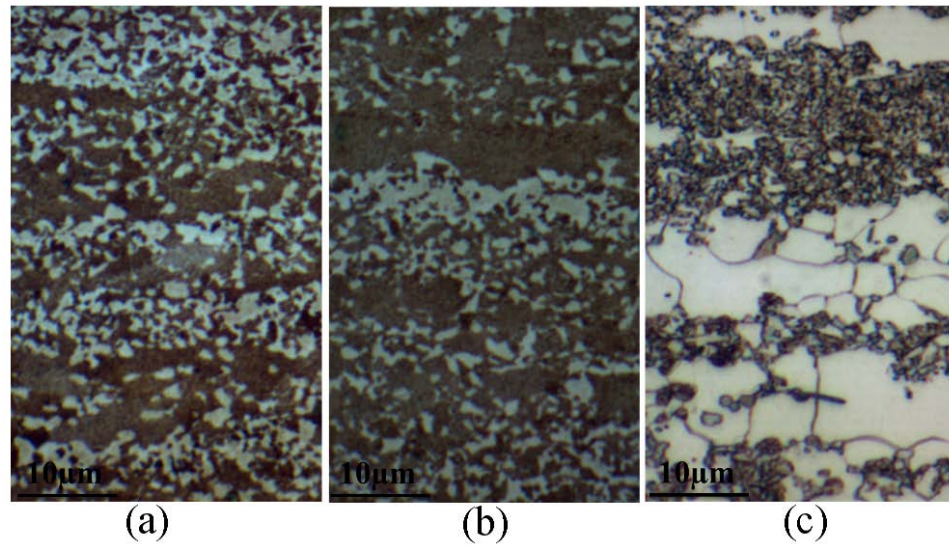


Figure 5.1.23 Optical microstructures of DP_NbV. (a) GI(A4), LePera etched, (b) GA(B1) LePera etched, (c) Supercool (C2), Nital etched.

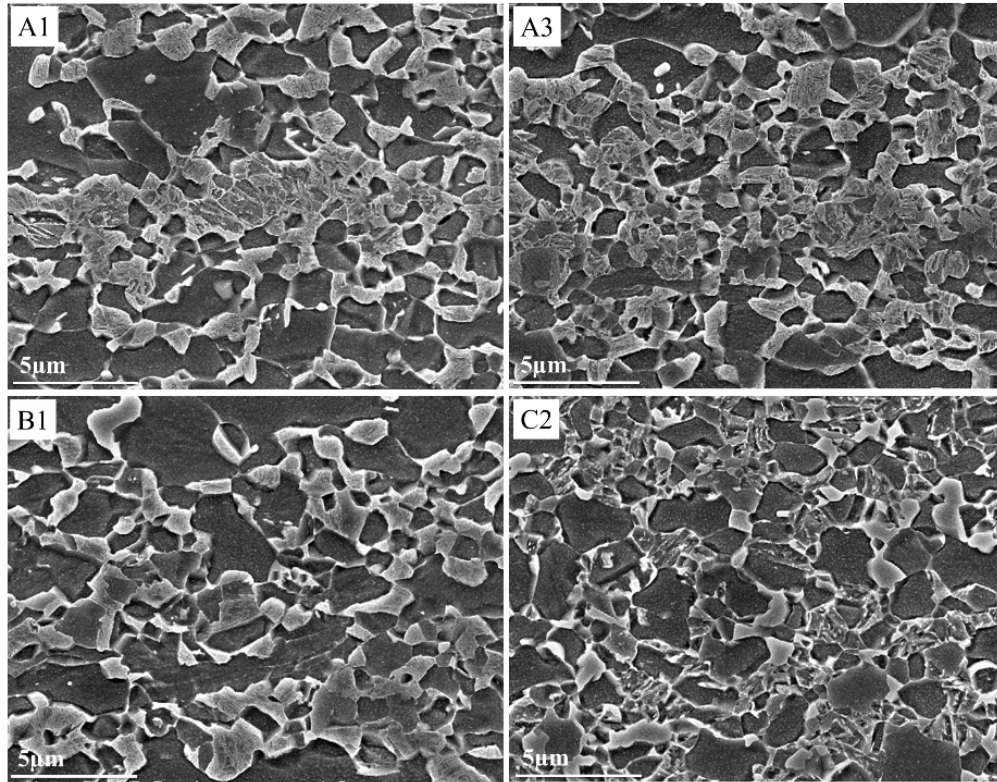


Figure 5.1.24 SEM microstructures of DP_NbV with full processing GI (A1 and A3), GA (B1) and Supercool (C2)

5.1.6 Micro hardness

In order to explain the lower tensile strength of the DPV steels under the same heat treatments, compared with the other four steels, the micro-hardness tests were conducted. The micro indentations were carefully located at the soft bands (brown and mainly ferrite or bainite) or hard bands (MA or tempered martensite), as can be seen in Figure 5.1.26. For GI (A1-A4) and GA (B1) processings, the VHNs are around 390 at hard region for all the DPV, DPVN and DPNbV steels, and are around 180 at soft region for DPV and DPNbV steels, while the a little higher hardness of soft region of DPVN is due to the non-recrystallized ferrite found in the microstructures. For supercool processing (C1-C2), the hardness of the hard region reduced significantly to around 300 due to the formation of tempered martensite, while the hardness of the soft region didn't drop much. The micro-hardness results indicate that the alloying elements V, Nb or

N don't affect the hardness of the martensite or ferrite so much. In the aspect of micro-hardness (10g), the lower tensile strength of DPV isn't due to the lower hardness of the two constituents. The additions of more alloying elements in the other four steels don't obviously increase the hardness of martensite or ferrite from the results of micro-hardness (10g) tests. The values of VHN for DPV, DPVN and DPNbV are listed in Tables 5.1.8-5.1.10 and were plotted in Figure 5.1.25.

Table 5.1.8 values of VHN in soft region and hard region for DP_V

DP_V	VHN_10g						
	A1	A2	A3	A4	B1	C1	C2
Soft region	200±15	185±15	199±12	185±15	187±23	188±8	184±10
Hard region	360±39	360±26	385±24	372±29	395±12	313±18	318±25

Table 5.1.9. VHN values of soft region and hard region for DP_VN, 10g, Gleeble1 at USS

DP_VN	A1	A2	A3	A4	B1	C1	C2
Soft region	202±2	205±7	180±7	210±11	196±2	183±8	179±9
Hard region	364±17	343±16	381±15	390±32	383±5	328±4	328±20

Table 5.1.10 values of VHN in soft region and hard region for DP_NbV

DP_NbV	VHN_10g						
	A1	A2	A3	A4	B1	C1	C2
Soft region	179±6	182±11	187±11	184±17	183±9	178±5	183±12
Hard region	352±9	345±13	389±24	370±10	371±27	315±13	302±22

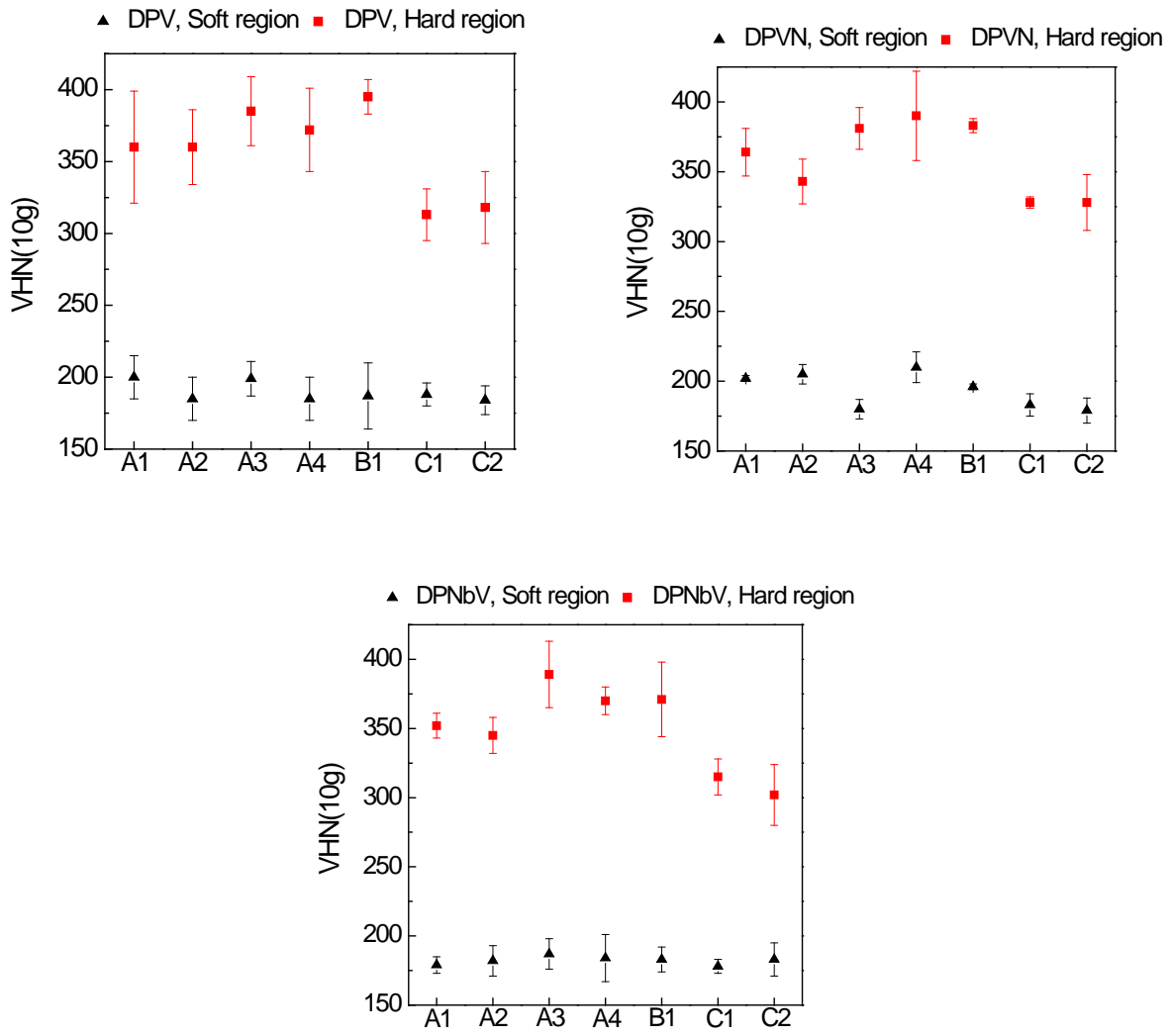


Figure 5.1.25. VHN (10g) of DP_V, DP_VN and DP_NbV at ferrite bands (soft region) and MA bands (hard region) respectively



Figure 5.1.26. Micro-hardness indents (VHN 10g) in DP_NbV, GI (A3), LePera etched

5.1.7 Results of dual phase steels with partial processing: study of austenite formation, dissolution behavior of cementite and recrystallization behavior of cold rolled ferrite

5.1.7.1 Effects of alloying elements on the austenite formation during intercritical annealing

In order to study the microstructural evolutions at each step of the full Gleeble processing, MTS heat treatment plans (partial processing of the full processing) were designed as shown in Figure 5.1.27. Figure 5.1.27 (a) shows the intercritical annealing and then water quenching processing referred to as group M. M1, M2 and M3 represent processing with holding time 1 min, 2min and 5min at 780°C respectively. Figure 5.1.27 (b) shows the processing that simulate the GI processing. T1, T2 and T3 represent processing with holding time 0s, 30s and 8min at 460°C respectively. The dashed curves represent air cooling and the solid arrows represent water quenching.

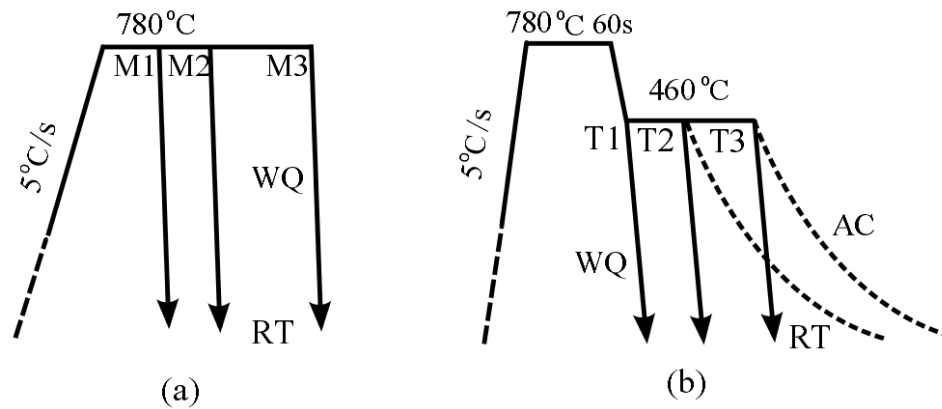


Figure 5.1.27 partial processing conducted in MTS system, (a) M1 1min, M2 2min, and M3 5min. (b) T1 0s, T2 30s and T3 8min. Air cooling (AC), water quenching (WQ)

Figure 5.1.28 shows the microstructures of DPV with processing M1. Figure 5.1.28 (a) is the LePera etched microstructure showing the martensite islands (white) and ferrite matrix (brown) , (b) is the Nital etched microstructure showing ferrite grains (white), (c) and (d) are the SEM microstructures. From these microstructures we found the main constituents are ferrite and martensite. Figure 5.1.29 shows the LePera etched microstructures of DPV with holding time 1, 2 and 5 minutes at IAT 780°C. Typical LePera etched optical microstructures of the five steels with processing group M are shown in Figure

5.1.31, and the typical SEM microstructures are shown in Figure 5.1.32. For all five steels with group M processing, the main constituents are ferrite and martensite. From the SEM microstructures of DP_VN, some non-recrystallized ferrite can also be found. The measured volume fractions of MA from the LePera etched microstructures are listed in Table 5.1.11, plotted in Figure 5.1.30, and shown in Figure 5.1.29 for DPV. The measured volume fractions of MA for DP_Nb, DP_NbV and DP_NbVN are close to or somewhat higher than the predicted values from JmatPro software, while the measured volume fractions of DP_V and DP_VN are a little lower than the predicted values. It is apparent that the formation of austenite during the intercritical annealing is retarded in the DP_V steel when compared with the others. The low volume fraction of martensite in DPV may contribute to the low strength. One interesting thing is that the measured volume fraction of MA for DPV with processing M1 is pretty low, around 20%, while the measured volume fraction of MA for DPNbV with processing M3 is quite high, around 85%. The low amount of austenite is closely related to the kinetics of austenite formation and will be discussed in view of stored energy in the following Section 5.4.

Table 5.1.11 Volume fractions of MA of the five steels with processing group M

	Volume fraction of MA (%)				
	DP_V	DP_Nb	DP_VN	DP_NbV	DP_NbVN
M1	18	51	34	47	41
M2	37	54	38	54	49
M3	39	64	39	85	57

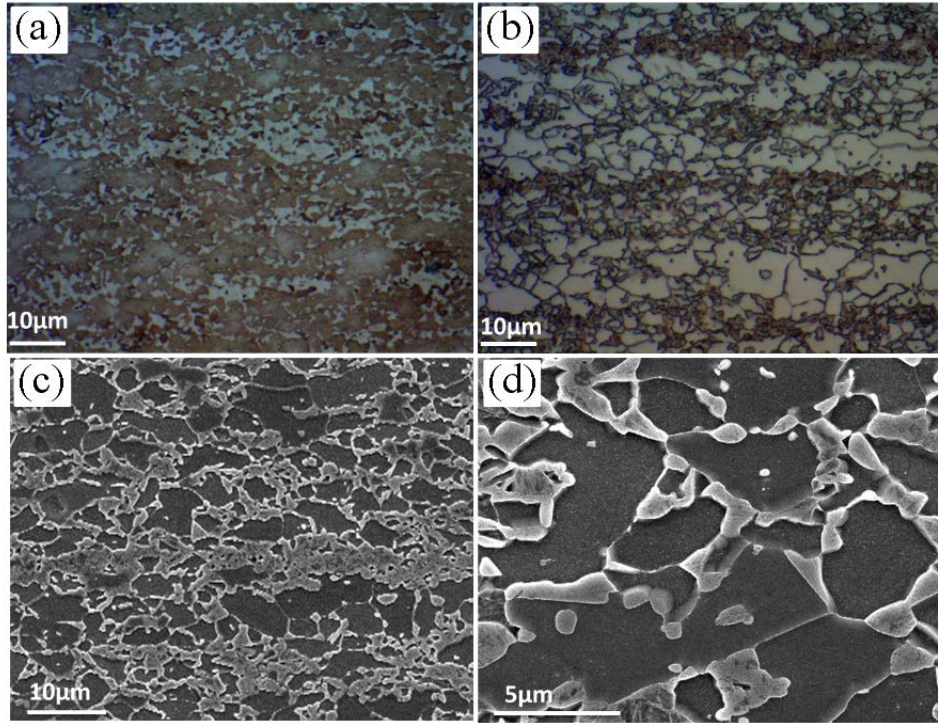


Figure 5.1.28. microstructures of DP_V with processing M1 (a) LePera etched, (b) Nital etched, (c) and (d) SEM microstructures of different magnifications

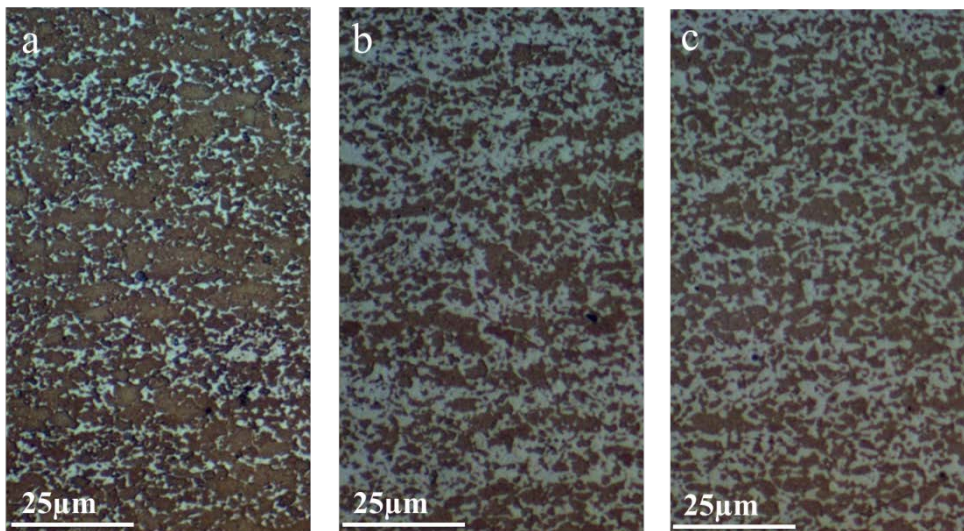


Figure 5.1.29. DPV, 60% cold rolled (a) 780°C, 1min, WQ, (b) 780°C, 2min, WQ and (c) 780°C, 5min, WQ. (LePera Etched, White MA, Brown Ferrite)

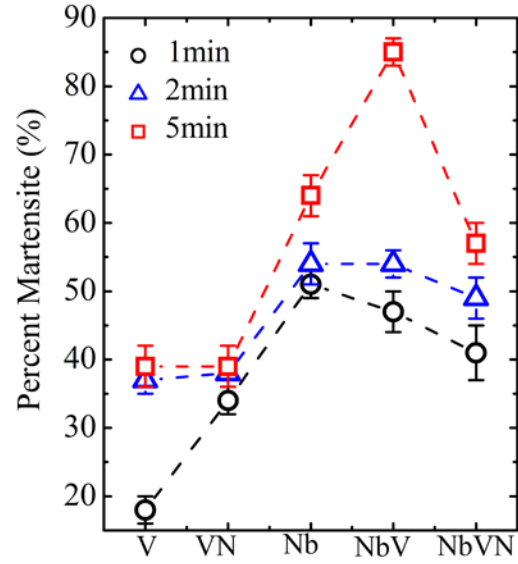


Figure 5.1.30 Volume fractions of the five steels with different holding time at IAT 780°C

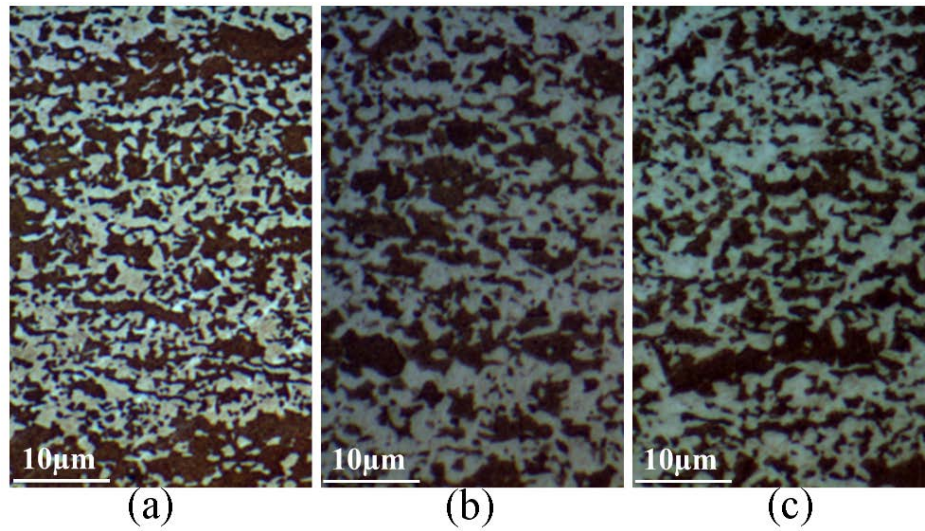


Figure 5.1.31 LePera etched microstructures (a) DP_VN, M1 (b) DP_Nb, M1(c) DP_NbV, M2

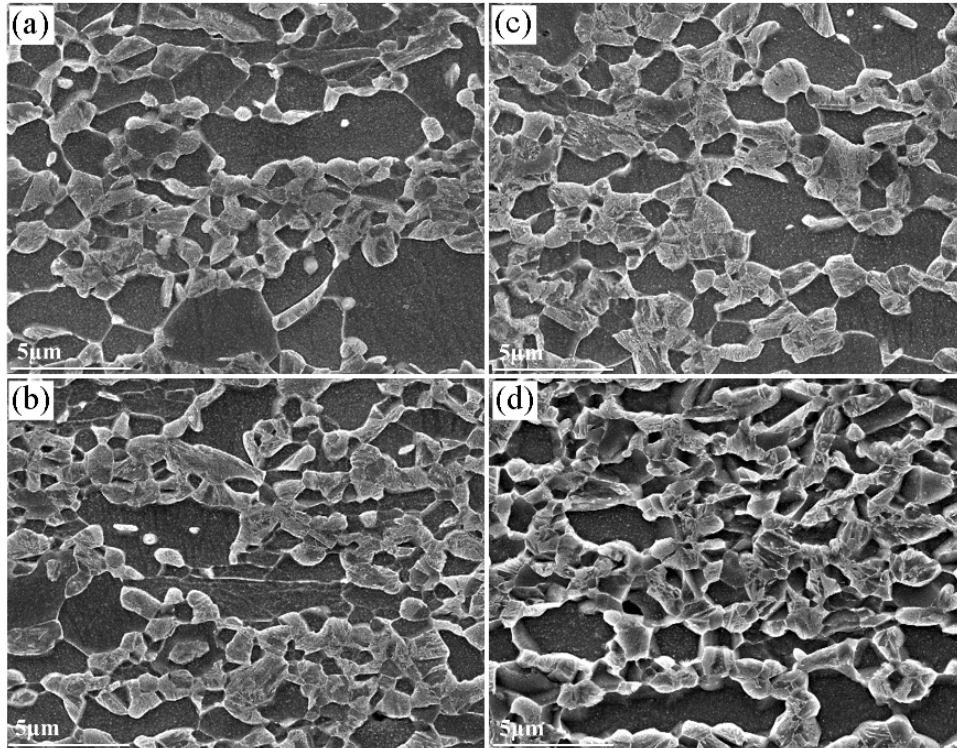


Figure 5.1.32 SEM microstructures of DP_VN, (a) M1, 780°C, 1min, (b) M2, 780°C, 2min, (c) M3, 780°C, 5min and (d) DP_NbVN, M2, 780°C, 2min

5.1.7.2 Dissolution behavior of cementite

This section will discuss the dissolution behavior of cementite in cold rolled sheets during intercritical annealing, which is important in the development of high strength dual phase steels since the hardenability and stability of intercritically formed austenite depends on the carbon concentration.

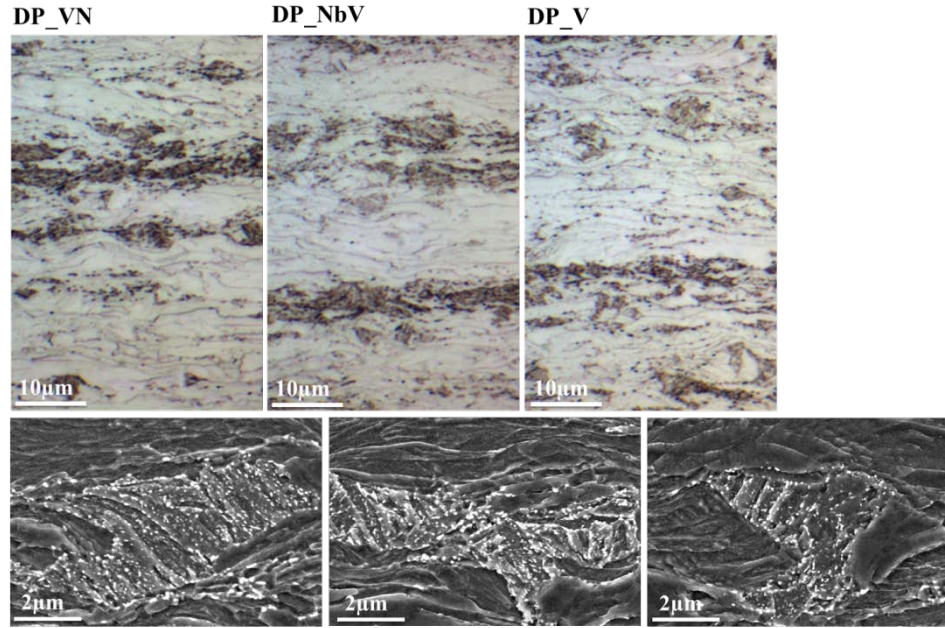


Figure 5.1.33. OM images (above 3 images) of DPVN, DPNbV and DPV (from left to right) and SEM microstructures of the corresponding steels (bottom, from left to right DPVN, DPNbV and DPV, respectively), the heat treatment is 650°C/5min, WQ, heating rate from RT to IAT 650°C is 5°C/s.

Figure 5.1.33 contains the optical microscopy (OM) images of DPVN, DPNbV and DPV after holding at IAT 650°C and then water quenched. We can clearly see the severely cold deformed ferrite with streamline grain boundaries in elongated ferrite (white region in the OM images), and also some cementite particles (black spots in OM images) in the ferrite matrix. The bottom 3 images are the corresponding SEM microstructures showing spheroidization of cementite in pearlite areas and cold deformed ferrite with deformation bands. These results indicate that 650°C is too low for recrystallization of ferrite and only some recovery of deformed ferrite can happen. Also at 650°C, spheroidization of pearlite started and re-precipitation of cementite along elongated ferrite grain boundaries occurred due to the redistribution of carbon and recovery of cold deformed ferrite.

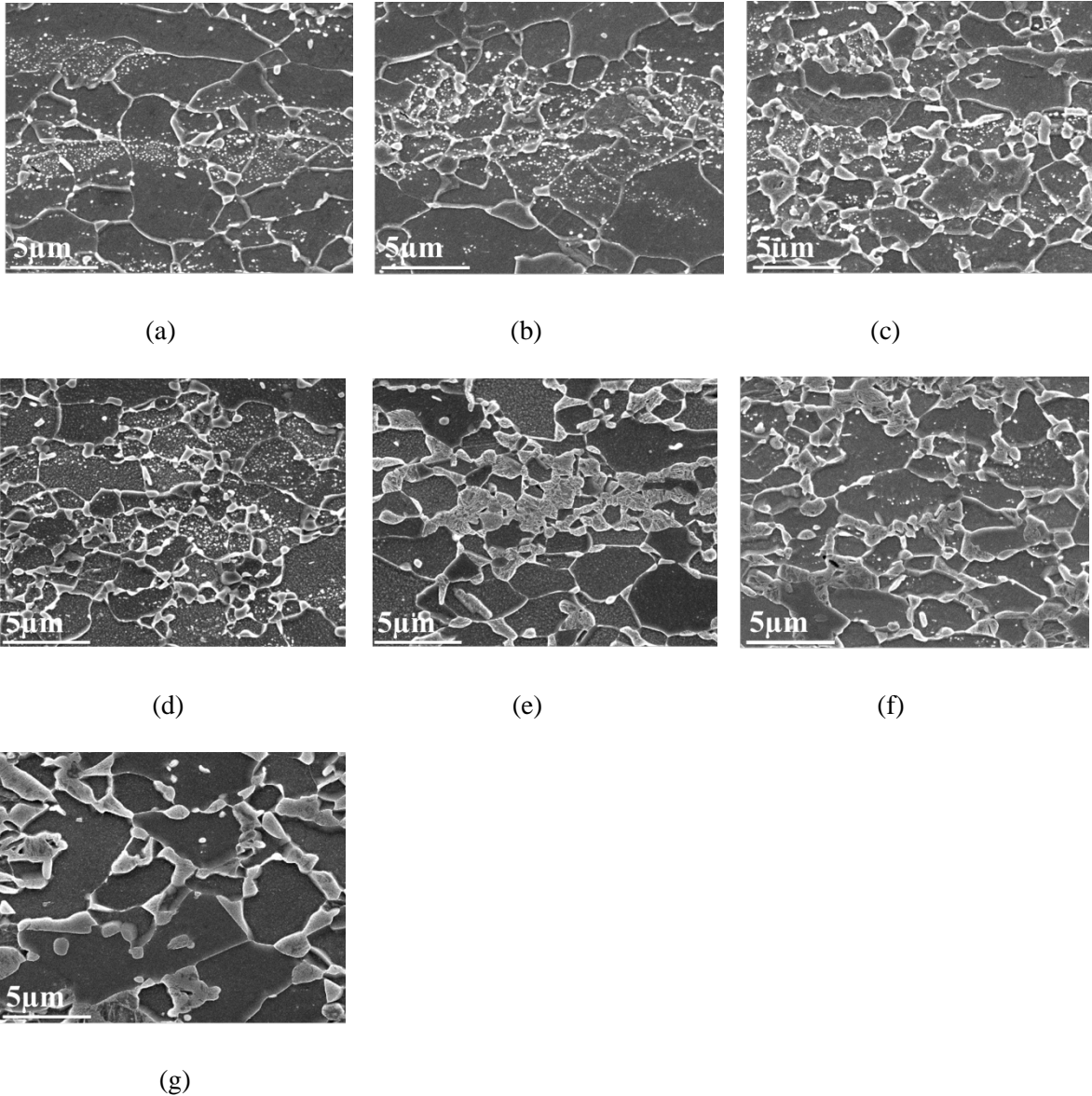


Figure 5.1.34. SEM microstructures of DPV (60%CR) (a) 700°C for 5minutes, (b) 720°C for 5 minutes, (c) 740°C for 5minutes, (d) 760°C for 1minute, (e) 760°C for 2minutes, (f) 780°C for 0s, and (g) 780°C for 1minute, water quenched.

Figure 5.1.34 shows the SEM microstructures of DPV (60%CR) at different IAT and intercritical holding time. Figures 5.1.34 (a)-(c) show the variations of microstructures of DPV after holding at 700°C, 720°C and 740°C for 5minutes and then water quenched. It is clear that there is dense cementite in the ferrite matrix, though the amount of cementite reduced a little at 740°C compared with that at 720°C and 700°C. It can also be seen that almost all the cold deformed ferrite has recrystallized and the matrix is

polygonal ferrite for all the 3 temperatures (700°C-740°C). When increasing the IAT to 760°C (Figure 5.1.34(d) and (e)), the cementite completely dissolved after 2 minutes holding, while for 1 minute holding, there is still dense cementite in some ferrite grains. For 780°C, most cementite dissolved but there is some remaining fine cementite in some ferrite grains (Figure 5.1.34 (f)) for 0s holding, and all the cementite completely dissolved after holding at 780°C for 1 minute, Figure 5.1.34 (g). From Figures 5.1.34 (a)-(g), it is also clear that increasing IAT and holding time can increase the amount of austenite formed during intercritical annealing.

The above study of the dissolution behavior of cementite is important for us to determine the intercritical annealing temperature to produce high strength dual phase steels. If the IAT is below cementite dissolution temperature, the carbon concentration in the intercritically formed austenite is not high enough due to the undissolved cementite, and so the hardenability or stability of the austenite is not sufficiently high to prevent the formation of ferrite or bainite during cooling from IAT, thus less amount of austenite was transformed to martensite, leading to lower strength of the dual phase steels after full processing. The IAT needs to be above the complete cementite dissolution temperature to make sure all the cementite dissolved during intercritical annealing and make the intercritically formed austenite as well as ferrite harder. The IAT 790°C or above for our continuous galvanizing lines processing (CGL) is a good choice in terms of the dissolution of cementite from the above results. Moreover, the hardenability or stability of intercritically formed austenite is also related to the amount of austenite, which will further be discussed in the next sections in detail.

5.1.7.3 Recrystallization behavior of cold rolled ferrite

It is assumed that the properties of ferrite matrix mainly contribute to the ductility of dual phase steels. In this section, the recrystallization behavior of cold rolled ferrite in the steel sheets with different alloying elements will be studied and discussed in detail. And our results indicate that the non-completed recrystallization of deformed ferrite in the final dual phase microstructures is harmful to the ductility,

while the recrystallized and polygonal ferrite in DPV is one of the factors that make DPVs possess best ductility (total elongations, hole expansion ratios) among the DPs with five different compositions.

Figure 5.1.35 shows the microstructures of DP_NbV at different states. Figure 5.1.35 (a) is the optical microstructure of cold rolled sample (LePera etched) and (b) is its SEM microstructure. We use LePera etchant to emphasize and trace the change of MA islands. As expected, both ferrite and martensite are elongated in the cold rolled state. Figure 5.1.35(c) is the optical microstructure of DP_NbV annealed at 680°C for 5 minutes and then water quenched and (d) is its SEM microstructure. From the SEM microstructure we hardly found any recrystallized ferrite. Comparing Figure 5.1.35 (a) and (c), we found that the originally homogeneously distributed MA islands disappeared, indicating the decomposition of MA during annealing at 680°C. With the decomposition of MA, the carbon was also redistributed and bands with high carbon content may form probably due to the segregation of manganese in banding form. The appearance of the banding structure can be detected from Figure 5.1.35 (c) showing one white band which may probably be the new formed MA band in the early stage. Spheroidization of cementite in pearlite area can also be seen from Figure 5.1.35 (d). These results are helpful for us to understand the dissolution of carbides and the redistribution of carbon content which is essentially very important to explain the formation of austenite during intercritical annealing and the formation of banding structure.

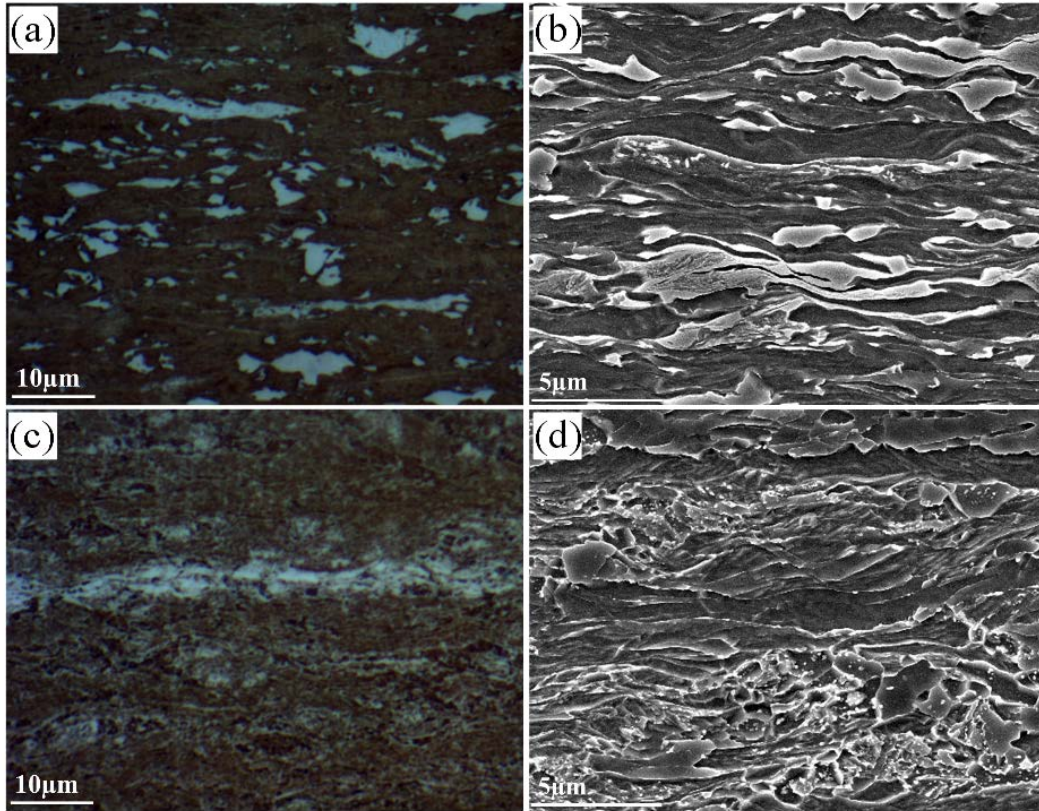


Figure 5.1.35 Microstructures of DP_NbV, (a) cold rolled, LePera etched, (b) cold rolled, SEM, (c) 680°C, for 5minutes, water quenched, LePera etched, and (d) 680°C for 5minutes, water quenched, SEM.

As discussed in the previous Section 5.1.3, the DP_V steels exhibit higher ductility than the other steels. One reason to explain this high ductility is that all the existed ferrite is the recrystallized polygonal ferrite which is much softer than the non-recrystallized ferrite. From the optical microstructures Figure 5.1.36 and SEM microstructures Figure 5.1.37, we can clearly see the different effects on the recrystallization behavior of ferrite of the different micro alloying elements (V, N, Nb or their combinations). For DP_V, almost all the ferrite is recrystallized polygonal ferrite. For DPVN and DPNb, both recrystallized and non-recrystallized ferrite (the amount of each needs to be determined) can be found. However, for DP_NbV and DP_NbVN little recrystallized ferrite can be found and almost all the ferrite remains at the cold-rolled elongated state. From these results of the 680°C annealed for 5 minutes and then water quenched samples, we see that the addition of Nb or VN can suppress the recrystallization

of ferrite more effectively than V, and the synergistic effect of Nb-V or Nb-V-N can completely suppress the recrystallization of ferrite at 680°C. However the real amount of recrystallized ferrite in the final structure depends on the intercritical annealing temperature (IAT) and the holding time at IAT, i.e., both thermodynamics and kinetics affect the recrystallization behavior of ferrite.

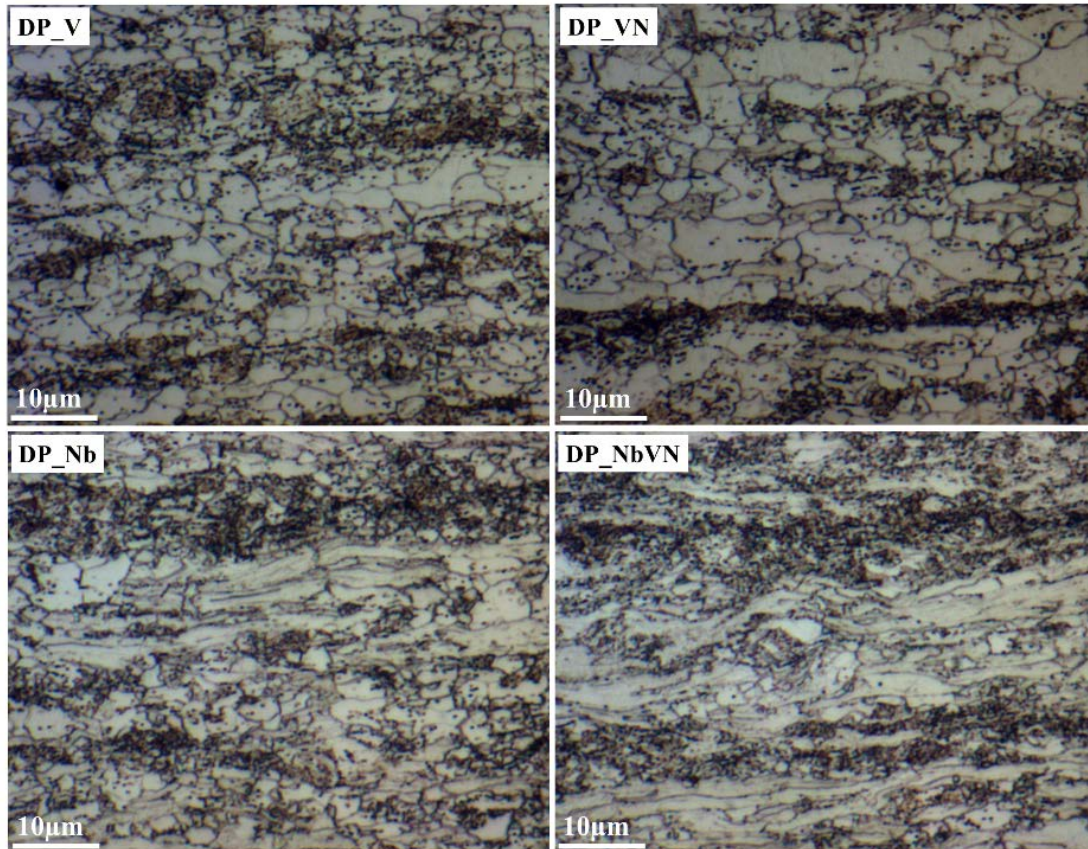


Figure 5.1.36 Optical microstructures of DP_V, DP_Nb, DP_VN, and DP_NbVN with processing at 680°C for 5 minutes, WQ

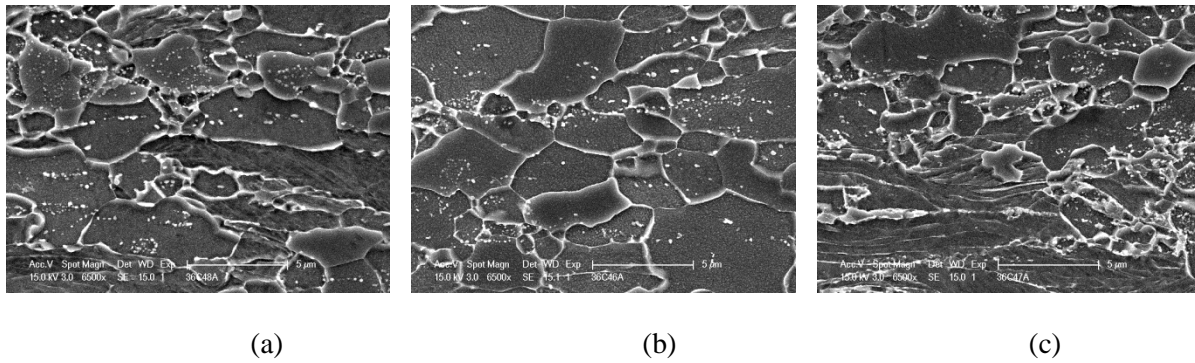


Figure 5.1.37. SEM microstructures of (a) DPVN, (b) DPV and (c) DPNb after holding at 680°C for 5 minutes and then water quenched.

The recrystallization behavior of cold rolled ferrite in DPV and DPVN was carefully studied and the results were shown in Table 5.1.12 and Figure 5.1.38. All these results clearly indicate that the addition of vanadium and nitrogen into the steel can much more effectively retard the recrystallization of cold rolled ferrite during intercritical annealing compared with DPV steels with very low nitrogen contents. This effect can be explained as that the solid solution nitrogen as well as the formation of fine VN precipitates or AlN precipitates in the ferrite in hot band steels, and after cold rolling new formed deformation induced precipitates in the cold rolled ferrite may all contribute to the strengthening of the cold rolled ferrite, and can effectively pin the dislocations thus retard the recovery and recrystallization of ferrite in DPVN. However, the verification of that which factor dominates this effect (solid solution N, VN or AlN) needs more work (e.g. HRTEM to check the precipitates and the nitrogen content in deformed ferrite).

Table 5.1.12. Volume fractions (%) of non-recrystallized ferrite at different intercritical annealing temperatures and holding times for DPV and DPVN

IAT/Time	1 minute		2 minutes		5 minutes	
	DPV	DPVN	DPV	DPVN	DPV	DPVN
700°C	50	56	3.5		0	
720°C	12	52	0.7	27	0	9.6
740°C	3	24	0	22	0	
760°C	0	14	0	16		

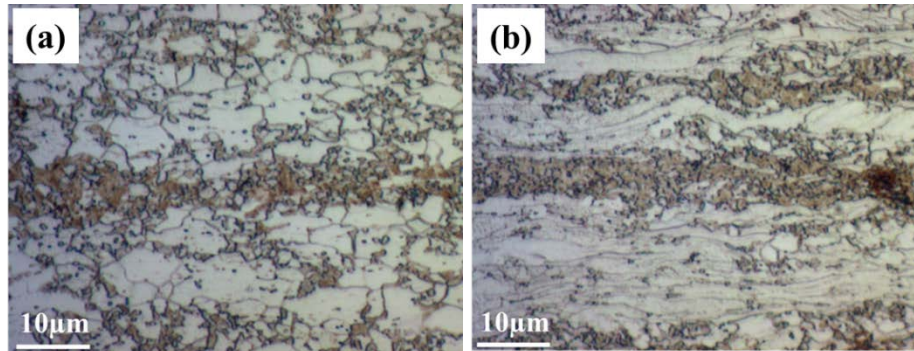


Figure 5.1.38. OM microstructures of (a) DPV, 780°C 0s WQ, and (b) DPVN, 780°C, 0s, WQ

We further studied the effects of V or VN on the recrystallization behavior of cold rolled ferrite with MTS heat treatment simulating full Gleeble processing. The SEM microstructures of DP_V and DP_VN with processing T2 or T3 (ACRT) (illustrated in Figure 5.1.27(b)) are shown in Figures 5.1.39-5.1.41. From these microstructures we can clearly see the difference between DP_V and DP_VN. There is no non-recrystallized “old” ferrite in DP_V, while a large amount of non-recrystallized “old” ferrite can be found in DP_VN with both processing T2 and T3 (ACRT). The similar amount of non-recrystallized ferrite in DP_VN with T2 and T3 (ACRT) can be found, indicating the 460°C temperature isn’t high enough for the ferrite to be recrystallized. The fully recrystallized polygonal ferrite in DP_V may probably account for the high ductility. As we can see from previous sections, there is still some non-recrystallized ferrite in DPVN with full CGL processings (e.g. GI A1, A5, A6 or supercool processing C1), which may be one reason for the lower ductility of DPVN compared with DPV. The holding time 1 minute at 780°C or 790°C for DPVN is clearly not long enough for deformed ferrite to completely recrystallize. These results indicate that in order to get proper ductility for DPVN or DPs with Nb alloying, it is necessary to make all the cold rolled ferrite recrystallized.

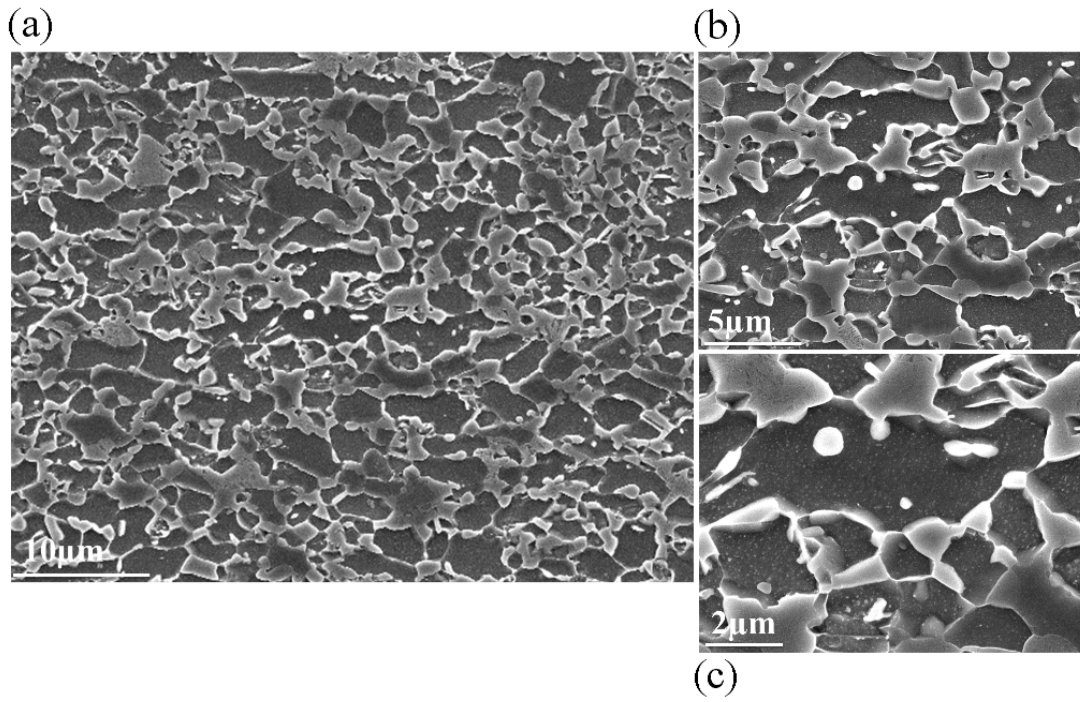


Figure 5.1.39 SEM microstructures of DP_V with partial processing T2 (460°C, 30s), ACRT

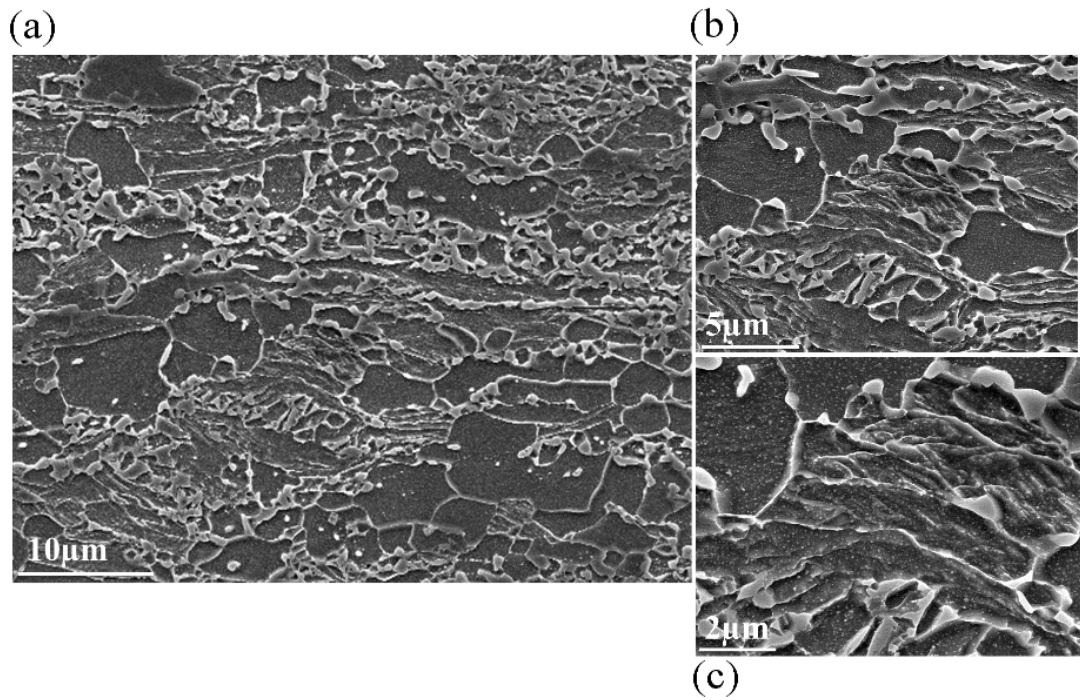


Figure 5.1.40 SEM microstructures of DP_VN with partial processing T3 (460°C, 8min), ACRT

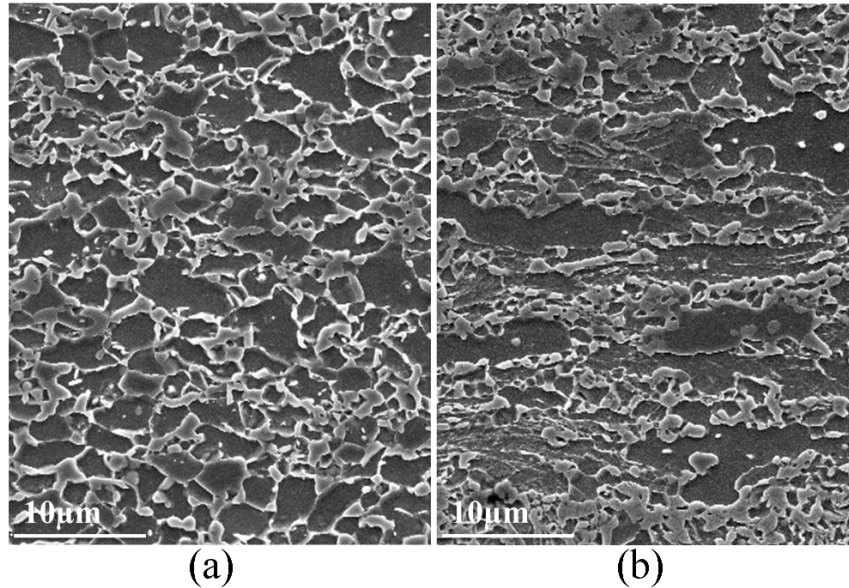


Figure 5.1.41 SEM microstructures (a) DP_V with partial processing T3 (460°C, 8min), ACRT (b) DP_VN, with partial processing T2 (460°C, 30s), ACRT

5.2 EFFECTS OF INTERCRITICAL ANNEALING TEMPERATURE AND COOLING RATE ON THE PROPERTIES OF DP STEELS

In order to get high enough strength ($> 980\text{MPa}$) of dual phase steels, higher intercritical annealing temperatures were applied to form more austenite during intercritical annealing stage, and thus hoping to result in more martensite in the final microstructure, as the tensile strength of dual phase steels is mainly determined by the amount of martensite. We designed two groups for DPs with vanadium addition (DPV) and vanadium nitrogen additions (DPVN). One group used IAT 790°C and the other group applied IAT 820°C to compare the influence of IAT on the final properties of dual phase steels with standard galvanizing processing.

Tables 5.2.1 and 5.2.2 listed the differences in tensile strength (ΔUTS) and yield strength (ΔYS) between DPs with IAT 790°C and the corresponding DPs with IAT 820°C . These data were also plotted in Figure 5.2.1. Instead of increase in UTS, the tensile strength decreased for DPV for about 40MPa

(expect one with highest cooling rates), and the decrease in UTS is even higher in DPVN (between 58MPa to 102MPa). The decrease in UTS is closely related to the final microstructure. As can be observed in Figure 5.2.3, for DPV with IAT 820°C, the amount of martensite didn't increase, while more bainite formed in the final microstructure (35% bainite in DPV 820°C-30°C/s-460°C-10°C/s-RT, and 31% bainite in DPV 820°C-30°C/s-460°C-30°C/s-RT).

Table 5.2.1. Heating rate to IAT (T) is 5°C/s, the numbers are the tensile strength (MPa).

Gleeble Heat Treatments	Steels	T=790°C	T=820°C	ΔUTS
T(1min), 30°C/s, 460°C(30s), 10°C/s, RT	DPV, 60%CR	952	908	-44
T(1min), 60°C/s, 460°C(30s), 10°C/s, RT	DPV, 60%CR	939	902	-37
T(1min), 30°C/s, 460°C(30s), 30°C/s, RT	DPV, 60%CR	955	909	-46
T(1min), 60°C/s, 460°C(30s), 30°C/s, RT	DPV, 60%CR	940	943	+3
T(1min), 15°C/s, 460°C(30s), 10°C/s, RT	DPV, 72%CR	981	925	-56
T(1min), 30°C/s, 460°C(30s), 10°C/s, RT	DPVN, 60%CR	1008	924	-84
T(1min), 60°C/s, 460°C(30s), 10°C/s, RT	DPVN, 60%CR	989	929	-60
T(1min), 30°C/s, 460°C(30s), 30°C/s, RT	DPVN, 60%CR	1023	921	-102
T(1min), 60°C/s, 460°C(30s), 30°C/s, RT	DPVN, 60%CR	993	935	-58

Table 5.2.2. Heating rate to IAT (T) is 5°C/s, the numbers are the yield strength (MPa).

Gleeble Heat Treatments	Steels	T=790°C	T=820°C	ΔYS
T(1min), 30°C/s, 460°C(30s), 10°C/s, RT	DPV, 60%CR	483	513	+30
T(1min), 60°C/s, 460°C(30s), 10°C/s, RT	DPV, 60%CR	477	442	-35
T(1min), 30°C/s, 460°C(30s), 30°C/s, RT	DPV, 60%CR	484	512	+28
T(1min), 60°C/s, 460°C(30s), 30°C/s, RT	DPV, 60%CR	487	501	+14
T(1min), 15°C/s, 460°C(30s), 10°C/s, RT	DPV, 72%CR	501	495	-6
T(1min), 30°C/s, 460°C(30s), 10°C/s, RT	DPVN, 60%CR	548	479	-69
T(1min), 60°C/s, 460°C(30s), 10°C/s, RT	DPVN, 60%CR	566	530	-36
T(1min), 30°C/s, 460°C(30s), 30°C/s, RT	DPVN, 60%CR	597	496	-101
T(1min), 60°C/s, 460°C(30s), 30°C/s, RT	DPVN, 60%CR	577	533	-44

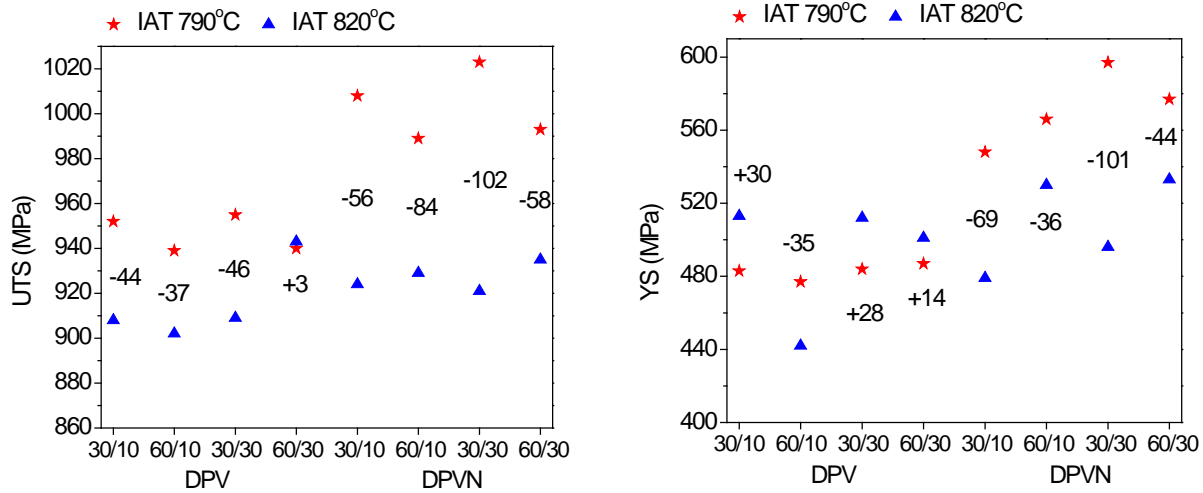


Figure 5.2.1. Tensile strength and yield strength of DPV and DPVN with IAT 790°C and 820°C, as listed in Tables 5.2.1 and 5.2.2. The first number in the horizontal axis is the cooling rate (°C/s) from IAT to zinc pot temperature, and the second is the cooling rate from zinc pot temperature to room temperature.

Figure 5.2.2 shows the LePera etched microstructures of DPV water quenched after holding at IAT 800°C for 1 minute (a), 2 minutes (b), 5 minutes (c) and IAT 820°C for 2 minutes (d). The results of the volume fractions of martensite are listed in Table 5.2.3. It was found that increasing the IAT to 800°C, the volume fraction of martensite will reach to around 40 percent for 1 min holding time, and with increasing the holding time, more austenite will be formed, but not too much, indicating that the equilibrium state will be reached faster at higher temperatures. For 820°C, the amount of austenite will be around 45% after 2 minutes holding time. At higher IAT, equilibrium phase balance will be reached faster due to higher carbon diffusivity. Using mass balance calculation, the austenite carbon content (C_A) can be estimated from the equation:

$$C_A = [C - C_F(1 - V_A)] / V_A \quad (5.2.1)$$

where C and C_F are the average carbon content of the steel and ferrite phase respectively. C_F is assumed to be 0.015 wt%, which is the supersaturated limit of the carbon concentration in ferrite phase from phase diagram. Clearly the carbon content of austenite decreased with increasing the amount of austenite. Thus the hardness and stability of austenite formed during intercritical annealing at higher IAT decreased and

the possibility to transform to bainite increased. Figure 5.2.4 schematically shows that reduced carbon content increased the bainite transformation temperature and promoted the austenite to transform to bainite, while other alloying elements (e.g. Mn, Cr or Mo) can stabilize austenite and delay the transformation of austenite to bainite. Figure 5.2.5 shows the results from JMatPro. As we see, when increasing annealing temperature from 780°C to 820°C for DPV, both Bs (above zinc pot temperature 460°C) and Ms temperatures increase, promoting the transformation of bainite from austenite. The SEM microstructures in Figure 5.2.3 confirm our explanations for the lower strength of DPs with higher IAT.

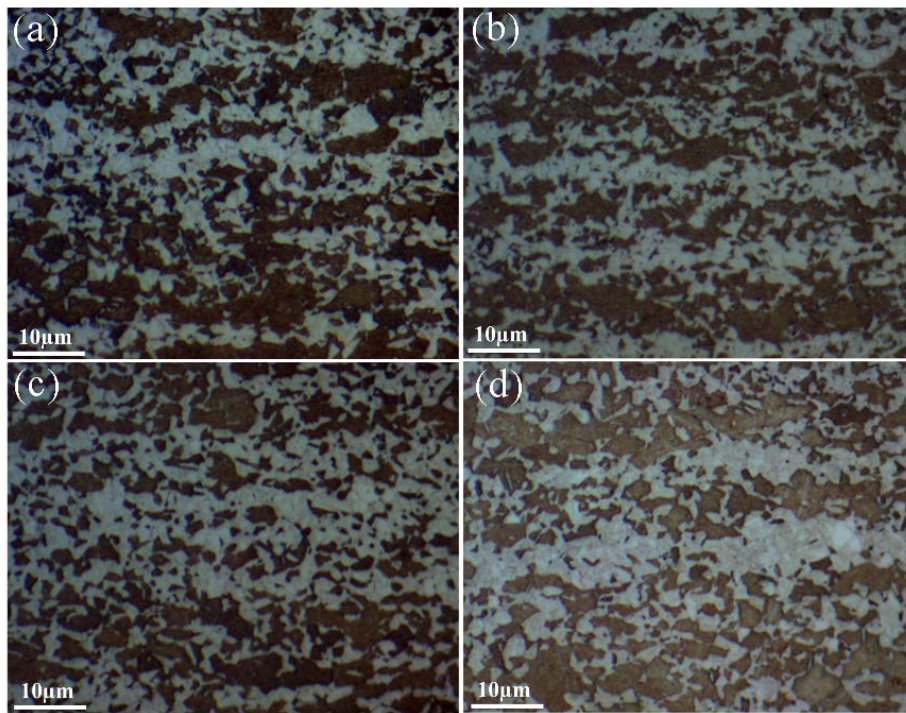


Figure 5.2.2. Optical microstructures (LePera etched) of DP_V, (a) 800°C, 1min, (b) 800°C, 2min, (c) 800°C, 5min, (d) 820°C, 2min (water quenched). MA white, ferrite brown

Table 5.2.3 Volume fraction of MA, a, 800°C, 1min; b, 800°C, 2min; c, 800°C, 5min; and d, 820°C, 2min (water quenched)

DP_V	Volume fraction of MA (%)			
a	b	c	d	
37±4	40±3	44±4	45±4	

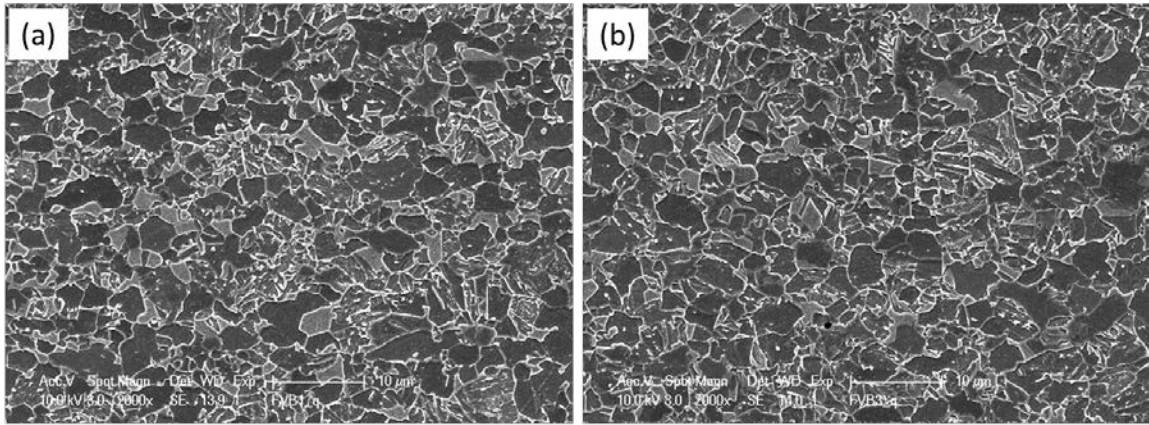


Figure 5.2.3. (a) DPV, 820°C/1min, 30°C/s, 460°C/30s, 10°C/s to RT, 35% bainite, 12% MA, (b) DPV, 820°C/1min, 30°C/s, 460°C/30s, 30°C/s to RT, 31% bainite, 15% MA.

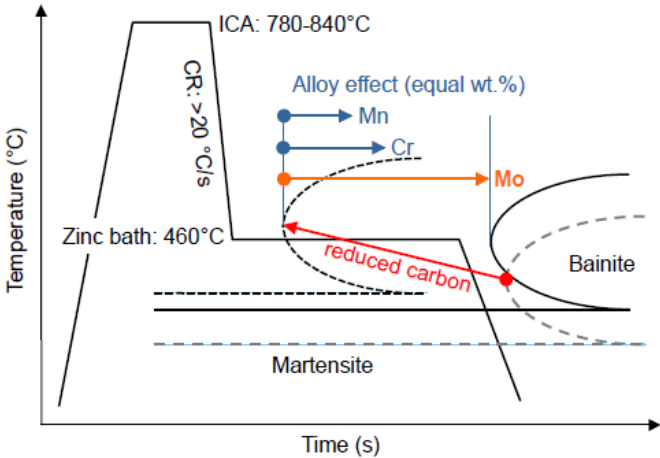


Figure 5.2.4. Illustration of the effects of different alloying elements on the transformation of austenite to bainite for galvanizing processing^[80].

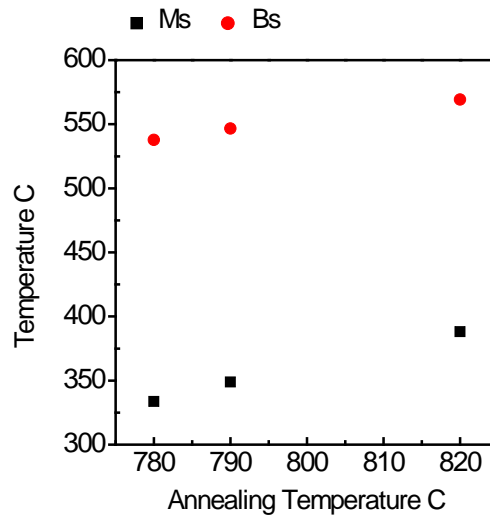


Figure 5.2.5. Predicted Bs and Ms temperatures using JMatPro of DPV at different intercritical annealing temperatures

As explained above, the lower strength of DPs processed at higher IAT is mainly due to the formation of bainite from austenite, which again results in insufficient amount of martensite in the final microstructure. When we further compare DPV and DPVN, it was found that the decrease in tensile strength and yield strength is much higher in DPVN than that in DPV, while the yield strength of DPV even increased or decreased not much for higher IAT. Besides the bainite transformation, the ferrite recrystallization or ferrite softening, Figure 5.2.6, the dissolving of VN and the formation of AlN in DPVN at higher IAT further decreased the tensile strength and yield strength. As for yield strength, more bainitic ferrite in DPV may be one reason for the increase in yield strength in some of the DPs with higher IAT (820°C).

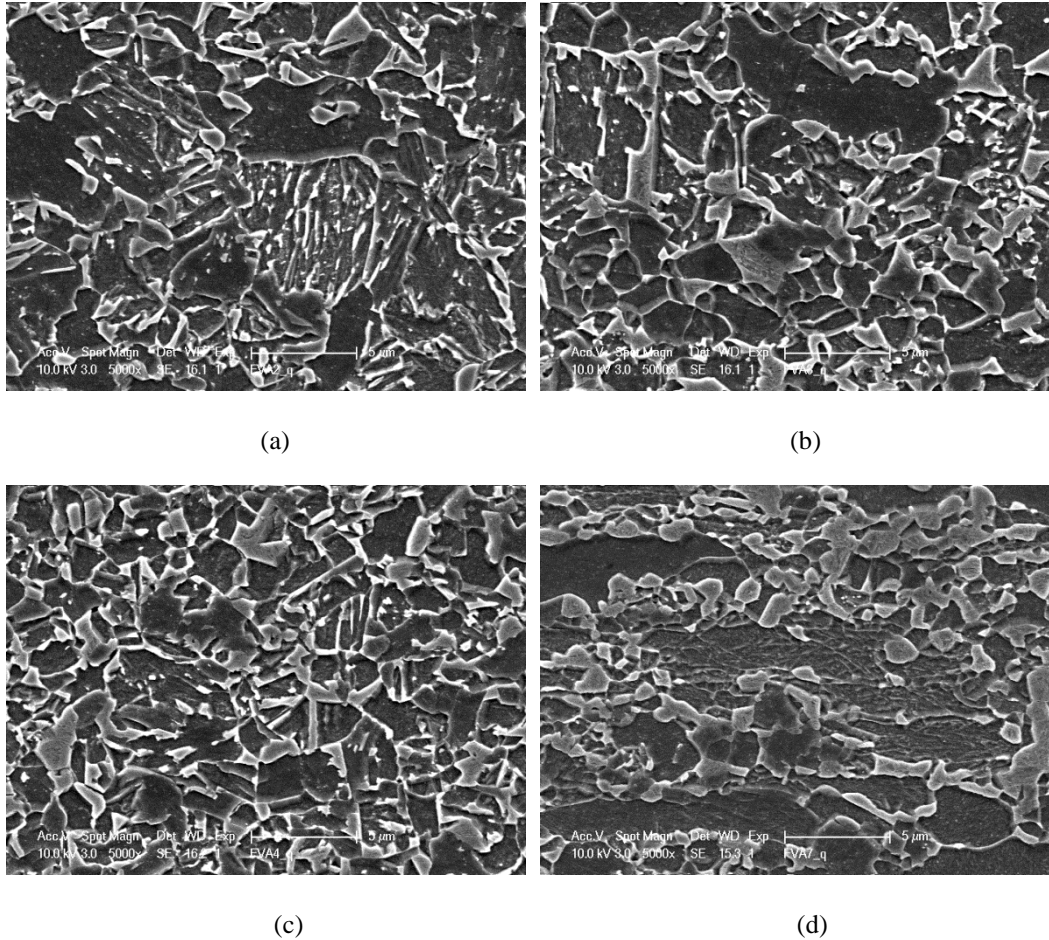


Figure 5.2.6. SEM microstructures of (a) DPVN, 820°C/(60°C/s)460°C/(10°C/s)RT, (b) DPVN, 820°C/(30°C/s)460°C/(30°C/s)RT, (c) DPVN, 820°C/(60°C/s)460°C/(30°C/s)RT (d) DPVN, 790°C/(30°C/s)460°C/(30°C/s)RT. For higher IAT 820°C, bainite microstructures can be clearly observed and all the ferrite are recrystallized, while for lower IAT 790°C, little bainite was found and some non-recrystallized ferrite still existed.

The role of cooling rate from IAT (820°C) to zinc pot temperature (460°C) can be observed when comparing the microstructures in Figure 5.2.7 (a) and 5.2.7 (b). At slower cooling rate (30°C/s), more ferrite formed, which indicates that during slower cooling, the ferrite transformation region was entered leading to the formation of ferrite. The amount of austenite was reduced when the steel entered the bainite transformation region or zinc pot temperature holding stage, and so the remained austenite possesses higher carbon concentration and the stability was raised, and so less amount of austenite was transformed to bainite during holding at 460°C. When using faster cooling rate 60°C/s from IAT to zinc pot

temperature, the ferrite transformation region was avoided and most of the intercritically formed austenite was remained when entering zinc pot holding stage, and so the higher amount of less stable austenite with lower carbon content was transformed to bainite during zinc pot temperature holding. The remaining austenite at the end of zinc pot holding stage was further transformed to MA (martensite plus retained austenite) during cooling to room temperature. This explains why we see much more amount of bainite when increasing cooling rate from IAT to zinc pot temperature, Figures 5.2.7 (a) and 5.2.7 (b).

The main role of cooling from IAT to zinc pot temperature (ZPT) is to avoid the pearlite transformation region and adjust the transformation of ferrite (avoid or enter the ferrite transformation region depending on the stability of the austenite before entering the zinc pot temperature holding stage), while the main role of cooling from ZPT to RT is to promote the transformation of the remaining austenite at the end of the zinc pot holding stage to martensite and avoiding the bainitic (or possibly ferrite, pearlite) transformation during cooling to RT. From Figure 5.2.3, it can be seen that increasing the cooling rate from ZPT to RT can reduce the amount of bainite and increase the amount of MA in the final microstructure, which supported this argument.

Adjusting the bainite start curve (Bs) (up, down, left and right) can adjust the transformation of austenite to bainite during zinc pot holding, which determined the total amount of austenite at the end of the zinc pot holding stage. One key to keep enough amount of martensite in the final microstructure in order to get high strength is to keep enough amount of austenite at the end of the zinc pot holding stage, which determined the total amount of MA in the final microstructure, since most of these austenite can be transformed to MA during fast cooling ($10^{\circ}\text{C}/\text{s}$ - $30^{\circ}\text{C}/\text{s}$, which can be realized in the industrial production) to RT.

The adjustment of the bainite start curve is directly related to the stability of the austenite or the carbon content in the austenite at ZPT, which is related to several factors including IAT, intercritical annealing time, cooling rate from IAT to ZPT, microalloying elements (e.g. Mo, Cr) and also the extent of the transformation of austenite to bainite during zinc pot holding, all of these factors have been discussed or will be further discussed in this thesis.

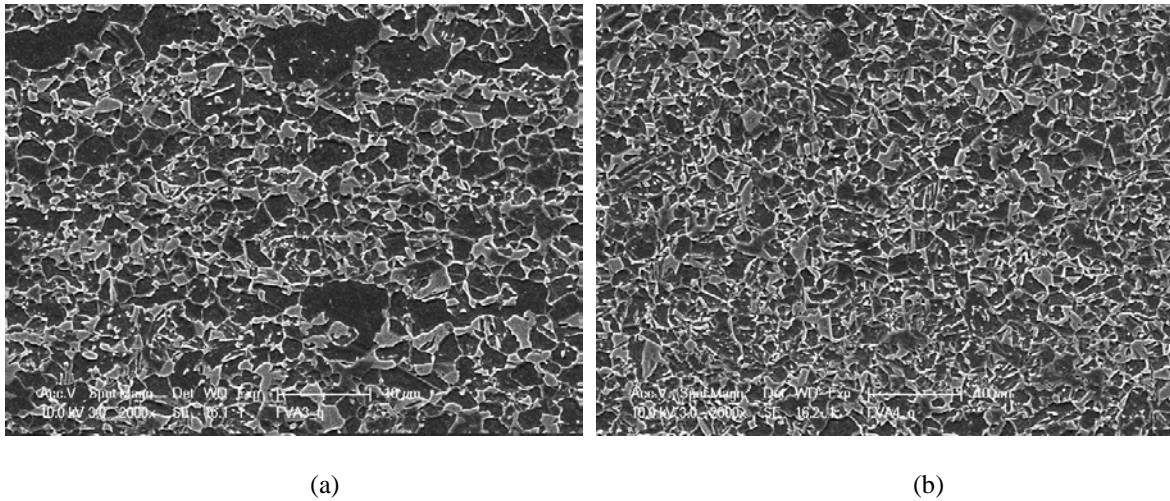


Figure 5.2.7. SEM microstructures of (a) DPVN, 820°C-30°C/s-460°C-30°C/s-RT, (b) DPVN, 820°C-60°C/s-460°C-30°C/s-RT

5.3 EFFECTS OF V OR VN ON THE SOFTENING RESISTANCE OF DUAL PHASE STEELS WITH EXTENDING HOLDING AT ZINC POT TEMPERATURE

This section discussed the effects of V or VN additions on the softening resistance during the processing of DP980 steels. Three steels i.e. DPV with vanadium addition, DPVN with vanadium and nitrogen additions and DPU commercial DP steels without V addition, were used to compare the effects of V or VN additions. Table 5.3.1 listed the chemical compositions of these steels (see Table 5.1.1 for the designed compositions of these steels). Figures 5.1.1 and 5.1.2 (in Section 5.1) illustrate the hot rolling, cold rolling and extended galvanizing treatments. The holding time at zinc pot temperature (460°C) was extended from standard 30s (A1) to 60s (A5) and 120s (A6) to simulate the actual DP steel producing conditions across several production CG lines where the time at 460°C can vary. The total elongations, uniform elongations and work hardening ratios between 4%-6% engineering strain are listed in Table 5.3.3 and were partially discussed in Section 5.1. Table 5.3.2 listed the tensile strength and yield strength of DPV, DPVN and DPU steels. Figure 5.3.1 and Figure 5.3.2 plotted the tensile strength and yield

strength versus holding time at zinc pot temperature. From these ultimate tensile strength and yield strength, we see that without vanadium addition, the strength of commercial DPs dropped (UTS from 954MPa to 931 MPa, and YS from 636MPa to 601 MPa), while with vanadium addition, the DPV steels do not lose strength (UTS from 942MPa to 983MPa, YS from 557MPa to 573MPa), and the strength of DPVN steels is also stable (UTS 1048-1050 MPa and YS 656-662MPa). This effective softening resistance from V or VN additions is absolutely very attractive in the industrial applications during producing DP steels, since the speed of bands during continuous line producing of DP steels can vary according to the actual size or amount of the steels used on the transferring bands, which means the holding time at 460°C can also vary from standard 30s to even 120s.

Table 5.3.1. Analyzed chemical compositions (wt.%) of DPV and DPVN. DPU is the commercial dual phase steels supplied by USS.

Steels	C	Mn	Si	P	Al	V	Cr	Mo	N	S	Ti
DPV	0.106	1.699	0.404	0.01	0.0334	0.061	0.502	0.297	0.0069	0.0024	0.0014
DPVN	0.101	1.727	0.414	0.01	0.0283	0.059	0.501	0.303	0.0135	0.0036	0.0014
DPU	0.11	2.4	-	-	0.045	-	0.25	0.35	0.005	-	-

Table 5.3.2. Tensile strength (UTS) and yield strength (YS) of dual phase steels with V or VN addition and commercial DPs without micro alloying elements. Each number is the average of two tests.

Heat treatment	DPV			DPVN			DPU		
	UTS (MPa)	YS (MPa)	n	UTS (MPa)	YS (MPa)	n	UTS (MPa)	YS (MPa)	n
A1 (30s)	942	557	0.16	1050	658	0.13	954	636	0.13
A5 (60s)	979	570	0.17	1049	656	0.13	952	624	0.13
A6 (120s)	983	573	0.17	1048	662	0.13	931	601	0.13

Table 5.3.3. Uniform elongation (UE, converted to 2 inch gauge length), total elongation (TE, converted to 2 inch gauge length), and work hardening ratios (between 4% and 6% engineering strain) of dual phase steels with V or VN addition and commercial DPs without micro alloying elements. Each number is the average of two tests.

Heat treatment	DPV			DPVN			DPU		
	UE (%)	TE (%)	n	UE (%)	TE (%)	n	UE (%)	TE (%)	n
A1 (30s)	8.6	13.9	0.16	6.7	11.3	0.13	5	9.8	0.13
A5 (60s)	8.6	13.1	0.17	6	9.7	0.13	5	9.7	0.13
A6 (120s)	7.7	12.6	0.17	5.3	9.1	0.13	5.7	11.5	0.13

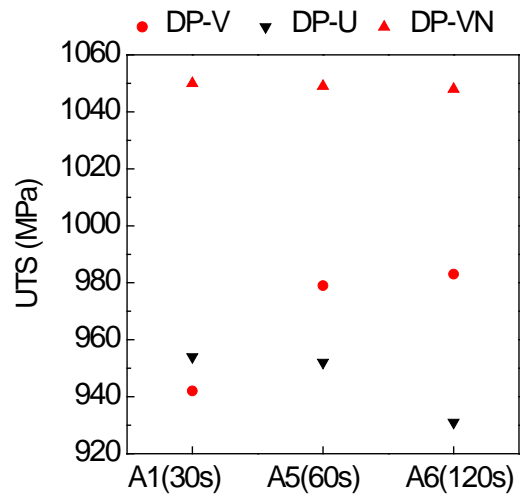


Figure 5.3.1. Tensile strength (UTS) of dual phase steels with V or VN addition and commercial DPs without micro alloying elements.

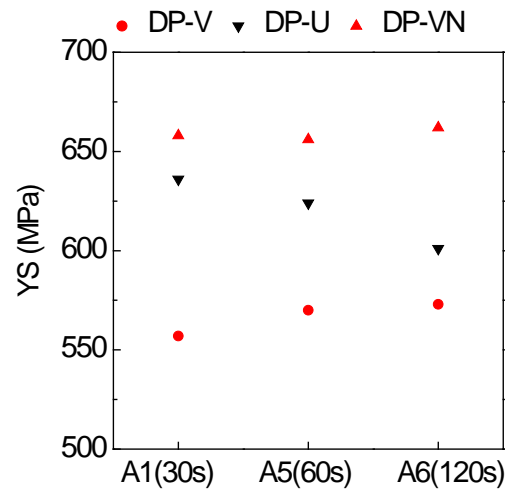


Figure 5.3.2. Yield strength (YS) of dual phase steels with V or VN addition and commercial DPs without micro alloying elements.

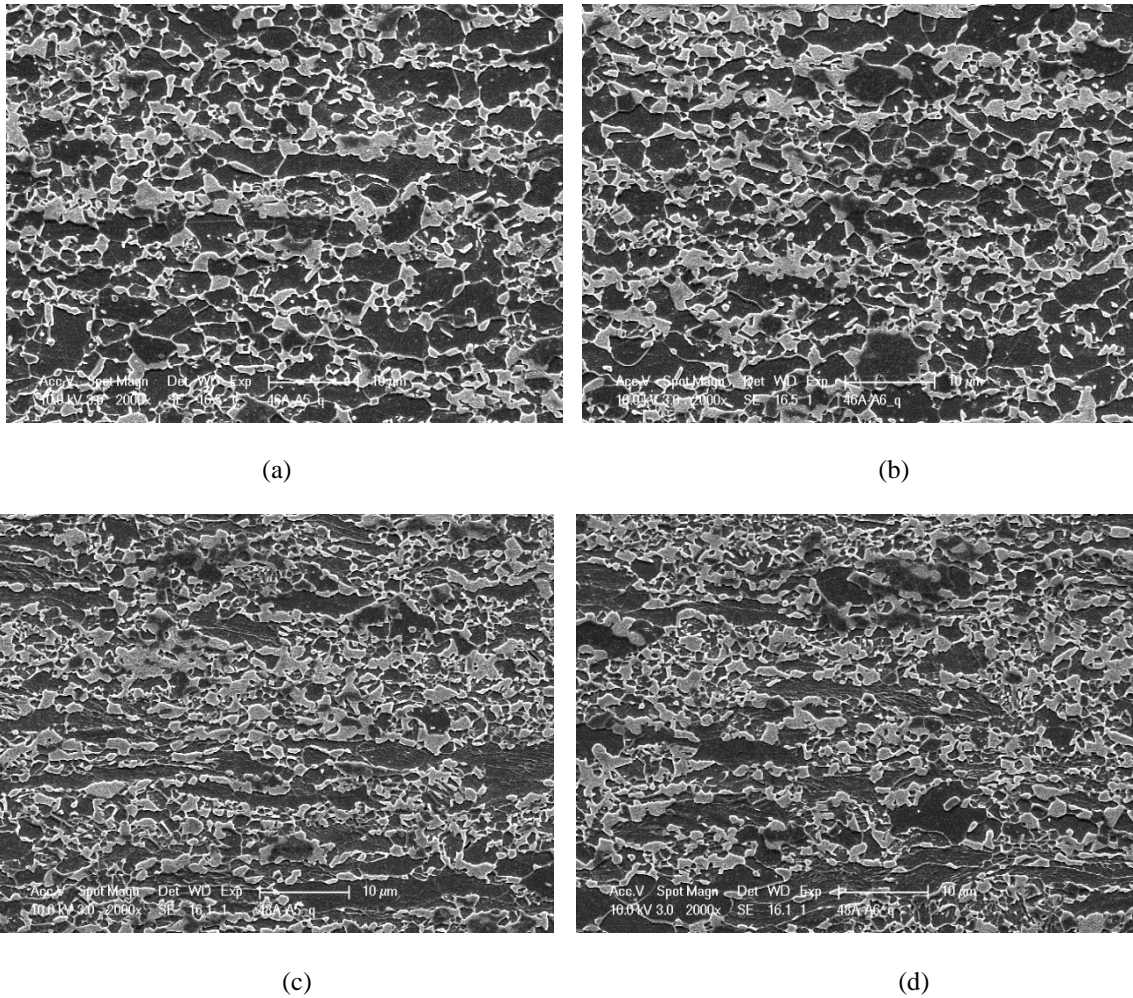


Figure 5.3.3. SEM micrographs of (a) DPV, A5 (460°C, 60s), (b) DPV, A6 (460C, 120°C), (c) DPVN, A5 (460°C, 60s), and (d) DPVN, A6 (460C, 120°C)

Figure 5.3.3 shows SEM microstructures of DPV and DPVN with A5 and A6 processing, corresponding to holding time at 460°C 60s and 120s respectively (the SEM microstructures of DPV and DPVN with A1 processing were shown in Section 5.1). Tables 5.3.4 and 5.3.5 summarized the volume fractions of MA, bainite and non-recrystallized ferrite in these DP steels. As can be seen, more martensite was found in DPVN compared with DPV in all the 3 processing, resulting higher strength in DPVN, as discussed in the previous section. With longer holding time more bainite formed and thus reduced the amount of martensite in the final microstructure, which is usually found in the producing of DP steels with extended time at zinc pot temperature, resulting softening of the DP steels. The amount of non-

recrystallized ferrite in DPVN does not decrease with longer holding time at 460°C, indicating 460°C is absolutely below the recrystallization temperature for the deformed ferrite in DPVN.

Table 5.3.4. Volume fractions (%) of MA and bainite in DPV with different holding time at zinc pot temperature

DPV	MA	Bainite
A1	23	None
A5	19.5	7.5
A6	20	8

Table 5.3.5. Volume fractions (%) of MA and bainite in DPVN with different holding time at zinc pot temperature

DPVN	MA	Bainite	Non-recrystallized Ferrite
A1	39	None	12
A5	29	8	17
A6	31	12.5	16

Our results in the present study indicate that the precipitation of VC_x or V(CN)_x can effectively compensate the softening partially due to bainite transformation and keep both of the tensile strength and yield strength as strong as or even stronger during tensile testing with the holding time at 460°C up to 120s. The evidence of the dense precipitations of VC_x or V(CN)_x will be presented and discussed below using HRTEM technique.

The high resolution TEM was used to study the mechanism of softening resistance from V or VN additions. For dual phase steels, it is assumed that the dislocations formed in ferrite grains near ferrite martensite phase boundaries during the formation of martensite from austenite contribute to the typical continuous yielding phenomenon of dual phase steels and also the interactions among dislocations and between dislocations and phase boundaries or grain boundaries can increase the strength of the DP steels. Moreover the residual stress due to the expansion of the volume during the formation of martensite from austenite can also strengthen the DP steels. Without vanadium addition, the softening phenomenon can frequently occur when extending the holding time at zinc pot temperature using lower transferring band speeds for real industrial producing. Some of the dislocations or residual stress was relieved during extending holding at 460°C, which results in the softening of the DP steels. In order to prevent the

softening of DP steels, one mechanism is to use finer precipitates to pin the dislocations or the elastically deformed crystals, so that when holding longer at 460°C, we still have dense preexisted dislocations and residual stress and retard the softening. HRTEM results of the vanadium containing precipitates, Figures 5.3.5 to 5.3.9 supported this idea.

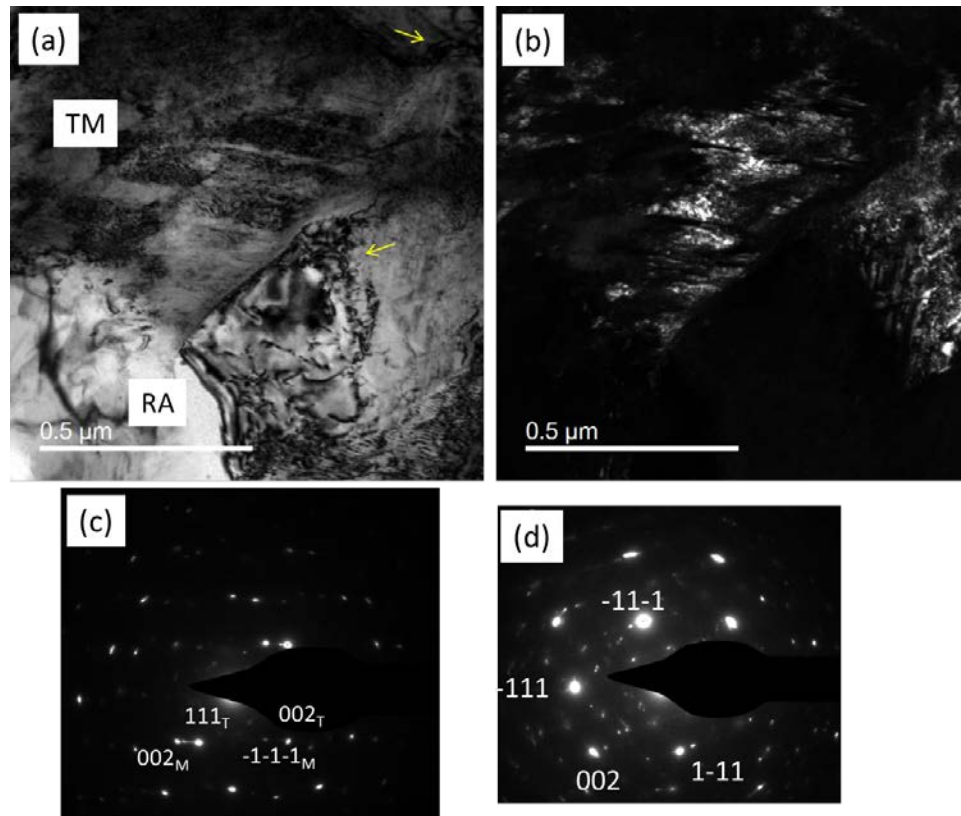


Figure 5.3.4. Bright field image (a) and Dark field image (b) of twinned martensite, SADP of twinned martensite TM (c), and retained austenite (RA) (d) in DPV, A5

Figure 5.3.4 shows bright field (BF) (a) and dark field (DF) images of martensite and retained austenite (MA). The selected area diffraction patterns of twinned martensite and retained austenite are shown in Figures 5.3.4(c) and (d) respectively. The yellow arrows in Figure 5.3.4 (a) indicate the dislocations near ferrite and martensite interphase boundaries, as expected from the phase transformation of austenite to martensite.

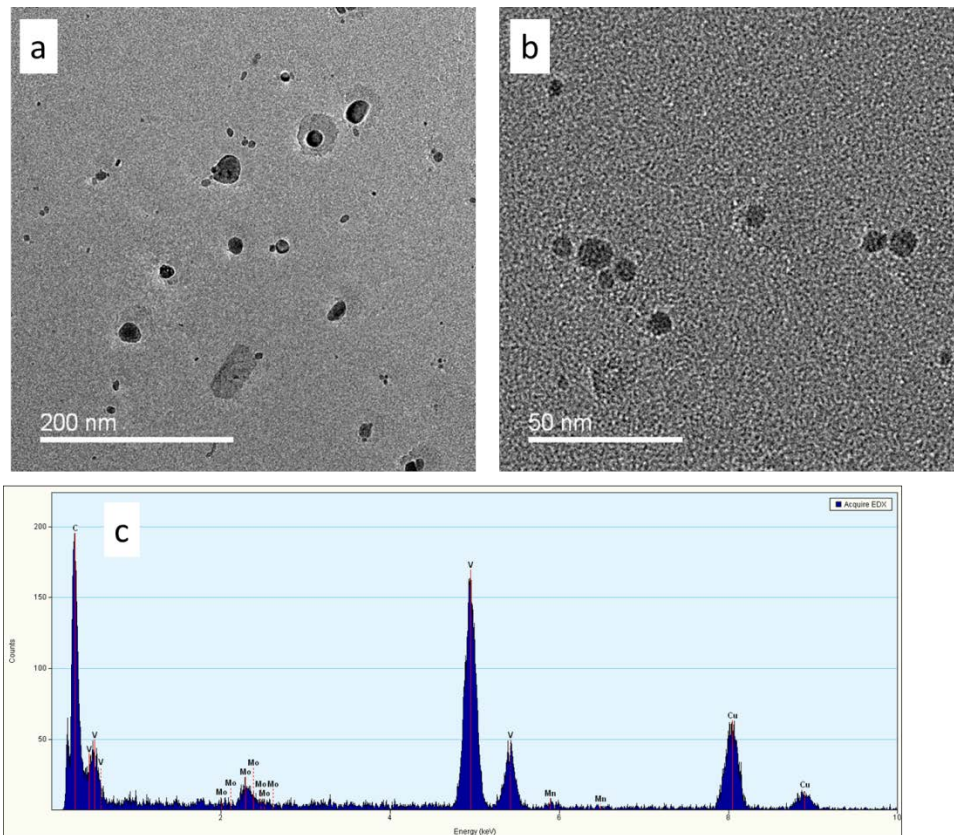


Figure 5.3.5. HRTEM images of VC_x precipitates in DPV, A5 (460°C/60s)

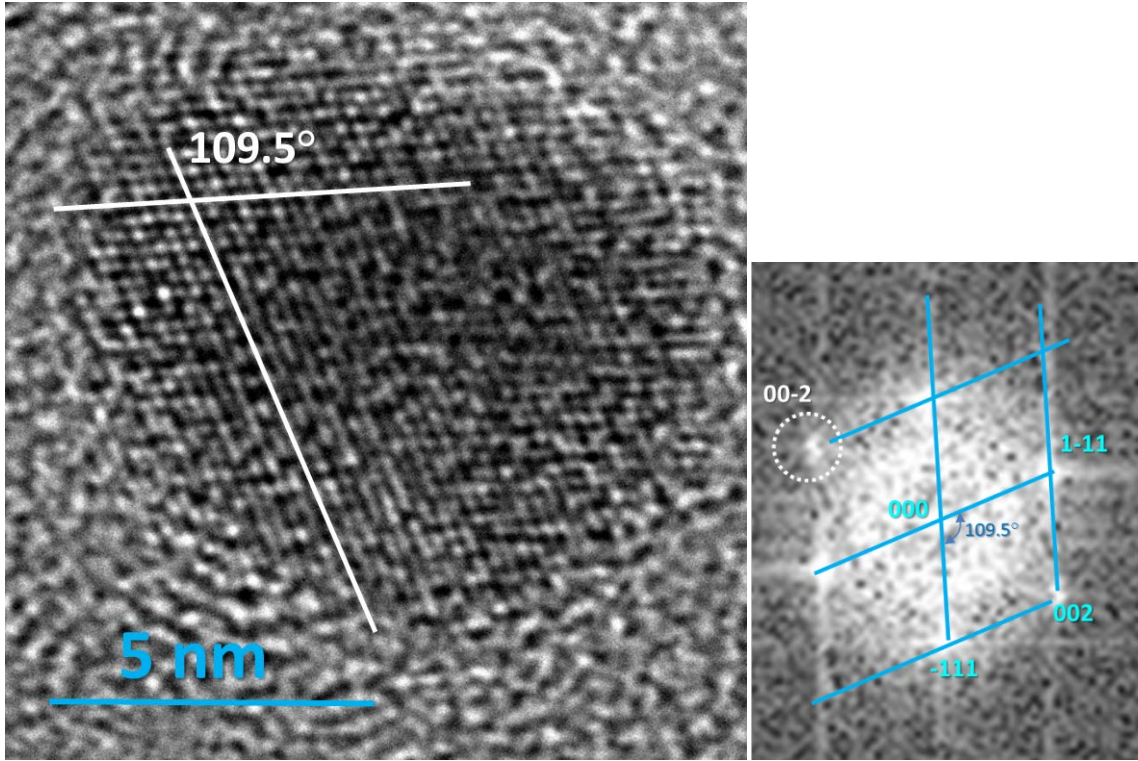


Figure 5.3.6. HRTEM and FFT of a larger VC in extracted replica. Note the quality of the lattice image of the particle edge is much better than that in the center, in DPV, A5.

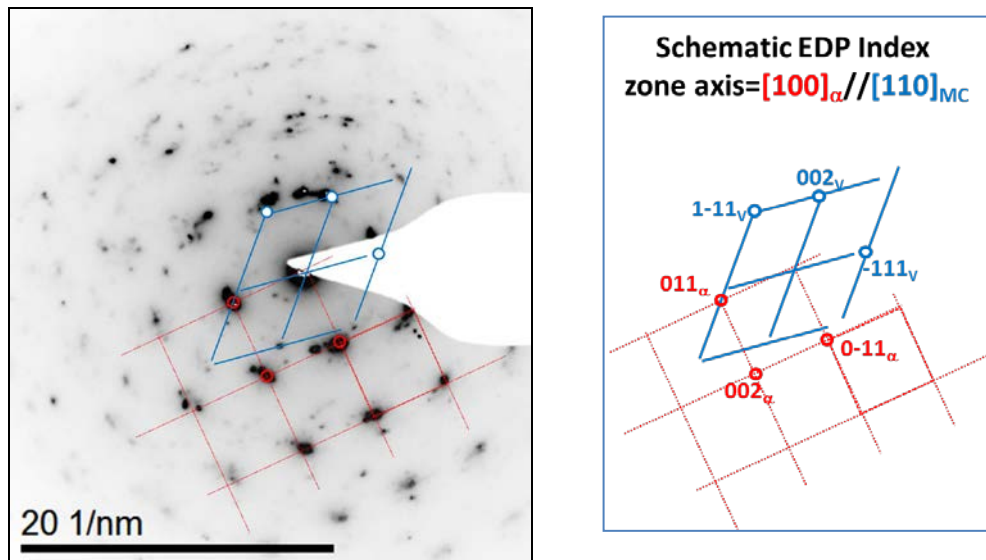


Figure 5.3.7. Typical and conventional electron diffraction pattern (EDP) from thin foil specimen, showing VC forms in α ferrite with Baker-Nutting orientation relationship in DPV, A5.

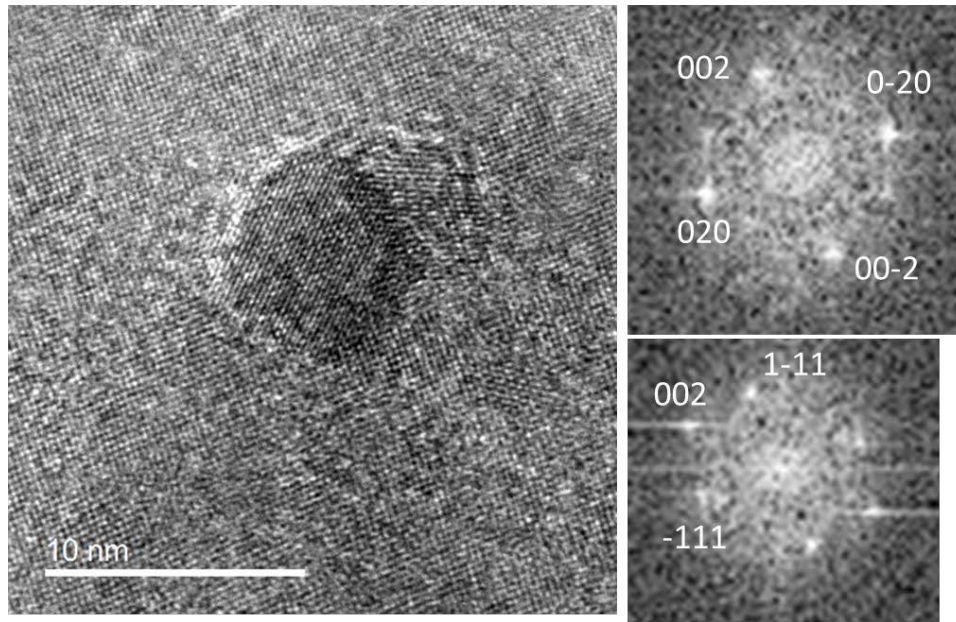


Figure 5.3.8. HRTEM images of VCx particle embedded in ferrite matrix in the foil of DPV, A5, the FFT patterns of VCx and ferrite confirmed the relationship between particle and ferrite matrix, i.e. Baker-Nutting orientation relationship.

The VCx precipitates were found in DPV, A5 replica, Figure 5.3.5. Figure 5.3.5 (c) shows EDX spectrum from one of the particles in Figure 5.3.5(b), and the vanadium peaks can be clearly seen which confirmed the vanadium contained precipitates. The size of the VCx precipitates is around 10nm. The Mo and Si (detected from other particles) peaks from the V particles indicate that the particles are probably alloyed with Mo or Si elements and to confirm the exact composition of the precipitates more work is needed.

In the present study, the VCx precipitates were found to have FCC crystal structure. Figure 5.3.6 shows one VCx particle with about 9.5 nm diameter. The HRTEM image reveals much better lattice image around the edge of the particle, while the center area has reduced lattice image quality, probably due to the internal defects or thickness. The overall image matches a typical VCx with face-center cubic crystal structure along $\langle 110 \rangle$ zone axis, as confirmed by the corresponding Fast Fourier Transformation (FFT).

The orientation relationship between VC precipitate and ferrite matrix was also studied here. Figure 5.3.7 shows one typical composite selected area diffraction pattern (SADP) from VC precipitate and ferrite matrix, along zone axis $\langle 110 \rangle_{VC} // \langle 100 \rangle_{\alpha}$, from thin foil specimen of the DPV, A5 steel. The orientation between VC and α can be identified as Baker-Nutting orientation relationship:

$$\{001\}_{\alpha} // \{001\}_{VC} \text{ and } \langle 110 \rangle_{\alpha} // \langle 100 \rangle_{VC}$$

This is typical for V-added steels, where the diffraction spot of 002_V is located about 2/3 from that of 002_{α} , on the same straight line, and can be used as an criterion to identify the Baker-Nutting orientation relationship. The HRTEM images of ferrite and VCx particle in the real space from another area again confirmed the Baker-Nutting orientation relationship between FCC VC particle and ferrite matrix, Figure 5.3.8.

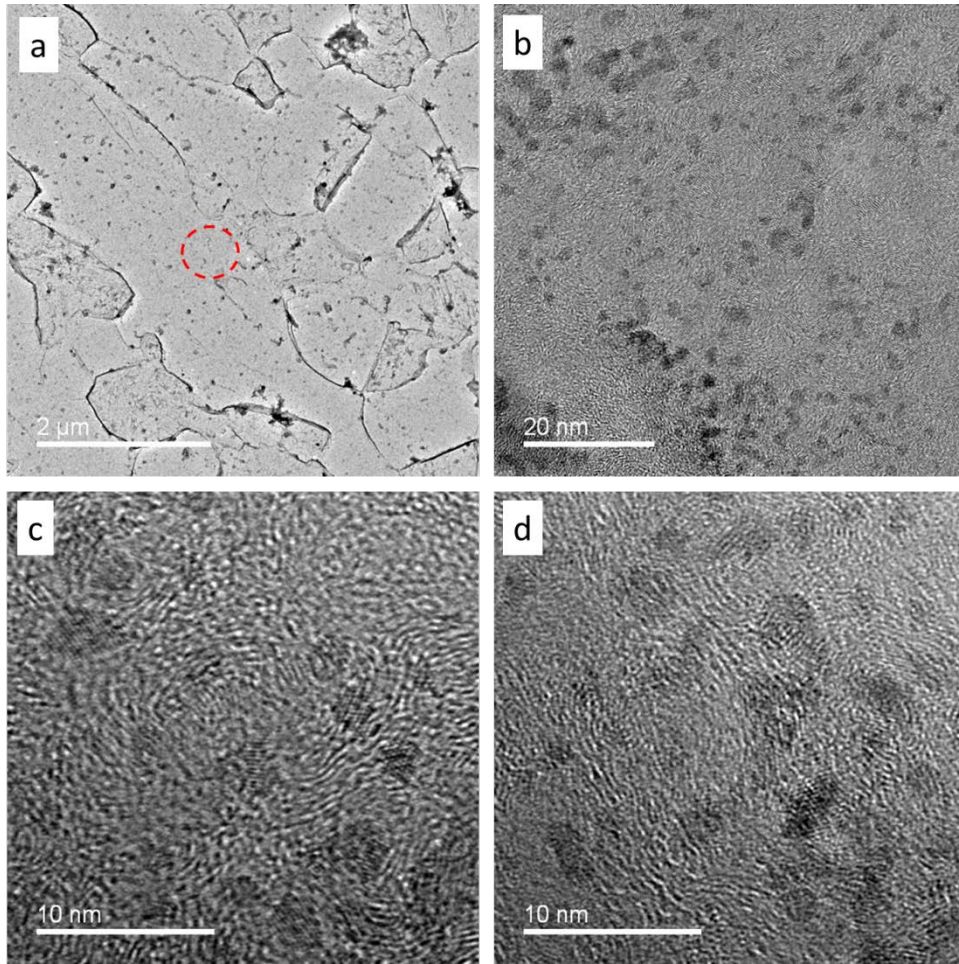


Figure 5.3.9. HRTEM images of VC_x or V(CN)_x precipitates in DPVN, A5 (460°C/60s).

Figure 5.3.9 shows the VC_x or V(CN)_x precipitates at DPVN (A5, 60s at 460°C). Figure 5.3.9(a) is a low magnification microstructure of replica sample, and clearly shows the morphology of ferrite grains and MA islands. Figure 5.3.9(b) is from the red circle (ferrite) in Figure 5.3.9(a), and Figures 5.3.9(c) and (d) are also from the inside of red circle in Figure 5.3.9(a). We see that the density of the vanadium containing precipitates is very high, and the size of the particles is around 3nm and the separations among the particles are less than 10nm. These vanadium containing carbides or carbonitrides probably contribute to the softening resistance and also play apparently through an effective role of precipitation hardening and also dislocation pinning by solute drag due to solute V.

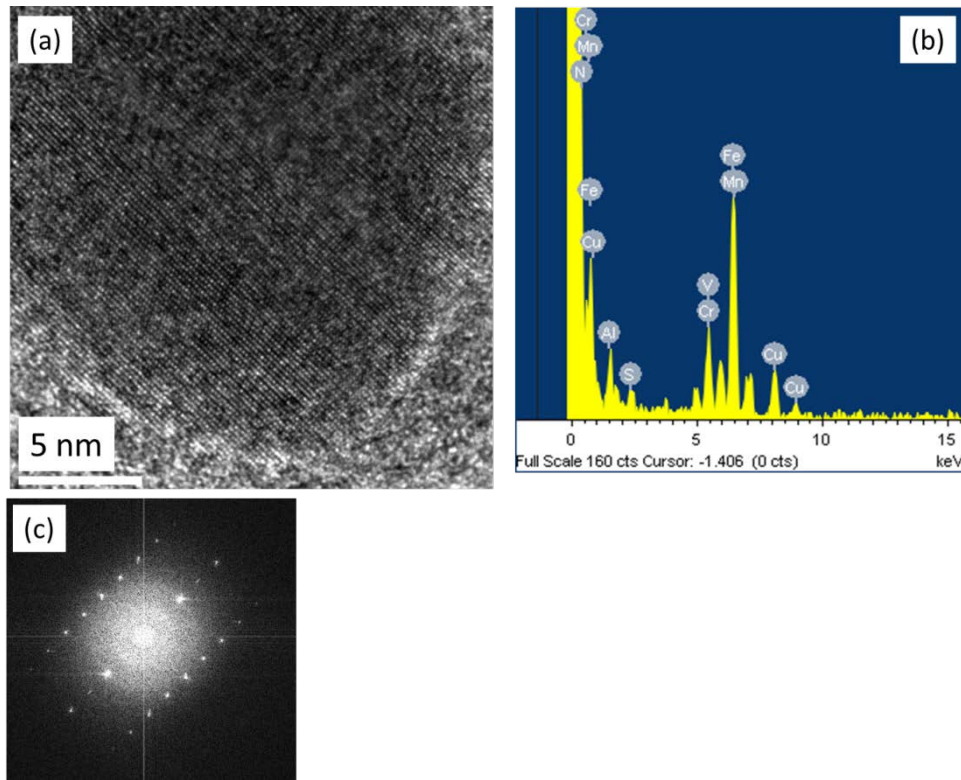


Figure 5.3.10. AlN found in DPVN, A5, replica

Figure 5.3.10 shows one AlN particle, (a) HRTEM lattices, (b) EDX indicating Al peaks and (c) FFT confirmed HCP crystal structure of AlN. The existing AlN particles in DPVN indicates the competition between Al and V to capture N to form nitrides. As pointed by R.J. Glodowski^[137], increasing the Al content will reduce the strengthening ability of VN precipitates in steels. So in order to effectively use VN to strengthen steels, the Al content should be controlled as low as possible.

5.4 INFLUENCE OF STORED ENERGY IN COLD ROLLED SHEET ON THE FORMATION OF AUSTENITE DURING THE SUBSEQUENT INTERCRITICAL ANNEALING OF V-BEARING DUAL-PHASE STEELS

5.4.1 Austenite formation during intercritical annealing

Previous results (Section 5.1) indicate that the strength of DPV subjected to Gleeble simulations of galvanizing (GI), galvannealing (GA) and supercooling processing is lower compared with DPVN and DPNbV with the same processing. The main reason for the lower strength of DPV was the relatively low amount of martensite in the final microstructure which is controlled, at least initially, by the amount of austenite formed during intercritical annealing. Table 5.4.1 shows the evolution of the amount of austenite during intercritical annealing of DPV, DPVN and DPNbV with 60% cold reduction. It is found that DPV contains 14% and 27% less amount of austenite than DPVN and DPNbV respectively, after holding at 780°C for 1 minute. When increasing the holding time at 780°C to 2 minutes, DPV and DPVN have similar amounts of austenite, but still about 15% less than that in DPNbV. If the holding time is extended to 5 minutes, the amounts of austenite of DPV and DPVN are about 43%, however, about 85% volume fraction of austenite was found in DPNbV which is about 2 times of the amount of austenite in DPV or DPVN. Such differences in the amount of austenite among these 3 steels are not well predicted using JMatPro, which predicts similar amount of austenite (45%-47%) for these 3 steels at equilibrium at 780°C. When holding the samples at 790°C and 820°C for 1 minute, 34% and 49% austenite were obtained for DPV with 60% cold rolling reduction respectively. Understanding the amount of austenite after 1 minute annealing at different intercritical annealing temperatures (IAT) is much more important than choosing the optimum IAT for steels with different compositions, since 1 minute intercritical annealing is a common initial step for most real continuous galvanizing lines and their simulations of galvanizing(GI) or galvannealing(GA). The amount of austenite formed at this stage determines, to a large extent, the maximum amount of martensite that can be obtained in the final microstructure.

From the results of the formation of austenite during intercritical annealing, it may be observed that the addition of Nb to the V-based steel can effectively increase the amount of austenite at the end of the intercritical annealing, resulting in the higher amount of martensite in the final microstructure. Furthermore, the addition of nitrogen to the V-based steel can also increase the amount of austenite for 1 minute intercritical annealing. According to these results, one method to improve the strength of DPV is to increase the amount of MA (martensite and retained austenite) in the final microstructure, which depends on the amount of austenite formed during intercritical annealing. One simple approach to increase the amount of austenite is to increase the IAT, however, more austenite means less carbon content in the austenite which makes the austenite less stable during cooling from IAT to the zinc pot temperature (460°C), so more austenite will be lost (or transformed to ferrite or bainite) during subsequent steps. The results of DPV and DPVN using IAT of 820°C indicate that increasing the IAT does not lead to further increase in strength as discussed in Section 5.2. Another method to increase the amount of austenite after 1 minute intercritical annealing, without significantly increasing the carbon content, is to increase the nucleation sites of austenite in the initial microstructure, i.e. in the initial cold rolled steel. The phase transformation to austenite preferentially occurs at the defect sites, e.g. interface between cementite and ferrite, dislocations, sub-grain boundaries or grain boundaries, since the significant distortion of the crystal lattice supplies more driving force for the phase transformation in the defective regions. Moreover the formation of austenite needs the supply of carbon from carbon rich region (e.g. cementite), and the diffusivity of carbon is higher in those defects (e.g. dislocation pipe diffusion in deformed ferrite with high density of dislocations) than in the perfect crystal lattice.

In order to get more austenite nucleation sites, the reduction in cold rolling was increased from 60% to 72%. More cold reduction introduced more defect sites into the initial microstructure which serve as the nucleation sites for austenite formation. More severely deformed ferrite grains contain more dislocations and sub-grain boundaries, resulting in higher stored energy. The 72% cold rolled DPV samples were used for intercritical annealing and then water quenching (WQ) (or air cooling (AC)) treatments using the MTS equipment. As shown in Table 5.4.1, the amount of austenite after 1 minute

annealing at 780°C, 790°C and 820°C are 57%, 63% and 83% respectively, much more than the amount of austenite formed in the 60% CR DPV with the same heat treatments. The amount of austenite is about 35% even when it was air cooled from IAT 780°C after 1 minute annealing, which indicates that more austenite may be reserved during subsequent processing. Figure 5.4.1 shows the SEM microstructures of the samples etched with 2% Nital and clearly indicate the changes of the amount of austenite formed after 1 minute intercritical annealing at 780°C (Figure 5.4.1b), 790°C (Figure 5.4.1c) and 820°C (Figure 5.4.1d) of DPV with 72% cold reduction. As expected, increasing the reduction of cold rolling significantly increased the amount of austenite formed during 1 minute intercritical annealing for DPV.

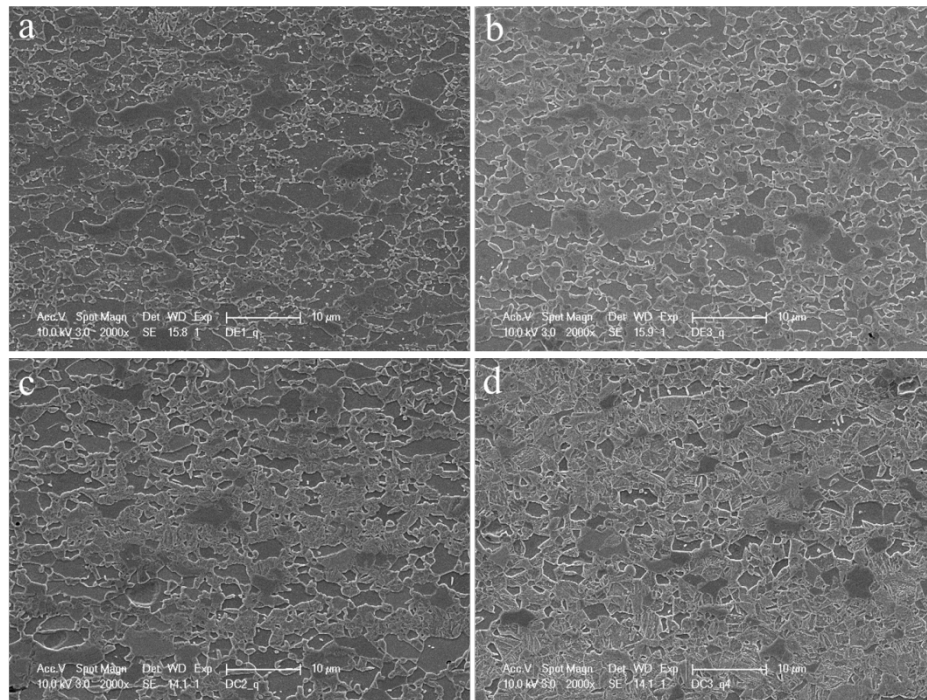


Figure 5.4.1. DPV, 72% cold rolled (a) 780°C, 0s, WQ, (b) 780°C, 1min, WQ and (c) 790°C, 1min, WQ and (d) 820°C, 1min, WQ (SEM micros, 2% Nital Etched)

Table 5.4.1. Austenite amount (%) after intercritical annealing and water quench (or air cooling AC) for cold rolled (60% vs 72%) DPV, DPVN and DPNbV steels. The number in the parentheses is the heating rate from room temperature to IAT.

	DPV60%	DPV72%	DPVN60%	DPNbV60%
780°C(5°C/s), 1min, WQ	20	60	34	47
780°C(5°C/s), 1min, AC		35		
780°C(5°C/s), 2min, WQ	39		38	54
780°C(5°C/s), 5min, WQ	42		43	85
780°C(5°C/s), 0s, WQ		17		
790°C(10°C/s), 0s, WQ		26		
790°C(5°C/s), 1min, WQ	34	63		
820°C(5°C/s), 1min, WQ	49	83		

5.4.2 Effects of stored energy on the formation of austenite during intercritical annealing

As seen in the previous section, increasing the cold rolling reduction, which is closely related to the stored energy in the matrix, speeds up the formation of austenite, resulting in more austenite after only 1 minute intercritical annealing at the IAT.

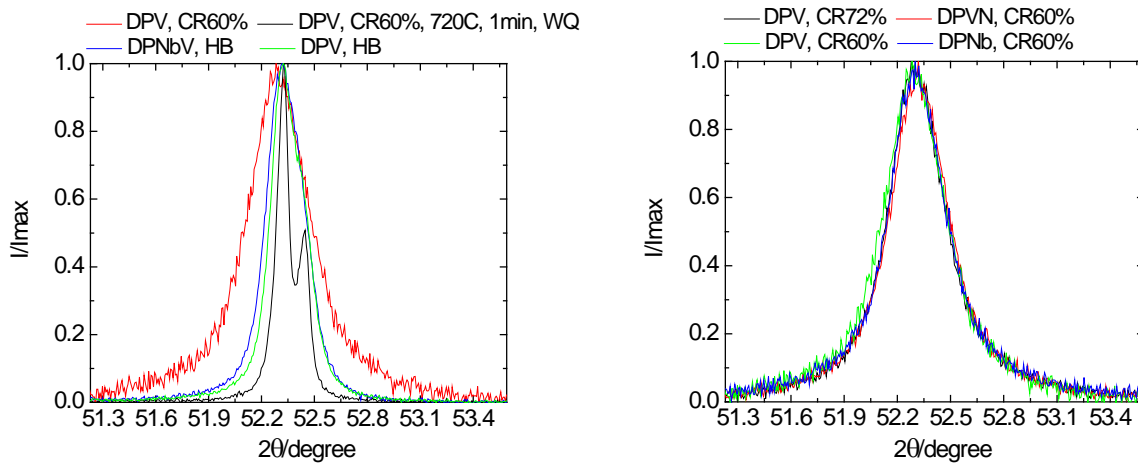


Figure 5.4.2. X-ray diffraction profiles of as cold rolled DPV(60%CR and 72%CR), DPVN(60%CR) and DPNb(60%CR), hot band steels of DPV and DPNbV, as well as annealed DPV(60%CR, 720°C for 1minute and then water quenched).

The comparison of stored energy of steels with different conditions can be made from the width of X-ray diffraction peaks, since the XRD peak broadening is closely related to the deformation of the crystals and higher stored energy will result in broader peaks. Figure 5.4.2 compared the first peaks of ferrite ($\{110\}$, 52.4° for Co $K\alpha_1$, and 52.3° for Co $K\alpha_2$) of steels with different condition. As expected the peak of DPV with 60% cold reduction is broader than that of hot band DPV, which is broader than the annealed steel (annealing at 720°C for 1 minute results in the recovery and recrystallization of deformed ferrite). However there is no obvious difference between hot band DPV and DPNbV steels. The four cold rolled conditions (DPV 60%CR, DPV 72%CR, DPNb 60%CR, and DPVN 60%CR) have almost the same $\{110\}$ peaks, which indicates that XRD peak broadening is not sensitive enough to distinguish the differences in stored energy among these cold rolled conditions. In order to get local and more detailed information about the stored energy of cold rolled steels, sub-grain method based on EBSD mappings will be applied in this section to overcome the limitations of the XRD peak broadening method which describes the global values of stored energy.

In order to see the relationship between stored energy and austenite formation, firstly we studied the hot band steels of DPV and DPNbV, which were later 60% or 72% cold rolled to get thin sheets for further treatments. Figures 5.4.3a and 5.4.3b show the IQ maps of the hot band (HB) DPV and DPNbV, where the blue lines are 15° - 180° grain boundaries, green lines are 5° - 15° grain boundaries and red lines are 2° - 5° grain boundaries. From the IQ maps we see that the ferrite grains are finer in DPNbV than those in DPV, which is due to the addition of Nb to DPV causing the further refinement of the grains. Figures 5.4.3c and 5.4.3d show the stored energy distribution of the hot band DPV and DPNbV obtained using sub-grain boundary method. The average stored energy of HB DPNbV ($1.21\text{J}/\text{cm}^3$) is greater than that of HB DPV ($1.09\text{J}/\text{cm}^3$) from the sub-grain method as listed in Table 5.4.2. Using IQ data, the stored energy was $4.69\text{J}/\text{cm}^3$ for HB DPV and $4.81\text{J}/\text{cm}^3$ for DPNbV respectively. The lower IQ values of DPNbV indicate more dislocations and lattice defects, resulting in higher stored energy. From the hardness values, we see that HB DPNbV is harder (VHN 323) than HB DPV (VHN 286). These results (listed in Table

5.4.2) from sub-grain method, IQ and hardness are consistent with each other, and indicate that the stored energy in HB DPNbV is higher.

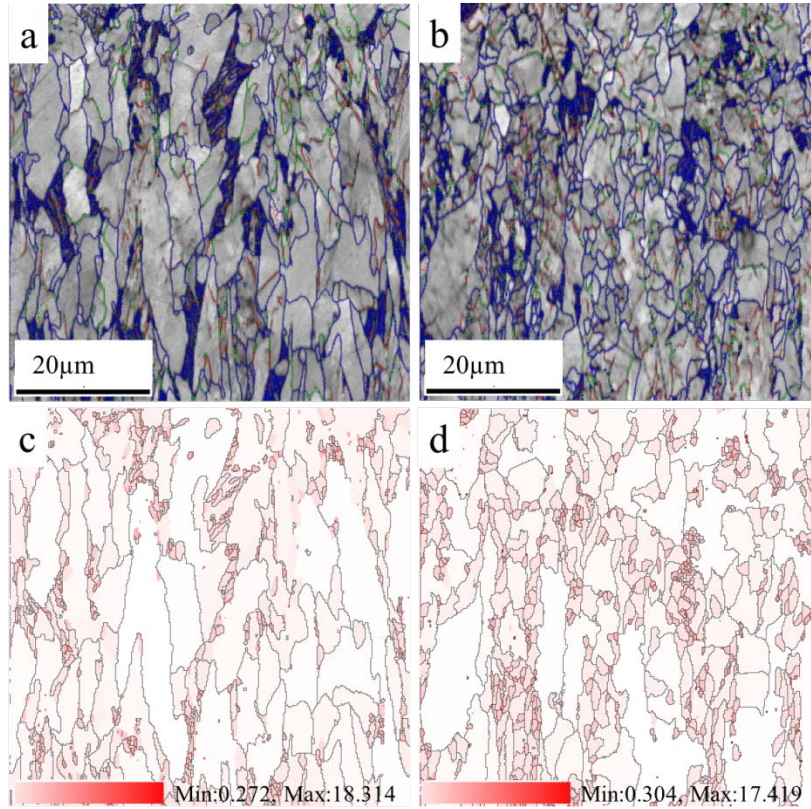


Figure 5.4.3. Image Quality (IQ) images of (a) DPV, HB, quarter, (b) DPNbV, HB, quarter. Blue lines for 15°-180° grain boundaries, green lines 5°-15° grain boundaries and red lines for 2°-5° grain boundaries. Stored Energy (SE) distribution maps of (c) DPV, HB, quarter, and (d) DPNbV, HB, quarter.

Cold rolling the hot band steels to thin sheets introduced even more deformation and dislocations into the steel. The stored energy using sub-grain method was determined in the following steels/conditions: 60% cold rolled (CR) DPV, 72% CR DPV and 60% CR DPNbV, and the results listed in Table 5.4.2 show that the stored energy is much higher than that of the corresponding HB steels. The stored energy of 60% CR DPNbV ($4.00\text{J}/\text{cm}^3$) is higher than that of 60% CR DPV ($3.64\text{J}/\text{cm}^3$) and lower than that of 72% CR DPV ($4.70\text{J}/\text{cm}^3$). After cold rolling, the results of the stored energy from sub-grain method showed that more dislocations and internal stresses were introduced into 60% CR DPNbV

compared with 60% CR DPV, which may be one reason for the higher amount of austenite in DPNbV after 1 minute intercritical annealing. Furthermore, by cold rolling DPV to 72% reduction, the stored energy raised up to $4.70\text{J}/\text{cm}^3$ from $3.64\text{J}/\text{cm}^3$, which is higher than the stored energy of 60% CR DPNbV. The higher stored energy of 72% CR DPV contributes to the higher amount of intercritically formed austenite after 1 minute intercritical annealing compared with 60% CR DPV and DPNbV. These results show that increasing the initial stored energy can effectively speed the formation of austenite during the first 1 minute of annealing. Figures 5.4.4 (a), 5.4.4 (b) and 5.4.4 (c) show the stored energy distribution of 60% CR DPV, 60% CR DPNbV and 72% CR DPV, respectively. All the stored energy distribution maps have the same size of $60\mu\text{m}\times 60\mu\text{m}$. From the IQ data, we still see that the stored energy of 60% CR DPNbV is higher than that of 60% CR DPV. However, the averaged IQ is higher (so a lower stored energy calculated from IQ data) for 72% CR DPV, which is due to the limitation of the IQ method, since the IQ data is also affected by the sample surface conditions and electron beam conditions. The hardness values of the cold rolled samples are also given in Table 5.4.2. The hardness of 60% CR DPNbV is higher than that of 60% CR DPV, and 72% CR DPV is harder than 60% CR DPV, which is consistent with the stored energy results from sub-grain method. 72% CR DPV and 60% CR DPNbV have almost the same hardness, which is acceptable since the hardness data describes global information, while the stored energy distribution from the sub-grain method gives us more detailed local information.

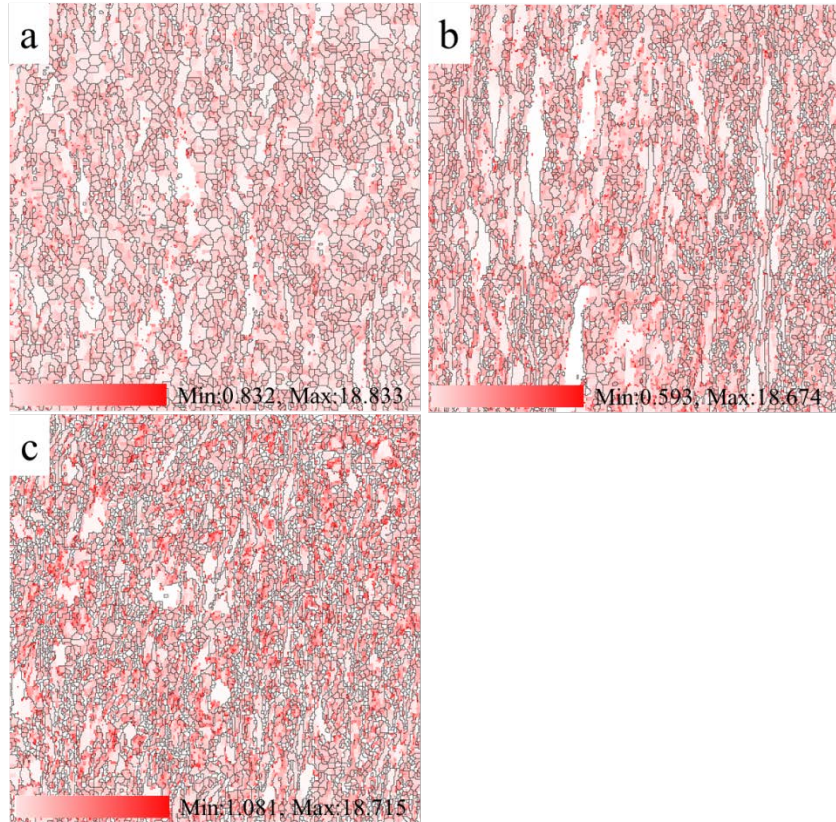


Figure 5.4.4. Stored Energy (SE) distribution maps of (a) DPV, 60% CR, (b) DPNbV, 60% CR, (c) DPV, 72% CR. The size of each image is 60 μm ×60 μm .

Table 5.4.2. Averaged stored energy calculated using different methods (J/cm^3) and the VHN values.

	IQ	Subgrain method	VHN(300g)
DPV, HB	4.69	1.09	286±21
DPNbV, HB	4.81	1.21	323±3
DPV, 60% CR	6.97	3.64	410±9
DPNbV, 60% CR	7.38	4.00	426±7
DPV, 72% CR	6.54	4.70	422±8
DPV, 60% CR, 740°C, 0s, WQ	5.41	3.46	292±6
DPNbV, 60% CR, 740°C, 0s, WQ	6.84	4.42	378±10
DPVN, 60% CR, 740°C, 0s, WQ	5.78	3.56	340±3
DPV, 72% CR, 740°C, 0s, WQ	6.73	4.35	363±4

In order to track how the stored energy affected the microstructure during heating to IAT, the samples were heated to 740°C with a heating rate of 5°C/s using the MTS furnace, and then immediately water quenched when the temperature reached 740°C. From the microstructures we see that more ferrite grains were recrystallized during heating to 740°C in 60% CR DPV than in 60% CR DPNbV, as we can

see more elongated ferrite grains in the microstructure of 60% CR DPVN in Figures 5.4.5 (a) and 5.4.5 (b). The addition of nitrogen to DPV retarded the recrystallization of the cold rolled ferrite. Figures 5.4.5 (a) and 5.4.5 (b) also show the stored energy distribution of 60% CR DPV and 60% CR DPVN respectively. The stored energy of 60% CR DPV after heating to 740°C calculated using sub-grain method is 3.46J/cm³, lower than that of the initial 60% CR DPV, due to the recrystallization of deformed ferrite, recovery, and relaxation of internal stresses and also lower than the stored energy of 60% CR DPVN (3.56J/cm³) after heating to 740°C. The stored energy calculated from IQ data also shows that the 60% CR DPVN has higher stored energy than 60% CR DPV after heating to 740°C, which is consistent with the results from sub-grain method. After heating to 740°C, the hardness dropped from VHN 410 to VHN 292 for 60% CR DPV, which is lower than the hardness of DPVN (VHN 340) as listed in Table 5.4.2. However, for 72% CR DPV and 60% CR DPNbV, very little of the cold rolled ferrite was recrystallized after heating to 740°C. Figures 5.4.5 (c) and 5.4.5 (d) show the stored energy distribution of 72% CR DPV and 60% CR DPNbV after heating to 740°C. These data clearly show a higher stored energy distribution than for 60% CR DPV and DPVN with the same heat treatment. The stored energy calculated with the sub-grain method of 60% CR DPNbV after heating to 740°C is 4.42J/cm³ and that of 72% CR DPV is 4.35J/cm³, which are much higher than that of 60% CR DPV and 60% CR DPVN with the same heat treatment. The stored energy decreased after heating to 740°C for 72% CR DPV from the initial cold rolled state, however there was a higher stored energy for 60% CR DPNbV after heating to 740°C, which is probably due to more unidentified points in the initial cold rolled DPNbV. As mentioned before, the sub-grain method critically depends on the orientation of each lattice point that can be well identified from EBSD and a significantly deformed lattice makes it difficult to clearly identify the orientations. Figures 5.4.5 (c) and 5.4.5 (d) show the distribution of stored energy of 60% CR DPNbV and 72% CR DPV after heating to 740°C using the sub-grain method. Using IQ data, the stored energy of 60% CR DPNbV after heating to 740°C is actually lower than that of the initial cold rolled state. Considering the limitations of sub-grain method and IQ method, we further checked the stored energy with hardness values. As shown in Table 5.4.2, the hardness of DPNbV dropped from VHN 426 to 378

and the hardness of 72% CR DPV dropped from VHN 422 to 363 after heating to 740°C and both are harder than DPV and DPVN with the same heat treatment. Combining the results from sub-grain method, IQ method and hardness values, we conclude that (1) during heating to 740°C, the stored energy decreased due to the recrystallization of ferrite, release of internal stress and decrease of dislocations; (2) the stored energy of 60% CR DPNbV and 72% CR DPV is much higher than that of 60% CR DPV and DPVN after heating to 740°C. The higher stored energy at 740°C will continue to serve as the driving force for the formation of austenite during holding at IAT (780°C, 790°C or 820°C), resulting in a larger amount of austenite in DPNbV and 72% CR DPV as discussed in Section 5.4.1.

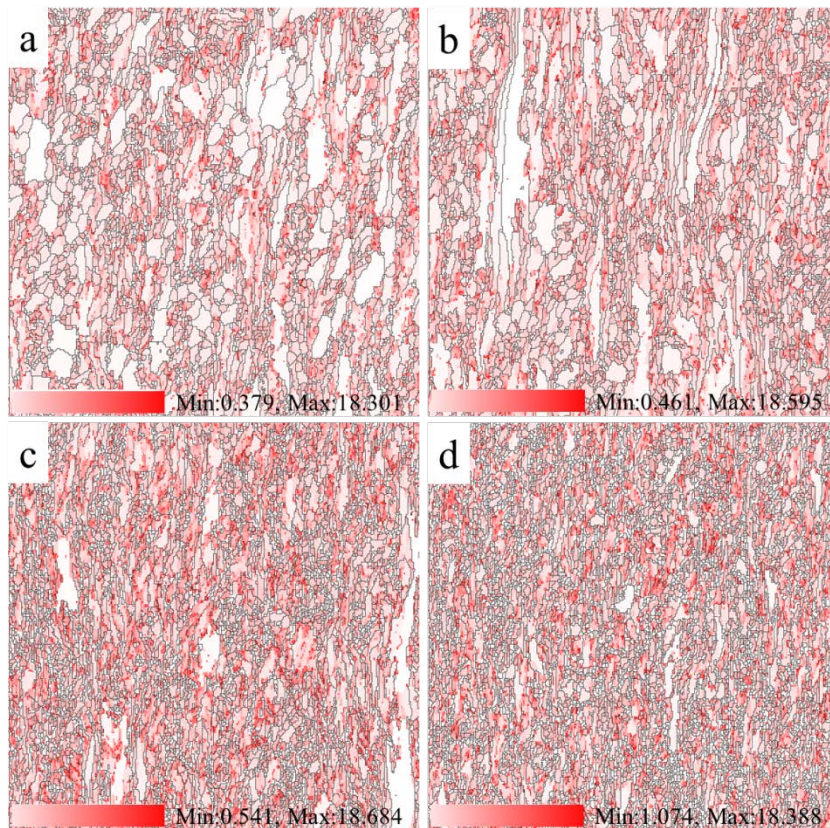


Figure 5.4.5. Stored Energy (SE) distribution maps of (a) DPV, 60% CR, 740°C, 0s WQ, (b) DPVN, 60% CR, 740°C, 0s WQ, (c) DPNbV, 60% CR, 740°C, 0s WQ, and (d) DPV, 72% CR, 740°C, 0s, WQ. The size of each image is 60 μ m \times 60 μ m.

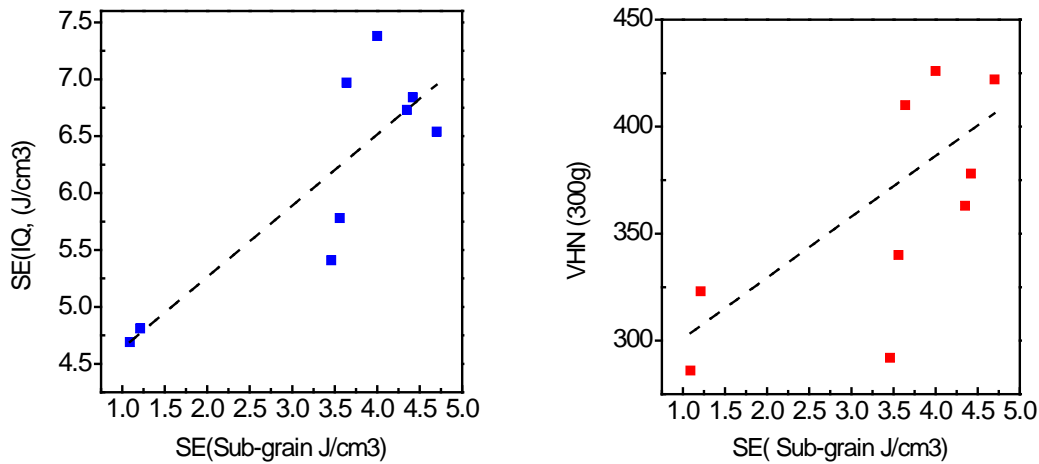


Figure 5.4.6. The positive relationship between SE from sub-grain method and SE from IQ data (left); the positive relationship between SE from sub-grain method and VHN (300g) hardness (right)

Table 5.4.3. Volume fraction of stored energy greater than 5, 10 or 14 J/cm³ for cold rolled (CR) samples

Stored Energy	>5J/cm ³	>10J/cm ³	>14J/cm ³
DPV, 60% CR, Quarter (%)	18.3	1.04	0.14
DPNbV, 60% CR, Quarter (%)	29.7	3.01	0.50
DPV, 72% CR, Quarter (%)	39.0	8.43	1.60

In the present work, the calculated stored energy from sub-grain method is consistent with the IQ values and hardness values. From Figure 5.4.6 we can see the positive relationship between the stored energy from sub-grain method and that from IQ data, and higher hardness value results in higher stored energy. The dashed lines in Figure 5.4.6 are obtained from linear fitting of the data and have positive slopes. The stored energy distribution calculated from sub-grain method can give us more detailed information. Table 5.4.3 shows the volume fraction of stored energy greater than 5, 10, or 14J/cm³ for 60% CR DPV, 60% CR DPNbV and 72% CR DPV, and we can see that the amount of stored energy greater than 5 J/cm³ in 72% CR DPV is about 2 times the amount of that in 60% CR DPV and also 10% more than that in 60% CR DPNbV, which indicates that the higher stored energy positions may facilitate the formation of austenite during intercritical annealing.

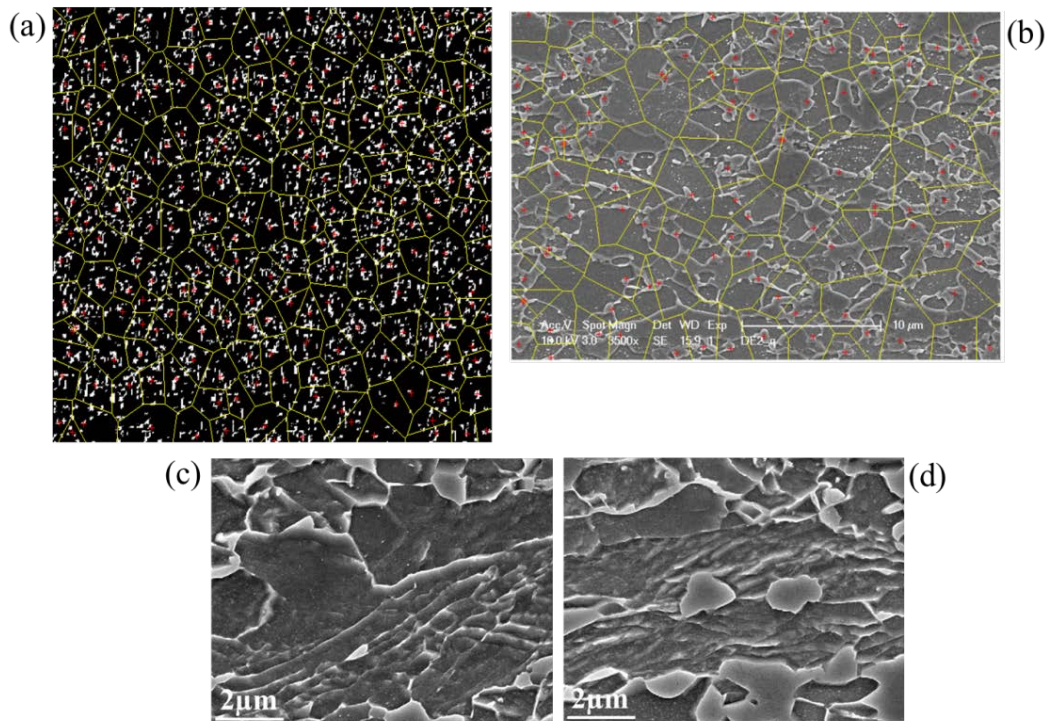


Figure 5.4.7. (a) shows the local volumes with SE higher than 8 J/cm^3 in the microstructure of initial 72% cold rolled steel, the size is $60 \times 60 \mu\text{m}$, and (b) illustrates the austenite found after heating to 760°C and water quenching immediately with no holding time. (c) and (d) are the SEM microstructures of DPVN with Galvannealing processing with nucleation of austenite at sub-grain boundaries in non-recrystallized ferrite

The relationship between high stored energy spots and austenite nucleation sites can be observed from Figure 5.4.7. With 72% cold reduction, the local stored energy volumes in the cold band with energies above 8 J/cm^3 are shown by the white dots in Figure 5.4.7 (a). By tessellating about clusters of these dots and analyzing using Voronoi tessellation, the inter-cluster distance was 5.04 microns. The initial formation of austenite in specimens cold rolled 72% and heated to and immediately quenched from 760°C to minimize austenite growth is presented in Figure 5.4.7 (b). The Voronoi tessellation of this austenite gave an inter-austenite grain distance of 5.23 microns. Figures 5.4.7 (c) and 5.4.7 (d) are the SEM microstructures of DPVN with Galvannealing processing, from which we can see the nucleation and growth of fresh austenite at sub-grain boundaries of non-recrystallized ferrite. This study showed that the

higher the bulk cold reduction and average stored energy, the more prevalent are the high stored energy volumes. This resulted in more sites for austenite formation and slammer and more closely spaced austenite grains.

We used the 72% CR DPV to do the Gleeble simulations of galvanizing (i.e. 790°C/1min, 460°C/30s, 10°C/s to RT), and found that the tensile strength of our DPV with 72% CR reached 981MPa, while the tensile strength of DPV with 60% CR with the same heat treatment is only about 921MPa. The increase in the tensile strength is due to the higher amount of martensite in the final microstructure which derives from the larger amount of austenite formed during intercritical annealing in the 72% CR DPV, as well as the finer grains due to higher cold reduction.

Table 5.4.4 listed 10 different Gleeble processing, and Figure 5.4.8 plotted the tensile strength of 60%CR DPV, DPVN and 72%CR DPV with these Gleeble processing. As can be seen, the DPV steels with 72%CR (red spots) are stronger than the corresponding DPV steels with 60%CR. The design of the steels (50% and 80% cold reductions) in the following sections is based on these preliminary results.

Table 5.4.4. Different Gleeble processing applied to DPV (60%CR and 72%CR) and DPVN (60%CR)

ID	Gleeble processing
1	790°C (1min), 15°C/s, 250°C(20s), 40°C/s, 460°C(30s), 10°C/s, RT
2	790°C (1min), 30°C/s, 250°C(20s), 40°C/s, 460°C(30s), 10°C/s, RT
3	790°C (1min), 15°C/s, 300°C(20s), 40°C/s, 460°C(30s), 10°C/s, RT
4	790°C (1min), 15°C/s, 350°C(20s), 40°C/s, 460°C(30s), 10°C/s, RT
5	790°C (1min), 15°C/s, 460°C(30s), 10°C/s, RT
6	790°C (1min), 15°C/s, 460°C(30s), 30°C/s, RT
7	790°C (1min), 30°C/s, 460°C(30s), 10°C/s, RT
8	790°C (1min), 30°C/s, 460°C(30s), 30°C/s, RT
9	790°C (1min), 60°C/s, 460°C(30s), 30°C/s, RT
10	790°C (1min), 60°C/s, 460°C(30s), 10°C/s, RT

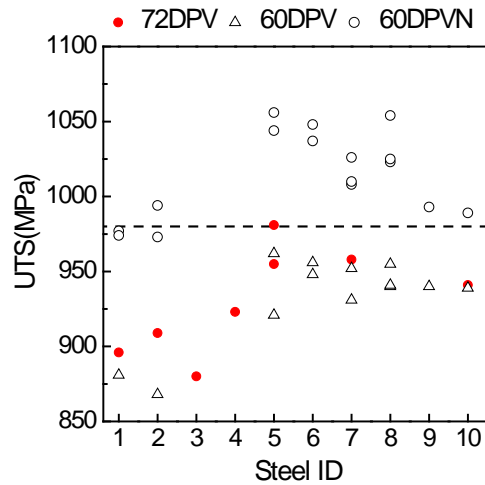


Figure 5.4.8. Tensile strengths (UTS) of DPV (60%CR and 72%CR) and DPVN with different Gleeble processing, the steel IDs are the same as those listed in Table 5.4.4

5.5 EFFECTS OF THERMOMECHANICAL AND VANADIUM ADDITIONS ON THE MICROSTRUCTURE AND MECHANICAL PROPERTIES OF DUAL PHASE STEELS WITH HIGH CR, MO CONTENTS

5.5.1 Chemical compositions and thermomechanical processing

The steels in this section and Section 5.6 are Fe-C-Mn steels with variable V, Cr, Mo contents as shown in Table 5.5.1. A series of laboratory heats were melted in a vacuum induction furnace. Ingots were then hot rolled on a laboratory hot mill. The thermomechanical process used for each type of steel is shown in a schematic diagram, Figure 5.5.1 (a). For hot rolling, the ingots were reheated at 1250 °C , and then rough rolled to 25 mm in several passes, and then finish rolled with 5 passes of reduction of 27.5 % each to a final thickness of 5 mm (0.2 inch), with a finishing temperature of 920 °C. Immediately after exiting the final pass, the steels were water sprayed with an average cooling rate 30°C/s to the coiling temperature of either 650 °C or 500 °C, and then cooled at 30 °C/h to room temperature. The materials were then cold

rolled 50% or 80% to achieve a final thickness of approximately 1.2 mm (or 80 % reduction to 0.84 mm thickness). The cold rolled sheets were sectioned for annealing simulations conducted on a Gleeble 3800. The Gleeble processing (standard galvanizing and supercool processing) are plotted in Figure 5.5.1 (b). Table 5.5.2 listed the conditions (addition of microalloying elements, coiling temperatures (CT) and cold rolling reductions) of initial cold rolled (CR) sheets as well as the sample IDs used in this section and Section 5.6.

Table 5.5.1. Chemical composition (wt. %) of the four steels used in this section and section 5.6

Element/steel	2A	2B	4A	4B
V	-	0.06	-	0.06
Cr	0.5	0.5	0.25	0.25
Mo	0.3	0.3	0.1	0.1
Others:	0.10 C, 1.75 Mn, 0.40 Si, 0.01 P, 0.03 Al, 0.002 S, 0.006 N			

Table 5.5.2. Conditions (addition of microalloying elements, coiling temperatures (CT) and cold rolling reduction) of initial cold rolled (CR) sheets with sample IDs used in this paper.

CR sheets conditions	ID (Vanadium free)	ID (with Vandium)
High Cr, Mo, CT=650°C, 80%CR	2A1A	2B1A
High Cr, Mo, CT=500°C, 80%CR	2A3A	2B3A
High Cr, Mo, CT=650°C, 50%CR	2A1E	2B1E
High Cr, Mo, CT=500°C, 50%CR	2A3E	2B3E
Low Cr, Mo, CT=650°C, 80%CR	4A1A	4B1A
Low Cr, Mo, CT=500°C, 80%CR	4A3A	4B3A
Low Cr, Mo, CT=650°C, 50%CR	4A1E	4B1E
Low Cr, Mo, CT=500°C, 50%CR	4A3E	4B3E

The supercooling treatments were based on the following predictions from JMatPro. After intercritical annealing at 790°C, JMatPro predicts that the austenite formed at 790°C, assuming equilibrium, would have the following critical temperatures, Table 5.5.3.

Table 5.5.3. Critical temperatures of austenite formed at 790°C of steels 2A and 2B, estimated from JMatPro commercial software.

	Bs (°C)	B50% (°C)	Ms (°C)	M50% (°C)	M90% (°C)
2A	548.3	505	351.7	317.0	236.5
2B	546.5	505	348.4	313.7	233.0

Therefore, the supercooling temperatures used were approximately M90(250°C), M50(320°C) and B90(390°C) for the intercritically formed austenite for either steel (2A or 2B).

The microstructural analysis of all the specimens was conducted using standard optical and electron optical techniques (OM, SEM and TEM). The SEM metallography was performed on a Philips XL-30 FEG-SEM microscope and the TEM was performed on FEI-Tecnaï-G2, JEOL-200CX or a 2100F microscope, both operated at 200KV. For Electron Backscattered Diffraction (EBSD) observation, 20kV voltage and the beam spot size of 5 were applied and the step size was 0.2 μm. The TSL OIM data collector software was used for the collection of the EBSD data and also the data analysis. The retained austenite was measured by LakeShore® magnetometer.

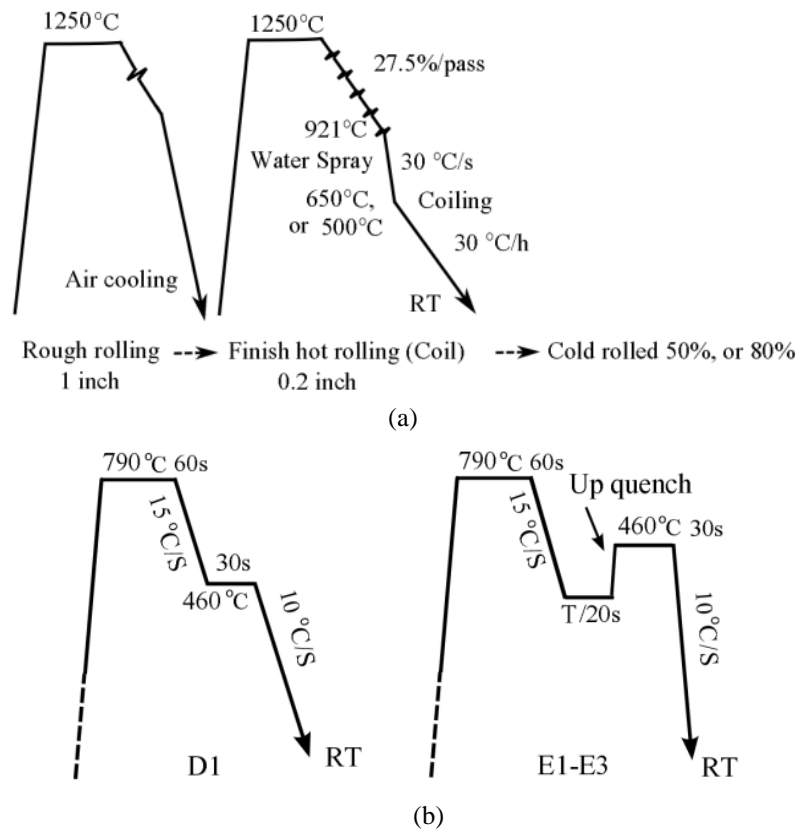
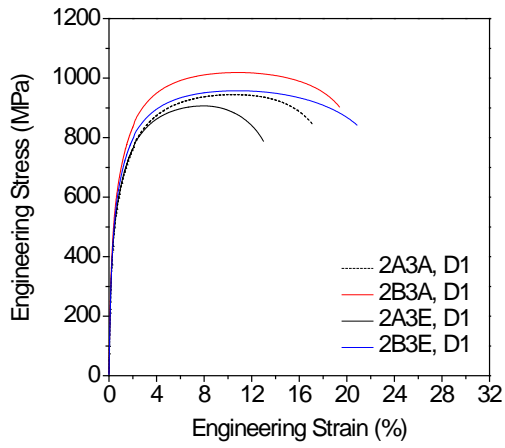


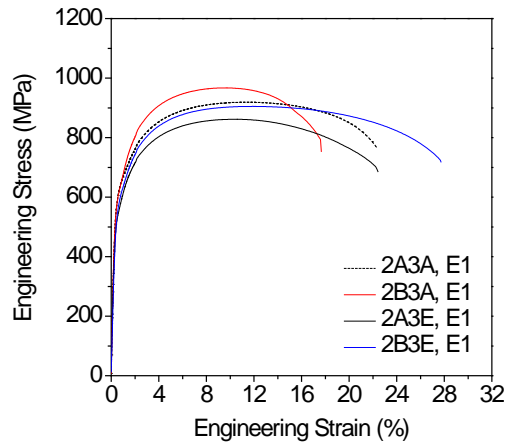
Figure 5.5.1 (a). Schematic diagram of hot rolling and cold rolling used for each type of steel in the current study, RT means room temperature. (b). Simulated CGL heat treatments used in this study. Anneal D1 was the standard GI anneal while E1 (T=250°C), E2 (T=320°C) & E3 (T=390°C) were the anneals incorporating the new supercooled feature. Note: For Process D1: Heating Rate: +5 °C/s and Cooling Rates: - 15 °C/s or -10 °C/s. For Processes E: Heating Rates: + 5 °C/s and + 42 °C/s and Cooling Rates: - 15 °C/s or - 10 °C/s

5.5.2 Mechanical properties of dual phase steels with high Cr, Mo contents

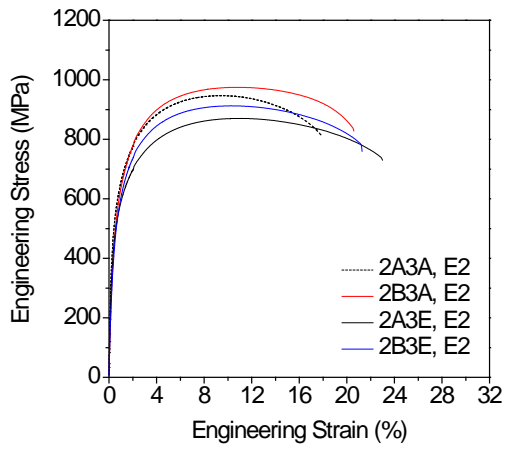
Some of the engineering stress- strain curves are shown in Figure 5.5.2. All of the curves show continuous yielding, which is typical for dual phase steels. Figures 5.5.2 (a)-(d) are the engineering stress-strain curves of DPs with D1, E1, E2 and E3 process respectively. From these curves, it can be seen that the tensile strength of DPs with higher (80%CR) cold rolling reduction is higher than that of DPs with lower (50%CR) cold rolling reduction, which is due to the difference in the final microstructures and will be discussed later. The corresponding true stress-strain curves are displayed in Figures 5.5.3 (a)-(d) for DPs with high Cr, Mo contents and low coiling temperatures (500°C). From the true stress-strain curves we can derive the work hardening exponents of the steels which will be discussed in detail later.



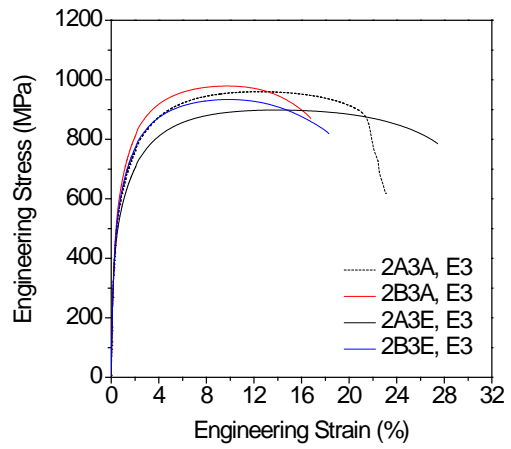
(a)



(b)



(c)



(d)

Figure 5.5.2. Engineering stress-strain curves of DP steels with high Cr, Mo contents and standard galvanizing and supercool processing

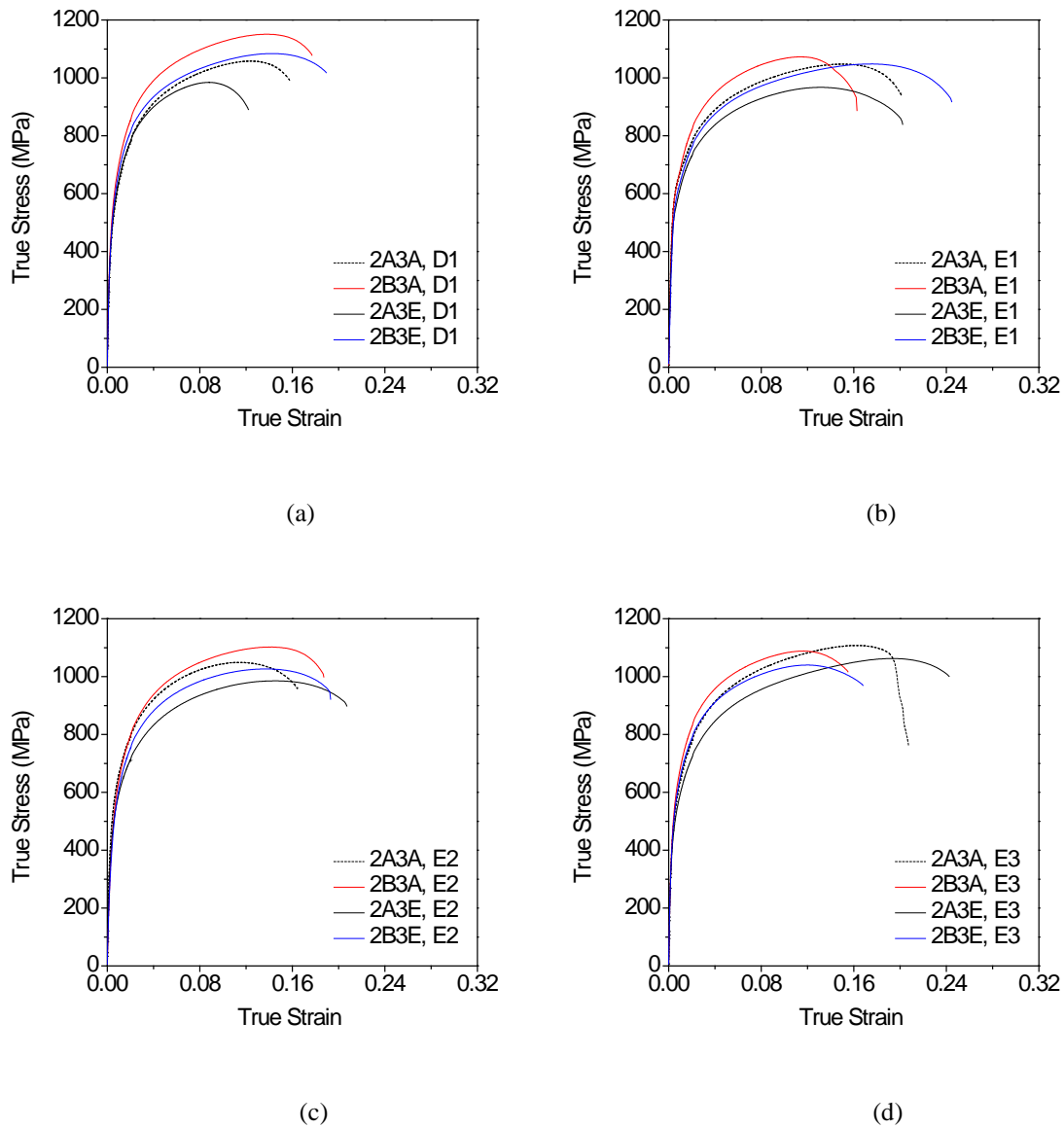


Figure 5.5.3. True stress-strain curves of DP steels with high Cr, Mo contents and standard galvanizing and supercool processing

Figure 5.5.4 summarized and plotted the tensile strength (UTS) of all 32 dual phase steels with different compositions (vanadium bearing and vanadium free), coiling temperatures (500°C and 650°C) and cold rolling reductions (50%CR and 80%CR). It can be found from Figure 5.5.4 that the addition of vanadium plays an essential role to get the required strength. All the dual phase steels with vanadium addition have higher tensile strength than those without vanadium addition. None of the dual phase steels

without vanadium addition can reach 980MPa UTS, and among the DPs with vanadium addition, 2B1A (D1), 2B3A (D1), 2B3A (E2) and 2B3A (E3) can meet the minimum requirement for DP980 steels. The dual phase steel 2B3A with standard galvanizing treatment (D1) can even have more than 1GPa UTS. From these results, we see that higher cold rolling reduction (80% in the present study) can give us more strength compared with low cold rolling reduction (50%CR in the present study), which is consistent with our previous results (see Section 5.4). Higher cold rolling reduction gives more defect sites in the initial CR sheets, resulting in more austenite nucleation sites during intercritical annealing stages. In addition, more cold rolling reduction can further refine the ferrite grain size due to more ferrite recrystallization sites. The increase in tensile strength due to the addition of vanadium is obvious and is summarized in Table 5.5.4. Except for 2B1A (D1 Δ UTS=11.3MPa, E1, Δ UTS= 9.9MPa) and 2B3A (E3, Δ UTS=19MPa), the increase in UTS is more than 30MPa for all other DPs. The highest increase in tensile strength even reached 80MPa for DP with high coiling temperature, 50%CR and D1 processing. This increase in UTS coming from vanadium is obviously very attractive in the industrial applications.

It can be seen that, with the addition of vanadium, UTS increased more in steels with 50%CR than in those with 80%CR, which indicates that vanadium is more helpful to increase strength for steels with low cold rolling reductions. Since more cold rolling reduction means higher production costs and replacement or adjustments of the existed cold rolling systems for steel companies, the efficient increase in UTS from vanadium addition for steels with low cold rolling reductions indicate that the addition of vanadium may be a good choice for the production of dual phase steels.

The effects of coiling temperatures on the tensile strength of dual phase steels with 50%CR are related to the addition of vanadium. Without vanadium addition, low coiling temperature (500°C) gives higher tensile strength due to the finer microstructures, while with the addition of vanadium, high coiling temperature (650°C) results in higher tensile strength even though the dual phase steels with high coiling temperature have coarser microstructures involving polygonal ferrite. This is mainly due to the precipitation hardening from vanadium additions in the polygonal ferrite, and will be further discussed later in Section 5.5.3 and Section 5.7.4.

The difference in tensile strength of DPs with different heat treatments (D1, E1, E2 and E3) can be easily seen. The dual phase steels with D1 process possess the highest tensile strength, while those with E1 (supercool temperature 250°C) process have the lowest tensile strength. We also find that the tensile strength increased with increasing the supercool temperatures from 250°C to 390°C, which is mainly due to the decrease in the amount of tempered martensite and the increase in the amount of fresh martensite in the final microstructures. The more detailed discussions of the microstructures of DPs with different heat treatments will be presented later.

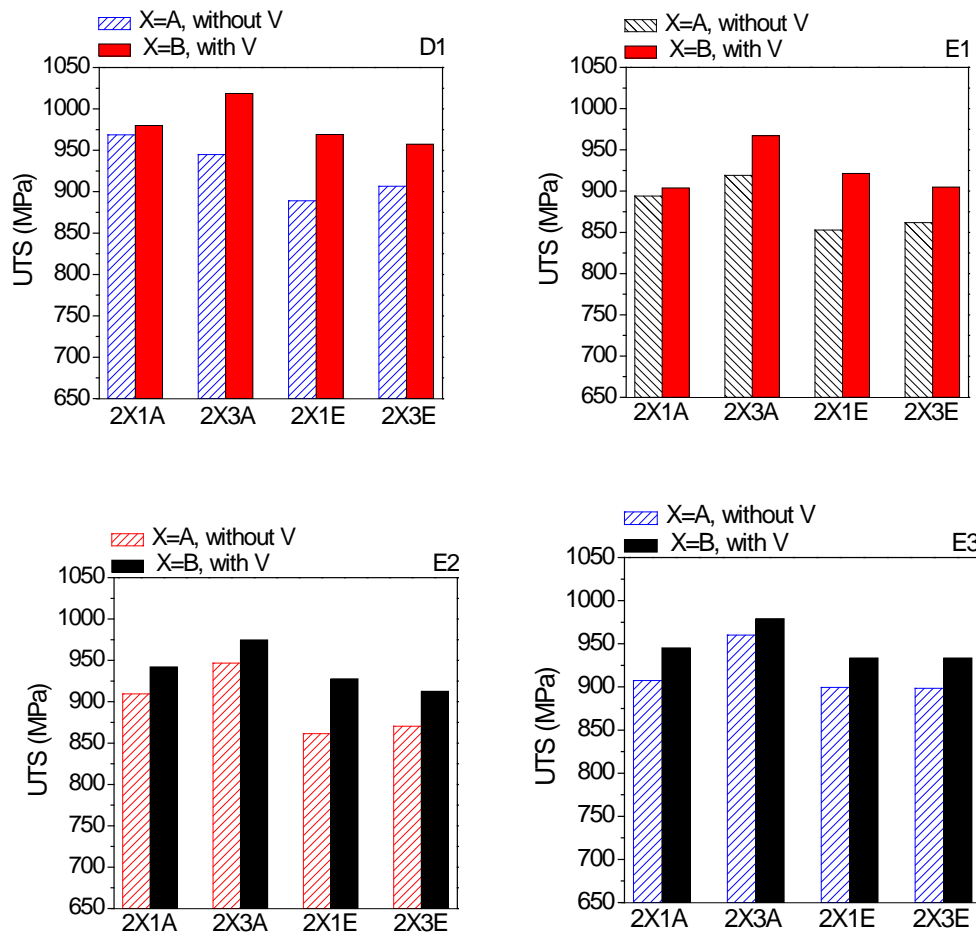


Figure 5.5.4. Tensile strength (UTS) of dual phase steels with standard galvanizing (D1) and supercool processing, X=A is vanadium free, X=B is vanadium bearing, 1 represents high CT 650°C and 3 represents low CT 500°C.

Table 5.5.4. Increase in the tensile strength due to the addition of 0.06% wt.% vanadium. UTS-A is the tensile strength of dual phase steels without vanadium addition in the first column, and UTS-B is the tensile strength of DPs with vanadium addition in the second column. Δ UTS is the increase in UTS.

		Δ UTS=UTS-B-UTS-A (MPa)			
UTS-A	UTS-B	D1	E1	E2	E3
2A1A	2B1A	11.3	9.9	32.7	37.9
2A3A	2B3A	73.9	48	27.9	19
2A1E	2B1E	80.1	68.6	66.1	34.1
2A3E	2B3E	50.9	43.1	42.2	35.3

Table 5.5.5. Increase in the yield strength due to the addition of 0.06% wt.% vanadium. YS-A is the yield strength of dual phase steels without vanadium addition in the first column, and YS-B is the yield strength of DPs with vanadium addition in the second column. Δ YS is the increase in YS.

		Δ YS=YS-B-YS-A (MPa)			
YS-A	YS-B	D1	E1	E2	E3
2A1A	2B1A	11.1	12.5	23.3	46
2A3A	2B3A	37.8	-4	20.1	4.7
2A1E	2B1E	26.6	91.3	51.5	40.7
2A3E	2B3E	29.8	30.7	-2.9	72.7

Figure 5.5.5 shows the yield strength (YS) of all the dual phase steels with high Cr, Mo contents. As expected, the dual phase steels with vanadium additions have high yield strength than the corresponding steels without vanadium addition. The yield strengths of dual phase steels with high Cr, Mo contents vary around 550MPa, and meet the minimum requirement for industrial applications for 980MPa grade dual phase steels. Table 5.5.5 listed the increase in yield strength due to the addition of 0.06% wt.% vanadium. The highest increase in YS is 91.3MPa for 2B1E (E1, vanadium bearing) compared with 2A1E (E1, vanadium free). The main reason for such significant increase in YS is due to dense VC_x precipitates which was confirmed from HRTEM results and will be discussed in detail later.

The total elongations of dual phase steels are plotted in Figure 5.5.6. It can be seen that for supercool processing (E1, E2 and E3) the total elongations of DPs with vanadium are lower than those without vanadium addition (except 2B3E (E1), 2B3A (E2) and 2B1A (E3)). For standard galvanizing heat treatment (D1), the total elongations of dual phase steels with high Cr, Mo and V addition are higher than the corresponding steels without vanadium addition, which indicates that the addition of vanadium increased both tensile strength and total elongations of dual phase steels with high Cr, Mo and D1

processing. These results show that vanadium effectively increased the ductility of dual phase steels with 980MPa grade.

From Figure 5.5.6, it is found that the total elongations increased with decreasing the coiling temperatures, and that DPs with low cold rolling reduction (50%CR) have higher total elongations compared with the corresponding DPs with high cold rolling reduction (80%CR). Figure 5.5.7 shows the yield strength to tensile strength (YS/UTS) ratios of all the dual phase steels with high Cr, Mo contents in the current study. The dual phase steels with and without addition of vanadium have similar YS/UTS ratios and DPs with low cold rolling reductions have higher YS/UTS ratios compared with DPs with high cold rolling reductions, since DPs with low cold rolling reductions have lower UTS than the corresponding DPs with high cold reduction.

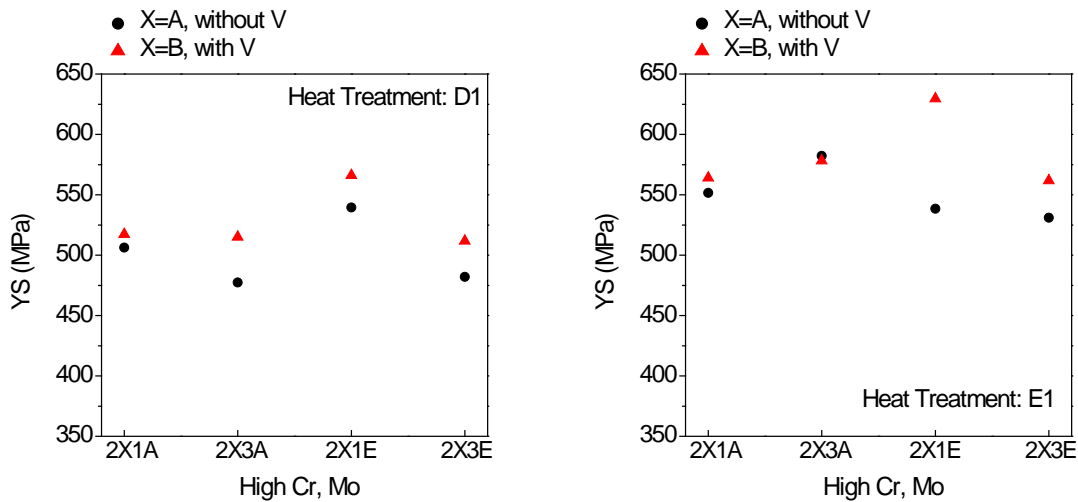


Figure 5.5.5. Yield strength (YS) of dual phase steels with standard galvanizing (D1) and supercool processing.

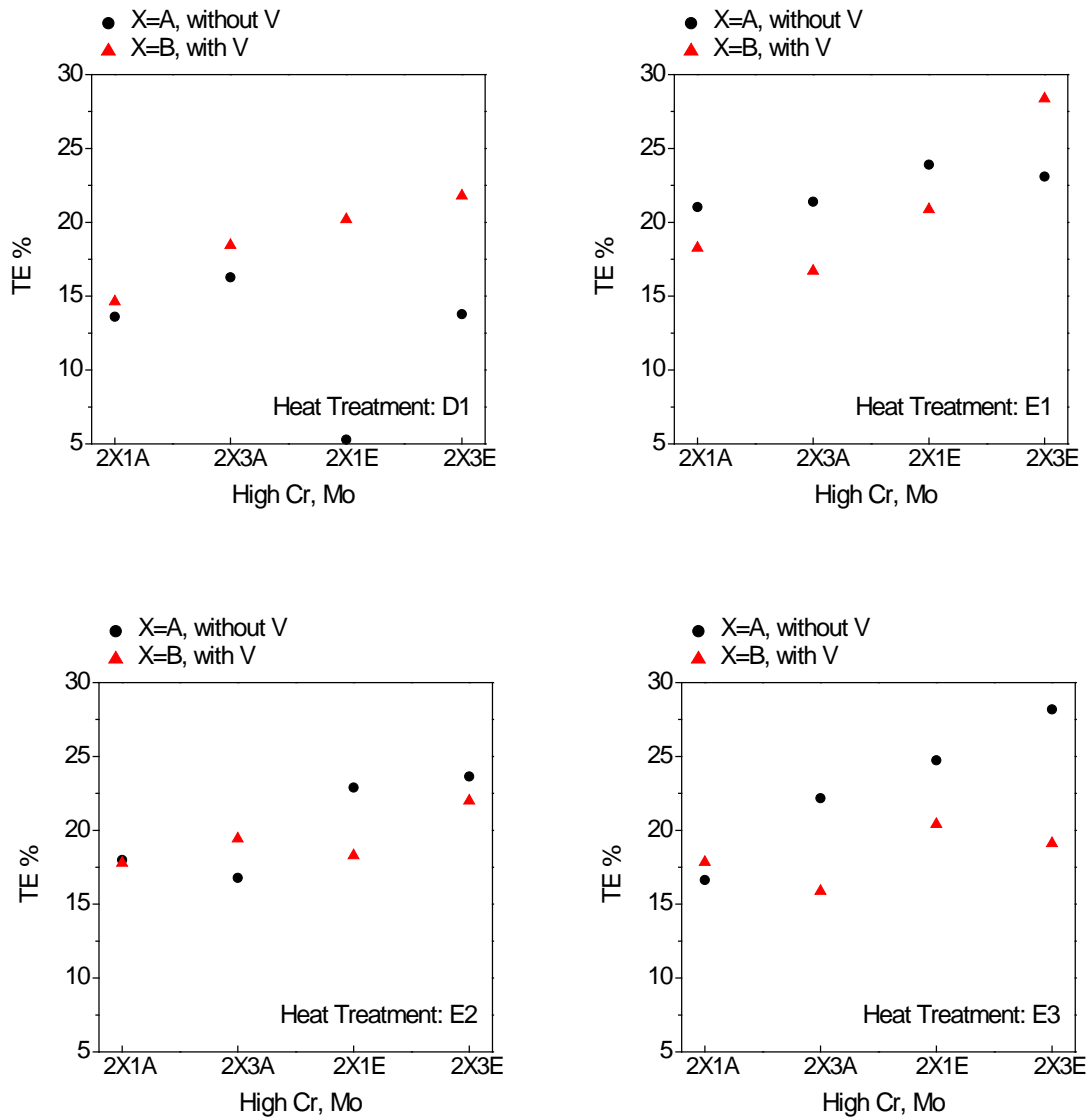


Figure 5.5.6. Total elongations (TE) of dual phase steels with standard galvanizing (D1) and supercool processing. TEs were converted to 50mm (2 inch) standard gage length specimen.

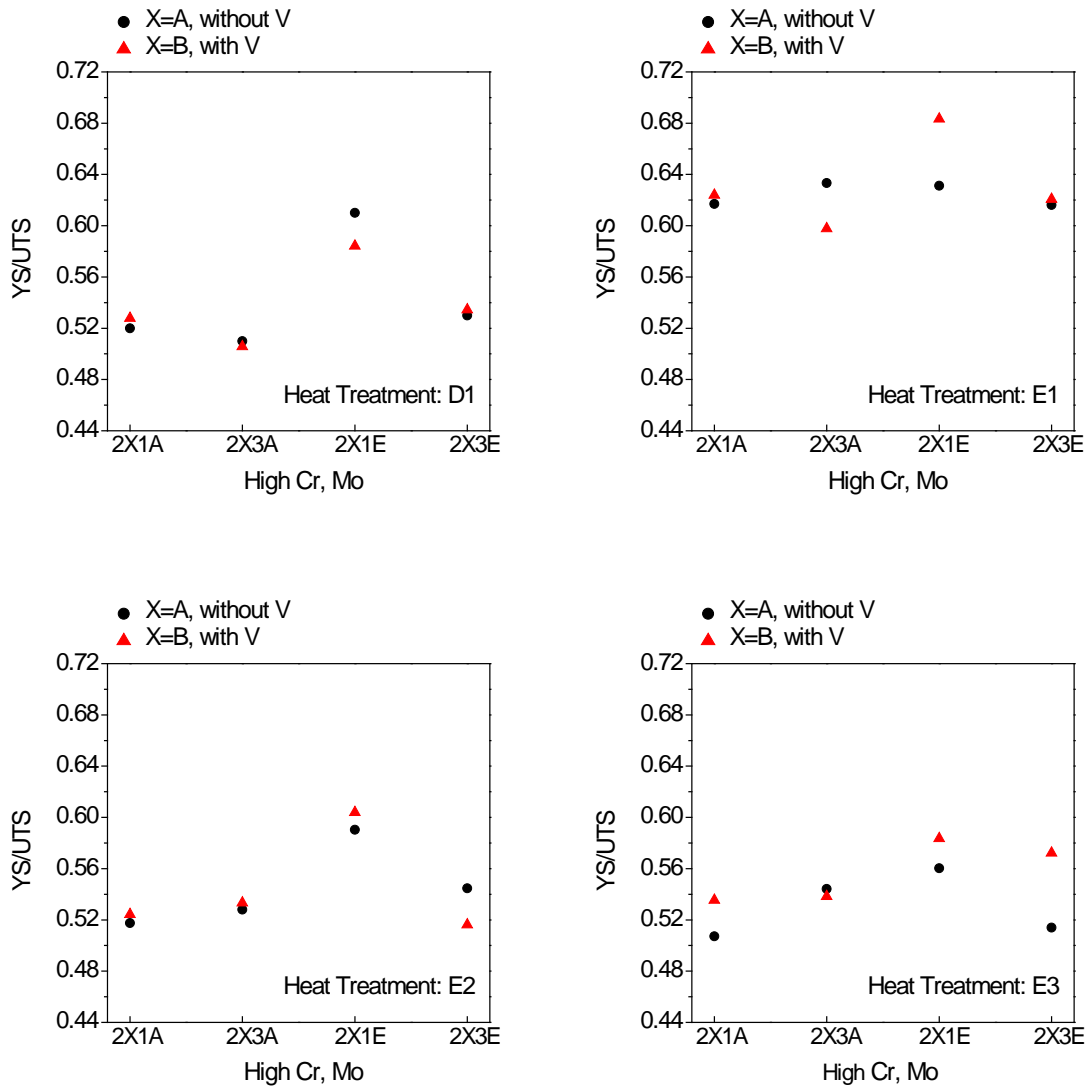


Figure 5.5.7. YS/UTS ratios of dual phase steels with standard galvanizing (D1) and supercool processing.

Table 5.5.6 summarized the tensile strength, reduction in area (% RA) and estimated hole expansion ratios (HER) of dual phase steels with high Cr, Mo. The hole expansion ratios were estimated using the empirical equation $HER = 1.15 \times RA\% - 19.6$, which was derived from our previous results of dual phase steels with different micro alloying elements. Figure 5.5.39 plotted reduction in area with different heat treatments. It is clear that dual phase steels with E1 processing have the highest %RA, while those with D1 processing have the lowest %RA. The reduction in area values decreased with

increase in the supercool temperatures, which is probably due to the decrease in the amount of tempered martensite when increasing the supercool temperatures from 250°C to 390°C. The addition of vanadium can effectively increase the tensile strength, but at the same time not necessarily decrease the reduction in area numbers, as we can see from Figure 5.5.39 that DPs with and without addition of vanadium show similar reduction in area values. These results indicate that addition of vanadium can effectively increase the tensile strength and at the same time retain good ductility. The measured hole expansion ratios will be given and discussed in Section 5.5.6. Table 5.5.7 listed the work hardening exponents (n-values) between 4%-6% strain of the high alloyed DPs and will be discussed in detail in Section 5.7.5.

Table 5.5.6. UTS, reduction in area (%RA) and estimated hole expansion ratios (HER) from reduction in area.

ID	UTS (MPa)	%RA	HER%	ID	UTS (MPa)	%RA	HER%
2A1A,E1	894.0	61.7	51.4	2B1A,E1	903.9	58.6	47.8
2A1A,E2	909.4	48.7	36.4	2B1A,E2	942.1	53.1	41.5
2A1A,E3	907.4	44.5	31.6	2B1A,E3	945.3	46.4	33.8
2A1A,D1	968.7	41.9	28.6	2B1A,D1	980.0	41.8	28.5
2A3A,E1	919.2	61.1	50.7	2B3A,E1	967.2	61.7	51.4
2A3A,E2	946.7	52.8	41.1	2B3A,E2	974.6	51.8	40.0
2A3A,E3	960.1	44.9	32.0	2B3A,E3	979.1	40.9	27.4
2A3A,D1	944.8	39.6	25.9	2B3A,D1	1018.7	43.8	30.8
2A1E,E1	852.8	55.9	44.7	2B1E,E1	921.4	53.1	41.5
2A1E,E2	861.5	50.1	38.0	2B1E,E2	927.6	45.9	33.2
2A1E,E3	899.4	45.2	32.4	2B1E,E3	933.5	38.6	24.8
2A1E,D1	889.0	29.5	14.3	2B1E,D1	969.1	40.1	26.5
2A3E,E1	861.8	57.4	46.4	2B3E,E1	904.9	57.7	46.8
2A3E,E2	870.3	46.5	33.9	2B3E,E2	912.5	52.0	40.2
2A3E,E3	898.3	48.8	36.5	2B3E,E3	933.6	45.8	33.1
2A3E,D1	906.6	49.0	36.8	2B3E,D1	957.5	45.4	32.6

Table 5.5.7. Work hardening exponents (n-values between engineering strain 4% and 6%) of dual phase steels with high Cr, Mo contents

ID	n (4%-6% engineer strain)	ID	n (4%-6% engineer strain)
2A1A, D1	0.1541	2B1A, D1	0.1485
2A3A, D1	0.1697	2B3A, D1	0.1578
2A1E, D1	-	2B1E, D1	0.1485
2A3E, D1	0.1474	2B3E, D1	0.1526
2A1A, E1	0.1627	2B1A, E1	0.1558
2A3A, E1	0.1586	2B3A, E1	0.1561
2A1E, E1	0.1527	2B1E, E1	0.1410
2A3E, E1	0.1599	2B3E, E1	0.1615
2A1A, E2	0.1753	2B1A, E2	0.1662
2A3A, E2	0.1672	2B3A, E2	0.1760
2A1E, E2	0.1663	2B1E, E2	0.1450
2A3E, E2	0.1819	2B3E, E2	0.1734
2A1A, E3	0.1735	2B1A, E3	0.1676
2A3A, E3	0.1802	2B3A, E3	0.1554
2A1E, E3	0.1810	2B1E, E3	0.1569
2A3E, E3	0.1881	2B3E, E3	0.1584

In the remainder of this section we try to explain the effects of vanadium addition, coiling temperatures and cold rolling reductions on mechanical properties of dual phase steels, based on microstructure. Figure 5.5.8 compared the microstructures of 2A3A (vanadium free, 80%CR and 500°C CT) and 2B3A (with vanadium, 80% CR and 500°C CT). It is clear that the addition of V refined both of the ferrite grain size and martensite island size. The amount of MA in 2B3A (D1) is slightly larger than that in 2A3A (D1). As a result, with low CT and 80%CR very fine microstructures were obtained with the proper amount of MA, so the tensile strength reached 1019MPa for 2B3A (D1). Figures 5.5.9 and 5.5.10 compared the microstructures of dual phase steels with low and high coiling temperatures. It is frequently found that DPs with high coiling temperatures have coarser microstructures (coarser ferrite grain size and MA islands) than those with low coiling temperatures. Without the addition of vanadium, for 50%CR samples, higher tensile strengths were obtained for low coiling temperatures due to the finer microstructures, while with the addition of vanadium, the tensile strength of DPs with high coiling temperatures are higher, though they have coarser microstructures. This is due to the precipitation hardening of vanadium carbides at higher coiling temperatures, which will be discussed in detail later. The coiling effects of vanadium addition can be more easily observed when we compare the strength of the corresponding hot band steels, which will be discussed later. Figure 5.5.11 compared the

microstructures of 2A3A (vanadium free, low CT and 80%CR) and 2B3A (with vanadium, low CT and 80%CR), with E3 (supercool temperature 390°C) processing. The increase in tensile strength of 2B3A (E3) comes from the higher amount of MA and refinement of ferrite grain size due to the addition of vanadium. In the final structures with E3 processing, little tempered martensite can be found. While for E1 (supercool temperature 250°C), most hard phases are tempered martensite, and only less than 8%MA can be found in the final microstructures which can be seen from Figures 5.5.12-5.5.15. Figures 5.5.12 (low magnification) and 5.5.13 (high magnification) compared the microstructures of 2B1A (with vanadium, high CT and 80%CR) and 2B3A (with vanadium, low CT, 80%CR) with E1 processing. It is obvious that most of the martensite was tempered and low coiling temperature resulted in much finer microstructures compared with the corresponding steels with high coiling temperature. It appears that the increase in tensile strength is mainly from the finer microstructures. Figure 5.5.14 compared the microstructures of 2A3A (vanadium free, low CT and 80%CR) and 2B3A (with vanadium, low CT and 80%CR), with E1 processing. The addition of vanadium refined both of the ferrite grain size and MA islands, while the amount of MA or tempered martensite are similar in 2A3A (E1) and 2B3A (E1). Figure 5.5.15 compared the typical microstructures of DPs with 50% cold rolling reduction and 80% cold rolling reduction. Clearly increasing the cold rolling reduction can refine the final microstructure and even remove the severe MA or tempered martensite bands which appeared in dual phase steels with 50%CR and high coiling temperatures, e.g. Figure 5.5.15 (a). In order to explain the effects of cold rolling reductions on the final microstructures and properties, EBSD results were shown in Figure 5.5.16. Figures 5.5.16 (a) (b) and (c) show the inverse pole figures of hot band (2A1C), 50%CR (2A1E) and 80%CR (2A1A) initial steels with high Cr, Mo contents, V free, high coiling temperature (650°C). Figures 5.5.16 (d) (e) and (f) show the stored energy distribution mappings of the corresponding hot band (2A1C, average stored energy 0.90J/cm³), 50%CR (2A1E, average stored energy 2.86J/cm³) and 80%CR (2A1A, average stored energy 3.66J/cm³) steels respectively. It is found that with higher cold rolling reduction, the ferrite grains were more severely elongated and also the stored energy is much higher for 80%CR steels than that for 50%CR steels. The higher stored energy in the initial cold rolled sheets with 80% cold

rolling reduction is one important reason for the finer microstructure and stronger DPs with Gleeble full processing (D1 and E1, E2, E3). The effects of stored energy on microstructures will be further discussed in detail in Section 5.7.1.

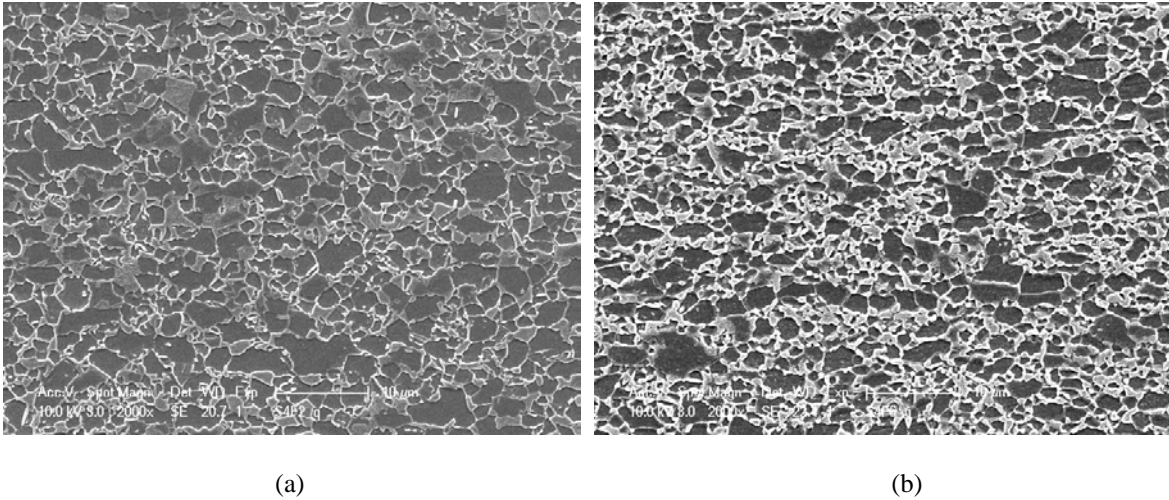


Figure 5.5.8. Comparison of SEM microstructures of dual phase steels with and without vanadium addition, (a) 2A3A (vanadium free), (b)2B3A (with vanadium addition). The heat treatment is D1 (standard galvanizing processing)

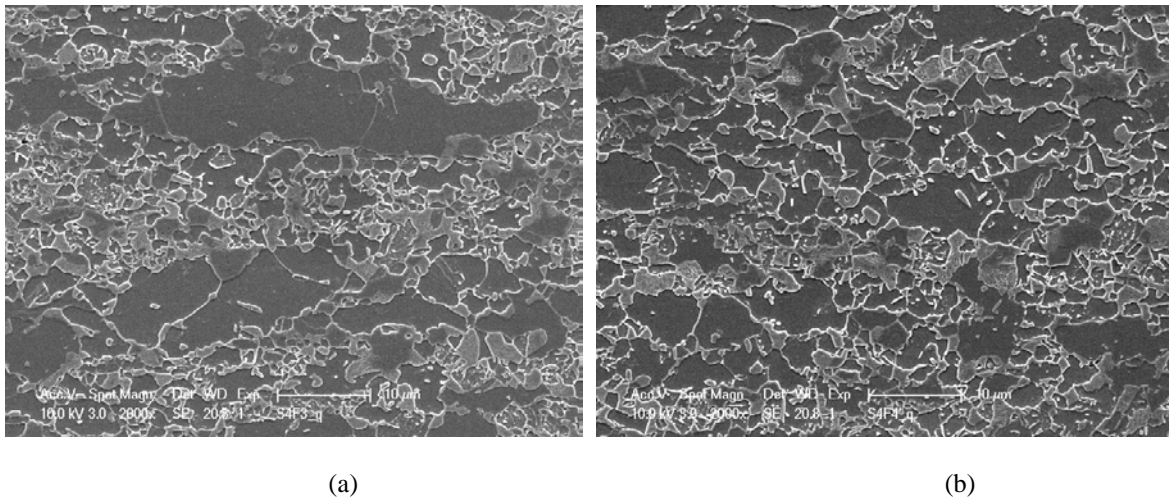
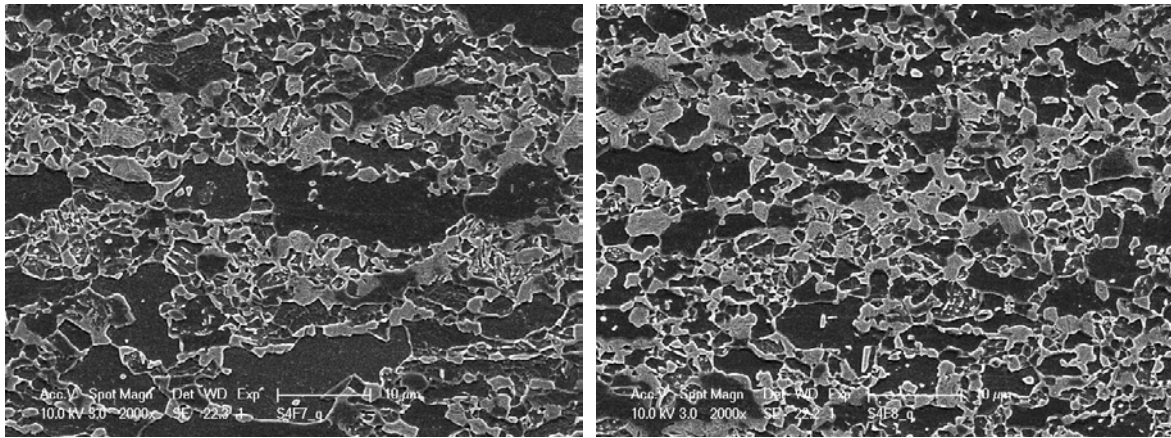


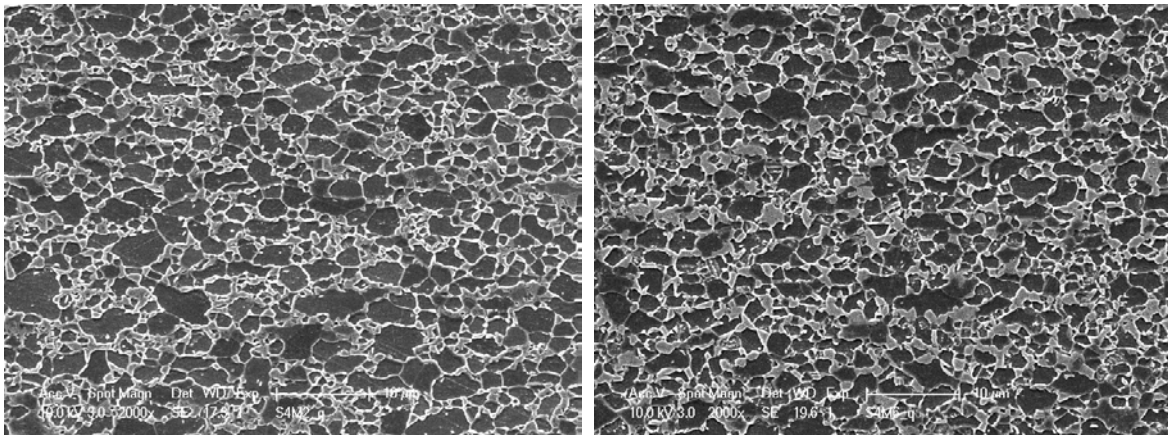
Figure 5.5.9. Comparison of SEM microstructures of dual phase steels with high and low coiling temperatures (CT), (a) 2A1E (CT=650°C, vanadium free), (b)2A3E (CT=500°C, vanadium free). The heat treatment is D1 (standard galvanizing processing)



(a)

(b)

Figure 5.5.10. Comparison of SEM microstructures of dual phase steels with high and low coiling temperatures (CT), (a) 2B1E (CT=650°C, with vanadium), (b) 2B3E (CT=500°C, with vanadium). The heat treatment is D1 (standard galvanizing processing)



(a)

(b)

Figure 5.5.11. Comparison of SEM microstructures of dual phase steels with and without vanadium addition, (a) 2A3A (vanadium free), (b) 2B3A (with vanadium addition). The heat treatment is E3 (supercool processing, supercool temperature 390°C)

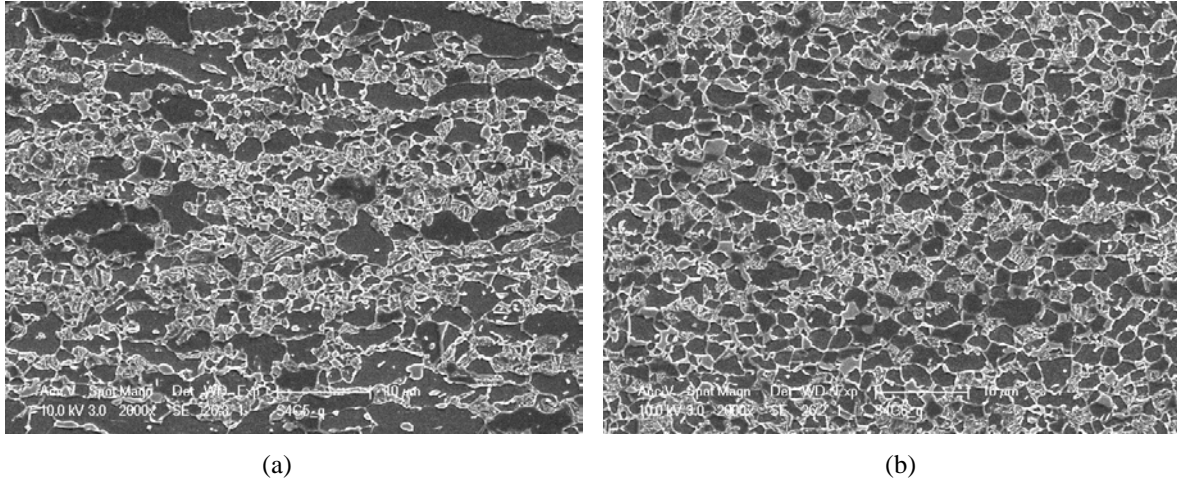


Figure 5.5.12. Comparison of SEM microstructures of dual phase steels with high and low coiling temperatures (CT), (a) 2B1A (CT=650°C, with vanadium addition, UTS=904MPa), (b)2B3A (CT=500°C, with vanadium addition, UTS=967MPa). The heat treatment is E1 (supercool processing, supercool temperature 250°C)

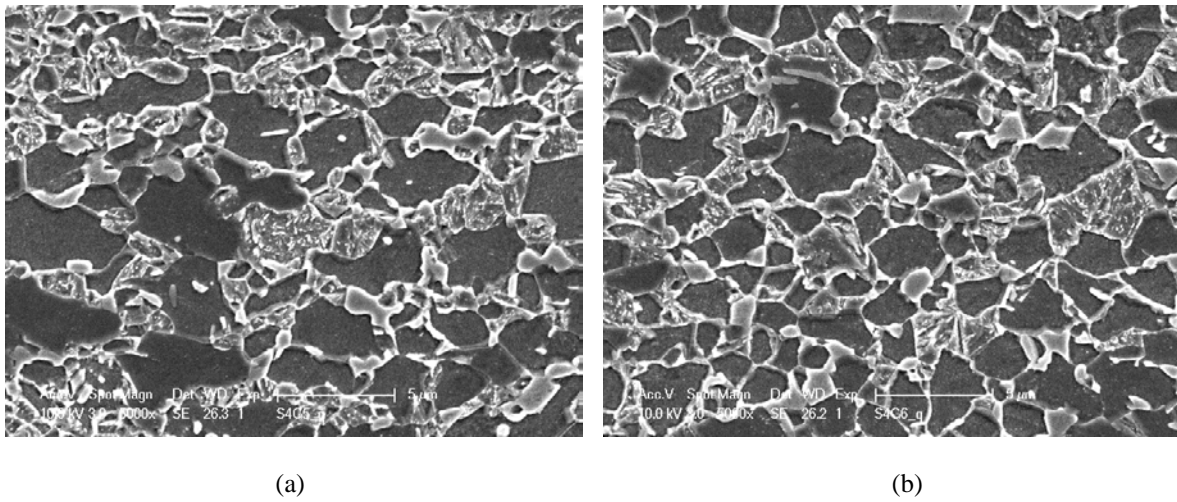
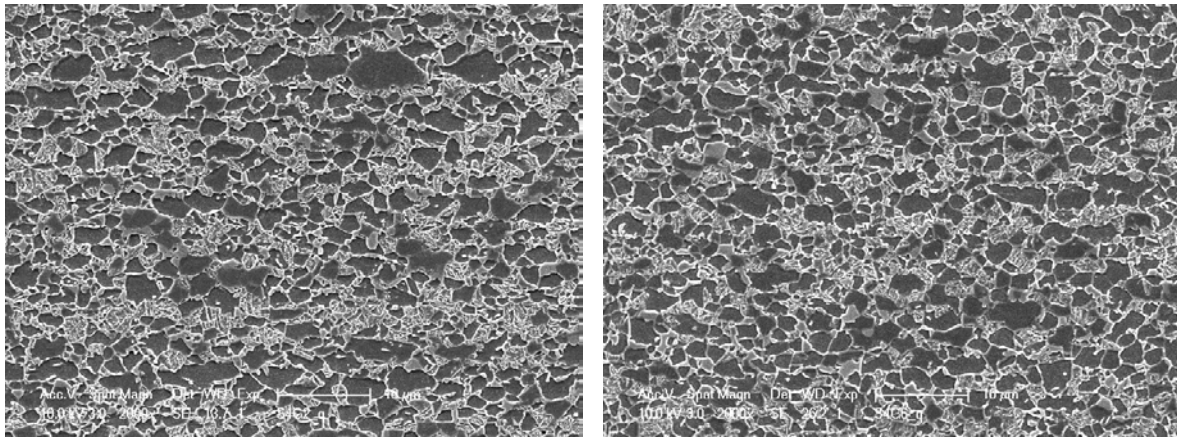


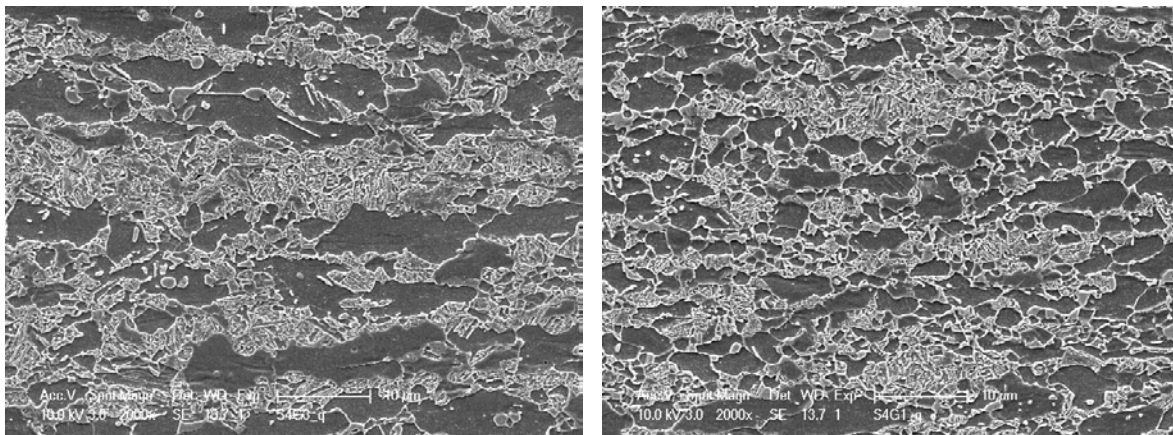
Figure 5.5.13. Comparison of SEM microstructures of dual phase steels with high and low coiling temperatures (CT), high magnification showing fresh MA and tempered martensite, (a) 2B1A (CT=650°C, with vanadium addition), (b)2B3A (CT=500°C, with vanadium addition). The heat treatment is E1 (supercool processing, supercool temperature 250°C)



(a)

(b)

Figure 5.5.14. Comparison of SEM microstructures of dual phase steels with and without vanadium addition, (a) 2A3A (vanadium free, UTS=919MPa), (b)2B3A (with vanadium addition, UTS=967MPa). The heat treatment is E1 (supercool processing, supercool temperature 250°C)



(a)

(b)

Figure 5.5.15. Comparison of SEM microstructures of dual phase steels with and with different cold rolling reductions, (a) 2A1E (50%CR, vanadium free, UTS=853MPa), (b)2A1A (80%CR, vanadium free, UTS=894MPa). The heat treatment is E1 (supercool processing, supercool temperature 250°C)

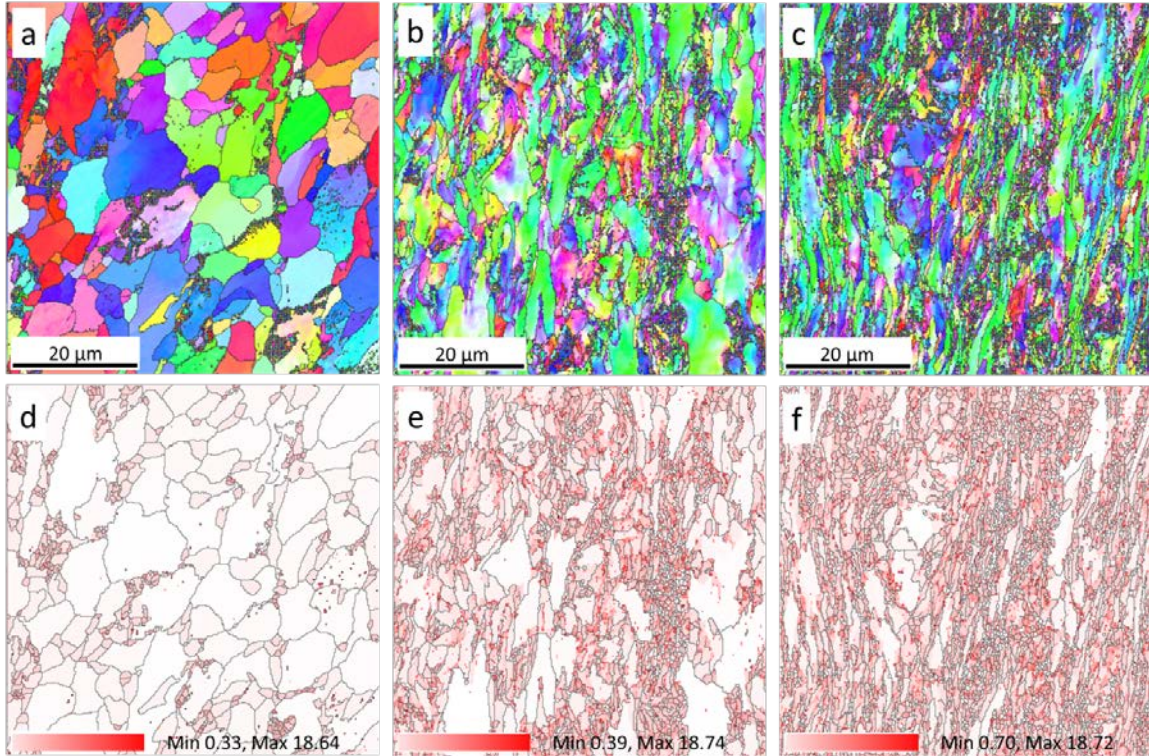


Figure 5.5.16. Steels with high Cr, Mo contents, vanadium free, high coiling temperature 650°C and different cold rolling reductions; inverse pole figures (IPF) (a) 2A1C, hot band, (b) 2A1E, 50%CR, and (c) 2A1A, 80%CR; stored energy distribution mappings (d) 2A1C, hot band, average SE 0.90J/cm³, (e) 2A1E, 50%CR, average SE 2.86J/cm³, and (f) 2A1A, 80%CR, average SE 3.66J/cm³. The horizontal direction is the normal direction and the vertical direction is the transverse direction.

More SEM microstructures of DPs with high Cr, Mo contents and different heat treatments (D1, E1-E3) can be found in Figures 5.5.17-5.5.22.

Figures 5.5.17 and 5.5.18 show the SEM microstructures of high alloyed DPs with E2 processing and high and low coiling temperatures, respectively. There are three different phases, i.e. ferrite, martensite and the third phase. From the high magnification micrographs in Figures 5.5.17 and 5.5.18, the third phase is mainly tempered martensite from the morphology (with the shape of martensite islands and tiny cementite white dots due to decomposition of martensite during tempering), though the existence of bainite still can't be excluded, which indicates that during cooling to and holding at 320°C, some of the intercritically formed austenite was transformed to martensite which will be tempered during holding at zinc pot temperature, and then during cooling to room temperature, the remaining austenite was

transformed to fresh martensite. It is helpful to compare 2B1A (E1, 250°C, 7% martensite, 32% tempered martensite) and 2B1A (E2, 320°C, 21% martensite, 6.3% tempered martensite) to understand the phase transformation during the full processing. When cooling to 250°C, most austenite was transformed to martensite, and so after tempering at 460°C, the previously formed martensite was replaced by tempered martensite, and after cooling to room temperature the remaining austenite was further transformed to fresh martensite or became retained austenite, while when cooling to 320°C, some of austenite (which is the amount of tempered martensite, about 6.3% measured from SEM micrographs) was transformed to martensite, which was tempered at zinc pot temperature and finally during cooling to room temperature, most of the austenite was transformed to fresh martensite (here about 21% martensite measured from SEM micrographs). The effects of vanadium on the refinement of microstructures are obvious when comparing 2A1A, E2 (Figure 5.5.17 (a)) and 2B1A, E2 (Figure 5.5.17 (e)), or 2A3E, E2 (Figure 5.5.18 (a)) and 2B3E, E2 (Figure 5.5.18 (e)).

When considering phase transformations at 390°C (E3 processing), it is clear that with high cold reduction and vanadium additions, the bainite transformation can be effectively suppressed during cooling to and holding at 390°C. Figure 5.5.20 shows SEM microstructures of high alloyed DPs with E3 processing. Bainite microstructures were clearly shown in Figure 5.5.20(a), (b) and (d), and for 2B1A (E3) most of the hard phase is martensite and only about 5% bainite presented in the final microstructure. Figure 5.5.22 also shows the microstructures of highly alloyed DPs with E3 processing and low coiling temperature, and again we found that without vanadium addition or low cold reduction (50%CR) (Figure 5.5.22 (a), (b) and(d)), more bainite can be found and for 2B3A (E3) little bainite (about 1.5%) can be found in Figure (5.5.22(c)). Figures 5.5.19 and 5.5.21 are the corresponding low magnification micrographs of Figures 5.5.20 and 5.5.22 respectively, which clearly show the effects of cold reduction on the grain refinement, i.e. with higher cold reduction (80%) the final microstructures are much finer and more homogeneous.

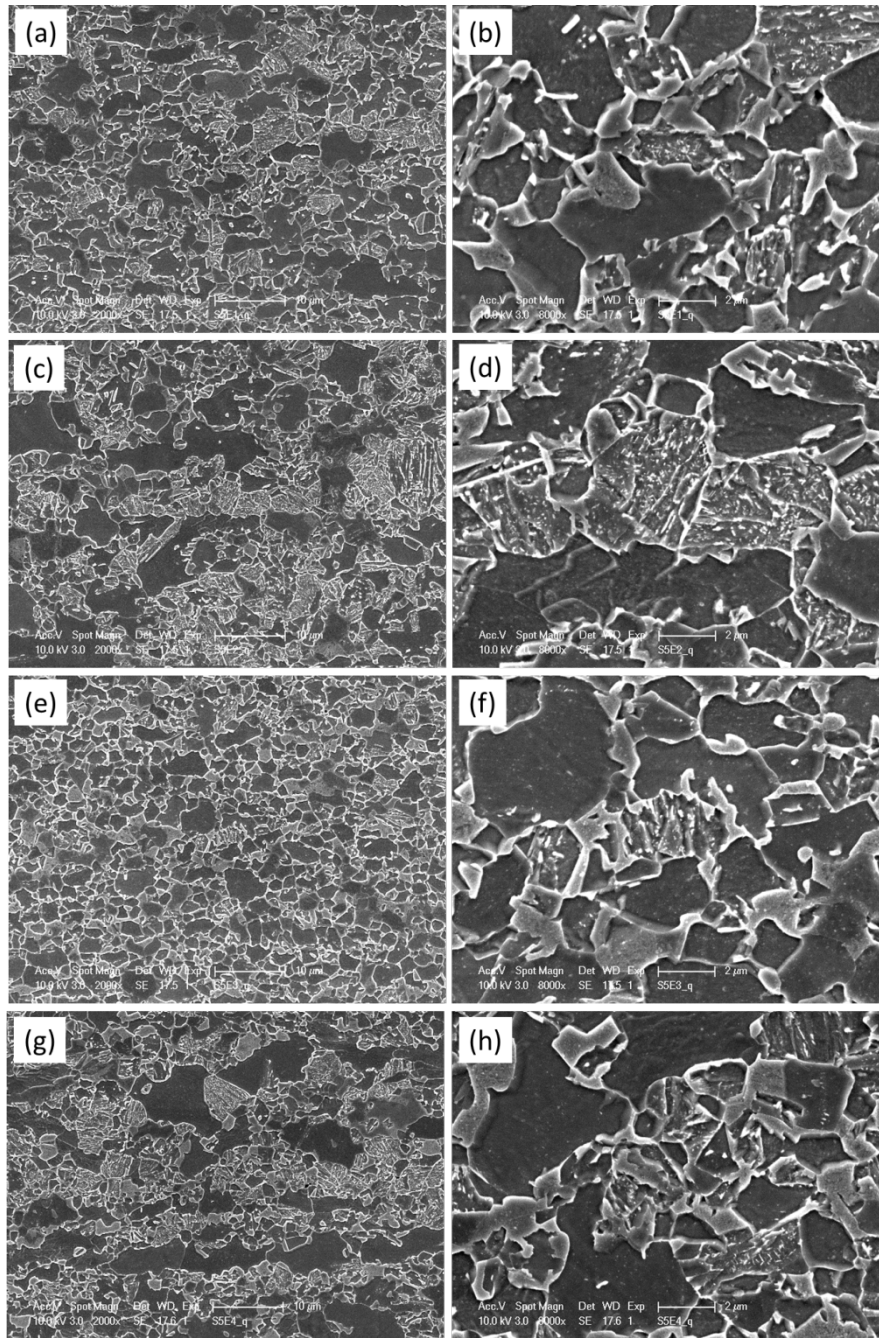


Figure 5.5.17. SEM microstructures of dual phase steels with high Cr, Mo contents, (a) (b) 2A1A, E2; (c) (d) 2A1E, E2; (e) (f) 2B1A, E2; (g) (h) 2B1E, E2.

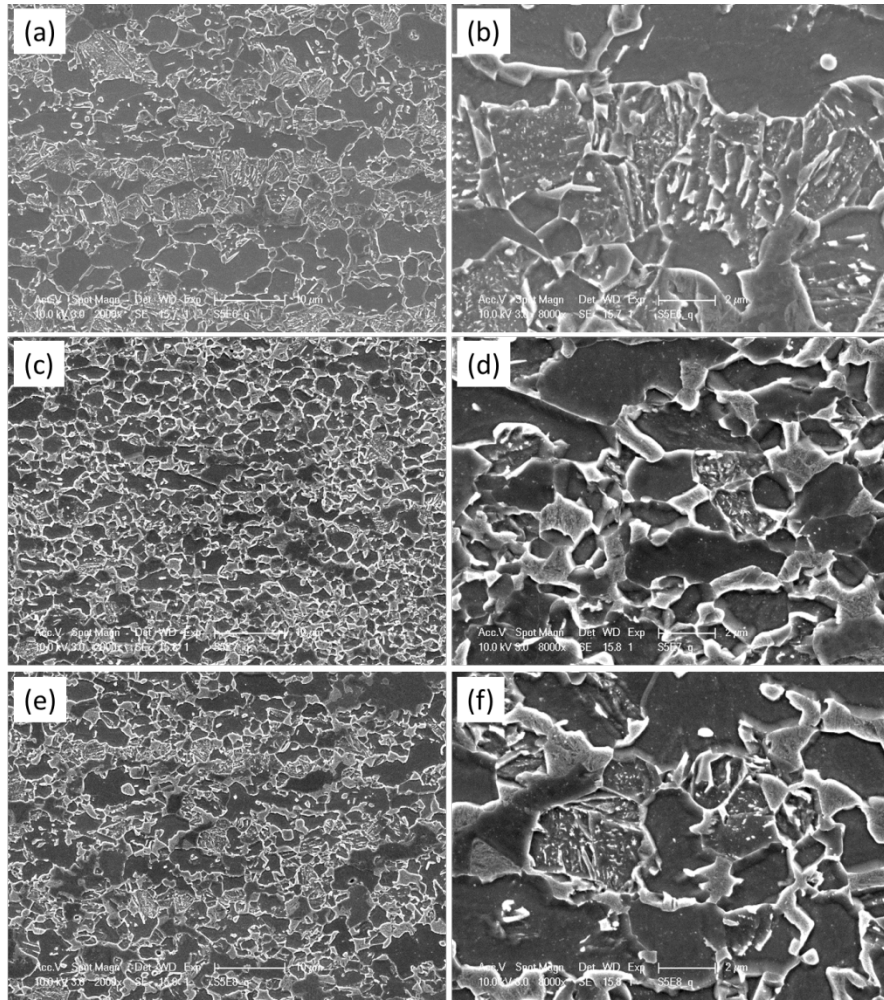


Figure 5.5.18. SEM microstructures of dual phase steels with high Cr, Mo contents, (a) (b) 2A3E, E2, (c) (d) 2B3A, E2, (e) (f) 2B3E, E2

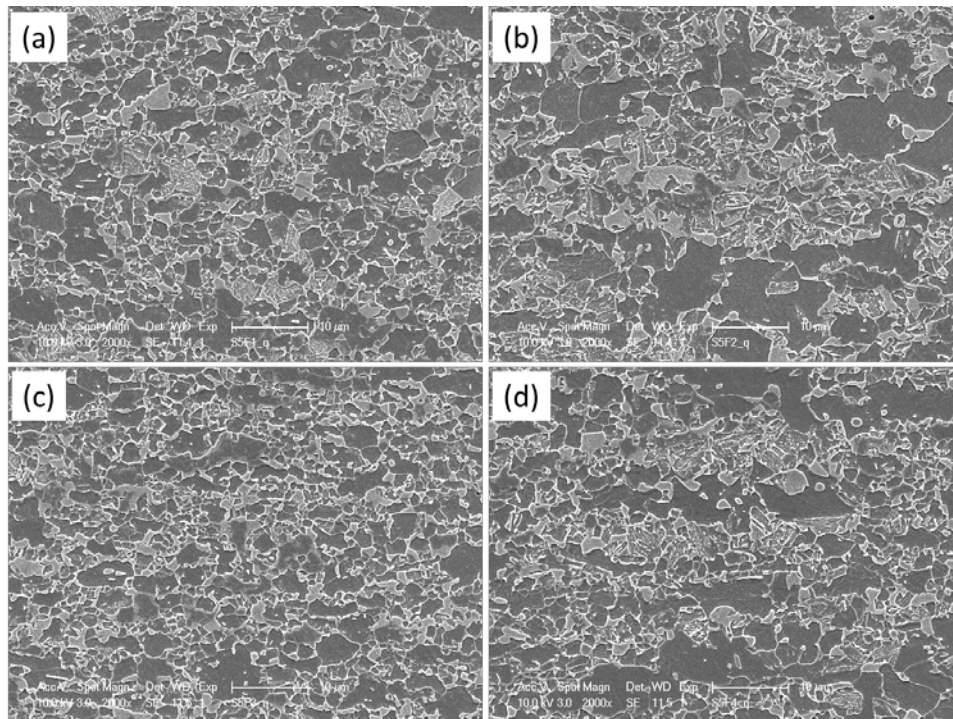


Figure 5.5.19. SEM microstructures of (a) 2A1A, E3 (b) 2A1E, E3 (c) 2B1A, E3 and (d) 2B1E, E3, Low magnification 2000x

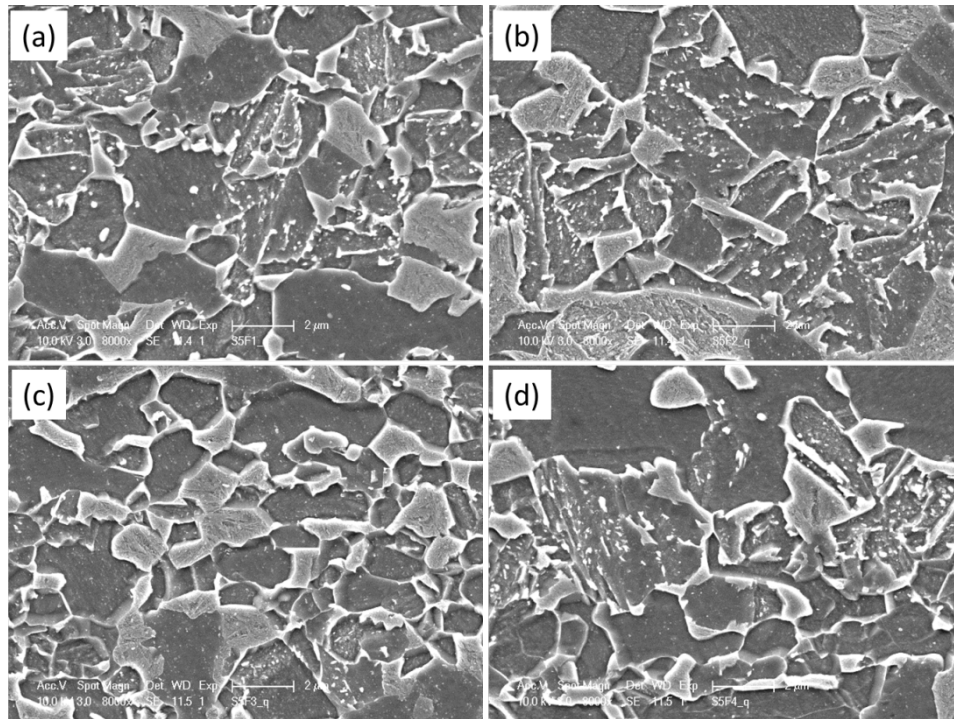


Figure 5.5.20. SEM microstructures of (a) 2A1A, E3 (b) 2A1E, E3 (c) 2B1A, E3 and (d) 2B1E, E3, High magnification 8000x

The volume fractions of martensite, tempered martensite and bainite of highly alloyed DPs are listed in Tables 5.5.8 to 5.5.9 and plotted in Figures 5.5.23 and 5.5.24 For D1 processing, the hard phase is martensite for 80%CR DPs and for 50%CR DPs, besides martensite some bainite can also be found, which indicates that intercritically formed coarse austenite is less stable than finer austenite grains and so some austenite was transformed to bainite during holding at the zinc pot temperature. It can be found that vanadium bearing DPs (D1) has a little more martensite than the corresponding DPs without vanadium additions and DPs with 80%CR possess more martensite than the corresponding DPs with 50%CR. More (about two times) bainite can be found in vanadium free steels when comparing 2A1E, 2A3E and 2B1E, 2B3E with D1 processing (Table 5.5.9), which indicates that austenite with vanadium is stronger and more stable. For E1 processing, the hard phase is mainly tempered martensite and some fresh martensite and retained austenite (discussed in Section 5.7.3) can also be found. The tempered martensite is the main

reason for the higher elongations and hole expansion ratios (discussed later) of DPs with supercooled E1 processing.

When comparing different processings (D1, E1-E3), DPs with D1 processing possess highest amount of martensite, and the amount of martensite decreased with decreasing supercool temperatures (from E3 to E1). The amount of tempered martensite increased with decreasing supercool temperature (i.e. the amount of TM is higher in DPs with E1 processing than that in DPs with E2 processing, while there is little TM in DPs with D1 and E3 processing), and DPs with E3 processing have highest amount of bainite among the four different processings.

Table 5.5.8. Volume fractions of martensite, bainite and tempered martensite in high alloyed DPs with 80% cold reduction.

Martensite	D1	E3	E2	E1
2A1A	25	8.5	14	5.5
2B1A	30	24	21	7
2A3A	28.5	14		7.5
2B3A	31.5	28	23	6
Bainite	D1	E3	E2	E1
2A1A	0	21	0	0
2B1A	0	5	0	0
2A3A	0	16		0
2B3A	0	1.5	0	0
TM	D1	E3	E2	E1
2A1A	0	0	17	27
2B1A	0	0	6.3	32
2A3A	0	0		29
2B3A	0	0	8.3	33

Table 5.5.9. Volume fractions of martensite, bainite and tempered martensite in high alloyed DPs with 50% cold reduction.

Martensite	D1	E3	E2	E1
2A1E	19	14	13	7
2B1E	22	14	14.3	4.5
2A3E	21	18	12	5
2B3E	32	19	21.5	5.5
Bainite	D1	E3	E2	E1
2A1E	14	22	0	0
2B1E	8	14	0	0
2A3E	9	9	0	0
2B3E	3	6	0	0
TM	D1	E3	E2	E1
2A1E	0	0	24.7	29
2B1E	0	0	19.3	38.5
2A3E	0	0	17.7	30.5
2B3E	0	0	13	36.5

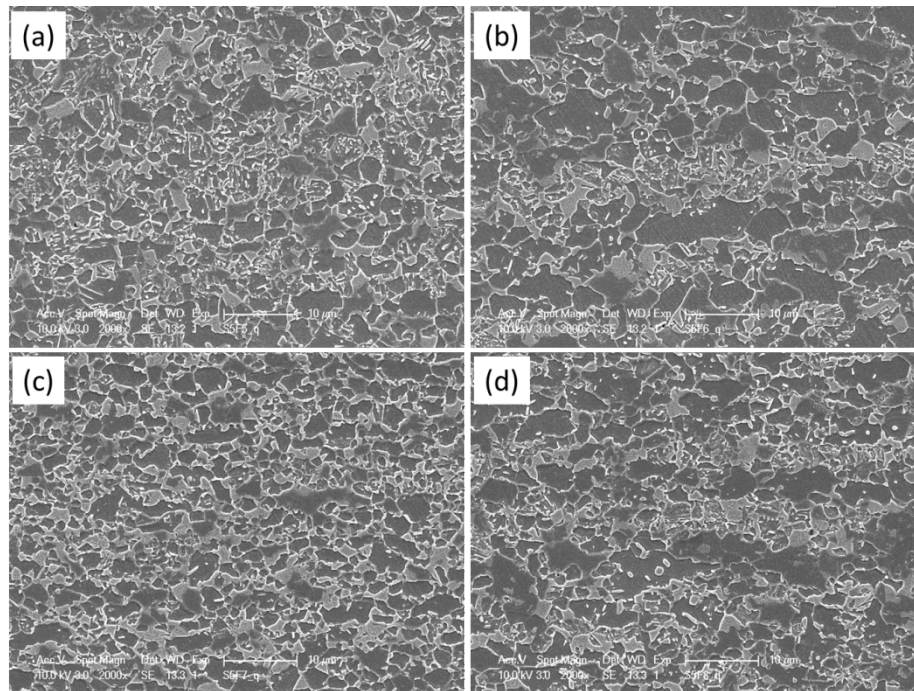


Figure 5.5.21. SEM microstructures of (a) 2A3A, E3 (b) 2A3E, E3 (c) 2B3A, E3 (d) 2B3E, E3, low magnification 2000x

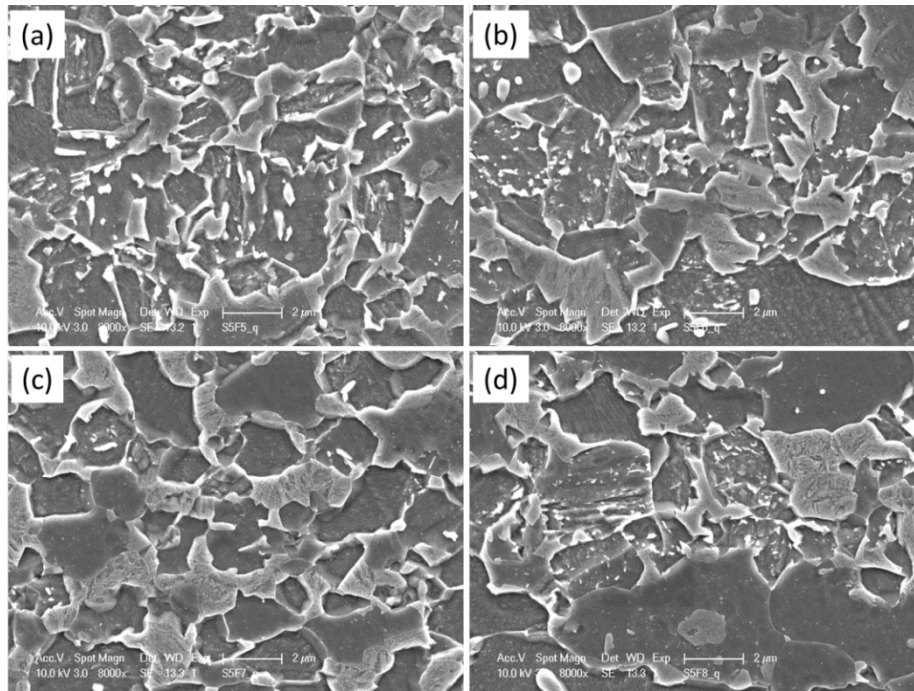


Figure 5.5.22. SEM microstructures of (a) 2A3A, E3 (b) 2A3E, E3 (c) 2B3A, E3 (d) 2B3E, E3, high magnification 8000x

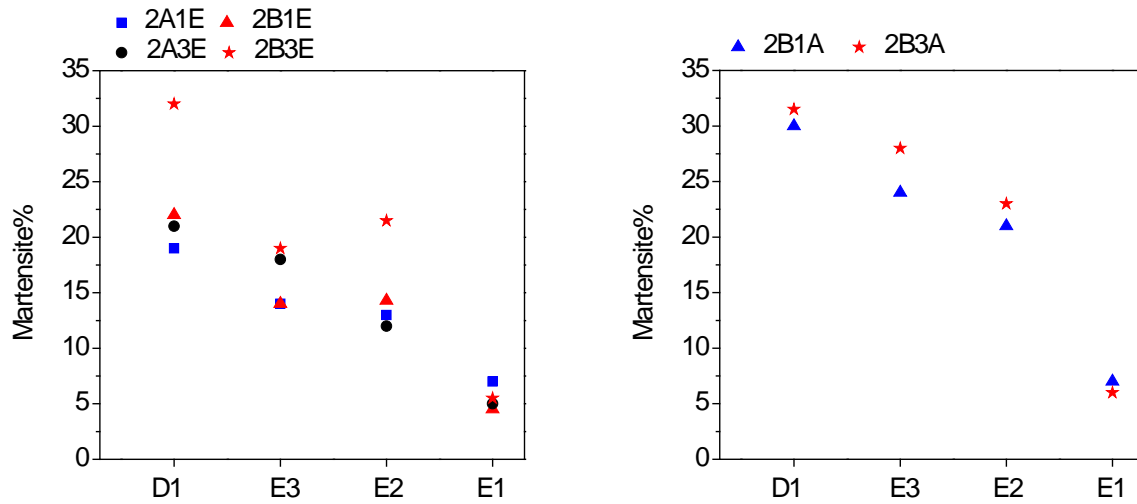


Figure 5.5.23. Volume fraction of martensite of high alloyed DP with different Gleeble full processings.

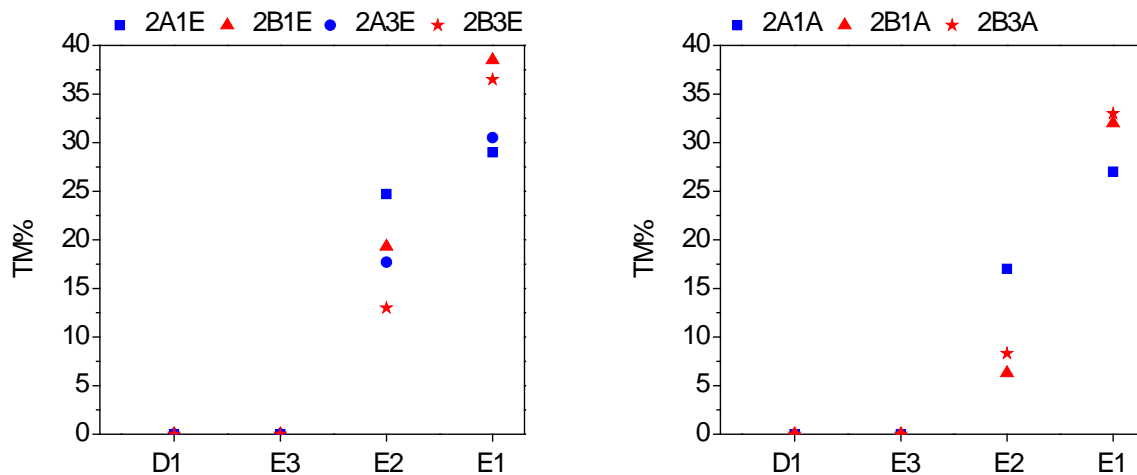


Figure 5.5.24. Volume fraction of tempered martensite (TM) of high alloyed DPs with different Gleeble full processings.

5.5.3 Effects of coiling temperature on the strength of vanadium bearing steels

The effects of coiling temperatures can be directly seen from the mechanical properties of hot band steels with different coiling temperatures. Figures 5.5.25 shows the microstructures of vanadium bearing and vanadium free hot band steels. As expected, higher coiling temperatures (650°C) result in ferrite and pearlite microstructures, while more bainite formed at lower coiling temperatures.

Figures 5.5.25(a)-(f) are the inverse pole figures of the microstructures of hot band steels with different coiling temperatures from EBSD scanning. Figures 5.5.25 (a) to (c) are IPFs of high alloyed vanadium free hot band steels with CT 650°C, 575°C and 500°C respectively, while 5.5.25 (d) to (f) are the corresponding hot band steels with vanadium addition. It can be observed that the microstructures or ferrite types are mainly determined by coiling temperatures, i.e. with high coiling temperature, polygonal ferrite formed while with low coiling temperatures acicular or bainitic ferrite dominates the microstructure which makes the steels much stronger at low coiling temperatures, as can be seen from the increase in both of tensile strength and yield strength listed in Table 5.5.11. The refinement of microstructure from vanadium addition is not obvious for these hot band steels.

The strengthening of the steels due to vanadium precipitation hardening is clear from the increase in both of tensile strength and yield strength listed in Table 5.5.11, as well as from Figure 5.5.26, which plots the VHN (300g) and CT data. The increase in strength for 650°C coiling temperature reached 94MPa (Δ UTS) and 110MPa (Δ YS), while the increase in strength for 500°C coiling temperature is only 5MPa for tensile strength or 9 MPa for yield strength, indicating the effective precipitation of vanadium carbides (or vanadium contained precipitates) at 650°C coiling temperature in polygonal ferrite, and the precipitation of vanadium carbides is sluggish and the effect of precipitation hardening is little at 500°C coiling temperature in acicular or bainitic ferrite. These effects of vanadium precipitation hardening on the strength of hot band steels seems to continue to affect the strength of cold rolled dual phase steels with full Gleeble processing.

Table 5.5.10. Mechanical properties (UTS, YS, TE and HE) of the dual phase steels with 50% cold rolling reduction, the Gleeble heat treatment E1: 790°C/60s, 15°C/s, 250°C/20s, 42°C/s, 460°C/30s, 10°C/s to RT

ID	YS (MPa)	UTS (MPa)	TE (%)	HE (%)
2A1E,E1	538	853	23.1	54.1
2A3E,E1	531	862	22.5	53.8
2B1E,E1	630	921	20.3	40.8
2B3E,E1	562	905	27.7	43.4

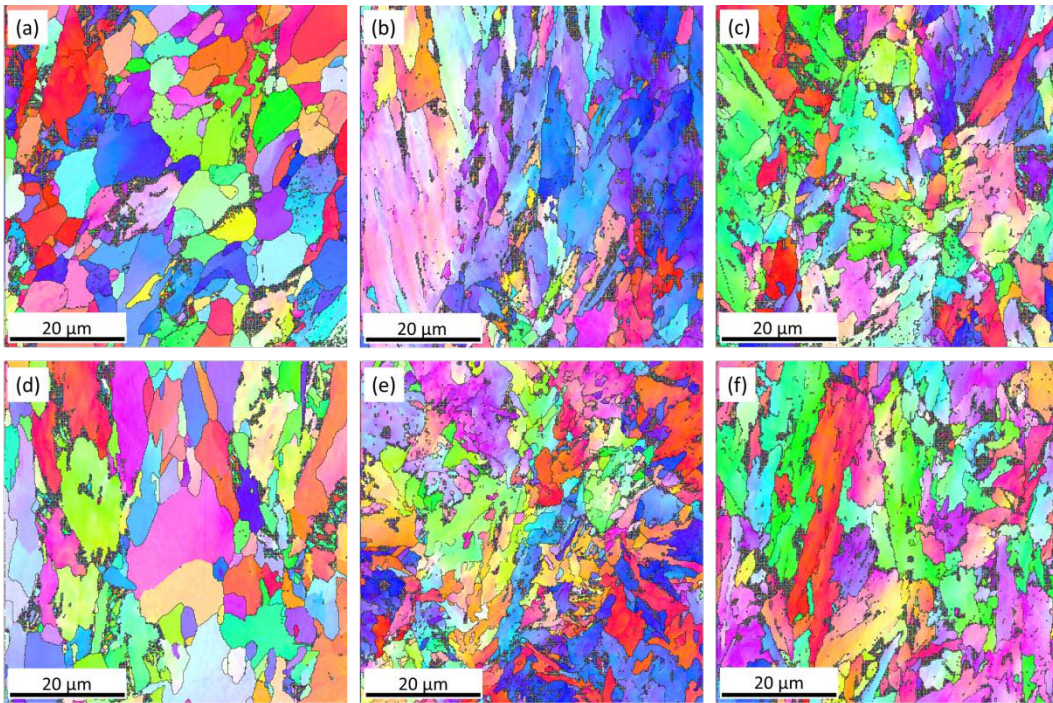


Figure 5.5.25. Inverse pole figures of hot band steels, vertical direction is RD, horizontal direction is ND. (a) 2A1C, (b) 2A2C, (c) 2A3C, (d) 2B1C, (e) 2B2C and (f) 2B3C. black lines are the high angle (15°) grain boundaries. The IPF triangle describes the relationship between colors and orientations.

Table 5.5.11. Tensile strength (UTS) of hot band steels with high Cr, Mo and with or without V addition. Each number is the average of two tests.

ID	UTS (MPa)	YS (MPa)	ID	UTS (MPa)	YS (MPa)	Δ UTS (MPa)	Δ YS (MPa)
2A1C	672	469	2B1C	766	579	94	110
2A2C	814	616	2B2C	884	638	70	22
2A3C	890	651	2B3C	895	660	5	9
2A4C	830	789	2B4C	963	921	133	132

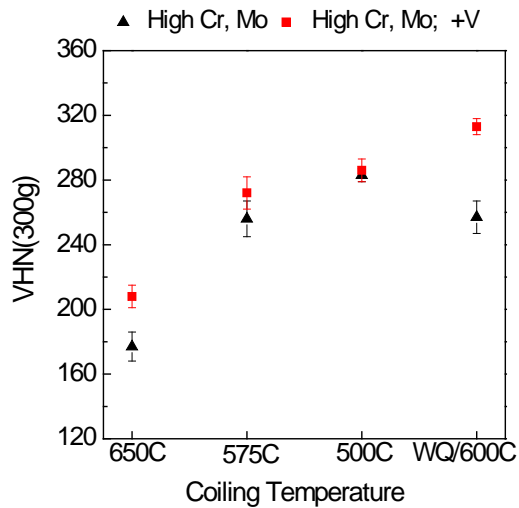


Figure 5.5.26. VHN of hot band steels with high Cr, Mo contents and different coiling temperatures

Table 5.5.10 listed the mechanical properties of high alloyed 50%CR steels with E1 processing. The mechanical properties (tensile strength, yield strength, total elongation and hole expansion ratios) of 2A1E-E1 and 2A3E-E1 are very close to each other, though the microstructure of 2A1E is coarser (leading to lower UTS) than that of 2A3E, which is due to the effect of coiling temperatures on the phase transformation as discussed earlier in this section. So other factors, e.g. the different amounts of hard phases (e.g. martensite, tempered martensite or retained austenite), shapes of phases, connections among phases, may explain the mechanical properties of 2A1E-E1 and 2A3E-E1. However the discussion of these factors will make the present topic (vanadium contribution) very complicated. When compare the mechanical properties of 2B1E-E1 and 2B3E-E1, the tensile strength of 2B1E-E1 is higher and the yield strength is even 68MPa higher than that of 2B3E-E1, though the microstructure of 2B1E-E1 is coarser than that of 2B3E-E1 which will be discussed further in the next section. The effect of vanadium is clearly revealed for steels with high coiling temperature when we compare the strength of vanadium free steels and vanadium bearing steels. These results indicate that the effective precipitation of vanadium carbides didn't dissolve during 790°C intercritical annealing and continue to strengthen the steels or resist the softening of ferrite and martensite during 460°C tempering for E1 (supercool processing with

supercool temperature 250°C) processing. Or possibly re-precipitation of vanadium carbides occurred during tempering at 460°C.

The hardness of individual phases was studied for condition E1 using nano-indentation hardness tests. About 150 nano-indentations were collected and the distribution of hardness was fitted using Gauss functions. The hardness of ferrite and tempered martensite (since the amount of fresh martensite is less than 8%, the possible existed small third peak of martensite was omitted) as the fitted peak positions of the lower and higher peaks were given in Figure 5.5.27.

As can be seen from Figure 5.5.27, 2B1E-E1 (ferrite 3.24GPa, TM 4.41GPa) has stronger ferrite and tempered martensite than 2B3E-E1 (ferrite 3.17GPa, TM 4.04GPa). The increase in the strength of ferrite is 0.4GPa and that of tempered martensite is 0.58GPa (2B1E-E1 vs. 2A1E-E1), while the increase in the strength of ferrite is only 0.21 GPa and that of tempered martensite is even -0.05GPa (2B3E-E1 vs. 2A3E-E1). These results further indicate that higher coiling temperature (650°C) can effectively reveal the vanadium precipitation hardening compared with lower coiling temperature 500°C.

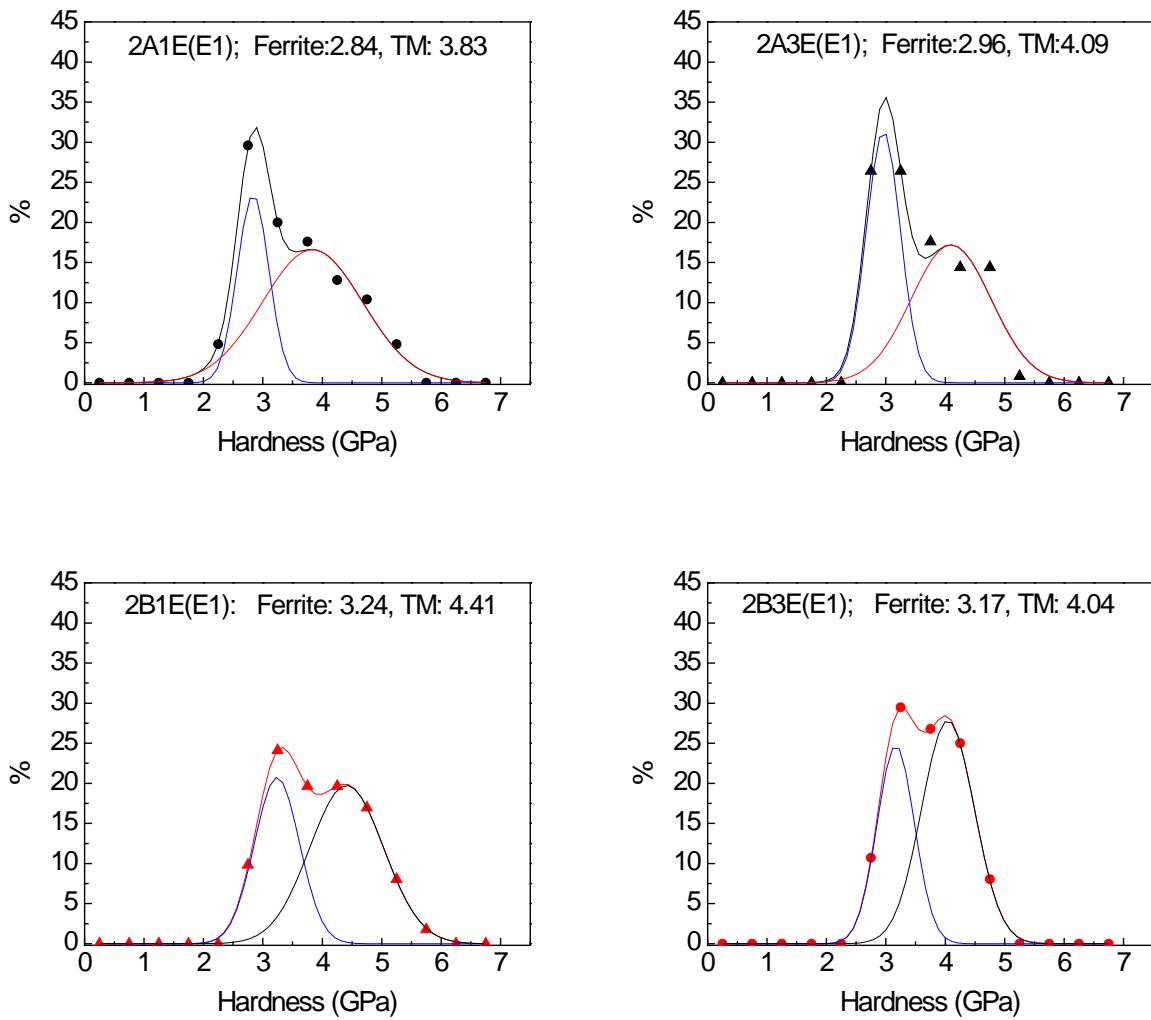


Figure 5.5.27. Nanohardness of ferrite and tempered martensite (TM) in 2A1E, 2A3E, 2B1E and 2B3E with E1 processing

5.5.4 Effects of coiling temperature and cold rolling reduction on ferrite grain size

Cold rolling followed by annealing is one way to effectively refine the microstructure. As can be seen from our results in this section, the ferrite grain size is mainly determined by cold reduction.

Figure 5.5.28 shows the ferrite grain size distributions of high alloyed 50%CR steels with E1 processing. The grain size distribution data were fitted with Gauss functions. For 2A1E-E1 and 2B1E-E1

with high coiling temperature 650°C of hot band steels, it is clear that two peaks fitted the data, exhibiting bimodal size distribution, as we can see some large ferrite grains in the microstructures, while for 2A3E-E1 and 2B3E-E1 with low coiling temperature 500°C of the corresponding HB steels, single peak fitted the data, indicating more uniform distribution of the ferrite grain size. The different size distributions for high and low coiling temperatures result from the effects of coiling temperature on the microstructures of hot band steels. Figure 5.5.30 contains the optical micrographs of hot band steels 2B1C (CT 650°C) and 2B3C (CT 500°C), showing that high coiling temperature results in polygonal ferrite while low coiling temperature leads to acicular or bainitic ferrite which is stronger than polygonal ferrite. The two types of ferrite possess different density of sub grain boundaries (acicular or bainitic ferrite formed at lower CT possesses higher density of sub grain boundaries or dislocations than polygonal ferrite formed at higher CT) and thus different stored energy. During subsequent cold rolling, more work was applied to reduce the thickness of 2B3C which is much stronger than 2B1C from our tensile test or hardness results, resulting in higher stored energy in 2B3E (CT 500°C, 50%CR) than in 2B1E (650°C, 50%CR) which will be further discussed later in Section 5.7. The higher density of sub-grain boundaries, dislocations, deformation bands or defect points in 2B3E or 2A3E results in higher density of ferrite recrystallization sites as well as austenite nucleation sites during intercritical annealing, leading to finer and more uniform distribution of ferrite grain size. On the other hand, the lower density of sub-grain boundaries in the deformed polygonal ferrite (or lower stored energy) as well as non-uniform internal stress state in 2B1E or 2A1E results in coarse microstructures and non-uniform distribution of ferrite grain size.

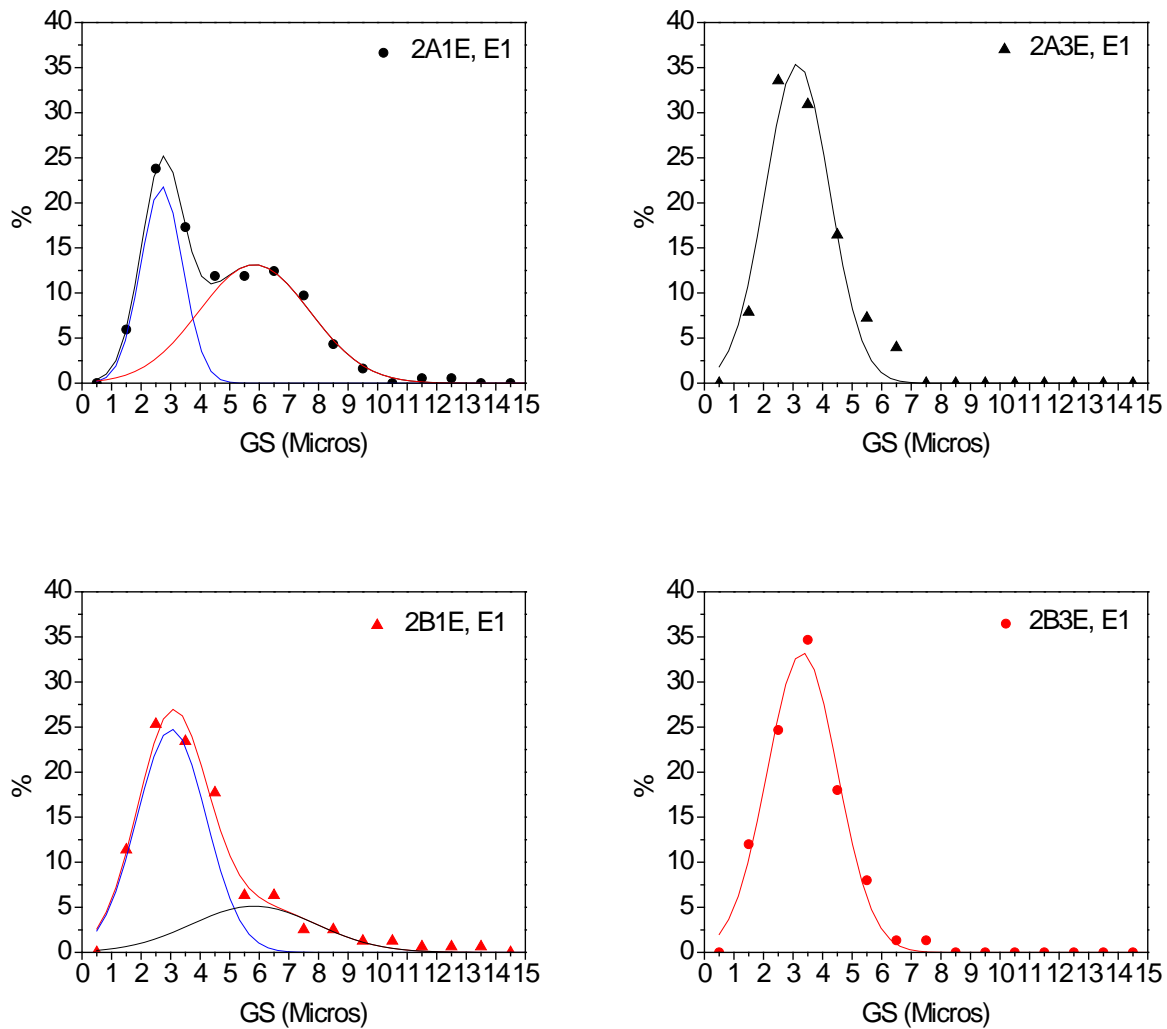


Figure 5.5.28. Distribution of ferrite grain size in 2A1E, 2A3E, 2B1E and 2B3E with E1 processing

Figure 5.5.29 shows the ferrite grain size distribution of high alloyed 80%CR steels with supercool E1 processing. Unlike the situation for 50%CR steels, single peak distribution was observed for all the four steels (2A1A-E1, 2B1A-E1, 2A3A-E1 and 2B3A-E1), indicating that more cold reductions can further refine the microstructure and eliminate abnormal large grains. When we compare 2A1A-E1 and 2A3A-E1 or 2B1A-E1 and 2B3A-E1, it can still be found that low coiling temperature results in more uniform and finer grain size (lower peak positions and peak width) than that for high coiling temperatures, which is still closely related to the stored energy of 2B1A (or 2A1A) and 2B3A (2A3A), as

we will see later for the discussion of stored energy of cold rolled sheets in Section 5.7. When we compare ferrite grains for 50%CR and 80%CR for low coiling temperature, the higher cold reduction results in finer and more uniform grain size distribution (lower peak positions and peak width, Figures 5.5.28(b), (d) and Figures 5.5.29(b) and (d)). Table 5.5.12 lists the average grain size and standard deviations of the eight steels with E1 processing, again we see that the grain size is smaller with 80%CR compared with the corresponding steels with 50%CR, and lowering coiling temperature can further refine grain size. Higher cold reduction and lower coiling temperature result in smaller standard deviation number, indicating more uniform grain size distribution. The effects of cold reduction on the refinement of grain size originates from the higher density of defects (dislocations, deformation bands, sub-grain boundaries and so on) in both of polygonal (high CT) and acicular ferrite (low CT) after 80%CR, resulting in higher stored energy of the initial steels and higher density of ferrite nucleation sites.

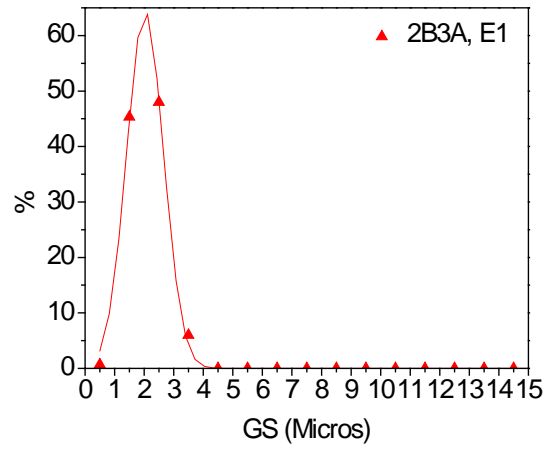
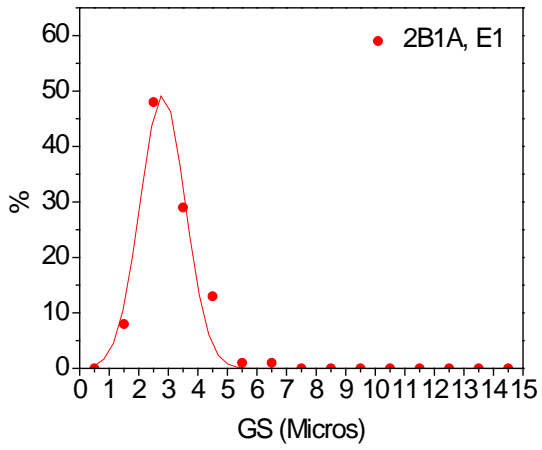
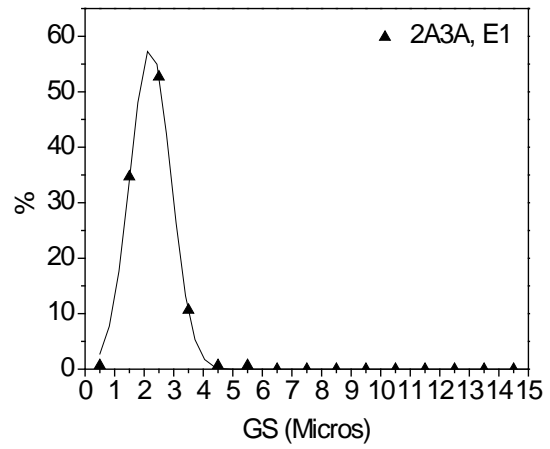
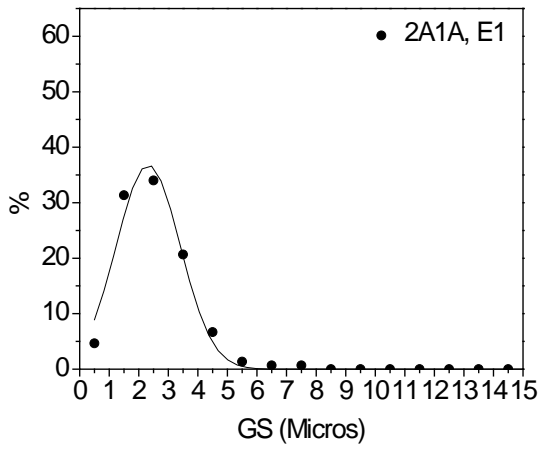


Figure 5.5.29. Distribution of ferrite grain size in 2A1A, 2A3A, 2B1A and 2B3A with E1 processing

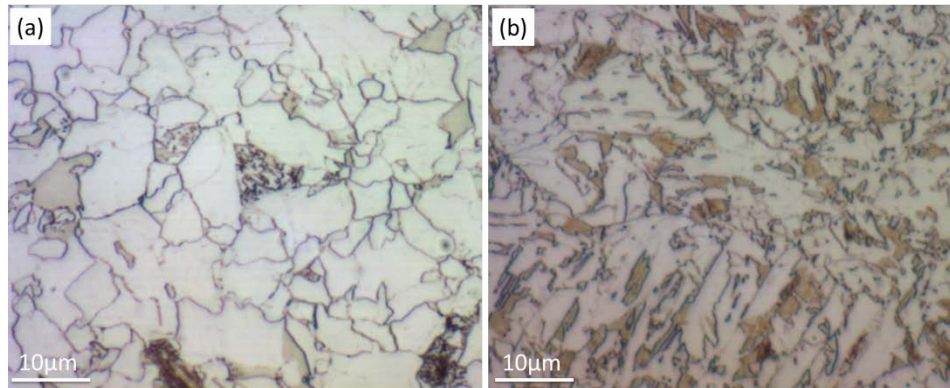


Figure 5.5.30. Optical microstructures of (a) 2B1C, HB steel with coiling temperature 650°C, VHN(300g) 210±3
(b) 2B3C, HB steel with coiling temperature 500°C, VHN (300g) 278±6, 2% Nital etched

Table 5.5.12. Ferrite grain size of high alloyed DPs with E1 processing.

Ferrite GS	Average GS (μm)	Ferrite GS	Average GS (μm)
2A1E, E1	4.66 ± 2.18	2A1A, E1	2.50 ± 1.10
2A3E, E1	3.42 ± 1.16	2A3A, E1	2.26 ± 0.68
2B1E, E1	4.08 ± 2.23	2B1A, E1	3.01 ± 0.94
2B3E, E1	3.40 ± 1.25	2B3A, E1	2.14 ± 0.56

5.5.5 Fracture study

In order to understand the fracture mechanism of DPs during tensile testing, the microstructures near the fracture surface were studied in this section. Figures 5.5.31 (a) and (b) show the SEM micrographs near the fracture surfaces of DP 2B1A and 2B3A with D1 processing respectively. As can be seen, both ferrite and martensite were elongated along tensile loading direction, and ferrite grains were much more severely elongated than martensite since ferrite is much softer than martensite. The crack nucleation sites or micro voids can be found between martensite islands, ferrite grain boundaries but the most preferential sites are the phase boundaries between ferrite and martensite which can be frequently found near the fracture surfaces, Figures 5.5.31 (a) and (b). Except finer martensite islands and ferrite grains, no significant difference can be observe for DP 2B1A (D1) and DP 2B3A (D1) from Figures 5.5.31 (a) and (b).

Figures 5.5.32 (a) and (b) are the SEM microstructures near tensile fracture surfaces of DP 2B1E and 2B3E with D1 processing respectively. Some similar fracture mechanisms can be found for DPs with

50%CR (Figure 5.5.32) and DPs with 80%CR (Figure 5.5.31), e.g. voids preferentially nucleated at ferrite martensite interphase boundaries, severely elongated ferrite which mainly contributed to the ductility of the dual phase steels.

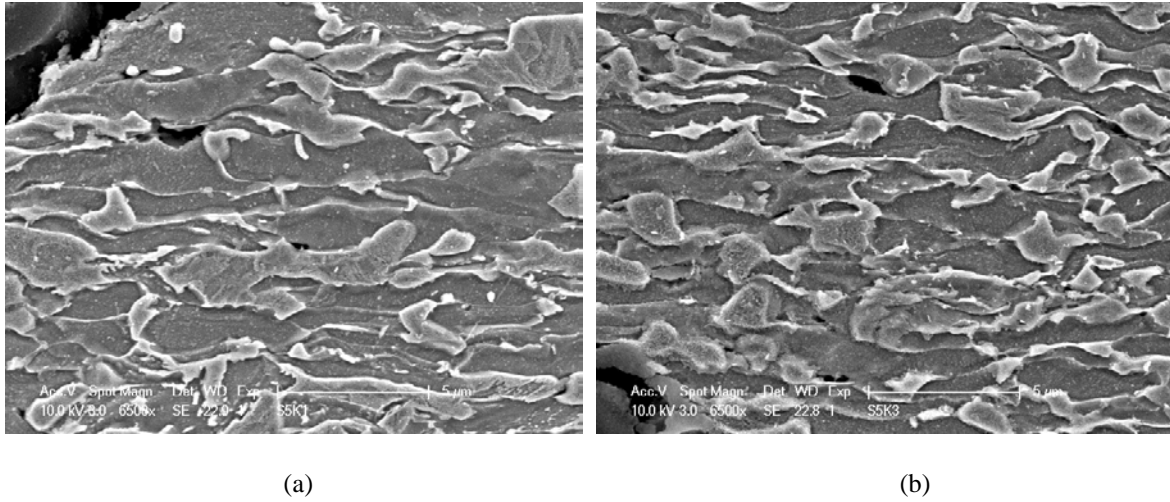


Figure 5.5.31. SEM micrographs near fracture surfaces, (a) 2B1A, D1, (b) 2B3A, D1

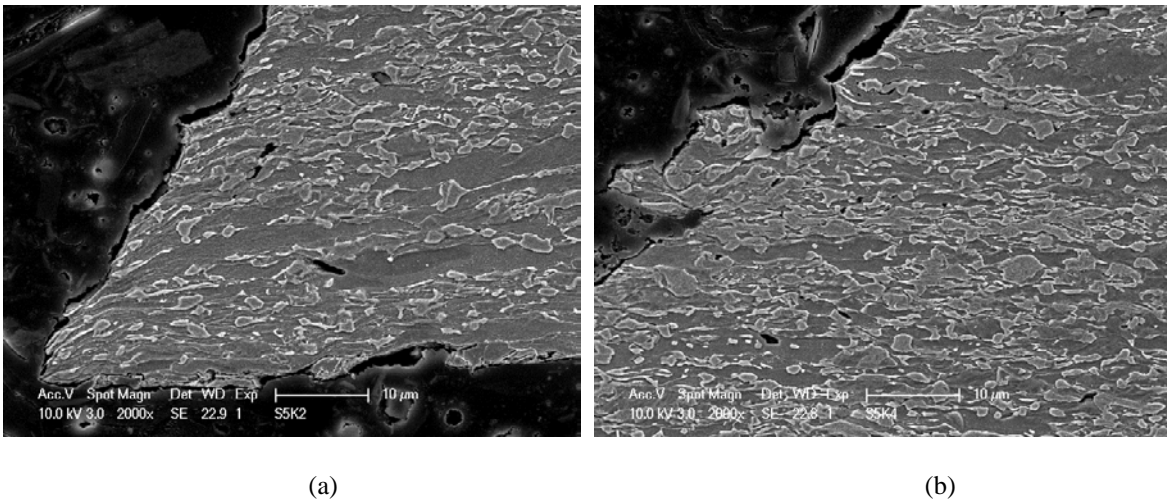


Figure 5.5.32. SEM micrographs near fracture surfaces, (a) 2B1E, D1, (b) 2B3E, D1

The fractography of the DPs will be discussed in this section. Figure 5.5.33 shows the scanning electron micrographs of fractured tensile specimens of 2B3A-D1, Figure 5.5.33 (a), and 2B3E-D1, Figure 5.5.33 (b). Figure 5.5.34 shows the SEM micrographs of fractured tensile specimens of 2B1E-E1

5.5.34(a) and 2B3E-E1 5.5.34(b). All these fractographs depict predominantly dimpled fracture for both standard galvanizing (D1) and supercool processing (E1), indicating good ductility of these steels.

It is observed that during tensile deformation of DP steels, ferrite will deform first and promote the nucleation of cracks either at ferrite-martensite interfaces or at precipitates in ferrite, then martensite deforms and cracks propagate either by cleavage or dimple mode. A. BAG[138] found that in the DP steels with carbide precipitates, the cracks take place predominately at the precipitates and the steel finally failed by cleavage fracture. For DP steels in the present study, there are few carbides (cementite) in the ferrite matrix due to the high enough IAT (790°C) at which all the cementite can be dissolved during intercritical annealing. Due to the absence of carbide precipitates, the cracks initiate mostly at the ferrite martensite interfaces, as can be seen in Figures 5.5.31 and 5.5.32, leading to the dimple failure mode, which is consistent with the observations made by A. BAG. From Figures 5.5.33 and 5.5.34, it can also be found that compared with 50%CR steels, the dimples in 80%CR steels are much finer and the distribution is more uniform, which can be explained from the microstructures. As discussed in the previous sections, the ferrite grain size and martensite island size are finer and uniform in 80%CR steels than those in 50%CR steels, and some large ferrite grains and martensite or tempered martensite packets existed in 50%CR DP steels with D1 or E1 processing. Fine martensite islands uniformly distributed in the fine ferrite matrix (e.g. Figure 5.5.8 (b) showing microstructures of 2B3A, D1), leading to high ferrite martensite interface area S_v and thus the number of crack initiation sites is large and the stress distribution is uniform. The further growth of the cracks depends on the local stress state, as a result, fine and uniform dimples formed in the 80%CR DP steels. On the other hand, large grain size and non-uniform microstructure lead to non-uniform stress state and large and non-uniform dimples in the 50%CR DP steels.

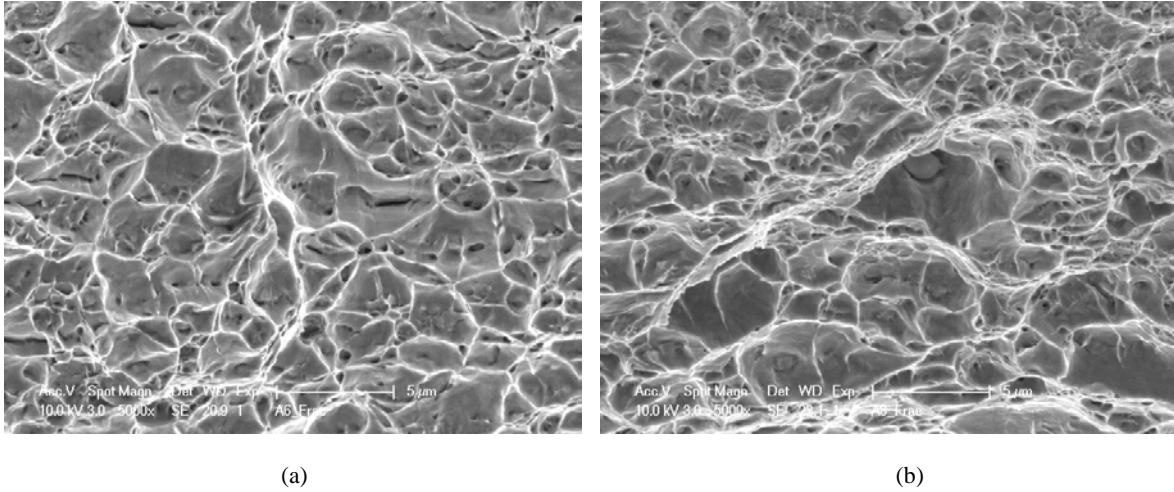


Figure 5.5.33. Fractured surfaces after tensile tests of (a) 2B3A, D1, (b) 2B3E, D1

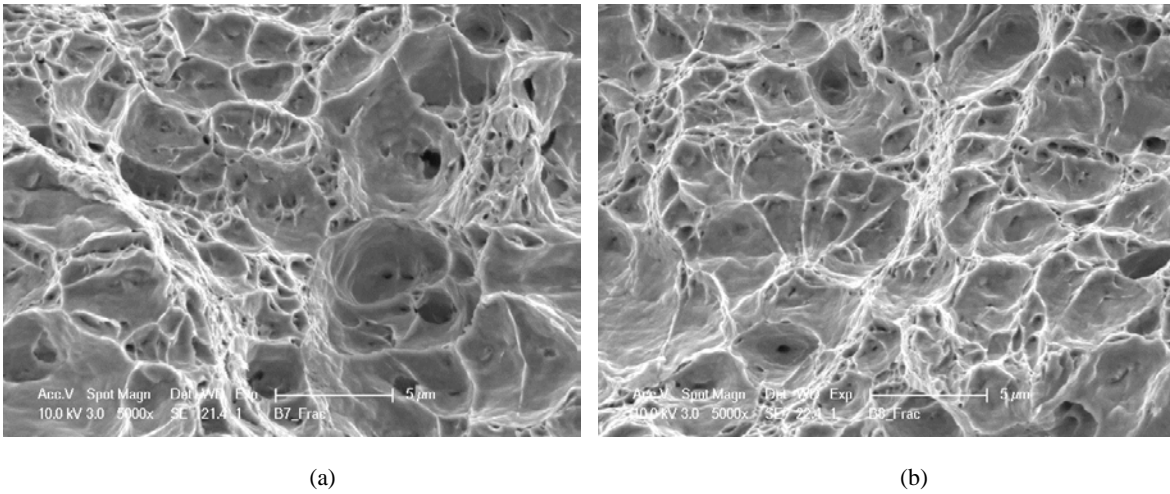


Figure 5.5.34. Fractured surfaces after tensile tests of (a) 2B1E, E1, (b) 2B3E, E1

5.5.6 Sheared edge formability-hole expansion ratio

Hole expansion ratio as one parameter to show the formability of sheared steel sheets is very important to the application of dual phases steels^[139-144] and was measured and discussed in this section. As seen in the earlier section, the vanadium bearing DPs possess the highest hole expansion ratios among the DPs with different micro alloying elements (V or Nb) and commercial 980 grade DPs, and also the DPs with supercool processing have much higher HER compared with standard galvanizing processing. In this

section we continue to study the hole expansion ratios of DPs with different processing and micro alloying conditions.

Figure 5.5.35 contains the low magnification optical images of expanded holes of steels 2A3A, 2B3A, 2A3E and 2B3E with D1 processing after hole expansion tests. The original diameter of the hole is 10mm punched at USS lab. The numbers in the images are the hole expansion ratios. Figures 5.5.35(c) and (f) are the images with higher magnification of the regions in the dashed squares in (b) and (e) respectively, showing the cracks completely through the thickness as an indicator of the failure of the tests. As can be seen, the main or first cracks through thickness prefer to occur near the rolling direction. The hole expansion ratios of vanadium bearing steels (2B3A-D1 and 2B3E-D1) are lower than the corresponding steels without vanadium addition, though these vanadium bearing steels have higher tensile strength. However the exhibited hole expansion ratios of these vanadium bearing steels are still comparable or even higher than the hole expansion ratios of the commercial DP780 steels.

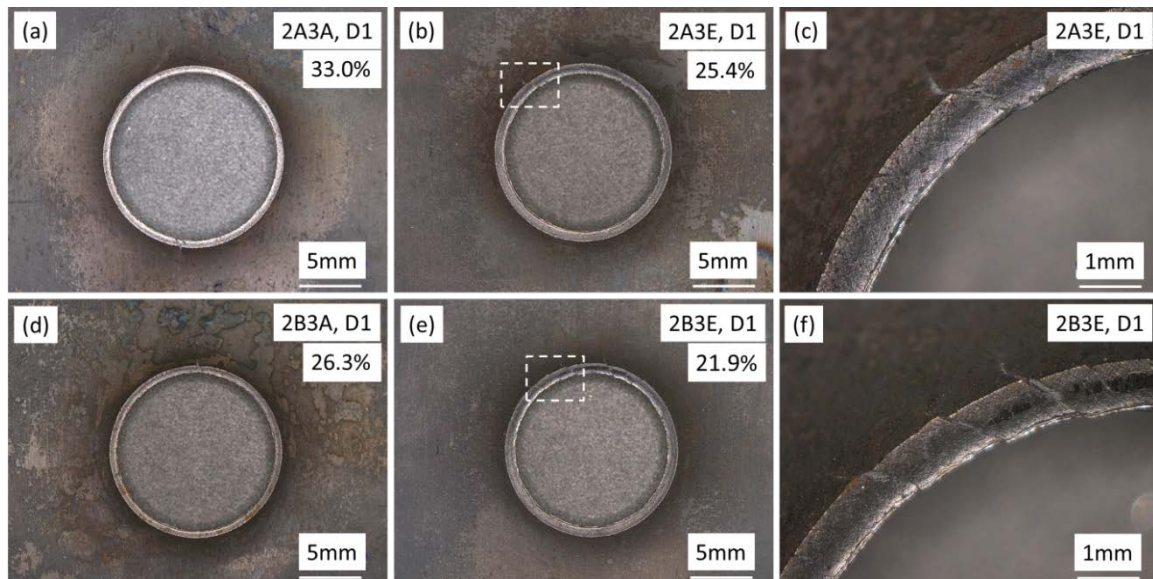


Figure 5.5.35. Hole expansion tested samples (a) 2A3A, D1, (b) 2A3E, D1, (c) high magnification image of the region inside the dashed square in (b), (d) 2B3A, D1, (e) 2B3E, D1, (f) high magnification image of the region inside the dashed square in (e). Vertical direction is the rolling direction

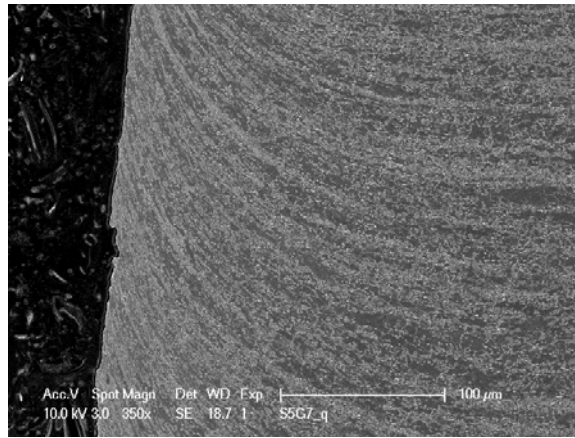
Figure 5.5.36 contains the micrographs of the regions near the punched hole before hole expansion tests of the steel 2B3E with D1 processing. From the low magnification image, the bending of

the ferrite and martensite bands can be clearly observed, while from higher magnification images Figures 5.5.36 (b) and (c), we can see severe deformation of ferrite and elongated martensite islands with larger size. The smaller martensite islands didn't deform as much as the larger ones. Figure 5.5.37 shows the microstructure of the regions near the sheared hole before hole expansion tests of the steel 2B3A with supercool E1 processing. Severe deformation of ferrite and tempered martensite can be found and the small martensite islands deformed only a little bit (after comparing the aspect ratios of martensite islands near sheared edge and those far away from the hole). Such microstructures near the hole are clearly different from the microstructures of the initial steels without punching, while as we know the tensile test properties are closely related to the initial non-deformed microstructure. It is supposed that the sheared edge formability or hole expansion ratios of the punched sheets can be related to the properties of the steel after it reached tensile strength, i.e. post uniform elongations and also reduction in area values, which will be discussed in Section 5.7.

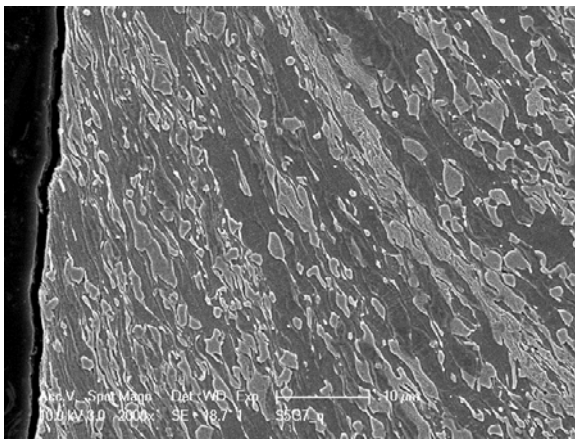
Figure 5.5.38 shows the low magnification images of the expanded holes after hole expansion tests of the steels 2A1E, 2B1E, 2A3E and 2B3E with supercool E1 processing and 50% cold reduction. Figures 5.5.38 (c) and (f) are the higher magnification images of the regions enclosed with the dashed white square in Figures 5.5.38(b) and (e) respectively, showing main cracks that completely crossed the thickness near the rolling direction. The numbers are the hole expansion ratios. As can be seen, the hole expansion ratios of vanadium bearing steels are lower (~10% lower) than those of the corresponding steels without vanadium addition. The hole expansion ratios of DPs with E1 processing are much (about 2 times) higher than those of DPs with D1 processing as expected. These hole expansion ratios are comparable or even higher than that of commercial DP590 steels. The higher hole expansion ratios of high alloyed DPs with E1 processing is due to the replacement of tempered martensite from harder martensite. The increase in the amount of softer (comparing with martensite) tempered martensite decreased the hardness difference between hard region and soft region (ferrite) and the dispersion of fine martensite islands also plays a role to further increase the strength of the matrix. Such combination of constituents can maintain higher strains or elongations of the microstructures before crack initiations or

failure both during punching and hole expansion test, leading to much higher hole expansion ratios and sheared edge formability.

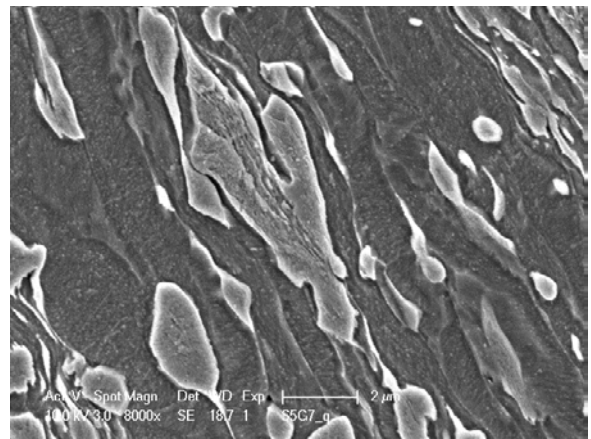
Figures 5.5.39 and 5.5.40 plotted the reduction in area values (RA%) and measured hole expansion ratios (HE%) with 4 different processings of the high alloyed DPs respectively. Table 5.5.13 listed the hole expansion ratios of high alloyed DPs with 80% cold reduction and 4 different processing. The hole expansion ratios decreased with increasing supercool temperatures and reached lowest for D1 processing, and the same trend can be observed for the relationship between reduction in area values and supercool processings. This good relationship between reduction in area values and hole expansion ratios confirmed previous argument that the sheared edge formability is closely related to the properties of the steels after reaching tensile strength. The decrease in HER with increase in supercool temperatures can be explained from the changes of microstructures as discussed before (Section 5.5.2).



(a)



(b)



(c)

Figure 5.5.36. Microstructures near the hole edge punched or sheared of 2B3E, D1, before hole expansion test, (a) 350x, (b) 2000x, and (c) 8000x

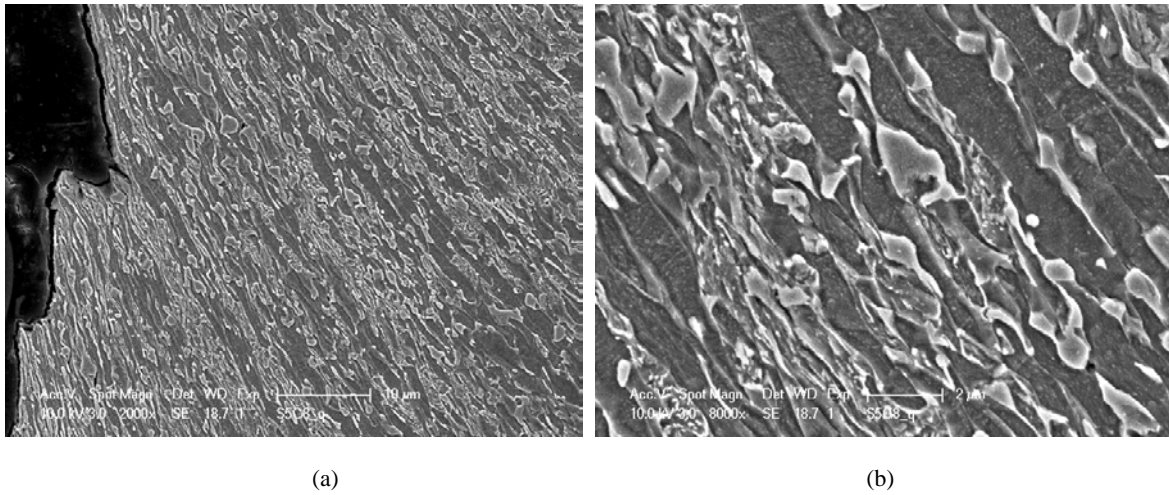


Figure 5.5.37. Microstructures near the hole edge punched or sheared of 2B3A, E1, before hole expansion test, (a) low magnification and (b) higher magnification

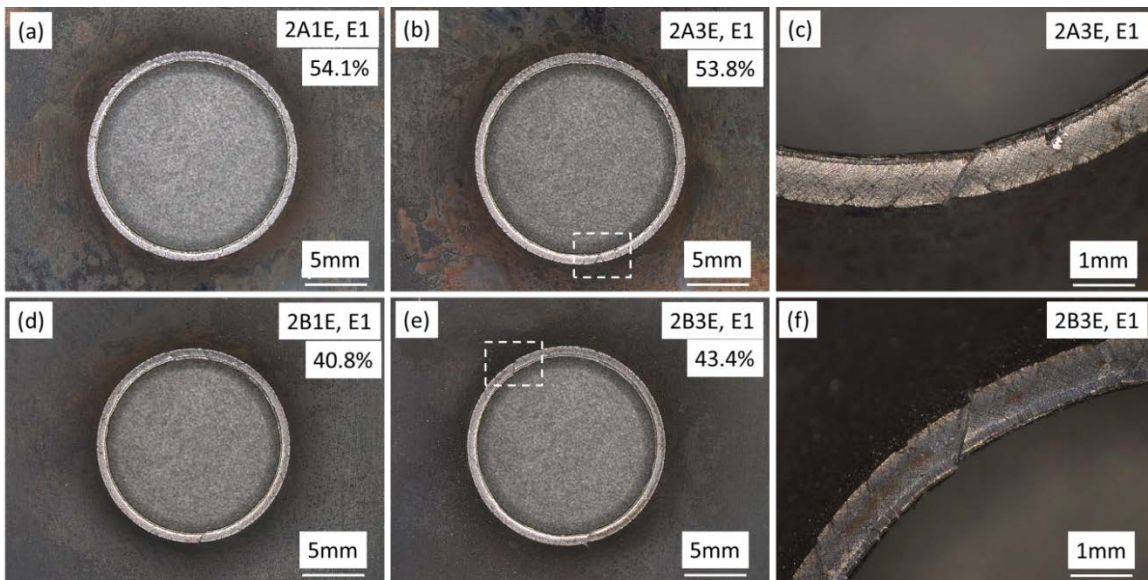


Figure 5.5.38. Hole expansion tested samples (a) 2A1E, E1, (b) 2A3E, E1, (c) high magnification image of the region inside the dashed square in (b), (d) 2B1E, E1, (e) 2B3E, E1, (f) high magnification image of the region inside the dashed square in (e). Vertical direction is the rolling direction

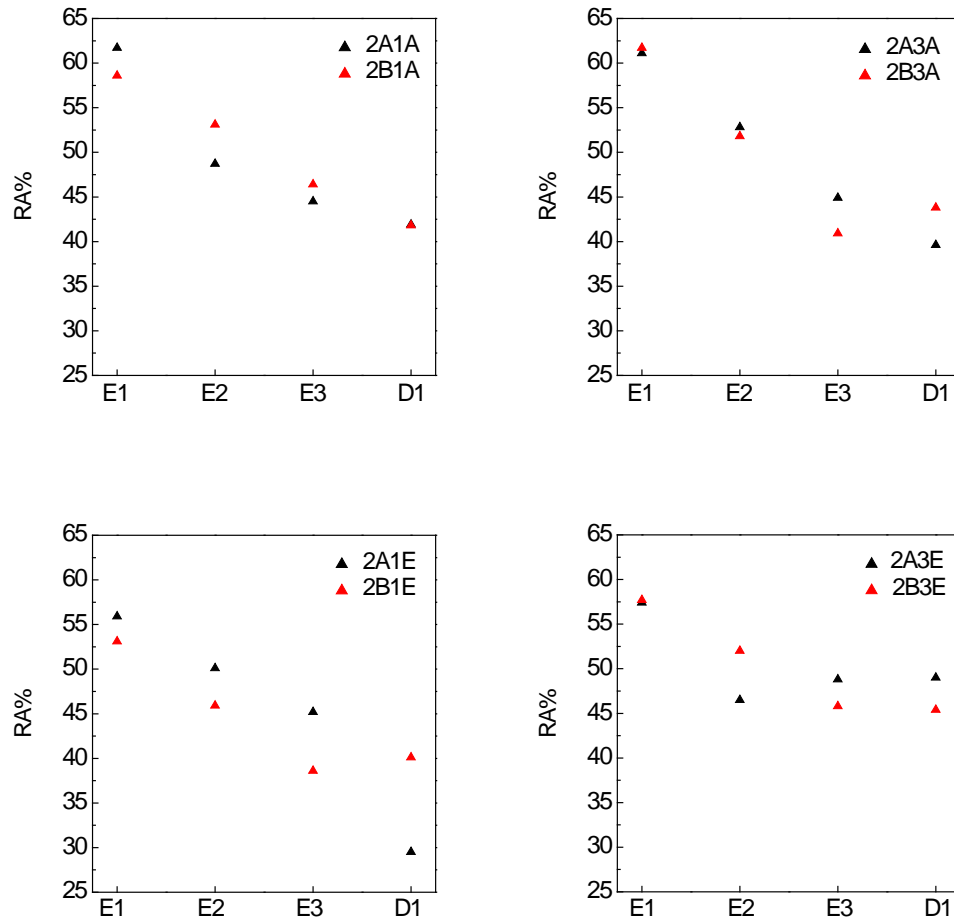


Figure 5.5.39. Reduction in area (%RA) of dual phase steels with standard galvanizing (D1) and supercool processing (E1, E2 and E3).

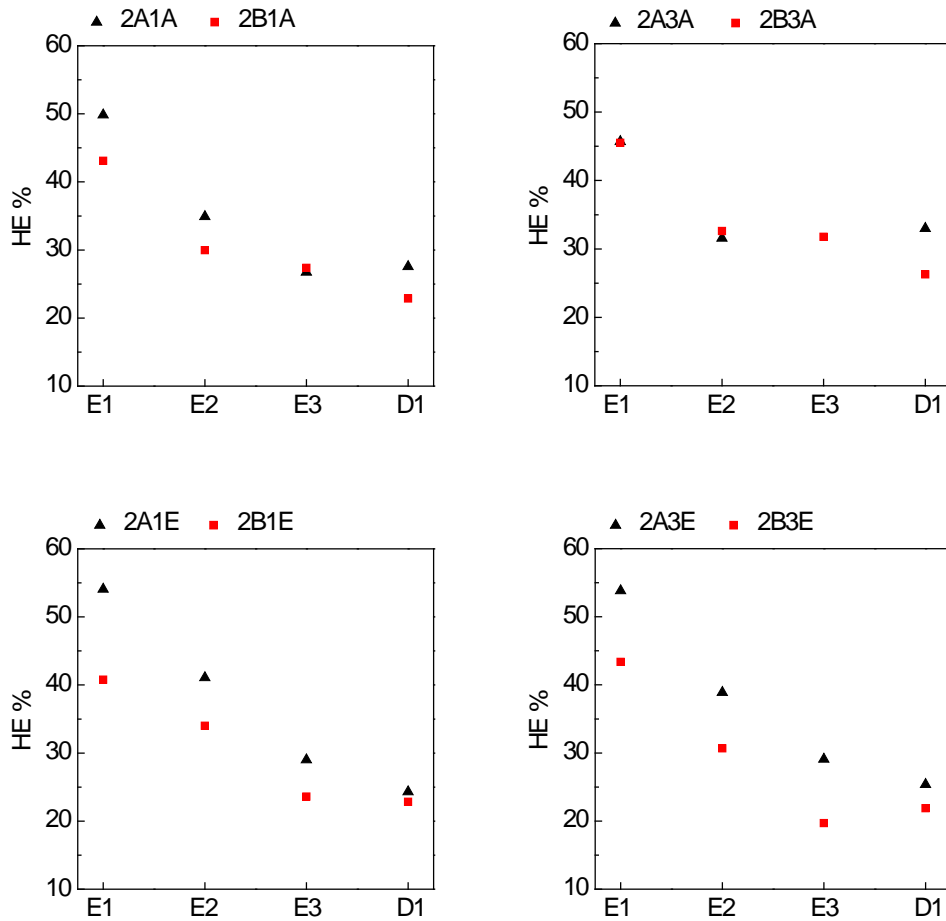


Figure 5.5.40. Hole expansion ratios (HE%) of dual phase steels with standard galvanizing (D1) and supercool processing (E1, E2 and E3).

Table 5.5.13. Measured hole expansion ratios (HER).

ID (V = 0)	HER%	ID (V= 0.06)	HER%
2A1A,E1	49.83	2B1A,E1	43.10
2A1A,E2	34.90	2B1A,E2	29.97
2A1A,E3	26.73	2B1A,E3	27.37
2A1A,D1	27.57	2B1A,D1	22.87
2A3A,E1	45.70	2B3A,E1	45.50
2A3A,E2	31.57	2B3A,E2	32.60
2A3A,E3	51.87	2B3A,E3	31.77
2A3A,D1	33.00	2B3A,D1	26.27

*The HER% of 2A3A, E3 may need to be retested.

Though with the same processing, the vanadium bearing DPs have lower hole expansion ratios than the vanadium free steels, the DPs with vanadium additions possess higher strength. In the remaining

of this section, the advantages from vanadium addition for the improvement of sheared-edge formability at the same strength levels will be emphasized.

Table 5.5.14 summarized the hole expansion ratios of vanadium free and vanadium bearing DPs at the same strength levels (~900MPa, ~920MPa and ~960MPa) and Figure 5.5.41 plotted these data in 3D form. We can clearly see the benefits from the addition of vanadium, i.e. the hole expansion ratios of vanadium bearing DPs are (>10%) higher than those of vanadium free DPs at the same UTS levels.

Figure 5.5.42 (a) plotted the UTS-HE data points of high alloyed DPs with and without vanadium additions, and in order to clearly see the effects of vanadium, Figure 5.5.42 (b) plotted the averaged UTS values at three different hole expansion levels, i.e. 20-30%, 30-40% and 40-50% intervals. It can be clearly observed that the data points of vanadium bearing DPs located on the right of the data points of vanadium free DPs, which indicates that the DPs with vanadium additions are stronger than the vanadium free DPs at the same hole expansion levels.

These results indicate that through changing the microstructures (e.g. change martensite to tempered martensite) the hole expansion ratio can be increased, but at the same time, we sacrificed the UTS. Without vanadium addition, though the hole expansion ratios reached up to about 50% after replacing M to TM, but the strength dropped below 900MPa, on the other hand, with the addition of vanadium, high strength (>900MPa) and high hole expansion ratios (>40%) can be obtained through changing M to TM using supercool E1 processing.

Table 5.5.14. Comparison of hole expansion ratios of vanadium free DPs and vanadium bearing DPs at the same UTS level, TE were converted to 2 inch specimens

ID (V free)	HE%	UTS (MPa)	TE(%)	ID (V bearing)	HE%	UTS (MPa)	TE (%)
2A1A, E2	34.90	909.4	18.0	2B1A, E1	43.10	903.9	18.3
2A1A, E3	26.73	907.4	16.6	2B3E, E1	43.37	904.9	28.4
2A3E, D1	25.37	906.6	12.6				
2A1A, D1	27.57	968.7	14.2	2B3A, E1	45.50	967.2	16.7
2A3A, D1	33.00	944.8	16.7				
2A3A, E1	45.70	919.2	21.4	2B1E, E1	40.77	921.4	20.9
2A3A, E2	31.57	946.7	16.8				

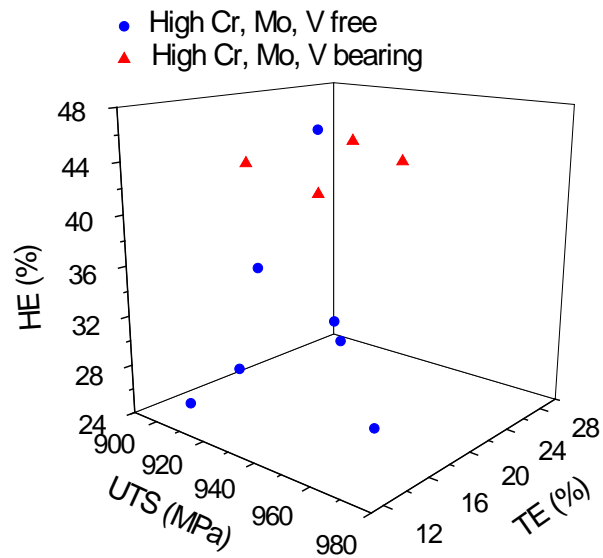


Figure 5.5.41. The data points were in Table 5.5.14 were plotted in 3D form.

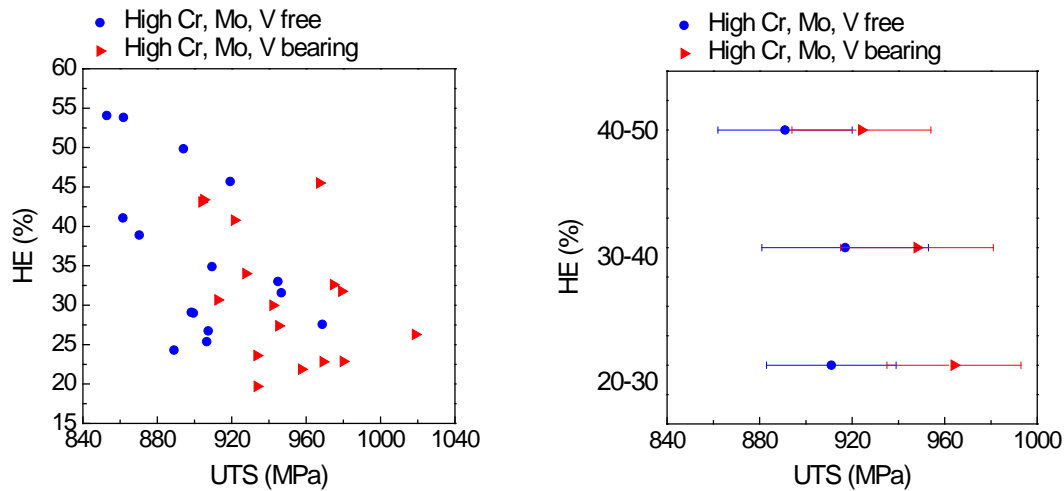


Figure 5.5.42. (a) data points (UTS-HE) of high alloyed DPs, (b) averaged UTS values at three hole expansion ratio levels, 20-30%, 30-40% and 40-50%.

5.6 EFFECTS OF THERMOMECHANICAL AND VANADIUM ADDITIONS ON THE MICROSTRUCTURE AND MECHANICAL PROPERTIES OF DUAL PHASE STEELS WITH LOW CR, MO CONTENTS

5.6.1 Mechanical properties of dual phase steels with low Cr, Mo contents

Figure 5.6.1 shows the engineering strain-stress curves of DPs with low Cr, Mo contents and different heat treatments (D1, E1-E3), and low coiling temperature (500°C) for hot band steels. The curves also exhibit continuous yielding as those of DPs with high Cr, Mo contents. Again we see that higher cold reduction gives higher strength. Though none of these steels can reach 980MPa UTS, the low alloyed DPs with vanadium additions are good candidates for 780MPa grade DPs and they also show much better total elongations. As can be seen, the addition of vanadium is essential for the steels in the present study to reach 780MPa for low alloyed steels and 980MPa for high alloyed steels, and in order to reach 980MPa, we can't further decrease the amount of Cr or Mo in steels. The low strength of low alloyed steels

compared with high alloyed steels is mainly due to the low amount of martensite in the final microstructures and will be discussed in detail later. Figure 5.6.2 plots the true strain-stress curves of DP steels with low Cr, Mo contents and different heat treatments and low coiling temperature (500°C) of hot band steels.

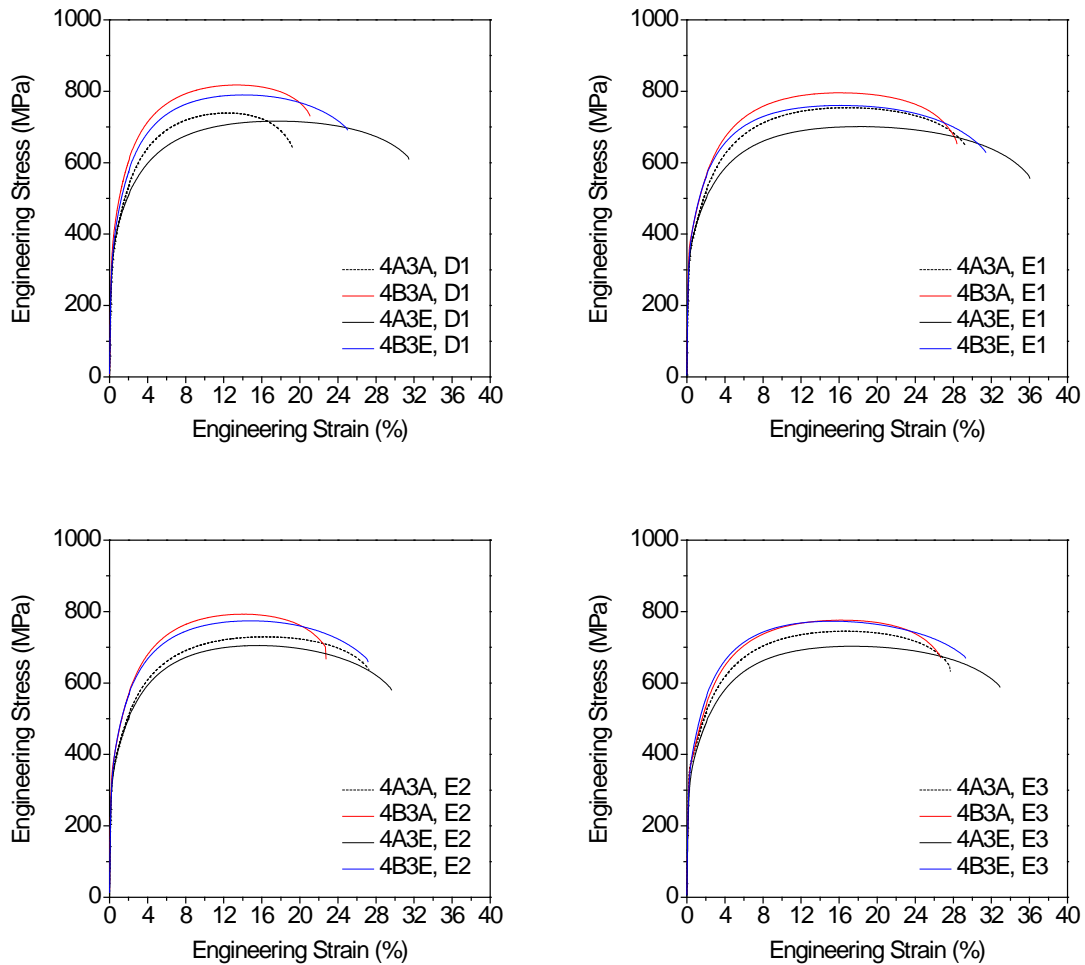


Figure 5.6.1. Engineering strain and stress curves of DP steels with low Cr, Mo contents and standard galvanizing and supercool processing

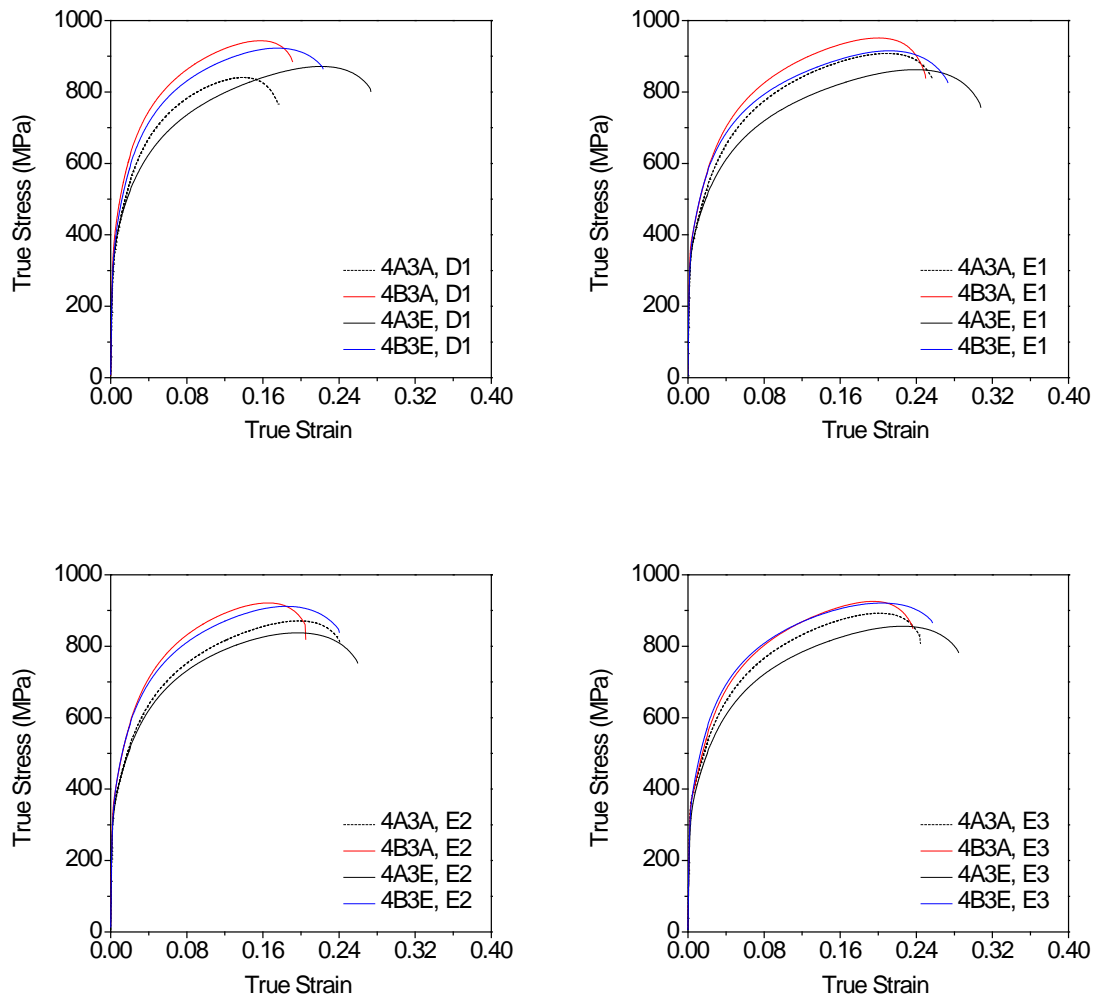


Figure 5.6.2. True strain-stress curves of DP steels with low Cr, Mo contents and standard galvanizing and supercool processing

Figure 5.6.3 contains four bar plots and summarized the tensile strength of all the 32 steels with low Cr, Mo contents. It is obvious that the addition of 0.06 w.t.% vanadium increased the tensile strength in all the cases as observed for DPs with high Cr, Mo contents. Overall, the steels with D1 process have the highest tensile strength and there is no significant difference of the tensile strength for the low alloyed steels with different supercool processing (E1, E2 or E3) which is due to the final microstructures and will be discussed later.

Table 5.6.1 summarized the increase in tensile strength due to the addition of 0.06 w.t.% vanadium. In most cases, the tensile strength increase (Δ UTS) is higher than 60MPa, and for 4B1E-D1, the increase in UTS even reached 90MPa. When compared with the Δ UTS for high alloyed DPs in the previous section, the increased tensile strength is much higher for low alloyed steels, which indicates that the addition of vanadium can more effectively strengthen DPs with low Cr, Mo contents. Again it can be found that the increase in tensile strength is higher for DPs with 50%CR than those with 80%CR. These results show that addition of vanadium is a good choice to further increase the strength when low alloyed (low Cr, Mo contents) compositions or low cold reductions were applied for production of dual phase steels. Table 5.6.2 summarized the increase in yield strength from the addition of vanadium for the steels with low Cr, Mo contents.

Figure 5.6.4 shows the yield strength data of low alloyed DPs with D1, E1, E2 and E3 processing. The yield strength of DPs with vanadium addition is higher than the corresponding steels without vanadium addition. There is no big difference of the yield strength for the 4 different processing, as can be seen that for low alloyed vanadium-bearing DPs YS is around 400MPa, and that of DPs without vanadium addition is around 350MPa. This may be explained as that all of the low alloyed steels have more than 80% ferrite and the strength of ferrite mainly determines the yield strength. The higher yield strength of vanadium bearing steels is due to the strengthening of ferrite from vanadium precipitation hardening.

The total elongations of all the 32 steels with different conditions are plotted in Figure 5.6.5. Though the vanadium bearing steels possess higher strength, they have lower total elongations overall. From Figure, it can also be found that the total elongations are higher for 50%CR steels than those with 80% cold reduction. No definite relationship between coiling temperatures and total elongations can be found from the present data and overall, the total elongations for E1 processing are best among the 4 processing. The total elongations for D1, E3 and E2 processing are similar and can't be distinguished clearly. This complicated situation for total elongation as well as other mechanical properties of low alloyed steels results from the final microstructures in which the hard phases can be martensite, bainite or

tempered martensite, since the transformation of the weak intercritical formed austenite is more complicated compared with the more stable austenite in high alloyed steels in the present study. The yield strength to tensile strength ratios (YS/UTS) are plotted in Figure 5.6.6. As can be seen that the YS/UTS ratios for D1 processing lie below 0.5, while YS/UTS ratios for E1 processing lie above 0.5, since DPs with D1 processing have the highest strength and the tensile strengths of DPs with E1 processing are lowest. The YS/UTS ratios for E2 and E3 processing are around 0.5. The YS/UTS ratios are similar for vanadium bearing DPs and vanadium free DPs, as in the case of high alloyed steels.

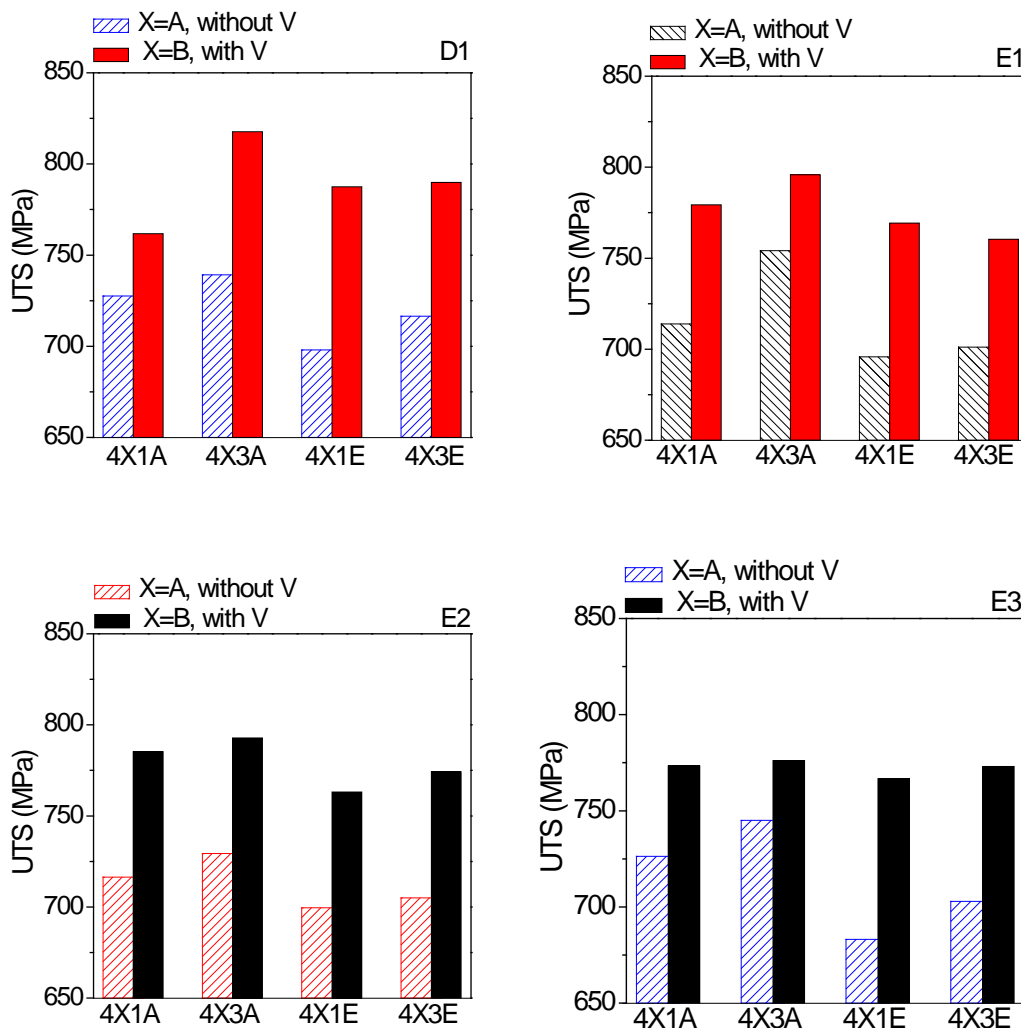


Figure 5.6.3. Tensile strength (UTS) of dual phase steels with standard galvanizing (D1) and supercool processing.

Table 5.6.1. Increase in the tensile strength due to the addition of 0.06% wt.% vanadium. UTS-A is the tensile strength of dual phase steels without vanadium addition in the first column, and UTS-B is the tensile strength of DPs with vanadium addition in the second column. Δ UTS is the increase in UTS.

		Δ UTS=UTS-B-UTS-A (MPa)			
UTS-A	UTS-B	D1	E1	E2	E3
4A1A	4B1A	34.2	65.5	68.8	47.1
4A3A	4B3A	78.6	41.7	63.5	31
4A1E	4B1E	89.6	73.4	63.5	83.6
4A3E	4B3E	73.4	59.2	69.2	70.2

Table 5.6.2. Increase in the yield strength due to the addition of 0.06% wt.% vanadium. YS-A is the yield strength of dual phase steels without vanadium addition in the first column, and YS-B is the yield strength of DPs with vanadium addition in the second column. Δ YS is the increase in YS.

		Δ YS=YS-B-YS-A (MPa)			
YS-A	YS-B	D1	E1	E2	E3
4A1A	4B1A	34.2	39.3	35.5	34.1
4A3A	4B3A	28.5	19.9	11	-0.5
4A1E	4B1E	68	82.6	71.3	80.8
4A3E	4B3E	17.3	40.7	24.8	44.6

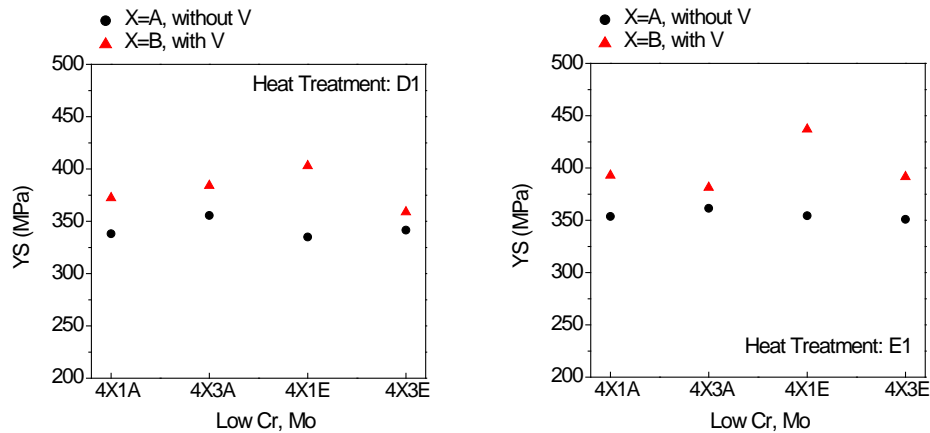


Figure 5.6.4. Yield strength (YS) of dual phase steels with standard galvanizing (D1) and supercool processing.

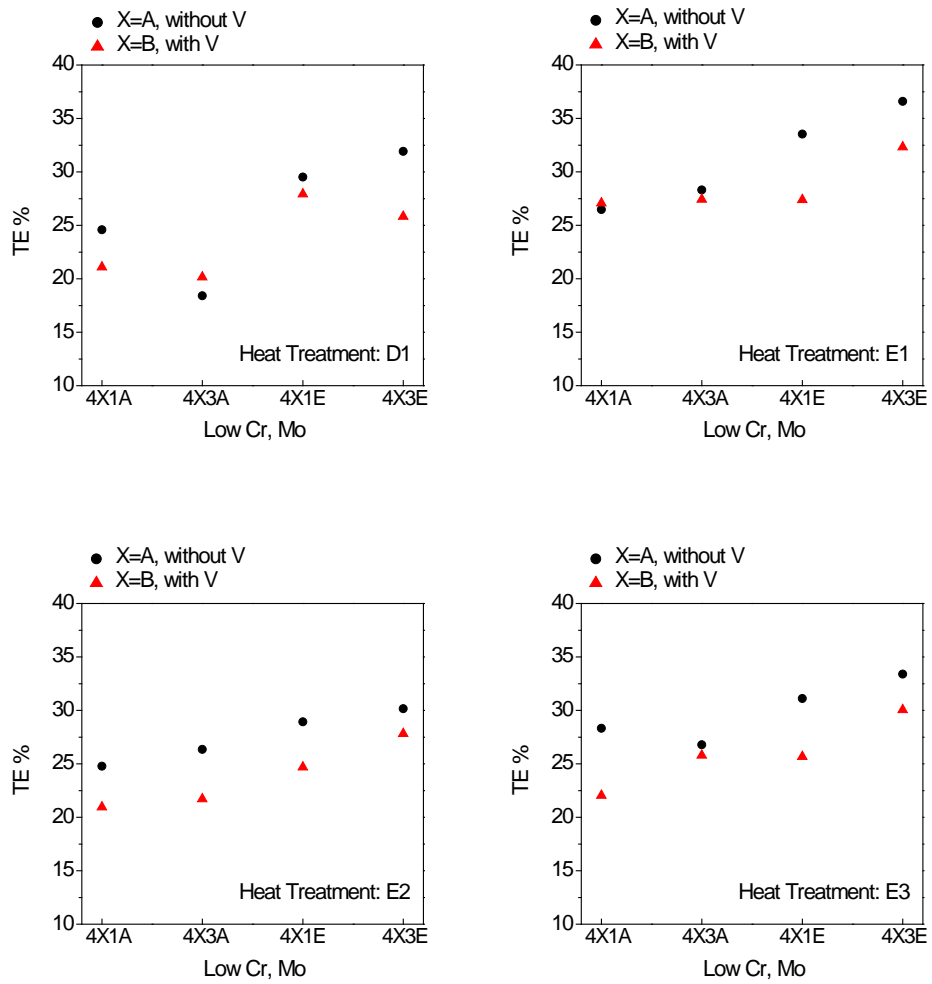


Figure 5.6.5. Total elongations (TE) of dual phase steels with standard galvanizing (D1) and supercool processing. TEs were converted to 2 inch standard specimen.

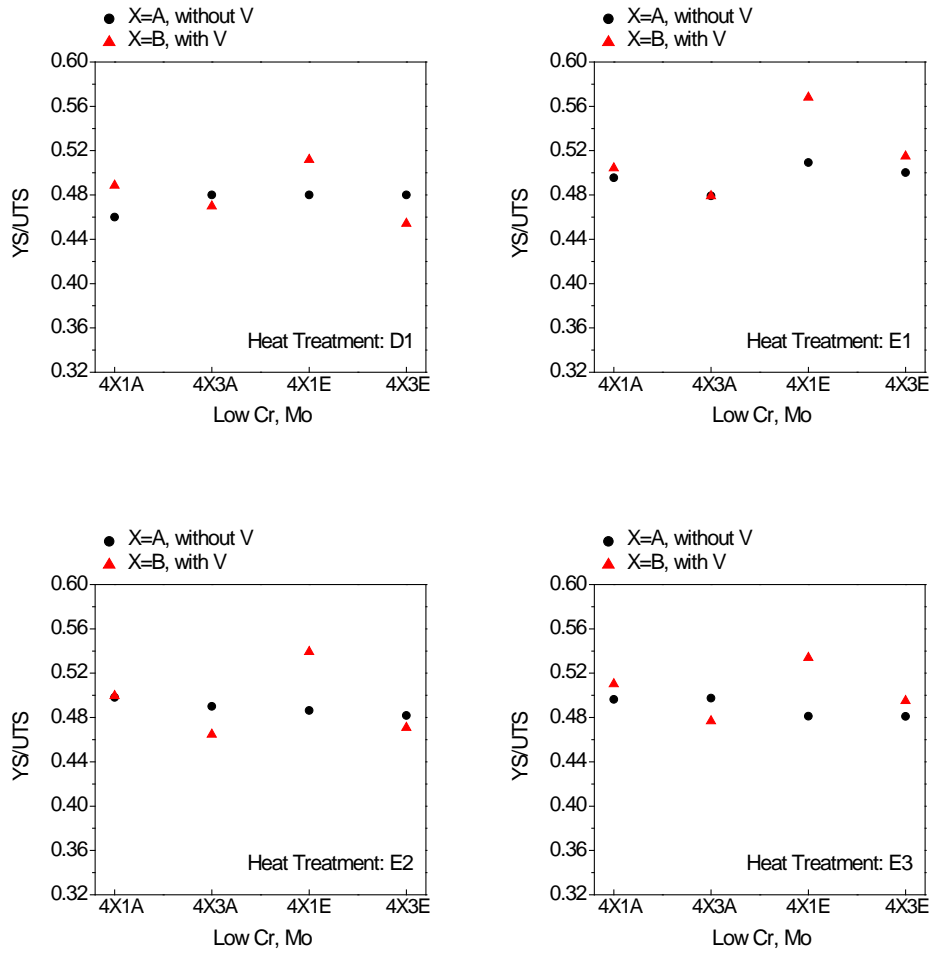


Figure 5.6.6. YS/UTS ratios of dual phase steels with standard galvanizing (D1) and supercool processing.

Table 5.6.3. Work hardening exponents (n-values between engineering strain 4% and 6%) of dual phase steels with low Cr, Mo contents

ID	n (4%-6% engineer strain)	ID	n (4%-6% engineer strain)
4A1A, D1	0.2462	4B1A, D1	0.2297
4A3A, D1	0.2407	4B3A, D1	0.2227
4A1E, D1	0.2423	4B1E, D1	0.2038
4A3E, D1	0.2439	4B3E, D1	0.2330
4A1A, E1	0.2421	4B1A, E1	0.2507
4A3A, E1	0.2614	4B3A, E1	0.2471
4A1E, E1	0.2311	4B1E, E1	0.1977
4A3E, E1	0.2433	4B3E, E1	0.2235
4A1A, E2	0.2472	4B1A, E2	0.2390
4A3A, E2	0.2541	4B3A, E2	0.2418
4A1E, E2	0.2348	4B1E, E2	0.2064
4A3E, E2	0.2493	4B3E, E2	0.2291
4A1A, E3	0.2578	4B1A, E3	0.2412
4A3A, E3	0.2597	4B3A, E3	0.2563
4A1E, E3	0.2439	4B1E, E3	0.2064
4A3E, E3	0.2594	4B3E, E3	0.2347

5.6.2 Microstructures of low alloyed DP steels and the discussions of the roles of Cr, Mo

This section focuses on discussing the microstructures of low alloyed DPs with different heat treatments (i.e. D1, E1-E3), since the mechanical properties are closely related to the microstructures.

Figure 5.6.7 shows some SEM microstructures of low alloyed steels with D1 processing, from which the effects of cold rolling reduction on the refinement of microstructures can be clearly observed. For 80% cold rolling reduction, both of the ferrite grain size and MA islands are finer than those with 50% CR. Low contents of alloying elements Cr, Mo and large packets of austenite formed during intercritical annealing reduced the stability of the austenite, and so more bainite (some is pearlite identified from the morphology) was transformed from austenite during cooling to and holding at zinc pot temperature. Bainite can be found in Figures 5.6.7 (b) and (d), which indicated the decrease in the stability of austenite. The addition of vanadium to 80%CR steels can further refine the grain size of ferrite and increase the amount of MA in the final microstructures, as seen in Figures 5.6.7 (a) and (c) and Table 5.6.4. With the addition of vanadium and high cold reduction, it is found that the bainitic formation can be suppressed, as we see that, in Figure 5.6.7 and Tables 5.6.4 and 5.6.5, less than 1% bainite was found in

4B1A (D1), about 6.5% bainite in 4A1A (D1), while about 14% and 12% bainite can be found in 4A1E (D1) and 4B1E (D1) respectively. These results indicate that finer austenite is more stable than coarse austenite and the addition of vanadium can increase the stability of intercritically formed austenite.

Figures 5.6.8 (a)-(h) show the SEM microstructures of vanadium free dual phase steels with low Cr, Mo contents and E1 processing, (a) is for high CT, 80%CR, (c) is for low CT, 80%CR, (e) is for high CT, 50%CR, (g) is for low CT, 50%CR. As can be expected, the ferrite grain size and MA island (or TM island) size are mainly determined from prior thermomechanical processing, i.e. low coiling temperature and high cold rolling reductions result in finer microstructures. Figures 5.6.8 (b),(d),(f),(h) are the corresponding microstructures at higher magnifications, and clearly show the tempered martensite and fresh MA. Some of the microstructures of low alloyed steels with E3 processing are shown in Figure 5.6.9, and Figure 5.6.10 shows the corresponding microstructures at higher magnification, which clearly show the bainitic ferrite. The amount of martensite of these four steels is around 10% and more bainite formed in steels with 50%CR, as can be seen from Figure 5.6.9 and Tables 5.6.4 and 5.6.5.

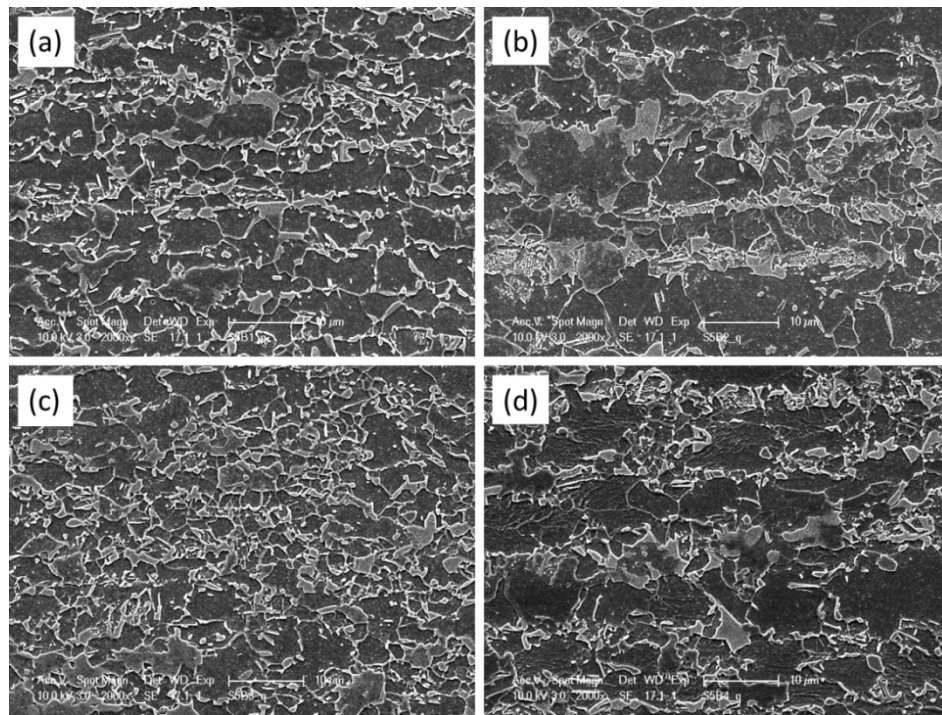


Figure 5.6.7. SEM microstructures of DP steels with low Cr, Mo contents, (a) 4A1A, D1, (b) 4A1E, D1, (c) 4B1A, D1, (d) 4B1E, D1.

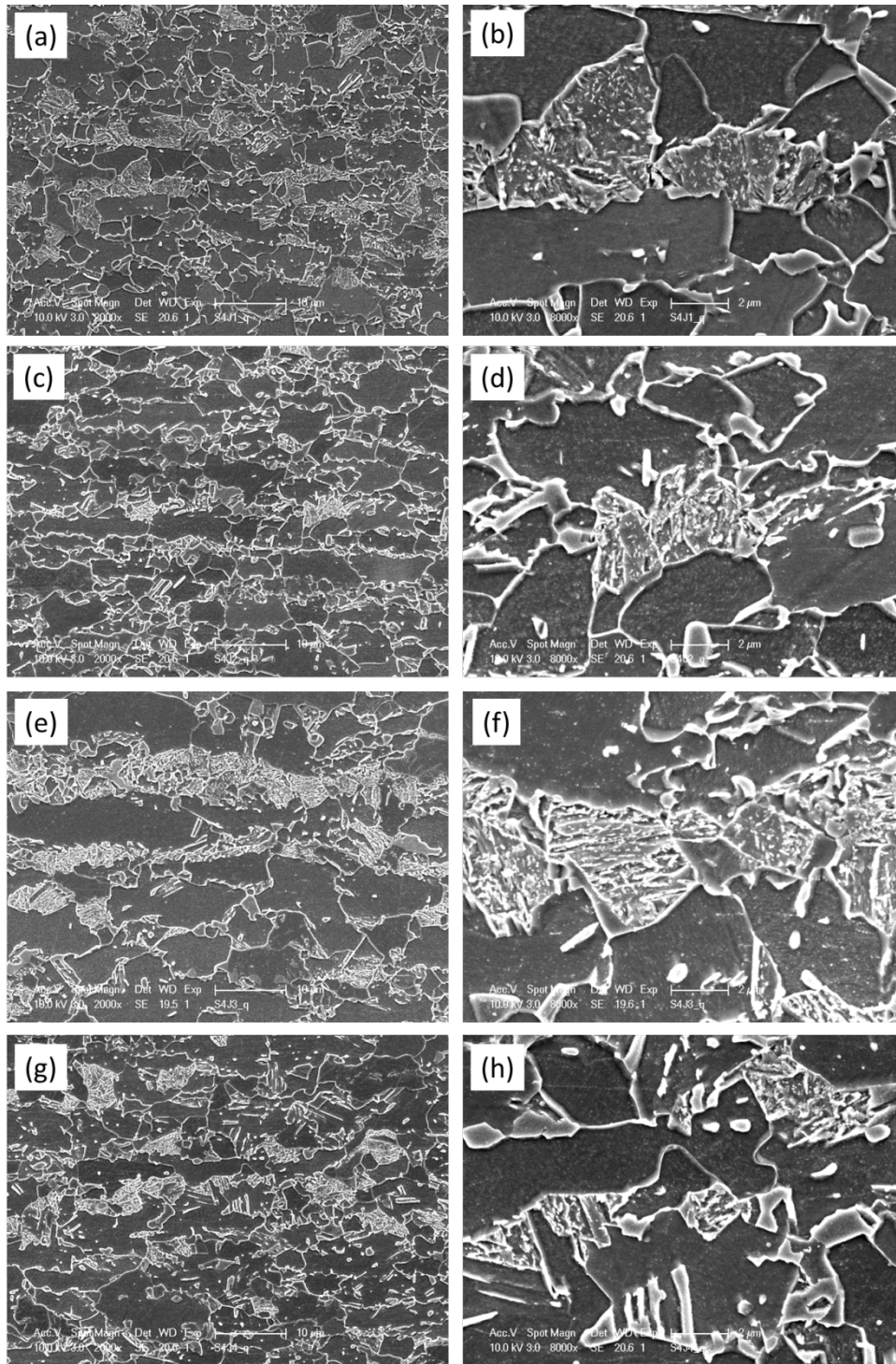


Figure 5.6.8. SEM microstructures of DP steels with low Cr, Mo and without vanadium addition, (a) (b): 4A1A, E1, (c) (d): 4A3A, E1, (e) (f): 4A1E, E1, (g) (h): 4A3E, E1.

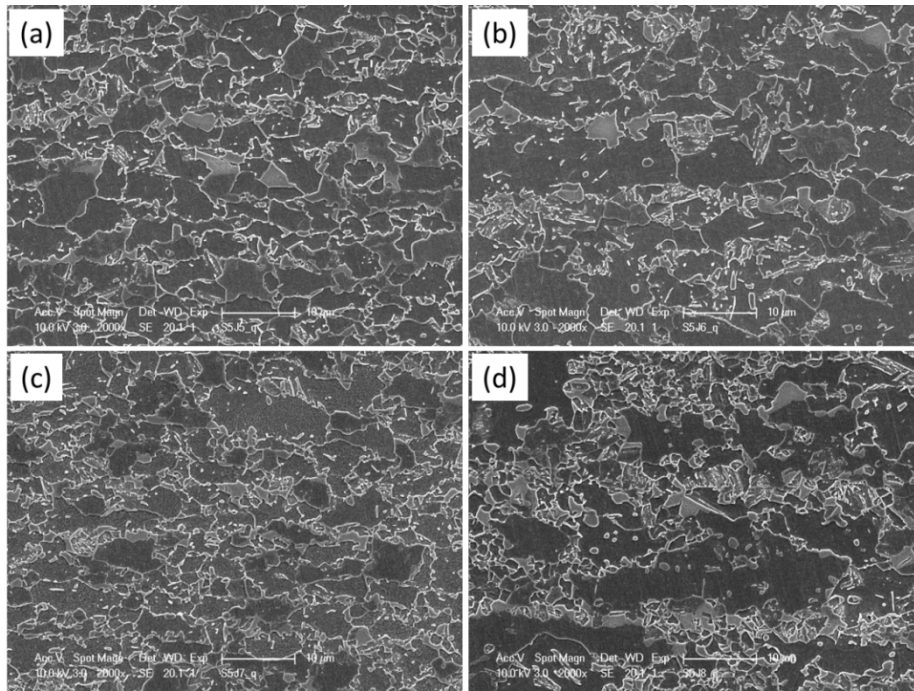


Figure 5.6.9. (a) 4A3A, E3, (b) 4A3E, E3, (c) 4B3A, E3, (d) 4B3E, E3. Low magnification 2000x

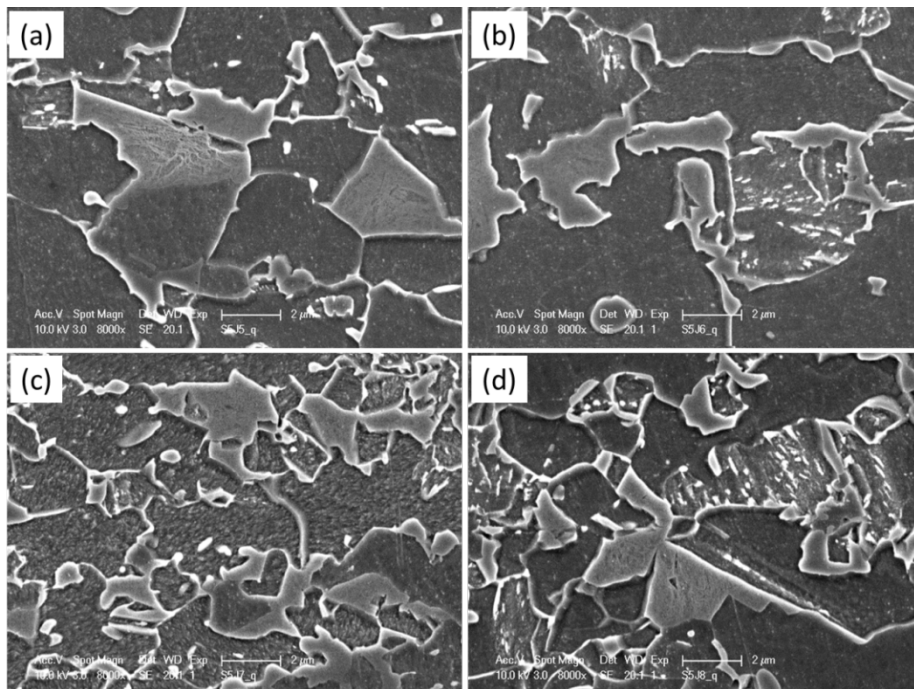


Figure 5.6.10. (a) 4A3A, E3, (b) 4A3E, E3, (c) 4B3A, E3, (d) 4B3E, E3. High magnification 8000x

The volume fractions of martensite, bainite and tempered martensite of these low alloyed steels were listed in Tables 5.6.4 and 5.6.5 and plotted in Figure 5.6.11. As discussed in the previous Sections, the strength of low alloyed DPs is much lower than that of high alloyed DPs. The main reason for the lower strength of low alloyed DPs is the lower amount of hard phases, i.e. the amount of martensite is more than 10% less than that in the corresponding high alloyed steels for D1 processing, while the total amount of martensite, bainite and tempered martensite is more than 10% less than that in the corresponding high alloyed steels, as can be seen in Tables 5.5.8-5.5.9 and Tables 5.6.4-5.6.5. The low amount of hard phases can also be clearly seen when comparing the SEM microstructures of low alloyed and high alloyed steels in the figures in this section and the previous section. These results indicate that with low Cr, Mo contents, the intercritically formed austenite is much weaker and unstable, thus during cooling to and holding at zinc pot temperature, more austenite was transformed to bainite, resulting in less amount of martensite in the final microstructures.

For these low alloyed steels, the hard phases consist of both martensite and bainite (though the existence of some pearlite still can't be excluded) for D1, E2 and E3 processings. The amount of martensite in 80%CR steels is similar to or more than that in the corresponding 50%CR steels for D1, E1-E3 processings, while more bainite (about 2 times more) can be found in 50%CR steels compared with the corresponding 80%CR steels for D1, E2 and E3 processings. The addition of vanadium increased the amount of martensite and decreased the amount of bainite in almost all the conditions, as can be seen in Tables 5.6.4 and 5.6.5. For E1 processing, the hard phases are mainly martensite and tempered martensite, and some bainite can also be found.

Table 5.6.4. Volume fractions of martensite, bainite and tempered martensite in low alloyed DPs with 80% cold reduction, 2%-6% bainite can be found for E1 processing.

Martensite	D1	E3	E2	E1
4A1A	11	9	10	10
4B1A	19.5	11	13	11
4A3A	12	9.5	11	14
4B3A	20	12.5	18	13
Bainite	D1	E3	E2	E1
4A1A	6.5	8.7	3	-
4B1A	0.5	6.5	2	-
4A3A	8	4.5	6	-
4B3A	2.3	5	2.5	-
TM	D1	E3	E2	E1
4A1A	0	0	0	8
4B1A	0	0	0	7
4A3A	0	0	0	2
4B3A	0	0	0	4

Table 5.6.5. Volume fractions of martensite, bainite and tempered martensite in low alloyed DPs with 50% cold reduction, 2%-6% bainite can be found for E1 processing.

Martensite	D1	E3	E2	E1
4A1E	10	8	10	7
4B1E	13	9.3	17	8
4A3E	12	11	10	8
4B3E	18	13	9	14
Bainite	D1	E3	E2	E1
4A1E	14	12	8	-
4B1E	11.5	9.7	6	-
4A3E	8	12	8	-
4B3E	8	8	8	-
TM	D1	E3	E2	E1
4A1E	0	0	0	12
4B1E	0	0	0	9
4A3E	0	0	0	7
4B3E	0	0	0	4.5

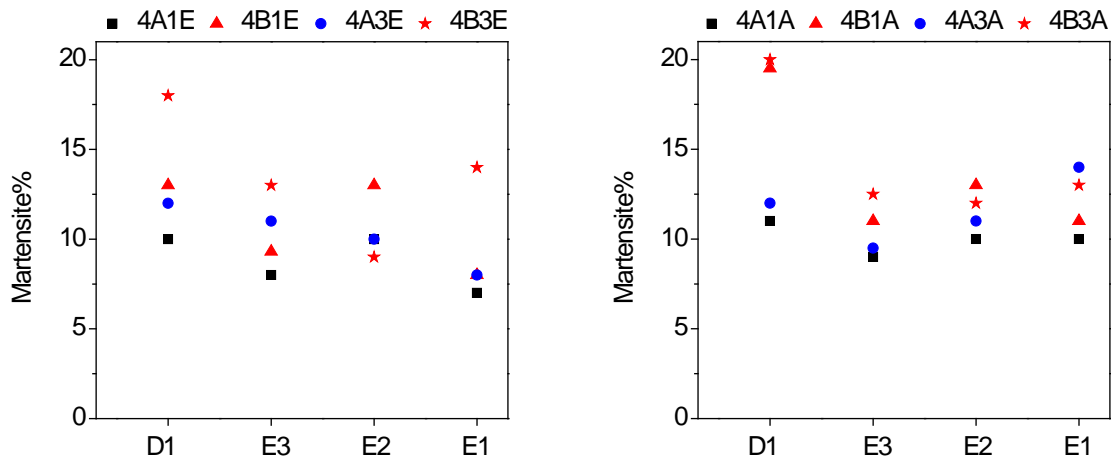


Figure 5.6.11. Volume fractions of martensite in low alloyed DP steels with different Gleeble processings.

5.6.3 Sheared-edge formability of low alloyed DP steels

This section will discuss the results of hole expansion ratios of low alloyed steels. Table 5.6.6 listed the hole expansion ratios of all the low alloyed steels with 32 conditions, and the corresponding UTS values were also included in the table. Table 5.6.7 listed the hole expansion ratios of USS commercial DP steels with different grades (i.e. DP590, DP780 and DP980). As can be seen from these two tables, at the same hole expansion level (~44% HE) as DP590, the new developed low alloyed DP steels have much higher UTS, while at the same strength level (~780 MPa) as DP780, the new developed low alloyed DP steels possess much higher hole expansion ratios.

Table 5.6.6. Hole expansion ratios of DPs with low Cr, Mo and various heat treatments. Top holder 6mm radius flat

ID (V free)	HE%	UTS (MPa)	ID (V bearing)	HE%	UTS (MPa)
4A1A, D1	43.73	727.6	4B1A, D1	28.20	761.8
4A1A, E1	44.90	713.9	4B1A, E1	30.60	779.4
4A1A, E2	48.23	716.4	4B1A, E2	30.80	785.2
4A1A, E3	52.37	726.3	4B1A, E3	40.13	773.4
4A1E, D1	37.33	697.9	4B1E, D1	26.17	787.5
4A1E, E1	44.87	695.8	4B1E, E1	53.87	769.2
4A1E, E2	51.93	699.6	4B1E, E2	25.23	763.1
4A1E, E3	47.77	683.1	4B1E, E3	31.10	766.7
4A3A, D1	39.63	739.1	4B3A, D1	33.17	817.7
4A3A, E1	57.57	754.1	4B3A, E1	47.43	795.8
4A3A, E2	43.33	729.3	4B3A, E2	40.50	792.8
4A3A, E3	45.33	745.1	4B3A, E3	44.33	776.1
4A3E, D1	50.67	716.4	4B3E, D1	30.13	789.8
4A3E, E1	48.03	701.2	4B3E, E1	44.47	760.4
4A3E, E2	38.27	705.0	4B3E, E2	27.67	774.2
4A3E, E3	49.70	702.9	4B3E, E3	28.63	773.1

Table 5.6.7. hole expansion ratios of USS commercial DP590 and DP780 tested at BAMPRI using the same procedure as for the tests in Table 5.6.6 i.e. Bottom holder 40mm hole, top holder 40mm hole and 6mm radius flat, and continuous die moving speed 0.5mm/s. The hole expansion ratios of USS commercial DP980 were tested in USS lab.

Specimen	HE%
DP590, USS	44.43
DP780, USS	21.06
DP980, USS	13.4 (A1, galvanizing), 14.9 (C1, supercool)

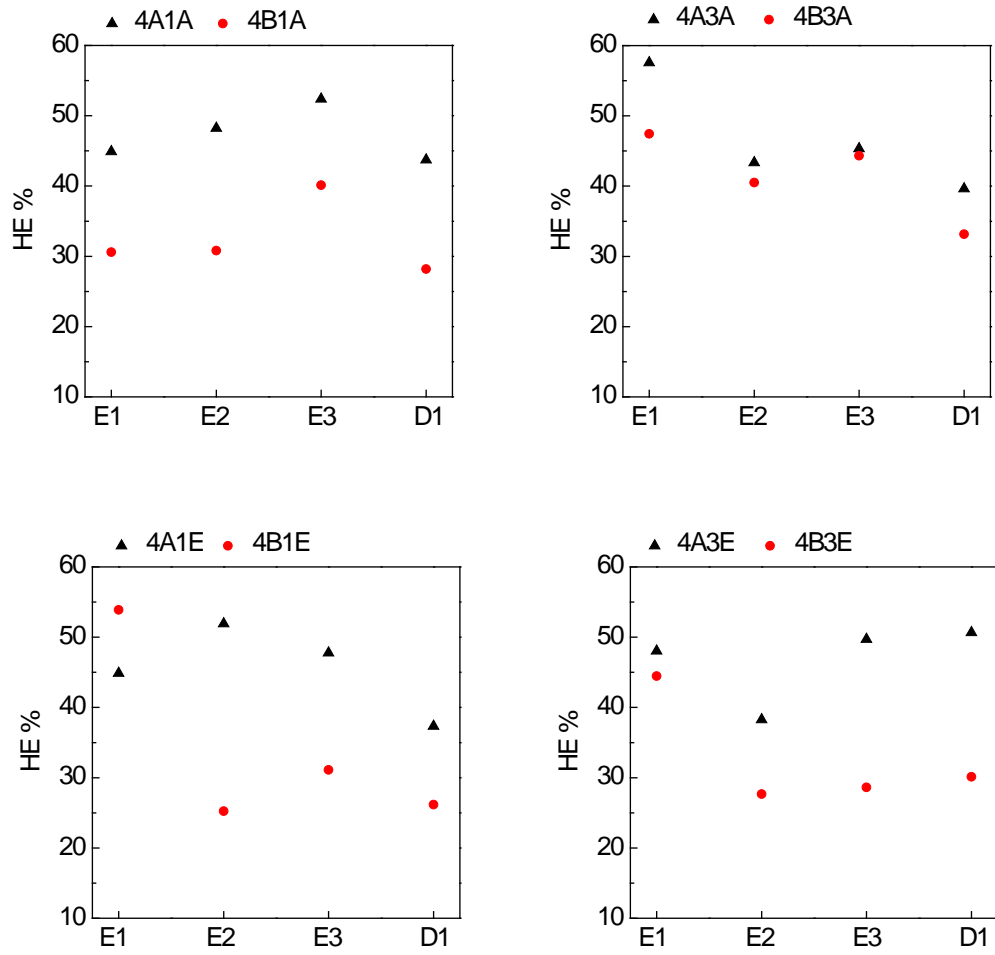


Figure 5.6.12. The relationship between hole expansion ratio and heat treatments.

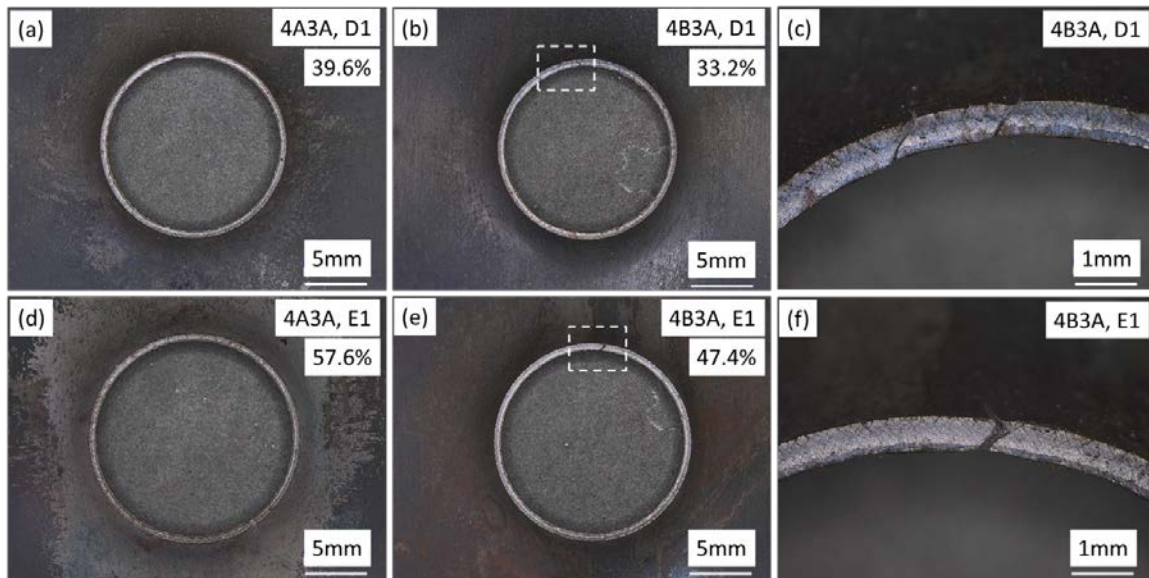


Figure 5.6.13. Hole expansion tested samples (a) 4A3A, D1, (b) 4B3A, D1, (c) high magnification image of the region inside the dashed square in (b), (d) 4A3A, E1, (e) 4B3A, E1, (f) high magnification image of the region inside the dashed square in (e). Vertical direction is the rolling direction

Figures 5.6.12 plotted the hole expansion ratio data of dual phase steels with different heat treatments. It is clear that the addition of vanadium increased the strength, however this decreased the hole expansion ratios with the same processing. The decrease in hole expansion ratio is higher for 50%CR steels compared with the corresponding steels with 80%CR. The decrease in HE is minimum for steels with 80%CR and low coiling temperature 500°C. There is no definite relationship between hole expansion ratios and different heat treatments, as observed in the steels with high Cr, Mo contents that the hole expansion ratios decreased with increasing the supercool temperatures and DPs with galvanizing processing have the lowest HE values. It is because even in the DPs with D1 processing, some bainite or even pearlite can be formed due to the lower stability of the intercritically formed austenite. The replacement of martensite to bainite which is softer and possesses higher ductility than martensite increased the hole expansion ratios, just as the tempered martensite replacing some of martensite can increase the hole expansion ratio. This weak relationship between hole expansion ratios and processings for low alloyed DPs is closely related to the microstructures, as we see in the previous section, for all the

four processings, the amount of martensite is around 10% and the hard phases consist of martensite, tempered martensite and bainite.

Figure 5.6.13 contains the low magnification optical images of expanded holes of steels 4A3A, 4B3A with D1 and E1 processings after hole expansion tests. The original diameter of the hole is 10mm punched at USS. The numbers in the images are the hole expansion ratios. Figures 5.6.13 (c) and (f) are the images with higher magnification of the regions in the dashed squares in (b) and (e) respectively, showing the cracks completely through the thickness as an indicator of the failure of the tests. As can be seen, the main or first cracks through thickness prefer to occur near the rolling direction. The hole expansion ratios of vanadium bearing steels (4B3A with D1 and E1 processings) are lower than the corresponding steels without vanadium addition, though these vanadium bearing steels have higher tensile strength. It can also be clearly seen that the hole expansion ratios of DPs with E1 processing are much higher than those of DPs with D1 processing.

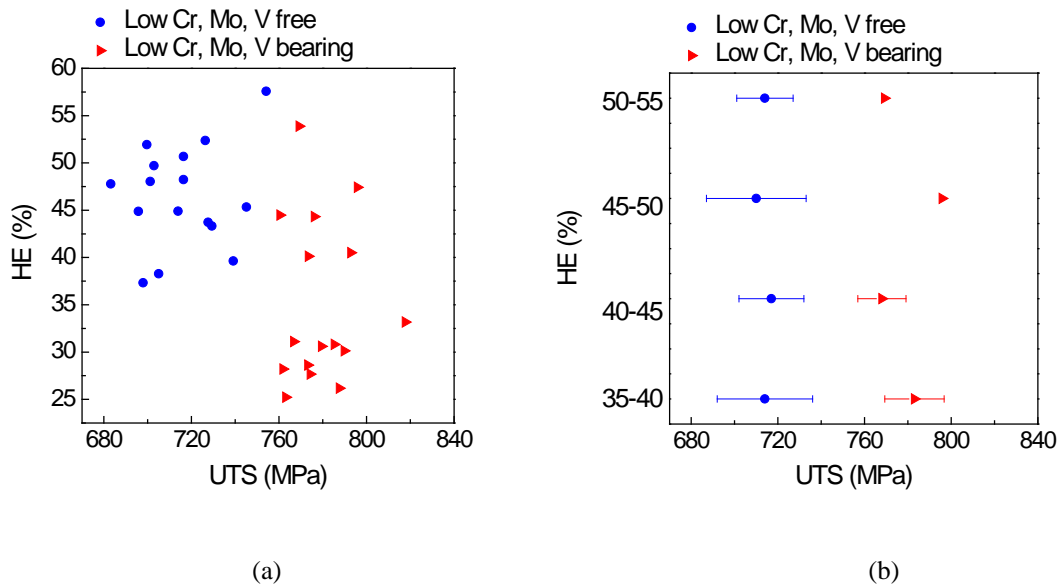


Figure 5.6.14. (a) data points (UTS-HE) of low alloyed DPs, (b) averaged UTS values at four hole expansion ratio levels, 35-40%, 40-45%, 45-50% and 50-55%.

Figure 5.6.14 (a) plotted the UTS-HE data points of low alloyed DPs with and without vanadium additions, and in order to clearly see the effects of vanadium, Figure 5.6.14 (b) plotted the averaged UTS

values at four different hole expansion levels, i.e. 35-40%, 40-45%, 45-50% and 50-55% intervals. It can be clearly observed that the data points of vanadium bearing DPs located on the right of the data points of vanadium free DPs, which indicates that the DPs with vanadium additions are stronger than the vanadium free DPs at the same hole expansion levels.

5.7 OVERALL DISCUSSIONS: IMPROVING THE STRENGTH-DUCTILITY BALANCE IN HIGH STRENGTH DUAL PHASE STEELS THROUGH THE ADDITION OF VANADIUM

5.7.1 Stored energy of initial cold rolled sheets

As discussed in Sections 5.4, 5.5, the microstructures of final dual phase steels (phase balance, size and distribution of ferrite, MA and so on) are closely related to the stored energy in the cold rolled steel sheets. We also see that stored energy can be increased by increasing cold reductions. In this section, the stored energy of initial cold rolled steel sheets of all the 16 steels (high alloyed and low alloyed steels with 2 cold reductions and 2 coiling temperatures).

Table 5.7.1. Stored energy (J/cm³) of cold rolled sheets with low Cr, Mo contents

CT=650°C	Average SE (sub-grain)	Average SE (Image Quality)	CT=500°C	Average SE (sub-grain)	Average SE (Image Quality)
4A1A	3.23	6.7458	4A3A	3.86	7.1276
4A1E	1.82	6.1890	4A3E	3.05	6.8780
4B1A	2.82	7.0620	4B3A	4.17	7.6154
4B1E	2.21	6.3098	4B3E	3.47	6.5979

Table 5.7.2. Stored energy (J/cm^3) of cold rolled sheets with high Cr, Mo contents

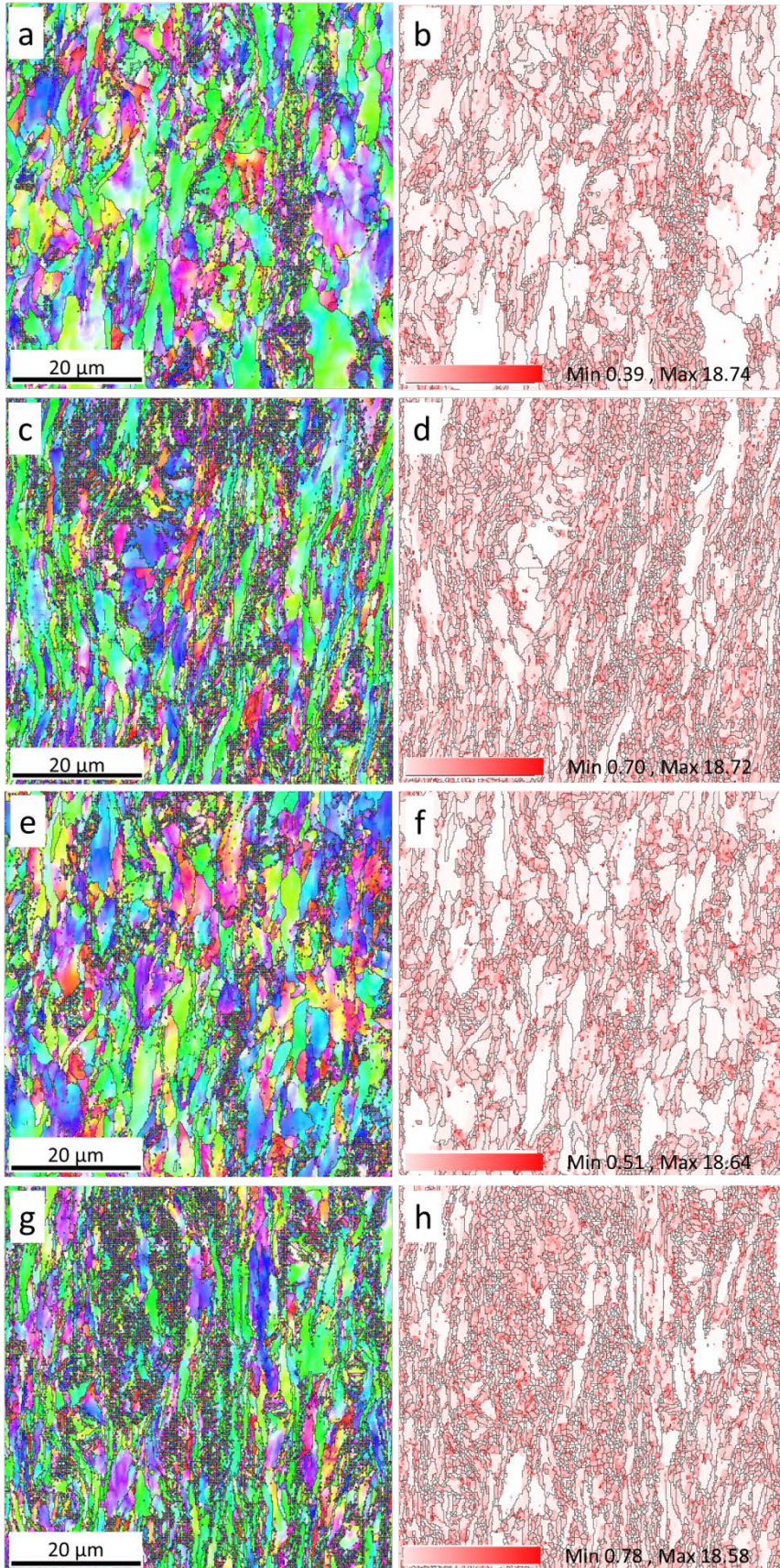
CT=650°C	Average SE (sub-grain)	Average SE (Image Quality)	CT=500°C	Average SE (sub-grain)	Average SE (Image Quality)
2A1A	3.66	7.1811	2A3A	4.36	8.1536
2A1E	2.86	6.2117	2A3E	4.11	7.3903
2B1A	3.74	7.3645	2B3A	4.13	8.1352
2B1E	3.08	6.3517	2B3E	4.00	7.2033

Table 5.7.3. VHN (300g) of cold rolled (50%CR and 80%CR) initial steel sheets with low Cr, Mo contents, and the increase in VHN (Δ VHN) due to the addition of 0.06% w.t% vanadium.

ID	VHN	ID	VHN	Δ VHN
4A1A	285±10	4B1A	322±6	37
4A1E	239±9	4B1E	281±10	42
4A3A	329±8	4B3A	339±6	10
4A3E	289±7	4B3E	294±8	5

Table 5.7.4. VHN (300g) of cold rolled (50%CR and 80%CR) initial steel sheets with high Cr, Mo contents, and the increase in VHN (Δ VHN) due to the addition of 0.06% w.t% vanadium.

ID	VHN	ID	VHN	Δ VHN
2A1A	316±12	2B1A	376±10	60
2A1E	278±10	2B1E	343±11	65
2A3A	415±10	2B3A	429±9	14
2A3E	367±15	2B3E	375±6	8



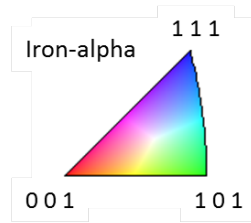


Figure 5.7.1. IPFs (a) 2A1E, (c) 2A1A, (e) 2B1E, (g) 2B1A; SE mappings (b) 2A1E, (d) 2A1A, (f) 2B1E, and (h) 2B1A. The IPF triangle describes the relationship between colors and orientations, and this triangle can be applied to all the IPFs in the following part of this thesis.

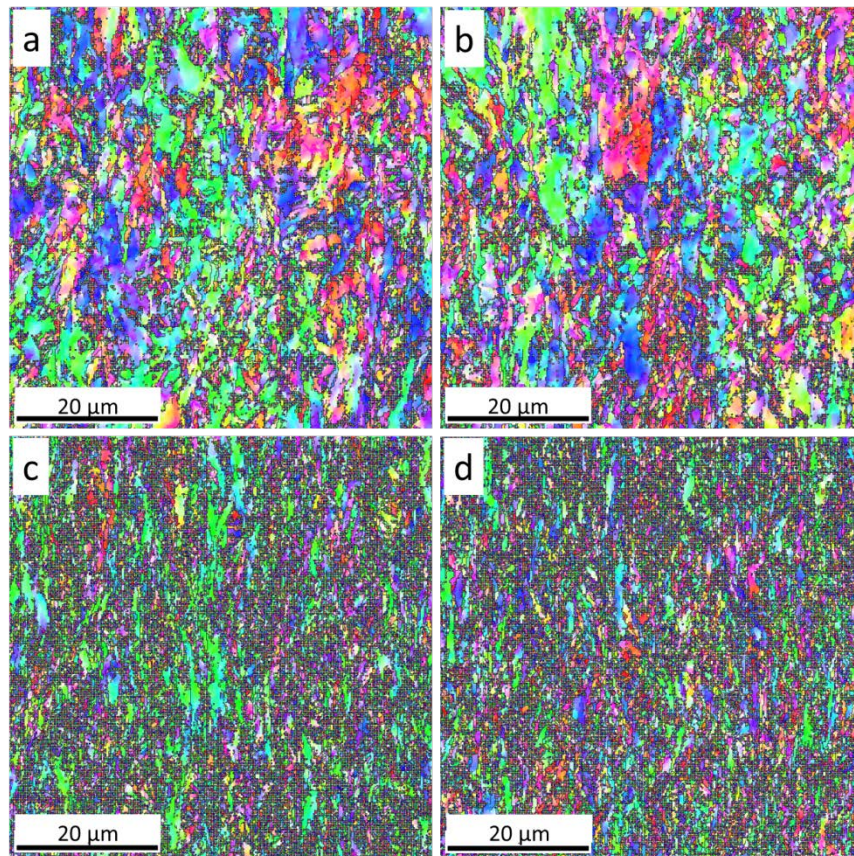


Figure 5.7.2. Inverse pole figures of (a) 2A3E, (b) 2B3E, (c) 2A3A and (d) 2B3A

Figure 5.7.1 shows the inverse pole figures (IPF, left four images) of DPs with high Cr, Mo contents and high coiling temperatures (650°C). Polygonal ferrite grains were deformed at 50% cold reduction and were further severely elongated along rolling direction as well as along transverse direction at 80% cold reduction for both vanadium free and vanadium bearing steels 2A1A and 2B1A. Figures

5.7.1(b) (d) (f) and (h) are the stored energy distribution mappings of the corresponding steels at the left side of Figure 5.7.1, from which it can be found that the stored energy is obviously higher in steels with 80%CR (Figures 5.7.1(d),(h)) than that in steels with 50%CR (Figures 5.7.1 (b), (f)). The averaged stored energies of low alloyed and high alloyed cold rolled sheets are listed in Tables 5.7.1 and 5.7.2. The vanadium bearing cold rolled sheets were more severely deformed than vanadium free cold rolled sheets when comparing Figures 5.7.1 (a), (e) and Figures 5.7.1 (c), (g), resulting in higher stored energy in vanadium bearing high alloyed steel sheets with high coiling temperature 650°C, as listed in Table 5.7.2. As we see in Section 5.5, hot band steels with vanadium additions (HB, 2B1C compared with HB, 2A1C) are much stronger than the corresponding steels without vanadium additions, and so more loads need to be applied in order to roll the vanadium bearing hot band steels to the same reduction (50% or 80%), which is one reason for the higher stored energy in vanadium bearing cold rolled sheets than that in the corresponding vanadium free cold rolled sheets.

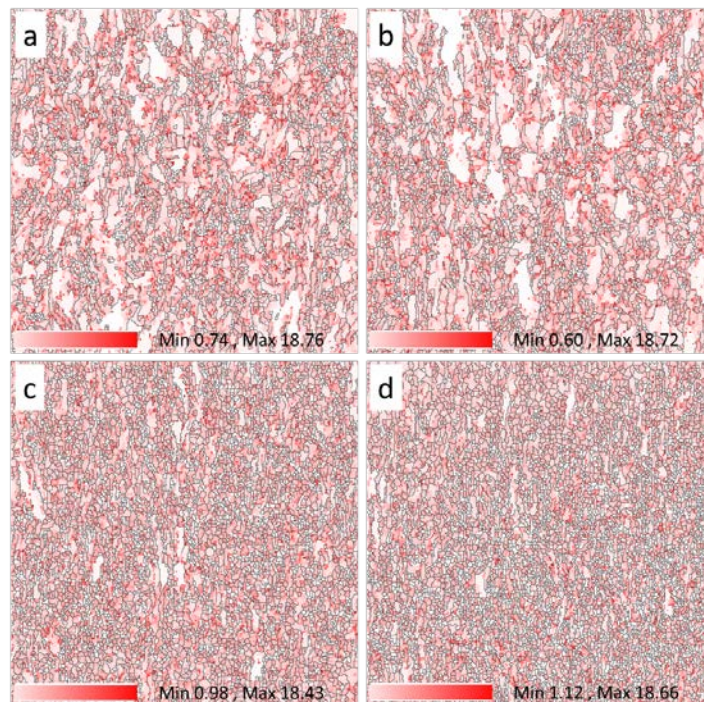


Figure 5.7.3. Stored energy mapping of (a) 2A3E, (b) 2B3E, (c) 2A3A and (d) 2B3A. The size of each image is 60 μ m \times 60 μ m

Figure 5.7.2 shows the inverse pole figures (IPF) of high alloyed cold rolled steel sheets with low coiling temperatures and Figure 5.7.3 are the corresponding stored energy distribution mappings calculated using the same software in Section 5.4. Unlike the case of clearly elongated polygonal ferrite grains, Figure 5.7.1, for sheets with low coiling temperature, the acicular or bainitic ferrite grains were deformed but the elongation was not as obvious as the polygonal ferrite grains at 50%CR, and when further rolled to 80% reduction, the acicular or bainitic ferrite grains were much more heavily deformed and the severe elongations of ferrite can be observed in Figures 5.7.2 (c) and (d). Comparing with 80%CR polygonal ferrite grains, the 80%CR low temperature ferrite grains or packets were broken down much more severely and thus much more defects or higher density of dislocations were introduced into the 80%CR sheets with low CT, resulting in much higher stored energy than the corresponding sheets with high CT, as can be seen from Table 5.7.2. For low coiling temperature, the addition of vanadium can't help increase the stored energy in cold rolled sheets (50% or 80%), indicating the strengthening is mainly from the phase transformation at low coiling temperature, i.e. low temperature ferrite dominates the strength, which can be supported by the fact that the increase in hardness or UTS is very limited with the addition of vanadium for hot band steels with low coiling temperature in Section 5.5. The stored energy from image quality (IQ) data were also listed in Tables 5.7.1 and 5.7.2, the order of which is consistent with the order of the SE from sub-grain method, while the absolute SE values from IQ data are higher, which is due to the difference between these two methods, since IQ data take into all the crystal and surface conditions and sub-grain method mainly considers the sub-grain boundaries in the deformed ferrite.

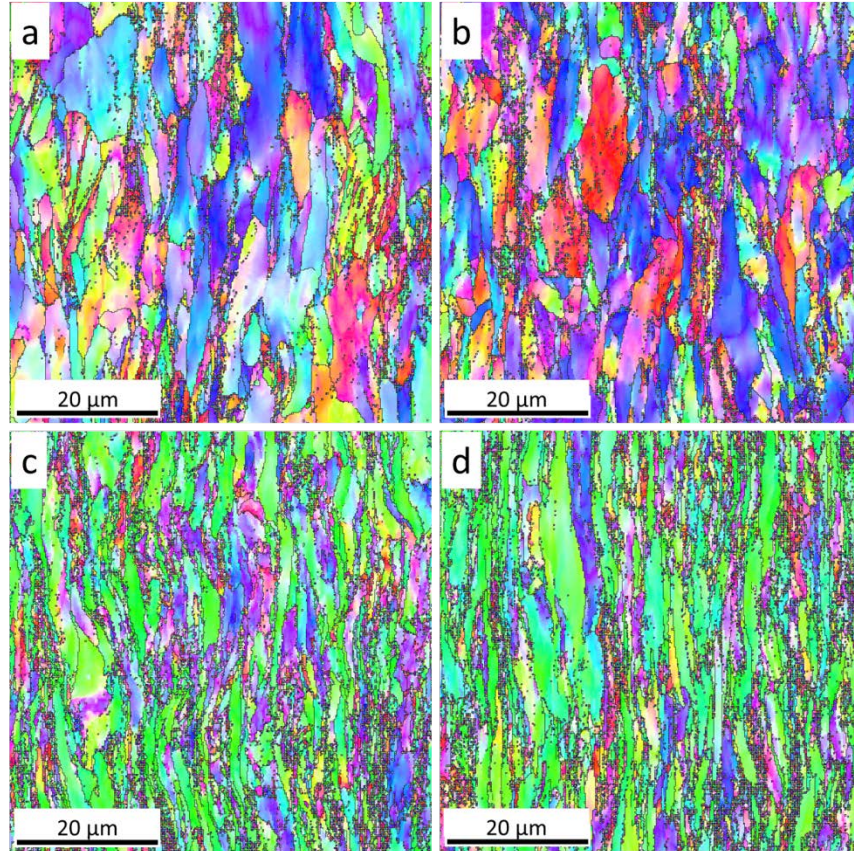


Figure 5.7.4. Inverse pole figures of (a) 4A1E, (b) 4B1E, (c) 4A1A and (d) 4B1A

Figure 5.7.4 illustrates the IPFs of low alloyed cold rolled steel sheets with high CT and Figure 5.7.5 are the corresponding stored energy mappings from sub-grain method. The effects of cold reductions on the microstructure and stored energy are similar to the case of high alloyed steels (Figure 5.7.1), i.e. polygonal ferrite grains were further elongated from 50%CR to 80% cold reduction and more stored energy was introduced after 80% cold reduction, as listed in Table 5.7.1. After 80% cold reduction, we can clearly see the texture (Ferrite $\langle 110 \rangle$ along rolling direction) in both vanadium free and vanadium bearing steels from Figures 5.7.4 (c) and (d). For low alloyed cold rolled steels with low CT, as shown in Figures 5.7.6 (IPF) and 5.7.7 (stored energy mappings from sub-grain method), the low temperature ferrite grains or packets were heavily deformed at 80% cold reduction and thus possess much higher stored energy, while at 50% cold reduction the elongation of ferrite is not obvious. It can also be seen that

the addition of vanadium increased the stored energy in this situation (low alloyed steels with low CT) for both 50%CR and 80%CR steels, see Table 5.7.1 and Figure 5.7.7. Overall, the stored energy of steels with low CT is higher than the corresponding steels with high CT, the high alloyed steels have higher stored energy compared with the corresponding steels with low Cr, Mo contents, and increasing the cold reduction to 80% can significantly increase the stored energy comparing that at 50%CR, however, the addition of vanadium can't help to increase the stored energy in all the cases, indicating the stored energy is mainly related to cold reduction and phase transformation, and the hardening from vanadium (precipitation and solid solution hardening) is not high enough in all the cases from the present study.

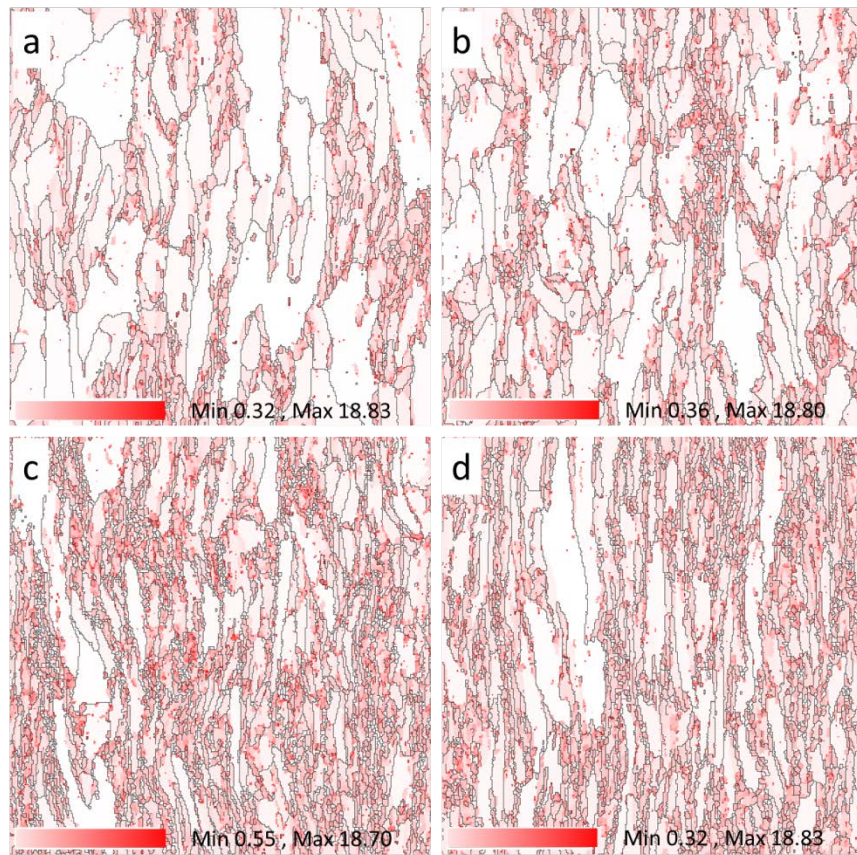


Figure 5.7.5. Stored energy mappings of (a) 4A1E, (b) 4B1E, (c) 4A1A and (d) 4B1A, the size is 60 μ m \times 60 μ m

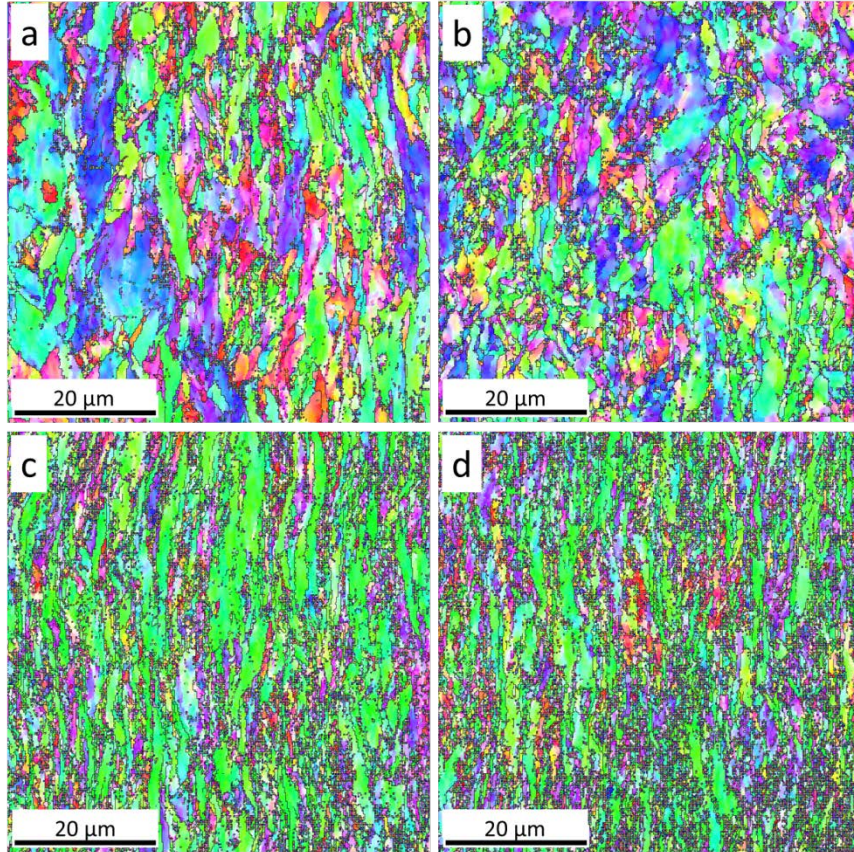


Figure 5.7.6. Inverse pole figures of (a) 4A3E, (b) 4B3E, (c) 4A3A, and (d) 4B3A

Tables 5.7.3 and 5.7.4 listed the hardness (VHN 300g) of all the 16 cold rolled sheets. It can be easily found that with high coiling temperature, the strengthening from vanadium is much higher than that at low coiling temperature, which is consistent with results of vanadium strengthening for hot band steels. The main reason is the effective precipitation hardening of vanadium precipitates at high coiling temperatures, which will be discussed in the following Section 5.7.4.

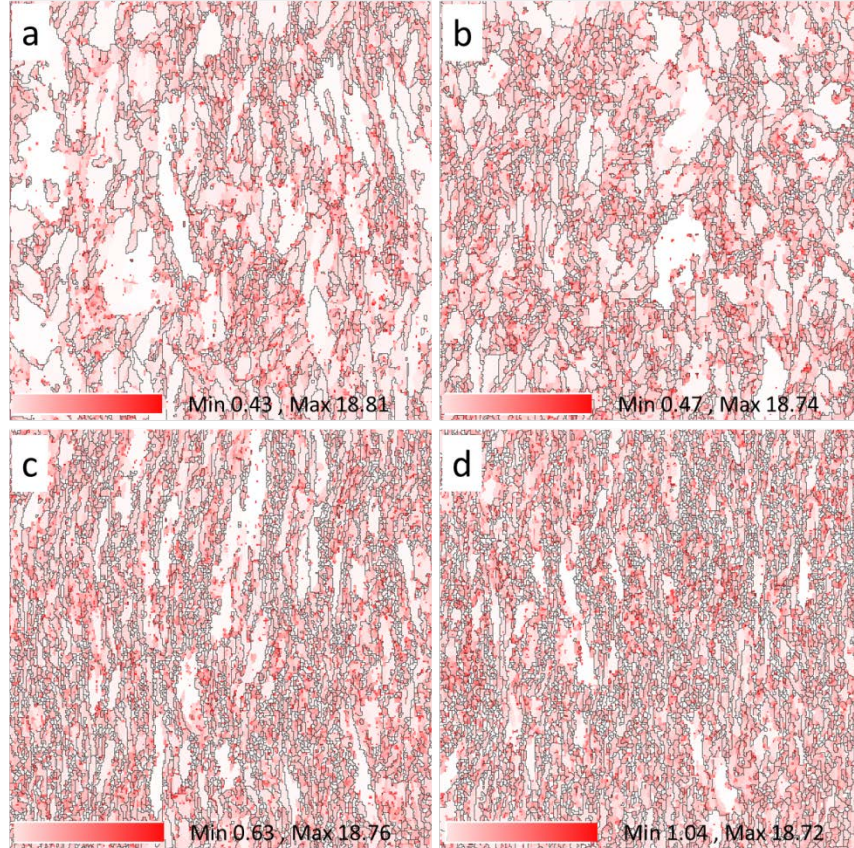


Figure 5.7.7. Stored energy mappings of (a) 4A3E, (b) 4B3E, (c) 4A3A, and (d) 4B3A, the size of each image is $60\mu\text{m}\times 60\mu\text{m}$

5.7.2 Mechanical properties of dual phase steels with various conditions

This section will compare and discuss the mechanical properties of high and low alloyed dual phase steels, which were partially discussed in Section 5.5 and Section 5.6 respectively.

Figure 5.7.8 summarized and plotted the tensile strength (UTS) of all 64 dual phase steels with different compositions, coiling temperatures and cold rolling reductions. For all the 4 heat treatments, dual phase steels with low Cr and Mo have low UTS (less than 800MPa), which can't meet the lowest requirement 980MPa for DP980 steels. So it is necessary to keep high content of Cr and Mo in order to reach high tensile strength. It can be found from Figure 5.7.8 that the addition of vanadium plays an

essential role to get the required strength. All the dual phase steels with vanadium addition have higher tensile strength than those without vanadium addition. None of the dual phase steels without vanadium addition can reach 980MPa UTS, and among the DPs with vanadium addition, 2B1A (D1), 2B3A (D1), 2B3A (E2) and 2B3A (E3) can meet the minimum requirement for DP980 steels. It can be seen that the addition of vanadium can more efficiently increase UTS in low alloyed (low Cr, Mo) steels than in high alloyed (high Cr, Mo) steels. Moreover, with the addition of vanadium, UTS increased more in steels with 50%CR than in those with 80%CR. These results indicate that vanadium is more helpful to increase strength for steels with low cold reductions and low alloy contents (low Cr, Mo in this study). Since more cold reduction means higher production costs and replacement or adjustments of the existed cold rolling systems for steel companies, the efficient increase in UTS from vanadium addition for steels with low cold reductions indicates that the addition of vanadium may be a good choice for the production of dual phase steels.

Figure 5.7.9 shows another way to plot the relationship among tensile strength and various processing (D1, E1, E2 and E3) and conditions (cold rolling reductions, coiling temperatures). All the red points are for DPs with 80% cold rolling reduction and the black points are for the corresponding DPs with 50% cold rolling reduction. As expected the DPs with higher cold rolling reduction (80%) possess high tensile strength. The reasons for the increase in tensile strength due to higher cold rolling reductions have been discussed in Sections 5.5 and 5.6.

Figure 5.7.10 illustrates the relationship between total elongation and tensile strength. The red line in Figure 5.7.10(a) is fitted for DPs with vanadium and black line is fitted for DPs without vanadium using exponential function ($TE\% \propto \exp(-UTS)$). In Figure 5.7.10(b) the red line is linearly fitted for DPs with vanadium and black line is linearly fitted for DPs without vanadium. It is found that the fitting lines for DPs with vanadium lie above the fitting lines for DPs without vanadium addition, which indicates that the vanadium addition increased the ductility of these DP steels. Figures 5.7.10(c) and (d) shows another way to view the increase in ductility through using vanadium addition. In Figures 5.7.10(c) and (d), the

red solid, red dashed, black solid and black dashed lines are for products of UTSxTE (MPa x %) of 26,000, 22,000, 18,000, 10,000, respectively. For D1 processing, DPs with vanadium lie between 22,000 and 18,000 lines, while DPs (except two points with lowest strength) without vanadium lie between 18,000 and 10,000 lines. The ductility of DPs with E1 processing is higher than those with D1 processing. Most of the points for E1 lie between the 18,000 and 22,000 curves and some of them even reached the 26,000 MPa% level.

A comparison of the tensile properties found in this current study with those from the literature is shown in Figures 5.7.11 and 5.7.12. Only dual phase steels with high Cr, Mo content and D1 processing are plotted in Figure 5.7.11. It is apparent from Figure 5.7.11 that the steels are located above the base line for strength – v s- % martensite in the final structure. The ductility values of DPs with V addition lie somewhat above the C-Mn trend line, Figure 5.7.12, while those of DPs without V addition lie below the C-Mn trend line, which indicates that the addition of vanadium increased the ductility of DP980 steels.

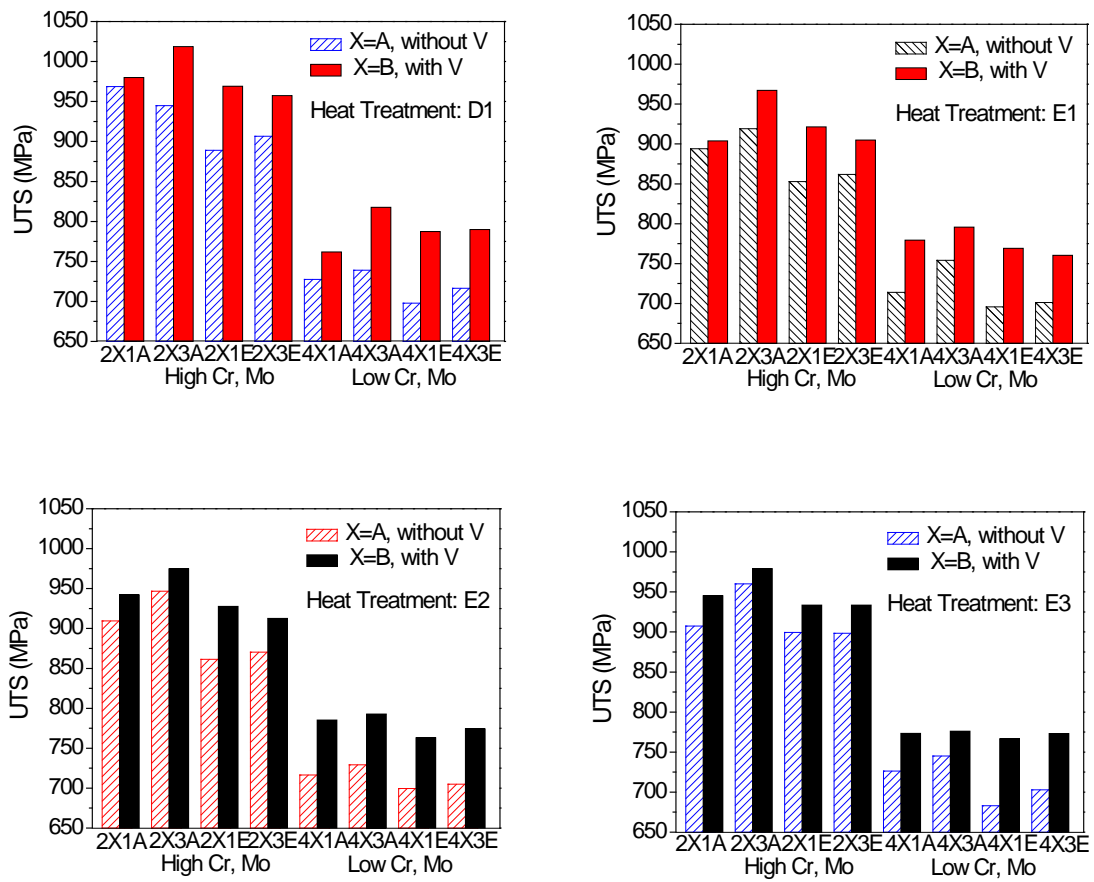


Figure 5.7.8. Tensile strength (UTS) of dual phase steels with standard galvanizing (D1) and supercool processing.

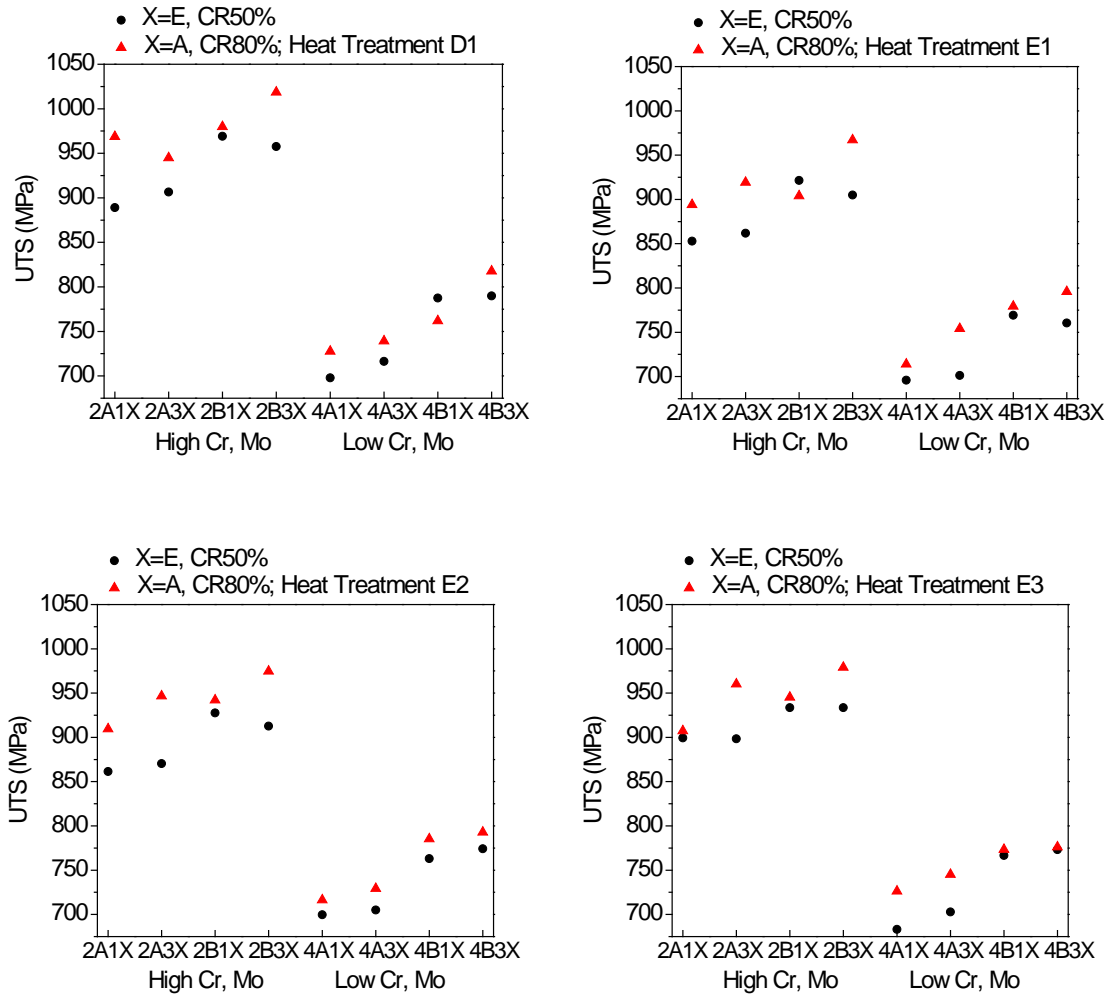
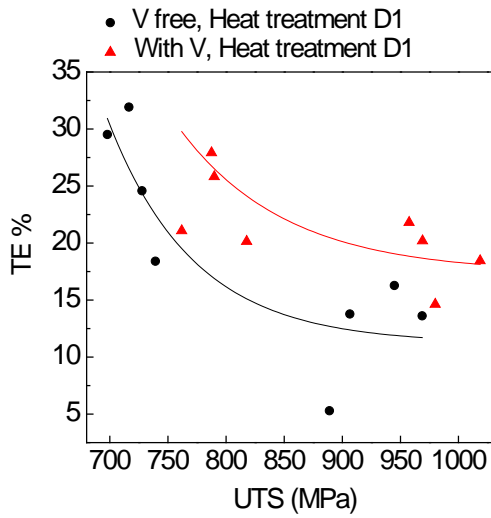
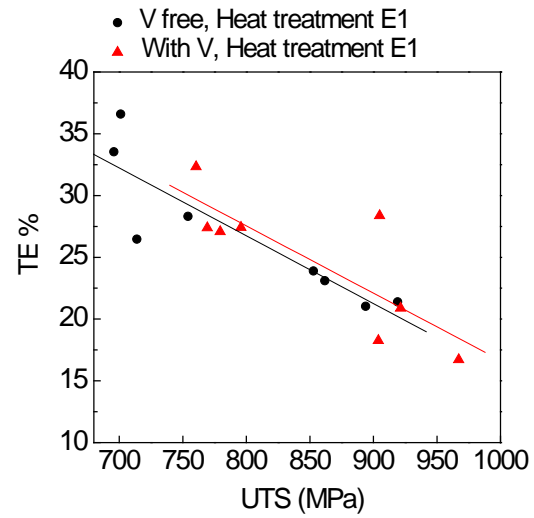


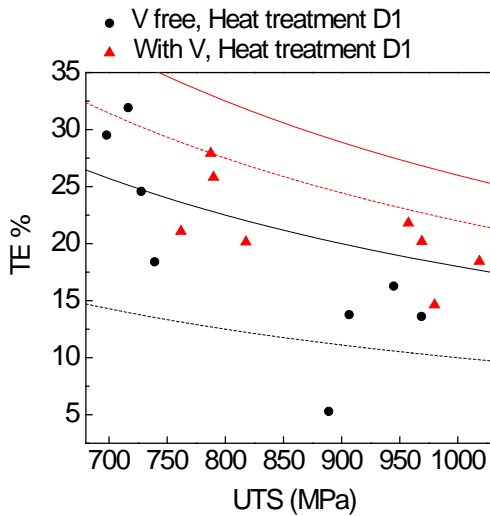
Figure 5.7.9. Tensile strength (UTS) of dual phase steels with standard galvanizing (D1) and supercool processing (E1, E2, and E3). The DPs with 80%CR are stronger than corresponding DPs with 50%CR.



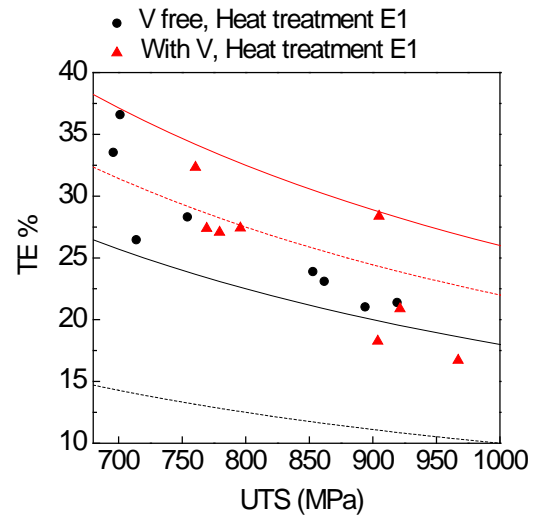
(a)



(b)



(c)



(d)

Figure 5.7.10. relationship between total elongations and tensile strength of DP steels with vanadium addition and without vanadium addition. (a) red line is fitted for DPs with vanadium and black line is fitted for DPs without vanadium using exponential function ($TE\% \propto \exp(-UTS)$). (b) red line is linearly fitted for DPs with vanadium and black line is linearly fitted for DPs without vanadium. (c), (d) red solid, red dashed, black solid and black dashed lines are for 26000, 22000, 18000, 10000 UTSxTE (MPa x %) respectively.

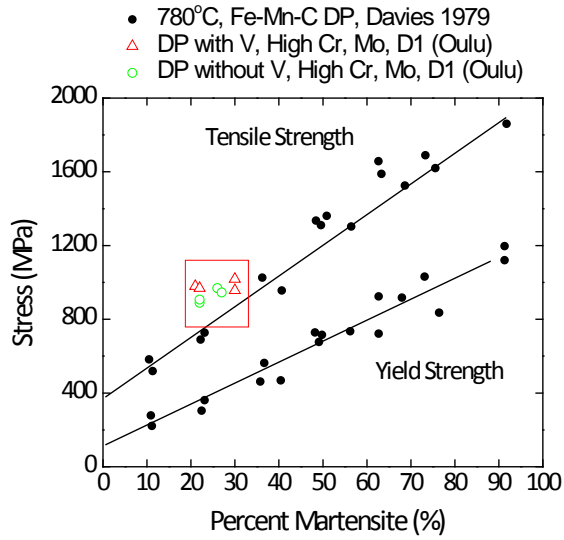


Figure 5.7.11. Comparison of MA volume fraction vs UTS with the corresponding values obtained by Davies. Only dual phase steels with high Cr, Mo and galvanizing (D1) processing are shown in the figure.

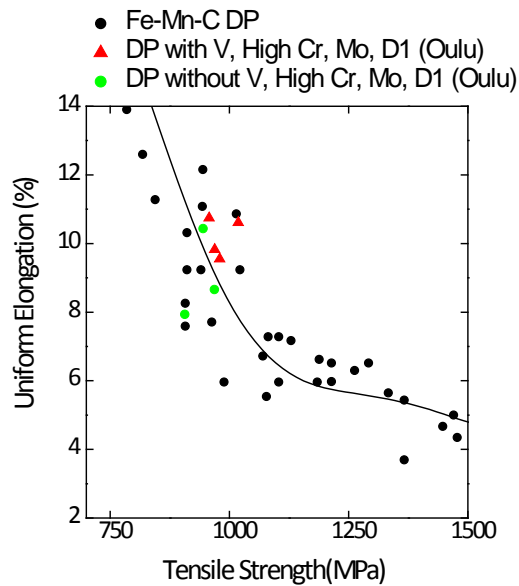


Figure 5.7.12. Comparison of UTS vs UE with the corresponding values obtained by Davies. . Only dual phase steels with high Cr, Mo and galvanizing (D1) processing are shown in the figure.

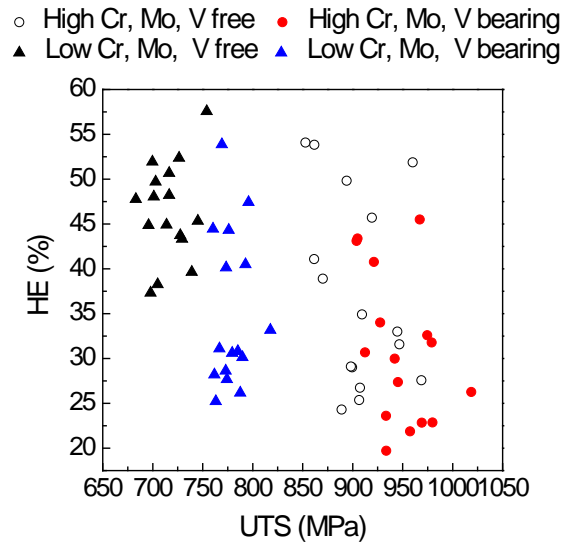


Figure 5.7.13. Relationship between hole expansion ratios (HE%) and tensile strength (UTS), all the data of 64 DP steels were included.

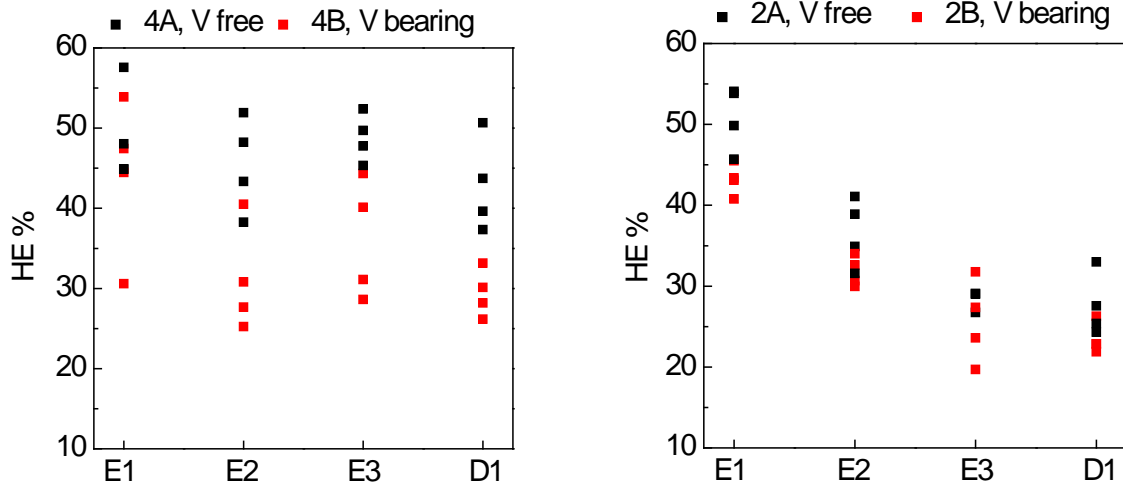


Figure 5.7.14. Relationship between hole expansion ratios (HE%) and heat treatment processing.

Figure 5.7.13 plots the hole expansion ratio (HE%) and tensile strength (UTS) data, and all the data of 64 steels with high or low Cr, Mo contents are included in this plot. Black triangles are for DPs with low Cr, Mo contents and no vanadium additions, blue triangles are for DPs with low Cr, Mo contents and with vanadium additions, white circles are for DPs with high Cr, Mo contents and no vanadium

additions, while red circles are for DPs with high Cr, Mo contents and with vanadium additions. Clearly, the data points of DPs with low Cr, Mo contents lie at lower strength region, while those of DPs with high Cr, Mo contents locate at higher strength region.

It looks that there is no clear relationship between tensile strength and hole expansion ratios, since at the same hole expansion ratio level, the tensile strength can vary as much as 300MPa, e.g. (1019, 26.3), (763, 25.2), and (683, 47.8), (967, 45.5), the difference in UTS reached 256MPa and 284MPa respectively. The weak relationship between UTS and HE% can be explained as that the hole expansion ratio represents the formability of the sheared steel, while UTS reflects the overall strength of the undeformed steel. As discussed in the previous sections, the hole expansion ratio is closely related to the reduction in area, which can also reflect the ductility of the steel after necking or after reaching peak strength (UTS). However, when we look at the data points of steels with high Cr, Mo and low Cr, Mo contents separately, it still can be found that hole expansion ratio decreases with increasing UTS.

Figure 5.7.14 shows the relationship between hole expansion ratios (HE%) and different processing (D1, E1-E3) of DPs with low Cr, Mo contents and high Cr, Mo contents respectively. The hole expansion ratios of DPs without vanadium addition (black squares) are higher than those of vanadium bearing DPs (red squares) for both of low Cr, Mo and high Cr, Mo steels. For low alloy DPs, there is no obvious trend for the 4 heat treatments, which is due to the microstructures as discussed in the previous sections. Most of the constituents is ferrite (more than 80%) and the hard region is a mixture of martensite, bainite (for D1) or martensite, bainite and tempered martensite for E1-E3 for low alloy steels. For high alloy DPs, it is clear that DPs with D1 processing possess lowest hole expansion ratios, since those steels consist of ferrite and martensite, and DPs with E1 processing have highest hole expansion ratios, since most of the hard phase is tempered martensite. The HE% decreases with increasing supercool temperatures from 250°C to 390°C, due to the decrease in the amount of tempered martensite (whose hardness is between martensite and ferrite) in the final microstructures.

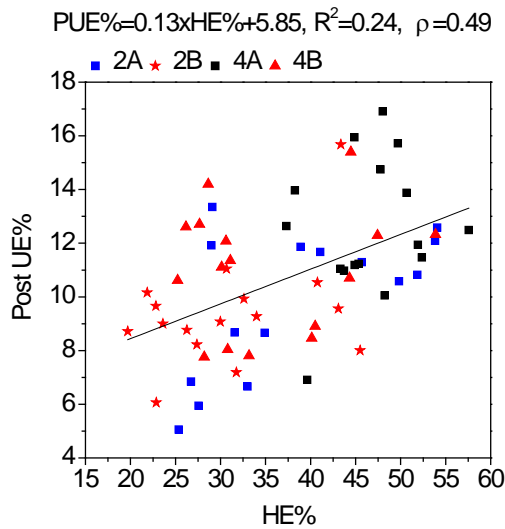


Figure 5.7.15. Post UE-HE data points for low alloyed and high alloyed steels with various conditions. The black line is fitted by linear equation, $PUE\% = 0.13 \times HE\% + 5.85$, the coefficient of determination R^2 is 0.24, and the Pearson's linear correlation coefficient ρ is 0.49.

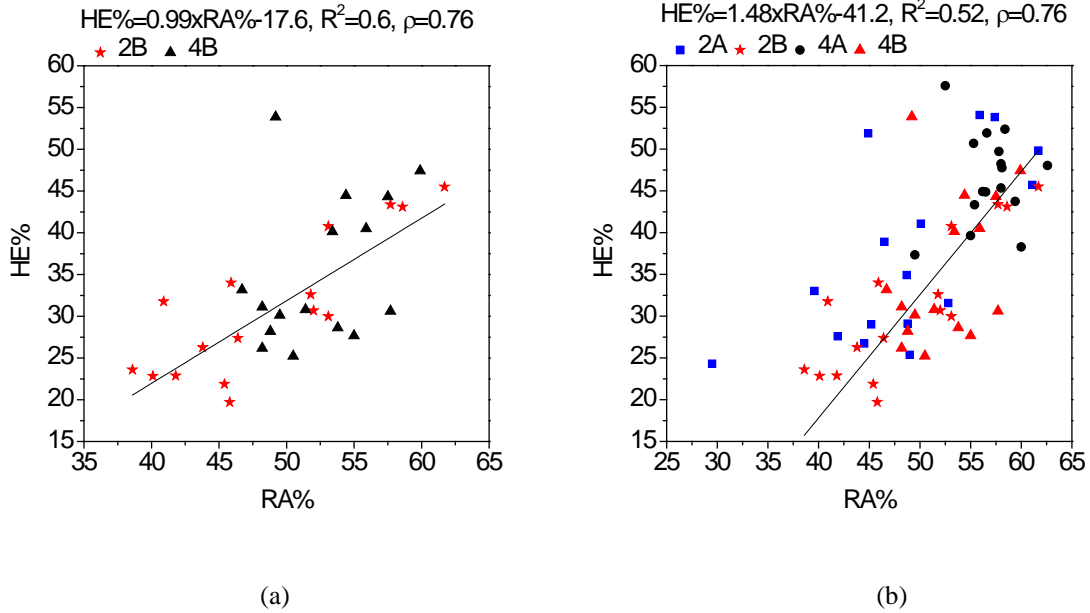


Figure 5.7.16. Reduction in area (RA)-HE data points for low and high alloyed steels with various conditions. The black lines were fitted by linear equations, (a) $HE\% = 0.99 \times RA\% - 17.6$, the coefficient of determination R^2 is 0.6, and the Pearson's linear correlation coefficient ρ is 0.76, the steels are with vanadium additions, (b) $HE\% = 1.48 \times RA\% - 41.2$, the coefficient of determination R^2 is 0.52, and the Pearson's linear correlation coefficient ρ is 0.76, the steels with and without vanadium additions are all included.

Since the hole expansion ratio or sheared edge formability is closely related to the properties of the severely deformed microstructures near hole due to machining (i.e. punching or shearing), in order to estimate the hole expansion ratios from tensile properties, two parameters can be considered, i.e. post uniform elongations and reduction in area, since both of them reflected the ductility of the steels after peak strength or necking.

Figure 5.7.15 plotted the post UE-HE data points for low and high alloyed steels with various conditions. The linear fitted equation is $PUE\% = 0.13 \times HE\% + 5.85$, whose coefficient of determination R^2 is 0.24, and the Pearson's linear correlation coefficient ρ is 0.49, which indicate the weak linear relationship between post uniform elongations and hole expansion ratios. However the positive relationship between post UE and HE can still be expected (since $\rho = 0.49 > 0$). Figure 5.7.16 plotted the reduction in area (RA)-HE data points for low and high alloyed steels with various conditions. Figure 5.7.16 (a) only included vanadium bearing steels (2B and 4B), and the linear fitted equation is $HE\% = 0.99 \times RA\% - 17.6$, whose coefficient of determination R^2 is 0.6 and the Pearson's linear correlation coefficient ρ is 0.76. Figure 5.7.16 (b) contained both vanadium bearing and vanadium free steels (2A, 2B, 4A and 4B), and the linear fitted equation is $HE\% = 1.48 \times RA\% - 41.2$, whose coefficient of determination R^2 is 0.52 and the linear correlation coefficient ρ is 0.76. These results indicate that there is much better linear relationship between hole expansion ratio and reduction in area than that between hole expansion ratio and post uniform elongation. Positive relationship between HE and RA can definitely be expected, however, on single linear equation can be used to represent all the situations, reflecting the complexity between microstructures and mechanical properties in the real steels.

5.7.3 Retained austenite and supercool temperatures

As discussed in Section 5.4, increasing the cold reduction gives us satisfied strength ($>980\text{MPa}$) for DPV with 72%CR, at the beginning of this section, the results of retained austenite in DPV (72%CR, the same

steel used in Section 5.4) with different supercool temperatures will be given in order to understand the relationship between the amount of retained austenite and supercool temperatures.

Table 5.7.5 shows the amount of retained austenite in the three supercooled DPV steels (72%CR) with different supercool temperatures (250°C, 300°C and 350°C). It shows that increasing the supercool temperature from 250°C to 350°C, the amount of retained austenite decreased, while the tensile strength increased. The volume fractions of retained austenite were estimated using the equation:

$$f_{\gamma} = 1 - \frac{M_s(c)}{M_s(ref)} \quad (5.7.1)$$

where $M_s(c)$ is the saturation magnetization of the austenite-containing sample, $M_s(ref)$ is the the saturation magnetization of the reference sample. The Field (G) vs Moment/Mass (emu/g) curves are shown in Figure 5.7.17.

Table 5.7.5. Retained austenite calculated from magnetic properties.

DPV(72%CR)	$M_s(ref)=212.86$ (emu/g)	M_s	$f_{\gamma}(\%)$	UTS(MPa)
790°C(1min), 15°C/s, 250°C(20s), 40°C/s, 460°C(30s), 10°C/s, RT		205.23	3.6	896
790°C(1min), 15°C/s, 300°C(20s), 40°C/s, 460°C(30s), 10°C/s, RT		208.18	2.2	880
790°C(1min), 15°C/s, 350°C(20s), 40°C/s, 460°C(30s), 10°C/s, RT		211.93	0.4	923

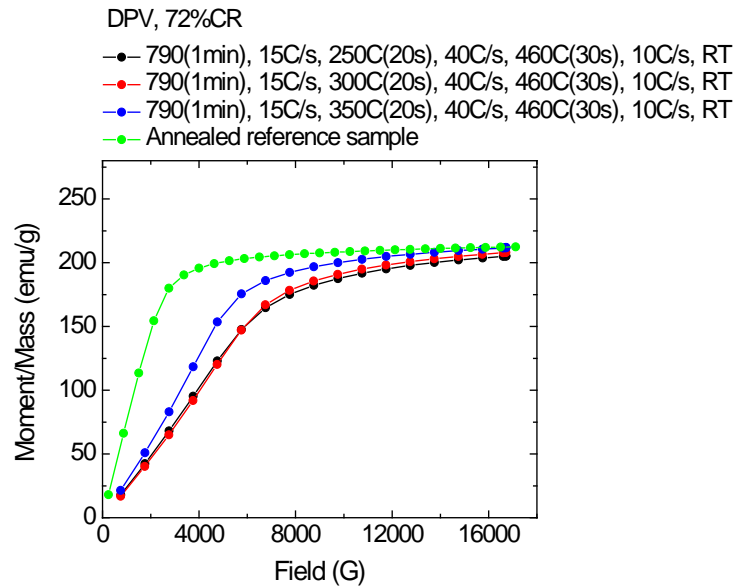


Figure 5.7.17. Magnetic Field (in G) vs Moment/Mass (emu/g) curves of DPV, 72%CR supercooled steels.

We also measured the amount of retained austenite in DPVs with high Cr, Mo contents (the same steels used in Section 5.5) and with different processing (D1, E1, E2 and E3), and the results were summarized in Table 5.7.6. As expected, DPs with E1 have the highest amount of retained austenite and those with D1 processing have the lowest amount of retained austenite, and the amount of retained austenite increased with decreasing supercool temperature from 390°C to 250°C. When lowering the supercool temperature (especially to 250°C), the diffusivity of carbon reduced significantly (compared with 460°C), and so the intercritically formed austenite can keep high carbon content by preventing carbon diffusion to form cementite. As we know the formation of other phases (e.g. cementite) with higher carbon concentration will reduce the carbon content of the remained austenite according to level law. The stable austenite with higher carbon content has higher ability to prevent the complete transformation to martensite during supercooling to 250°C from intercritical annealing temperature, resulting in more austenite retained in the final microstructure. Another explanation may be that during supercooling to 320°C or 390°C, some bainite formed, and so the remaining austenite is enriched with

carbon due to carbon partitioning during bainitic phase transformation. As a result austenite was stabilized against martensitic transformation during further cooling to room temperature.

Another thing we see is that the amount of retained austenite is higher in DPs with 50%CR than that in DPs with 80%CR.

As we have seen in Section 5.1, DPs with supercool processing possess best ductility (e.g. highest total elongations). The results of the relationship between total elongation and the amount of retained austenite in DPNbV with 7 different processing, Figure 5.1.12, indicate the positive relationship between them. It is found that DPNbVs as well as DPs with other microalloying elements have the highest amount of retained austenite (~8%) with supercooling processing (250°C) compared with other processing (Galvanizing or Galvannealing processing). From the results of reduction in area and hole expansion ratios (sheared edge formability) in Section 5.1, it was found that DPs with supercooling processing C1 possess nearly two times the hole expansion ratios of those with Galvanizing processing A1, and the HE% of DPV with C1 processing even reached 53%. Based on these results, we varied the supercool temperatures in order to get best balance between strength and ductility, as discussed in Sections 5.5 and 5.6. The reduction in area values and hole expansion ratios of DPV with high Cr, Mo contents both increased with decreasing the supercool temperature (from 390°C to 250°C), see Figures 5.5.39, 5.5.40, and 5.7.14. Besides the reason from the phase balance (i.e. variation of the amount of tempered martensite, fresh martensite, or bainite), the retained austenite also plays an important role on the reduction in area values as well as hole expansion ratios. In the previous Section 5.7.2, we clearly see that the ductility of DPs with high Cr, Mo contents and with E1 processing (supercool temperature 250°C) is much higher than that of DPs with standard galvanizing processing D1, Figure 5.7.10. Most of the DPs with E1 processing fall into the TRIP region (UTS x TE between 18000 and 22000 MPa%), and some of them even locate at the region of Generation III steel (UTS x TE exceeds 22000 MPa%). One reason for the good ductility of DPs with supercool processing is the higher amount of retained austenite in DPs with lower supercool temperatures as discussed in this section.

The importance of the retained austenite is that as in TRIP steels (transformation induced plasticity)^[145], the strain-induced transformation of small amounts of retained austenite into martensite during plastic deformation leading to strong hardening, excellent elongation and strength. So during the development of high strength dual phase steels, the amount of retained austenite should be considered and carefully controlled in order to get proper ductility of the dual phase steels.

Table 5.7.6. Amount of retained austenite from magnetic measurements

ID	Ms(emu/g)	%RA	ID	Ms(emu/g)	%RA
2B1E, E1	185.78	8.56	2B3E, E1	184.67	7.67
2B1E, E2	187.67	7.63	2B3E, E2	182.83	8.59
2B1E, E3	193.30	4.86	2B3E, E3	191.49	4.26
2B1E, D1	201.58	0.79	2B3E, D1	193.45	3.28
2B1E, Anneal	203.18	-	2B3E, Anneal	200.00	-
2B1A, E1	185.82	2.43	2B3A, E1	187.50	5.12
2B1A, E2	185.88	2.40	2B3A, E2	190.00	3.85
2B1A, E3	189.53	0.48	2B3A, E3	195.93	0.85
2B1A, D1	190.20	0.13	2B3A, D1	195.29	1.17
2B1A, Anneal	190.45	-	2B3A, Anneal	197.61	-

Note: Ms is the value at field 16.66kG.

5.7.4 Precipitation hardening from the benefits of vanadium additions

The precipitation hardening from vanadium carbide or vanadium nitride in various types of steels has been extensively studied^[146-149], and this section will discuss the precipitation hardening from vanadium carbides in high strength dual phase steels processed by continuous galvanizing line simulations. The effects of thermomechanical processing before annealing process will be emphasized and the whole process (from reheating to final galvanizing processing) will be carefully checked to discuss the precipitation of vanadium carbides.

The obvious increase in tensile strength (e.g. $\Delta UTS = 68.6$ MPa for 2B1E, E1) and yield strength (e.g. $\Delta YS = 91.3$ MPa for 2B1E, E1) due to the addition of 0.06 w.t% vanadium indicates that vanadium

can effectively increase the strength of dual phase steels processed with CGL procedures. Our results revealed that precipitation hardening of nano-sized VCx precipitates plays an important role to increase the strength and this section will discuss the precipitation hardening from vanadium contained precipitates.

Figure 5.7.18 shows the HRTEM images of vanadium contained nano-sized precipitates from carbon replicas of DP 2B1E, E1. The particles in 5.7.18 (c) are from the region in (a) and the EDX peaks are from the big particle in (c). The strong vanadium peaks confirmed the particles are vanadium contained precipitates. More EDX spectrums were obtained from the particles in (a) and the peaks are similar to (d), e.g., all with vanadium peaks. The Ni peaks are from the nickle grid, and Si, Mo peaks indicate that these particles are probably alloyed with Si and Mo as discussed in previous Section 5.3. Most of the particles are very fine (with size 2-5 nm), Figure 5.7.18 (a) and (b), and some big particles with size ~10nm can also be found, Figure 5.7.18(c). The dense fine precipitates in ferrite grains (identified from the morphology at low magnification) can effectively increase the strength according to the Orowan mechanism which can be described by the following equation^[146, 147]:

$$\sigma_{ppt} = \frac{0.8MGb}{L_{VC}} \text{ (MPa)} \quad (5.7.2)$$

where G is the shear modulus, b is the Burgers vector, M is the Taylor factor, and L_{vc} is the average inter-particle spacing, and is given by

$$L_{VC} = \sqrt{\frac{2}{3} \left(\sqrt{\frac{\pi}{f}} - 2 \right) \cdot r_{VC} \text{ (m)}} \quad (5.7.3)$$

where r_{VC} ($d_{vc}/2$) is the average radius and f is the volume fraction of precipitates (e.g., VCx particles).

As discussed in the previous sections, the amount of increase in strength is much more for high coiling temperatures compared with low coiling temperatures for both hot band steels and DPs with full CGL processing. The high coiling temperature, 650°C, is a preferential temperature for precipitation

hardening of VCx from our results of hot band steels and these precipitates continue to affect the cold rolling processing as can be seen from the hardness results of cold rolled sheets, and the strength of DPs after full CGL processing, which can be inferred from the strength and microstructures of the DPs with low and high coiling temperatures (e.g., 2B1E, E1 and 2B3E, E1, which have similar microstructures, and the microstructure in 2B1E, E1 is even coarser than that in 2B3E, E1).

To understand how the precipitates can effectively strengthen the dual phase steels, it is necessary to look carefully at every step (from reheating for hot rolling to final CGL processing) to trace the precipitation behavior of vanadium contained particles.

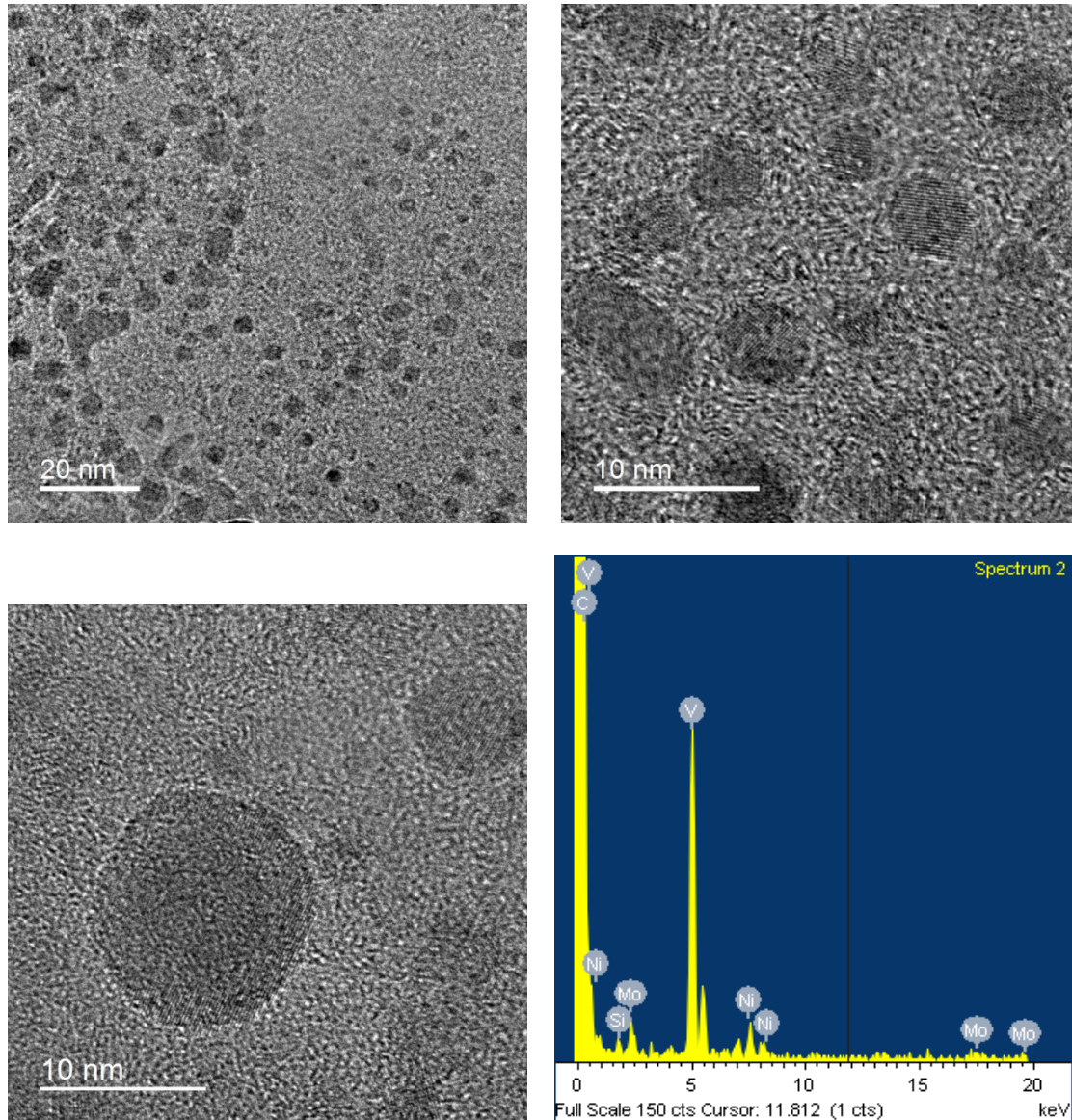


Figure 5.7.18. HRTEM images of DP 2B1E, E1 (50%CR, high CT 650°C), showing fine and dense VCx precipitates in ferrite matrix.

To effectively use the precipitation hardening from vanadium carbides or carbonitrides, it is necessary to sufficiently dissolve all the vanadium into austenite during reheating, and carefully control the subsequent thermomechanical processing (rough rolling, finish rolling, coiling et. al.) and even the final processing (e.g., dual phase producing process) for the vanadium carbides or carbonitrides to sufficiently precipitate as fine and dense precipitations in the ferrite matrix. As the precipitation of vanadium carbides is very sluggish in austenite, the extensive precipitation of vanadium carbides is

expected to mainly occur in the ferrite matrix instead of in austenite or martensite, which is consistent with our TEM results that vanadium carbides can be frequently found in the ferrite matrix of our dual phase steels. Compared with other alloying elements (e.g., Nb or Ti), vanadium has a rather high solubility in austenite even at temperatures as low as 1050°C. For the reheating temperature, 1250°C, in this study, all the vanadium dissolved in the austenite, which can be supported by the data in Figure 5.7.19 (a) and the calculated results from JMatPro in Figure 5.7.21 (a). Above 1100°C, the vanadium content in V(C,N) is zero meaning no vanadium carbonitride precipitates and all the vanadium is in the solid solution state, as can be seen from Figure 5.7.19(a). Figure 5.7.21(a) indicates that vanadium contained particles start to precipitate until cooling to 790°C from the austenitizing temperature. After rough rolling, all the vanadium dissolved in austenite can be expected. After cooling to the finish rolling temperature, 921°C, most vanadium is still in the solid solution state as indicated from Figure 5.7.19(a) which gives very low vanadium content in V(C,N) and Figure 5.7.21(a) which shows no V(C,N) precipitation above 800°C at the equilibrium state.

After finish rolling, the precipitation of vanadium carbides or carbonitrides started and the extent (e.g., volume fraction, density or size) closely depends on the coiling temperatures. As discussed above (Section 5.5), the coiling temperatures can significantly affect the strength of hot band vanadium bearing steels, e.g., the increase in UTS is 94MPa and the increase in YS is 110MPa when we compare HB steels 2A1C and 2B1C both with high coiling temperature 650°C, while the increase in UTS is only 5MPa and the increase in YS is just 9MPa when we compare HB steels 2A3C and 2B3C both with low coiling temperature, 500°C. These results are consistent with the results reported in literature and the precipitation hardening from vanadium contained precipitates contributed to this significant increase in strength. The reason for the effects of coiling temperatures on the vanadium precipitation has been partially discussed earlier (Section 5.5).

Figure 5.7.19 (b) illustrates the driving force-temperature relationship for VC and VN in steels cooled from austenitization temperature to until 600°C. As can be seen from Figure 5.7.19 (b), the driving force $\Delta G_m/RT$, which is a free energy difference between the product and parent phases, increased with

decreasing the temperature for both VC and VN, and the slopes for VN lines changed due to the phase transformation of austenite to ferrite. From this relationship between driving force and temperature, it can be expected that decreasing coiling temperature can increase the driving force and thus promote the vanadium precipitation at the temperature range from 600°C to about 1030°C (VN) or 830°C (VC). When further decreasing coiling temperature to 575°C or even 500°C, the precipitation behavior of vanadium contained particles changed due to phase transformation to different types of ferrite and decreasing in the diffusivity of carbon. As can be seen in Figure 5.7.19(b), the VC line has only one single slope since the calculation takes only one type of ferrite into consideration. When cooing to temperatures 575°C or 500°C, more acicular or bainitic ferrite formed instead of polygonal ferrite formed at 650°C. Our results of mechanical properties of hot band steels indicate that the precipitation hardening from vanadium is very limited in acicular or bainitic ferrite which can be explained as that when lowering coiling temperatures the bainitic ferrite with more internal stress or strain and dislocations or low angle grain boundaries trapped more amount of carbon, which can be inferred from the fact that no pearlite found in HB steels with low coiling temperatures while the microstructure in HB steels with high coiling temperature consist of polygonal ferrite and pearlite, and thus retarded the formation of VC precipitates in the bainitic ferrite. Also low temperatures decreased the diffusivity of carbon and thus retarded or even prevented the redistribution of carbon and the formation of vanadium carbides from the view point of kinetics of precipitation. Another possible reason is that the Gibbs free energy of VC is raised at acicular or bainite ferrite due to more defects and higher stored energy compared with polygonal ferrite and thus reduced the driving force for precipitation or at least decreased the slope of the line (driving force-temperature relationship line) when further lowering temperature. All these factors explained the very limited precipitation hardening for HB steels with low coiling temperature compared with those steels with high coiling temperatures.

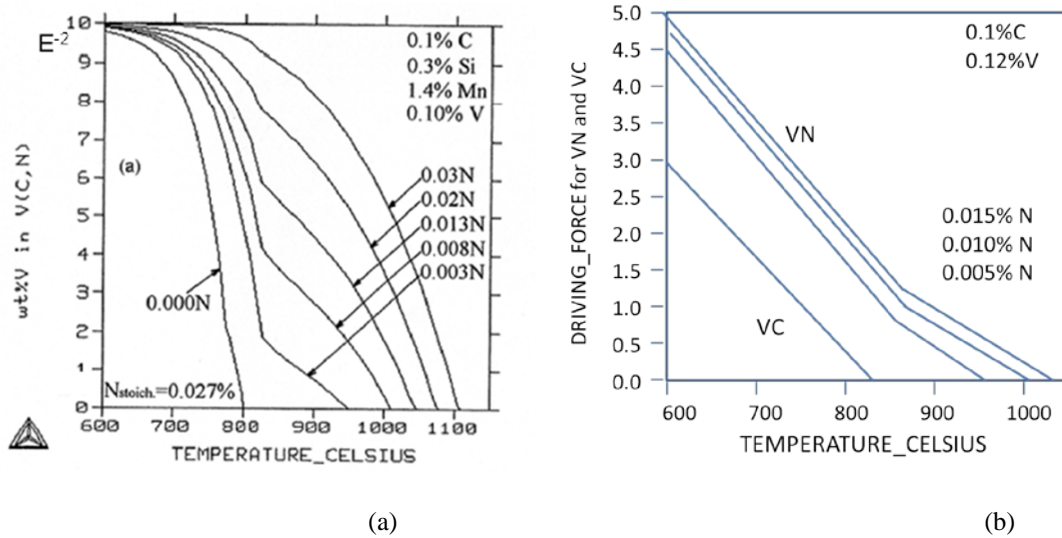


Figure 5.7.19. (a) example showing the precipitation of nitrides, nitrogen-rich carbonitrides and carbides in 0.10% V steels at various nitrogen contents, (b) chemical driving force, $\Delta G_m/RT$, for precipitation of VC and VN in 0.12% V steel^[150].

From the above discussion, dense vanadium contained precipitates can be expected in the polygonal ferrite in the hot band vanadium bearing steels according to the significant increase in strength (UTS and YS). After cold rolling, these existing precipitates are assumed to remain in the cold rolled ferrite and moreover, new precipitates may form during cold rolling due to strain induced precipitation effects. Figure 5.7.20 shows HRTEM images of VC_x particles in 2B1E 50% cold rolled sheets before heat treatments. As expected, vanadium contained particles can be easily found under TEM. Figure 5.7.20 (a) and (b) show some big particles with size about 10nm, and (c) shows some fine particles with size less than 5nm. The EDX in 5.7.20(d) is from the particles indicated by the arrow in (c) and the strong vanadium peaks confirmed that these particles are vanadium contained precipitates. Again Si and Mo peaks can also be found indicating that these particles are alloyed with Si and Mo. The Cu peaks are from the copper grid which supported the carbon replica films. For HB vanadium bearing steels with low coiling temperature, 500°C, a little vanadium precipitation effect is expected and most vanadium is in solid solution state in bainitic ferrite (Bs 578°C with austenitizing temperature, 921°C, for 2B from JMatPro prediction) as can be seen in Section 5.5.2. After cold rolling (50% or 80%), deformation

induced precipitation is not obvious for these hot band steels with low CT, 500°C, according to the hardness results of cold rolled high alloyed steels listed in Table 5.7.4.

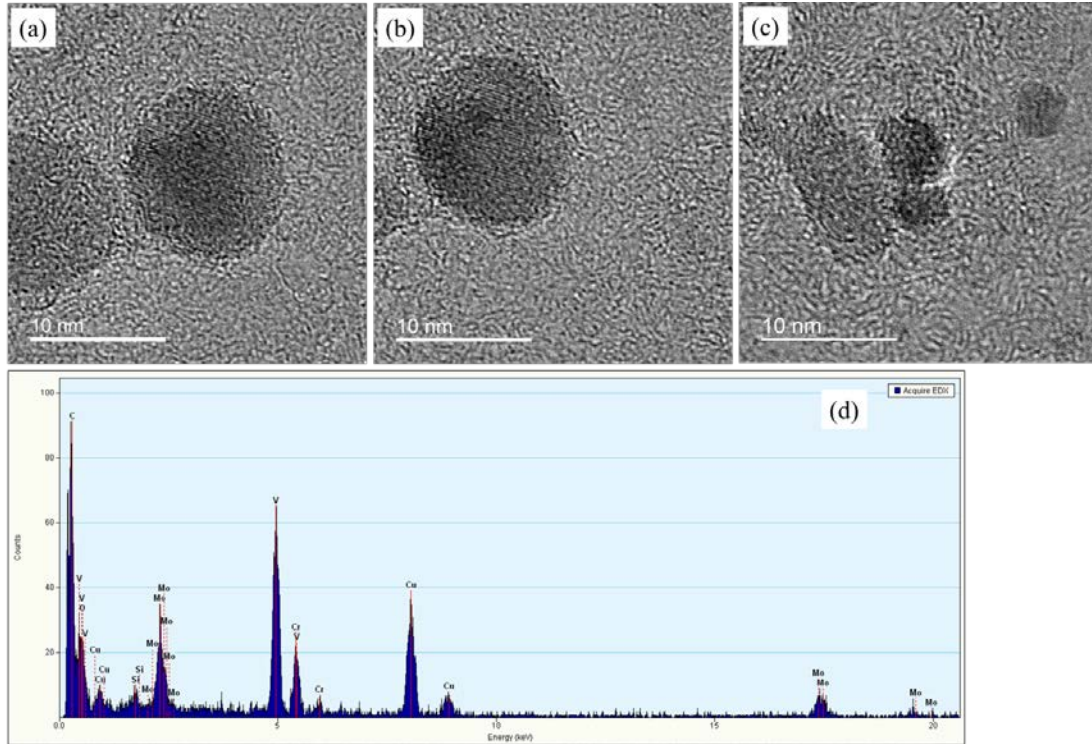


Figure 5.7.20. HRTEM images of VC_x particles (a-c) in 2B1E (50%CR) cold rolled sheets (without heat treatments), (d) is the EDX from the particles indicated by the arrow in (c).

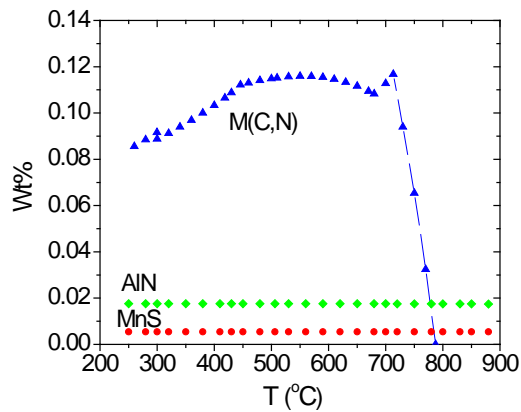
Starting from the cold rolled sheets, to understand how vanadium can strengthen dual phase steels needs to study the precipitation behavior during intercritical annealing and subsequent processing (e.g., cooling to different supercool temperatures and holding at zinc pot temperature). The predicted amount of vanadium contained precipitates (Figure 5.7.21(a)) and the compositions of the precipitates (Figure 5.7.21(b)) at equilibrium state for 2B steel from JMatPro is helpful to explain the precipitation behavior during intercritical annealing and cooling. From this prediction, the vanadium contained particles (M(C,N)) start to precipitate at temperature $\sim 790^{\circ}\text{C}$ (787°C predicted by JMatPro), which means that at IAT 790°C the driving force for precipitation is low, i.e., the free energy difference between product M(C,N) and parents is small, and on the other hand the driving force for the dissolution of existed

vanadium contained precipitates is also low for the same reason. At lower temperatures (e.g. 250°C-460°C), though the driving force for precipitation is high, the formation of precipitates takes longer time due to the low mobility of alloying elements and diffusivity of carbon. For cold rolled sheets with high CT 650°C, the dense existing precipitates continue to affect the strength of dual phase steels with final processing (Galvanizing or supercool processing). During intercritical annealing at 790°C, little existed precipitates in deformed polygonal ferrite dissolved due to low driving force for dissolution, while the steel experienced recovery of ferrite, re-precipitation of cementite, recrystallization of ferrite, nucleation of austenite, dissolution of cementite and growth of fresh austenite at the end of intercritical annealing. The recrystallization of ferrite may take place around $V(CN)_x$ as nucleus and still maintain the fresh ferrite with high dense of precipitates. The coherency with the ferrite matrix is assumed to be similar to that when particles precipitate from solid solution state into ferrite, thus in this way, the old existed dense precipitates can still effectively strengthen the steels as the fresh precipitated particles according to the strengthening mechanism of precipitation hardening. Austenite nucleated at high carbon area, e.g. deformed pearlite, vanadium carbides as nucleus, or high stored energy area where high dislocation density, carbon segregation around dislocations, and high carbon diffusivity can be expected, and during the migration of austenite ferrite phase boundary into vanadium carbides area, the intercritical formed austenite or martensite can also be hardened by vanadium precipitation in this case, though this effect is not as significant as that in ferrite. Following annealing at IAT for 1 minute, the steel was cooled to zinc pot temperature 460°C or supercool temperatures (250°C-390°C), and then after holding for some time (20-30s) cooled to room temperature. Since the total time is less than 2 minutes and almost all the vanadium has been consumed after coiling at 650°C and cold rolling, the precipitation of vanadium contained carbides after annealing is expected to be little, and thus the strengthening of dual phase steels with high CT is mainly from the existed dense precipitates during high temperature coiling. For cold rolled sheets with low CT 500°C, most vanadium is in the solid solution state in the cold rolled bainitic ferrite, during holding at IAT 790°C, it is possible for the precipitation of vanadium carbides, though the driving force is not high, and during the following processing (holding at zinc pot temperature or

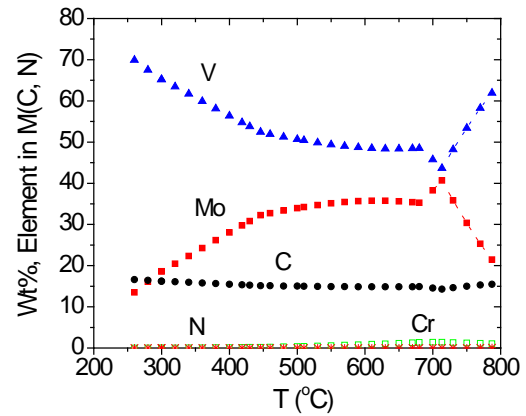
supercool temperatures, and tempering at zinc pot temperature after supercool stage) the precipitation can still occur due to high driving force at low temperature though the precipitation is not complete which is limited by the precipitation kinetics since the diffusivity is very low. Thus the increase in strength due to vanadium for DP steels with low CT is mainly from the solid solution hardening of the vanadium atoms and some of the precipitated vanadium contained particles during CGL processing.

The precipitation hardening is more effective in steels with 50%CR than those with 80%CR, since with severe cold reduction 80%, the significant microstructure refinement further strengthened the DP steels and thus the precipitation hardening effect is relatively lower among all the strengthening factors. The most successful usage of precipitation hardening of vanadium contained particles can be observed when comparing DPs 2A1E, 2B1E, E1 ($\Delta UTS=68.6\text{MPa}$, $\Delta YS=91.3\text{MPa}$), 4A1E, 4B1E, D1 ($\Delta UTS=89.6\text{MPa}$, $\Delta YS=68\text{MPa}$), all of which are with high CT and low cold reduction. It can also be found in Figure 5.7.21(b) that the vanadium carbonitrides are also alloyed with Mo, which is consistent with our EDX results which indicate that the particles contain Mo, Si besides the main alloying element V. The content of N in $M(C,N)$ is nearly zero indicating that most of the vanadium contained particles are vanadium carbides. Figure 5.7.21(c) shows that almost all the nitrogen is attached to Al forming AlN and little nitrogen left in ferrite, martensite (austenite) or $M(C,N)$. These results show that in the present steels (high Al, low N and high V), the vanadium carbides actually played role to strengthen DP steels instead of vanadium nitrides. To effectively use the vanadium nitrides to strengthen DP steels, the contents of Al should be lowered and the amount of nitrogen should be increased.

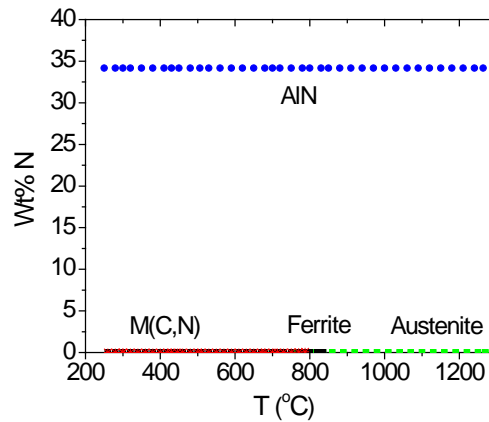
From the above discussion, the precipitation hardening from the benefits of vanadium additions definitely influenced the yield strength, work hardening and finally the tensile strength of dual phase steels, which can clearly be seen from the results of mechanical properties of vanadium free and vanadium bearing steels in Sections 5.5 and 5.6.



(a)



(b)



(c)

Figure 5.7.21. Predicted results from JMatPro4.0 of 2B (vanadium bearing steel), (a) amount of precipitates (M(C,N), M is alloying elements, AlN and MnS), (b) weight percent of different elements in M(C,N) and (c) contents of nitrogen in different phases (Austenite, ferrite, M(C,N) and AlN) at different temperatures at equilibrium states.

5.7.5 Work hardening of vanadium bearing dual phase steels

Work hardening behavior is very important for structural application of dual phase steels. The strain hardening exponent or work hardening ratio (n) in the Hollomon equation^[151]:

$$\sigma = K\epsilon^n \quad (5.7.4)$$

is an indicator for work hardenability of the material (e.g. metals). As discussed in previous Section 2, without any assumptions of deformation mechanisms, the instantaneous slope n of $\ln\sigma$ - $\ln\epsilon$ line can well describe the work hardening behavior of dual phase steels. The higher the n value, the more the material will be hardened during deformation and so the material can deform or be stretched more before plastic deformation instability or necking. The uniform elongation (elongation before peak loading or necking) is closely related to n , e.g., Davies^[83] has reported a good agreement between uniform elongation and n , and higher n values usually result in higher uniform elongations. Dual phase steels exhibit high strain hardening behavior (especially at initial plastic deformation stage) as one of its characteristic properties, and the high work hardening ratios between yield strain 0.2% and uniform strain can effectively increase strength after yielding of the material, and thus it leads to higher peak strength (UTS) and low yield strength to tensile strength ratios. This section will discuss the work hardening behavior of vanadium bearing dual phase steels with various conditions, the mechanical properties of which can be found in Sections 5.5 and 5.6.

Table 5.7.7. Strain hardening exponents n -values (4%-6% engineering strain) and uniform elongations of DPs with high Cr, Mo contents.

ID	n (4%-6% engineer strain)	UE% 2inch	ID	n (4%-6% engineer strain)	UE% 2inch
2A1A, D1	0.1541	7.66	2B1A, D1	0.1485	8.58
2A3A, D1	0.1697	9.62	2B3A, D1	0.1578	9.68
2A1E, D1	-	4.99	2B1E, D1	0.1485	10.53
2A3E, D1	0.1474	8.72	2B3E, D1	0.1526	11.64
2A1A, E1	0.1627	10.46	2B1A, E1	0.1558	8.71
2A3A, E1	0.1586	10.10	2B3A, E1	0.1561	8.70
2A1E, E1	0.1527	11.31	2B1E, E1	0.1410	10.33
2A3E, E1	0.1599	11.01	2B3E, E1	0.1615	12.70
2A1A, E2	0.1753	9.34	2B1A, E2	0.1662	8.72
2A3A, E2	0.1672	8.10	2B3A, E2	0.1760	9.50
2A1E, E2	0.1663	11.22	2B1E, E2	0.1450	9.02
2A3E, E2	0.1819	11.77	2B3E, E2	0.1734	10.96
2A1A, E3	0.1735	9.80	2B1A, E3	0.1676	9.62
2A3A, E3	0.1802	11.36	2B3A, E3	0.1554	8.70
2A1E, E3	0.1810	12.83	2B1E, E3	0.1569	11.41
2A3E, E3	0.1881	14.84	2B3E, E3	0.1584	10.40

Table 5.7.8. Strain hardening exponents n-values (4%-6% engineering strain) and uniform elongations of DPs with low Cr, Mo contents.

ID	n	(4%-6% engineer strain)	UE% 2inch	ID	n	(4%-6% engineer strain)	UE% 2inch
4A1A, D1		0.2462	13.61	4B1A, D1		0.2297	13.32
4A3A, D1		0.2407	11.49	4B3A, D1		0.2227	12.34
4A1E, D1		0.2423	16.88	4B1E, D1		0.2038	15.32
4A3E, D1		0.2439	18.05	4B3E, D1		0.2330	14.72
4A1A, E1		0.2421	15.29	4B1A, E1		0.2507	15.00
4A3A, E1		0.2614	15.82	4B3A, E1		0.2471	15.12
4A1E, E1		0.2311	17.59	4B1E, E1		0.1977	15.06
4A3E, E1		0.2433	19.69	4B3E, E1		0.2235	16.93
4A1A, E2		0.2472	14.73	4B1A, E2		0.2390	12.92
4A3A, E2		0.2541	15.31	4B3A, E2		0.2418	12.81
4A1E, E2		0.2348	16.99	4B1E, E2		0.2064	14.07
4A3E, E2		0.2493	16.19	4B3E, E2		0.2291	15.10
4A1A, E3		0.2578	16.86	4B1A, E3		0.2412	13.58
4A3A, E3		0.2597	15.55	4B3A, E3		0.2563	15.10
4A1E, E3		0.2439	16.35	4B1E, E3		0.2064	14.33
4A3E, E3		0.2594	17.68	4B3E, E3		0.2347	15.86

Tables 5.7.7 and 5.7.8 listed the strain hardening exponents n-values by linearly fitting the $\ln\sigma$ - $\ln\epsilon$ data in the engineering strain range 4%-6%. The n-values in this range are more important for industrial applications of dual phase steels. The uniform elongations are also listed in the Tables. Figure 5.7.22 plotted the n-values versus uniform elongations data, and the black line is the linearly fitted line with linear equation $UE\% = 63xn + 0.13$. The coefficient of determination for linear fitting R^2 is 0.71 and the calculated Pearson's correlation coefficient ρ is 0.84, which indicate that there is strong positive relationship between strain hardening exponent and uniform elongations. These results show that higher uniform elongation or ductility can be expected for dual phase steels with higher strain hardening exponent.

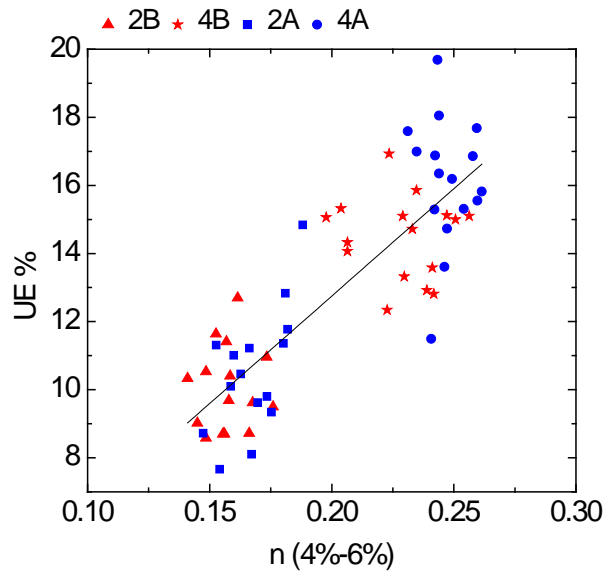


Figure 5.7.22. UE-n-value data points for low alloyed and high alloyed steels with various conditions (all the data of the 64 steels in Tables 5.7. and 5.7. were included). The black line is fitted by linear equation, $UE=63xn+0.13$, the coefficient of determination R^2 is 0.71, and the Pearson's linear correlation coefficient ρ is 0.84.

The strain hardening exponents between engineering strain 0.2% and 0.5% are given in Tables 5.7.9 and 5.7.10 for steels with high coiling temperature. It is to be noted that the linear relationship between $\ln\sigma$ and $\ln\epsilon$ indicates that true stress and true strain obey the metal plastic deformation law, i.e. Hollomon equation, and so in this strain range, the deformation is treated as plastic deformation instead of linear elastic deformation. Regardless of what deformation (plastic or elastic) it is in this range, the strain hardening exponents in this very beginning strain range do give us some information on different strengthening mechanisms. Figure 5.7.23 plotted the strain hardening exponents in these two tables. The higher n-values for high alloyed steels compared with low alloyed steels mean more stress was needed to increase the same small amount of strain at low strain range, which indicates that the ferrite was effectively hardened by higher contents of Cr, Mo for steels 2A and 2B. At the low strain range, the strain hardening exponents of vanadium bearing steels are higher than those of vanadium free steels with the same heat treatments, which is probably from the pinning effects of vanadium carbides or solute vanadium atoms if the initial microstructures and dislocation density are assumed to be similar for

vanadium bearing steels and the corresponding vanadium free steels. In the higher strain range, e.g. 4%-6%, the strain hardening exponents of higher alloyed steels are lower than those of low alloyed steels, which may be explained as that since the ferrite grains are finer in high alloyed steels, the mean free path among dislocations is shorter than that in the coarse ferrite grains in low alloyed steels, thus in the higher strain range, the possibility of annihilation of dislocations is higher, which is one reason that results in lower strain hardening exponents in high alloyed steels.

Table 5.7.9. Work hardening exponent n-values between engineering strain 0.2% and 0.5%.

Sample ID	V-free	Engineering strain 0.2%-0.5%	V-bearing	Engineering strain 0.2%-0.5%
1	2A1E, D1	0.4676	2B1E, D1	0.4965
2	2A1E, E3	0.4286	2B1E, E3	0.5109
3	2A1E, E2	0.4430	2B1E, E2	0.5590
4	2A1E, E1	0.4738	2B1E, E1	0.6048
5	2A1A, D1	0.4995	2B1A, D1	0.4953
6	2A1A, E3	0.4131	2B1A, E3	0.4759
7	2A1A, E2	0.4496	2B1A, E2	0.4302
8	2A1A, E1	0.4213	2B1A, E1	0.6325

Table 5.7.10. Work hardening exponent n-values between engineering strain 0.2% and 0.5%.

Sample ID	V-free	Engineering strain 0.2%-0.5%	V-bearing	Engineering strain 0.2%-0.5%
1	4A1E, D1	0.2689	4B1E, D1	0.4204
2	4A1E, E3	0.2478	4B1E, E3	0.2693
3	4A1E, E2	0.3134	4B1E, E2	0.3295
4	4A1E, E1	0.2521	4B1E, E1	0.2449
5	4A1A, D1	0.2186	4B1A, D1	0.2562
6	4A1A, E3	0.2058	4B1A, E3	0.2424
7	4A1A, E2	0.2597	4B1A, E2	0.2804
8	4A1A, E1	0.2414	4B1A, E1	0.1975

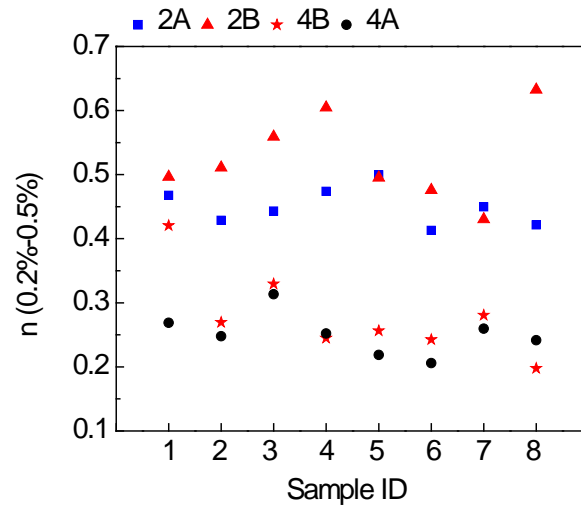


Figure 5.7.23. Work hardening ratios between engineering strain 0.2% and 0.5%, i.e. just after yielding of the steels, of the steels with high coiling temperatures 650°C, the sample IDs are listed in Tables 5.7.9 and 5.7.10

Some of the typical $\ln\sigma$ versus $\ln\varepsilon$ curves of Gleeble processed dual phase steels were plotted in Figures 5.7.24 and 5.7.25. Figure 5.7.24 (a) compared the work hardening behavior of 2B1E and 2A1E with supercool E1 (250°C) processing, from which two stage work hardening behavior can be observed for these two steels. As can be seen, before true strain 0.26% the two curves almost overlapped together, from which similar initial microstructures which were discussed in Section 5.5 and dislocation density can be expected for 2A1E, E1 and 2B1E, E1. After true strain ε about 0.26%, the two curves started to separate from each other, and the DP steel 2B1E (E1) was hardened more than 2A1E (E1), which reflected the pinning effects of vanadium precipitates. During work hardening at the first after yielding, i.e. ferrite grains with high dislocation density near ferrite martensite phase boundaries plastically deformed firstly, the existed high density of vanadium carbides as shown in Section 5.7.4 segregated and pinned the dislocations and increased the stress needed to move these dislocations. So the work hardening ratio ($n_1=0.60$) of 2B1E (E1) is much higher than that ($n_1=0.45$) of 2A1E (E1) at the first stage. The second work hardening stage started after the plastic deformation of tempered martensite (TM). The work

hardening ratio is lower at the second stage than that at the first stage. It can be found that the transition strain from first stage to second stage for 2B1E (E1) is higher than that for 2A1E (E1), which indicates that the TM is harder in 2B1E (E1) than that in 2A1E (E1), since the existed vanadium carbides may also strengthen the austenite and then TM as discussed in the previous Section 5.7.4. The work hardening ratios at the second stage for DP 2B1E (E1) and 2A1E (E1) are similar, while the a little bit lower n value for 2B1E (E1) can be explained as that due to the later transition strain, more dislocations accumulated in ferrite grains before TM deformed and so at the second stage, higher dislocation density in 2B1E (E1) result in higher possibility for dislocation annihilation and dynamic recovery which lowers the work hardening ratio.

From the above discussion, it is clear that the higher work hardening ratio at the initial plastic deformation stage and the raise in the strength level is mainly due to the precipitation hardening of dense vanadium carbides. One point should be noted is that the yielding discussed here is different from the yield strength in Sections 5.5 and 5.6, since they were analyzed in two different ways. The 0.2% yield strength is obtained by drawing a parallel line at 0.2% engineering strain to the elastic portion from the engineering strain – stress curves, i.e. the value at 0.2% plastic strain, which corresponds to the strength somewhat before the end of first stage work hardening discussed here, while for the continuous yielding for DPs, the real yielding point is difficult to find and here the plastic deformation is treated to start at early strain (e.g. 0.2% engineering strain) which seems to be helpful to understand different strengthening mechanisms at different deformation stages.

The two stage work hardening behavior can also be observed for DP 2A3A (E1) and 2B3A (E1) as shown in Figure 5.7.24(b), which plotted $\ln\sigma$ versus $\ln\varepsilon$ curves of these two steels. After yielding, firstly ferrite deformed attributing to the first stage work hardening, and then during the second work hardening stage, both of ferrite and tempered martensite deformed. As can be seen, before 1% strain, the two curves almost overlapped indicating the initial microstructure of 2A3A (E1) and 2B3A (E1) are similar, while after 1% strain, the strength increased more for 2B3A (E1) with increasing strain compared with that for 2A3A (E1), which probably revealed the effects of precipitation hardening from vanadium

carbides. As discussed in the previous Section 5.7.4, unlike the dense precipitation in the initial microstructure in 2B1E (E1), more vanadium is still dissolved in the ferrite matrix though the precipitation of vanadium carbides can still be expected in 2B3A (E1). After proper deformation (e.g. here 1%) more vanadium carbides precipitated due to the strain induced precipitation mechanism and pinned the moving dislocations, resulting in higher stress to further move the dislocations or deform the steel, and thus the work hardening ratio of 2B3A (E1) is larger than that of 2A3A (E1) after 1% strain. The blocking or pinning effects from vanadium precipitations increased the work hardening ratio after 1% true strain at the second stage of work hardening.

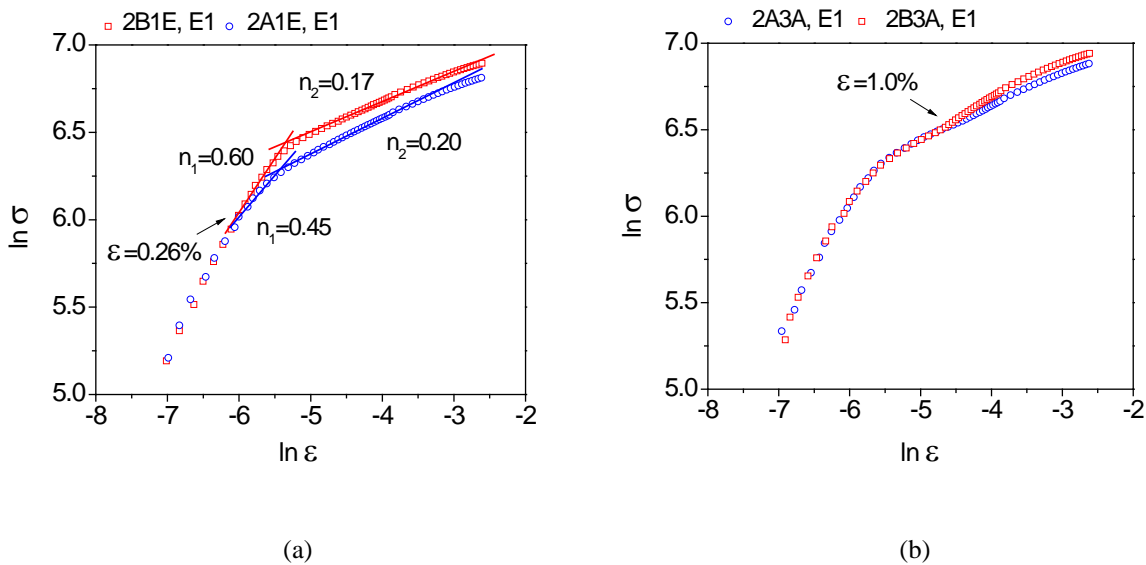


Figure 5.7.24. $\ln\sigma$ - $\ln\epsilon$ curves of DPs with E1 processing.

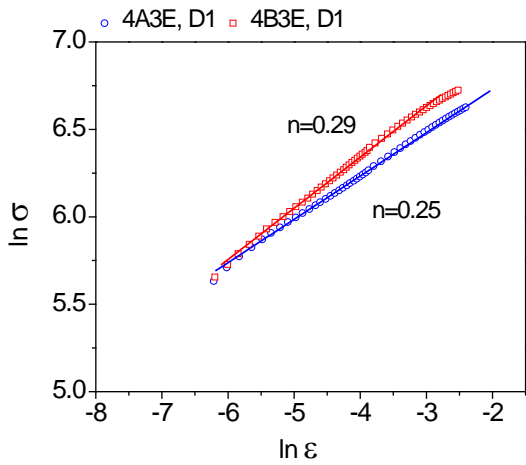
The work hardening behaviors of DPs with low Cr, Mo contents were studied and the $\ln\sigma$ versus $\ln\epsilon$ curves were plotted in Figures 5.7.25 (a) and (b) for 4A3E, 4B3E, 4A3A and 4B3A with D1 processing. For these steels, only one work hardening stage can be found, as can be seen from Figure 5.7.25 that the data points (marked by circle and square) can be well fitted using one linear function. As we know, the first work hardening stage is from the plastic deformation of ferrite and the second stage is due to plastic deformation of both ferrite and martensite (or tempered martensite), so the one stage work hardening for low alloyed DPs with D1 processing in Figure 5.7.25 can be explained as that due to the

low amount of martensite which is less than 15% or even 10%, the deformation of ferrite mainly contributed to the work hardening ratios and before reaching uniform elongation (or maximum strength), no martensite deformed or the contribution from the deformation of martensite is too small to be detected from the $\ln\sigma$ - $\ln\varepsilon$ curves, and on the other hand, low amount of martensite means higher carbon concentration in martensite, results in harder martensite and makes the martensite difficult to deform. The work hardening ratios of 4A3A (D1) and 4B3A (D1) are about the same, and the a little bit higher n value of 4B3E (D1) than that of 4A3E (D1) may come from the pinning effects from solute vanadium which is weaker than precipitation pinning effect. The similar n-values for the four low alloyed steels in Figure 5.7.25 indicate that the precipitation hardening is not obvious in steels with low coiling temperature. The $\ln\sigma$ - $\ln\varepsilon$ curve of 2B3A (D1) was also plotted in Figure 5.7.25(b), which shows non-linear relationship between $\ln\sigma$ and $\ln\varepsilon$. The two stage work hardening behavior can be observed after linearly fitting the lower portion and upper portion of the $\ln\sigma$ - $\ln\varepsilon$ curve, and the n-values of the two stages were also given in the figure. Unlike the steels with E1 processing in Figure 5.7.24 where there is an obvious transition point between first and second stages, there is only a transition interval (or region) for 2B3A (D1) as can be seen from Figure 5.7.25(b). One reason for this continuous progressive transition region between first and second work hardening stages for 2B3A (D1) is the deformation of ferrite martensite phase boundaries, as we see in Section 5.5 very fine martensite islands uniformly distributed in ferrite matrix with fine ferrite grains which leads to very high area fraction of ferrite martensite phase boundaries. So the extensive deformation or relative movement of phase boundaries contributed to the transition region and then after the deformation of martensite, the second work hardening stage started. Since tempered martensite is softer than martensite, the TM can deform more severely than martensite, which may explain the much clearer transition point in DPs with E1 processing (Figure 5.7.24) compared with those with D1 processing (Figure 5.7.25(b)).

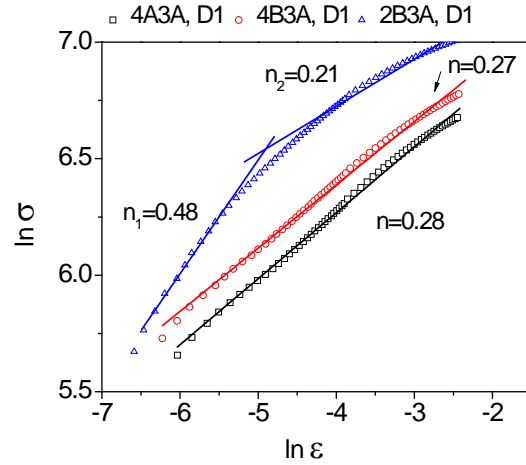
Another typical relationship of $\ln\sigma$ - $\ln\varepsilon$ curves for vanadium bearing and vanadium free steels is illustrated in Figure 5.7.25(c) which plotted the $\ln\sigma$ - $\ln\varepsilon$ curves of 2A3E (E1) and 2B3E (E1). Two-stage work hardening behavior can also be observed for these two curves. The higher n-value and lower stress

for 2B3E (E1) is due to the higher density of dislocations in the initial microstructures of 2B3E (E1) compared with 2A3E (E1). The interaction of dense dislocations as well as the pinning effects from precipitation and solute alloying elements leads to the higher work hardening ratio at the initial plastic deformation stage, on the other hand, the existed higher density of dislocations makes the steel start to plastic deform more easily and so the stress is lower at the earlier strain for 2B3E (E1). The work hardening ratios of 2A3E (E1) and 2B3E (E1) are about the same at the second stage, which means the deformation of tempered martensite (harder phase), blocking, generation and annihilation of dislocations dominated the work hardening behavior at the second stage, while the pinning effects of precipitation or solute alloying elements is not significant at the second stage.

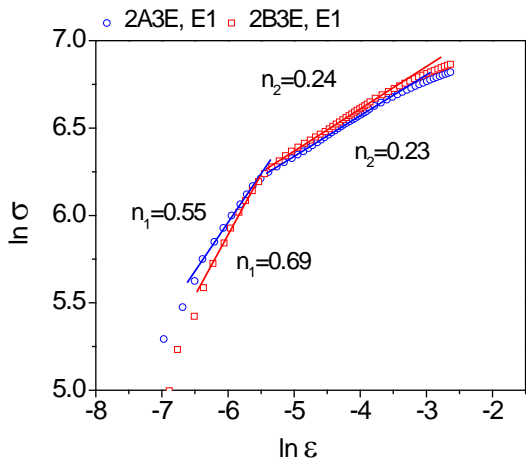
From the above discussions, we see that the analysis of work hardening behavior is very useful and can give us much information on different mechanisms at different deformation stages. However due to the complicated microstructures and situations, it is still difficult to completely and clearly understand the relationship between plastic deformation and microstructures, which involves considerations of dislocations, precipitations, microstructures and so on.



(a)



(b)



(c)

Figure 5.7.25. $\ln \sigma$ - $\ln \epsilon$ curves of DPs with D1 and E1 processing.

6.0 CONCLUSIONS

This project focuses on the development of high strength vanadium bearing dual phase steels with good ductility using continuous galvanizing line simulations. Several important factors during producing of DP steels were carefully investigated, e.g., intercritical annealing temperature, dissolution of cementite, holding time at zinc pot temperature, recrystallization behavior of cold rolled ferrite and so on. The mechanical properties of DPs with vanadium additions and with other alloying elements (e.g. Nb) were compared and discussed, and the main reason for the relatively lower strength of DPV was solved. For the annealing part (full Gleeble processing), it was found that through the modification of standard galvanizing processing to supercool processing, significant improvement of ductility (elongations and sheared edge formability) can be obtained, while for the pre-annealing part, we carefully investigated different parameters (coiling temperatures, cold reductions) of the thermomechanical processing, and found under proper conditions, the precipitation hardening from vanadium carbonitrides and refinement of microstructures can effectively strengthen the DP steels. With low Cr, Mo contents, the mechanical properties of the new developed DP steels are between DP590 and DP780 steels, which is attractive due to the lower cost. All the developed high strength DP steels contain low carbon contents (0.1%), which assured the good spot welding properties. Finally the sheared edge formability of the developed DP steels was systematically studied and some confusing problems (e.g. the relationship between hole expansion ratios and reduction in area or post uniform elongations, the effects of modification of hard phases on the hole expansion ratios) were carefully discussed. The main conclusions of each section were given in the following part of this section.

Section 5.1:

The results of this section have shown that the nature of the microalloying addition can influence the final microstructures and properties. The properties fell into three bands: (i) highest strength-low ductility (DPNbVN and DPNbV steels), (ii) intermediate strength and ductility (DPVN and DPNb steels), and (iii) lowest strength-highest ductility (DPV and commercial steels). The low strength of the DPV steel is mainly due to the low amount of martensite in the final microstructures which is caused by the low amount of austenite found after the intercritical anneal.

Complete dissolution of cementite during intercritical annealing is necessary in order to increase the hardenability and stability of the austenite, and thus increase the strength of the dual phase steels. Our choice of intercritical annealing temperature (790°C) can assure the complete dissolution of cementite after 1 minute intercritical annealing. The ductility of DP steels can be affected by the state of ferrite, i.e. DPs with recrystallized polygonal ferrite (e.g. DPV) possess better ductility than those with non-recrystallized elongated ferrite (e.g. DPVN). Among the DPs with 5 different compositions, DPV steels have the best sheared edge formability (hole expansion ratios).

The supercooling treatments C1 and C2 (790-250-460°C) indicate that it is possible to have high levels of strength, YS/UTS ratio and ductility at the same time.

Section 5.2:

In order to increase the strength of DPV steels, it is necessary to increase the amount of martensite in the final microstructures. The results in this section indicate that increasing the IAT, which can effectively increase the amount of austenite formed during 1 minute intercritical annealing, can't increase the amount of martensite in the final microstructures and the strength of DP steels, due to the low hardenability and stability of the austenite with low carbon contents. Instead of forming martensite, much of the austenite was transformed to bainite, and increasing cooling temperature (from 15°C to 60°C/s) can't effectively help to prevent the bainitic transformation and increase the strength to the required value (980°C). The intercritically formed austenite at higher IAT with low hardenability and stability makes the situations and phase transformations much more complicated.

Section 5.3:

This section investigated the effects of precipitation hardening from vanadium carbonitrides on the strength of dual phase steels. The results of this section indicate that the fine and dense vanadium contained precipitates in the final microstructures (the formation of vanadium carbonitrides was discussed in Section 5.7 in detail) can effectively prevent the decrease in strength (YS and UTS) with extending holding (from 30s to 120s) at zinc pot temperature 460°C for DPV and DPVN steels.

This section also carefully studied the crystal structures, chemical compositions of vanadium contained precipitates, as well as the orientation relationship between precipitates and the ferrite matrix using high resolution TEM. The aluminum nitride found in DPVN suggested that in order to effectively use the precipitation hardening of vanadium nitrides, the amount of aluminum should be low enough.

Section 5.4:

The tensile strength of dual phase steels is mainly the result of martensite present in the final microstructure, so to increase the strength of DP steels, one method is to increase the amount of martensite in the final matrix. The amount of martensite is controlled by the amount of austenite formed during intercritical annealing, which is one common step for producing DP steels. From the results of this section, we found that the amount of austenite formed during intercritical annealing is affected by the microalloying elements, and with the addition of Nb or N to DPV more austenite can be formed after 1 minute intercritical annealing. We also found that increasing the reduction of cold rolling, more austenite will be formed after 1 minute intercritical annealing.

The higher amount of austenite formed during intercritical annealing in 72% CR DPV is related to the higher stored energy in the initial microstructure. The sub-grain method was used to calculate the stored energy of our steels with different conditions. The calculated stored energy from sub-grain method is consistent with the IQ data and hardness values. From the stored energy data, we conclude that the 60% CR DPNbV and 72% CR DPV have higher stored energy than 60% CR DPV in the initial cold rolled microstructure. Even after heating to 740°C, the stored energy of 60% CR DPNbV and 72% CR DPV is higher than that of 60% CR DPV and DPVN. The higher stored energy is expected to speed the formation

of austenite during intercritical annealing and results in larger amounts of austenite. With more reduction by cold rolling, we got tensile strength higher than 980MPa after full CGL process simulation.

Sections 5.5-5.7:

The results of this study have shown that the presence of vanadium, coiling temperatures, levels of Cr and Mo contents, as well as cold rolling reductions can influence the final microstructures and properties of DP steels. The results show that low levels of Cr and Mo contents lead to lower strength, due to the lower hardness and stability of intercritically formed austenite and thus lower amount of martensite existed in the final microstructures.

In order to get high strength (>980MPa), the addition of vanadium is essential. For a 0.06% wt.% addition of vanadium, the tensile strength can be increased by 60-90 MPa in most cases, which is mainly from the finer microstructures (higher stored energy of initial cold rolled sheets, resulting in more ferrite recrystallization sites and austenite nucleation sites, which is essential for finer ferrite grain size and finer M islands), higher the amount of fresh M in the final microstructures (due to more stable austenite formed during intercritical annealing stage), and precipitation hardening of fine and dense vanadium carbides (which is related to coiling temperatures and subsequent processing).

For standard galvanizing processing (D1), the results indicate that the addition of vanadium can effectively increase the UTS up to 1019 MPa, and at the same time increase the total elongations compared with the corresponding DPs without vanadium addition of high alloyed steels.

From the present results, higher cold rolling reductions can result in much stronger DP steels, while low coiling temperature can give finer microstructures but not necessarily higher tensile strength, since the addition of vanadium plays an important role here. From our results, the hardening of ferrite by precipitation of vanadium carbides can effectively increase the strength if the coiling temperature 650 °C was applied. The grain refinement mainly is determined by cold reduction, which significantly affects the kinetics of intercritical austenite formation and nucleation of recrystallized ferrite.

Standard Galvanizing processing gives the highest strength. With supercool processing, good ductility and sheared edge formability can be attained. Most of our DPs steels reached the properties of

TRIP steels (18K), and some even located in the GERIII (22K) region. The ductility (in view of UTSxTE, UE vs. UTS) was raised with the addition of vanadium. At the same strength levels, vanadium bearing DPs possess higher sheared edge formability than vanadium free DPs.

7.0 FUTURE WORK

Through the study of this project, several problems regarding the production of high strength dual phase steels have been solved or carefully discussed, e.g. intercritical annealing temperature, cooling rates, and pre-thermomechanical processing, as can be seen in the conclusion section. Based on the conclusions drawn from this study, the following suggestions were made for future work:

1: Since Al can form AlN, whose solubility is lower than VN, making it a competitor to V for the available N, this reduced the precipitation strengthening from VN. In order to effectively use the vanadium in high strength DP steels, the Al content should be further lowered. Steels with low Al content can be used for future study. The effects of nitrogen on the properties of vanadium bearing DP steels need to be studied systematically by varying the contents of nitrogen.

2: The spot weldability of selected fully Gleeble processed steels needs to be evaluated using the spot welding equipment. The spot weldability of vanadium bearing DP steels can be compared to the vanadium free DP steels of similar strength levels or with the same heat treatment processing to clearly reveal the effects of vanadium additions.

3: The deformation mechanism during the expansion of the punched hole needs to be further studied in order to more deeply understand the reasons why DP steels with supercool processing possess higher hole expansion ratios than those with galvanizing process or vanadium bearing DP steels are stronger than vanadium free DP steels at the same levels of hole expansion ratios. These work includes the study of the microstructures and hardness of the sheared edge before hole expansion test and also how the cracks go through the thickness of the samples during testing, e.g. the relationship between crack propagation path and different phases. Some of these issues have already been studied, e.g. the crack tips

preferentially go along martensite and ferrite phase boundaries and can be stopped by the hard martensite island. These results and discussions were not contained in this thesis and more work is still under doing.

4: This thesis studied vanadium bearing DP980 steels with UTS 980MPa. For the next step, DP1180 steels with UTS 1180MPa level can be investigated. The development of DP1180 steels is clearly much more difficult. More amount of martensite is needed after full galvanizing processing, and so more C, Mn, Mo, and Cr need to be added in order to prevent the bainitic transformation during zinc pot holding of the higher amount of intercritically formed austenite. However, more amount of martensite will significantly reduce the elongations and higher amount of Mn may lead to severe martensite banding. The precipitation strengthening from vanadium may be helpful to obtain such high strength and thus lower some amount of martensite to get higher elongations and ductility.

APPENDIX A

AMOUNTS OF MARTENSITE AND ALN PARTICLE

Figures A1-A4 show the typical Lepera etched microstructures of DPV, DPNbV, DPVN and DPNb annealed at 780°C for 1 minute, 2 minutes and 5 minutes and then water quenched. The volume fractions of MA (white color, brown is ferrite matrix) are given in the figure captions and also listed in Table 5.1.11. After comparing these images, it is clear that with the addition of Nb, the amount of austenite formed during intercritical annealing is much higher than that in alloys with only V additions. However, the niobium bearing steels possess more severe martensite banding than those with only vanadium additions.

Figures A5-A7 show the EBSD mappings (IQ images and inverse pole figures (IPF)) and the IQ peak fitting curves of DPV, DPNbV and DPVN with GI (A3) standard galvanizing processing. The volume fractions of martensite, MA (martensite plus retained austenite), polygonal ferrite, non-recrystallized ferrite and retained austenite from IQ peak fittings are listed in Tables A1-A3. The background of the IQ peak method and the detailed calculations of volume fractions from IQ peak fitting can be found in the thesis of Dr. Jinghui Wu^[152]. Though the values of percent martensite of these three steels are different from (much less than) the values measured from SEM microstructures (see volume fractions of MA in Table 5.1.7), it still gives us the fact that DPNbV possesses highest amount of MA, while DPV possesses lowest amount of MA. Such differences come from the limitations of the EBSD-IQ fitting method, e.g. limited scanning area (may not be typical), throwing away pixels belonging to

martensite when removing the pixels of grain boundaries, and the risk of damaging the surfaces when preparing the samples. Moreover, EBSD method is time consuming and expensive. So the volume fractions of different phases at the present study were measured from OM or SEM images at several positions of quarter region. From these EBSD mappings, we can also see that DPNbV and DPVN steels have more small angle grain boundaries ($2-5^\circ$ and $5-15^\circ$).

Figure A8 shows one AlN particle at the ferrite grain boundary (carbon replica) for DPNbV (0.025%Al, 0.06%V) with GI (A3) standard galvanizing processing. All the steels in the present study contain 0.025-0.3% aluminum. The observed AlN particles in these DP steels indicate that Al can react with nitrogen (even the content of nitrogen is only 0.006%) to form aluminum nitride and thus the strengthening effects of VN precipitates will be significantly deteriorated. The 0.025% of Al concentration is not low enough to effectively use the strengthening of VN precipitates.

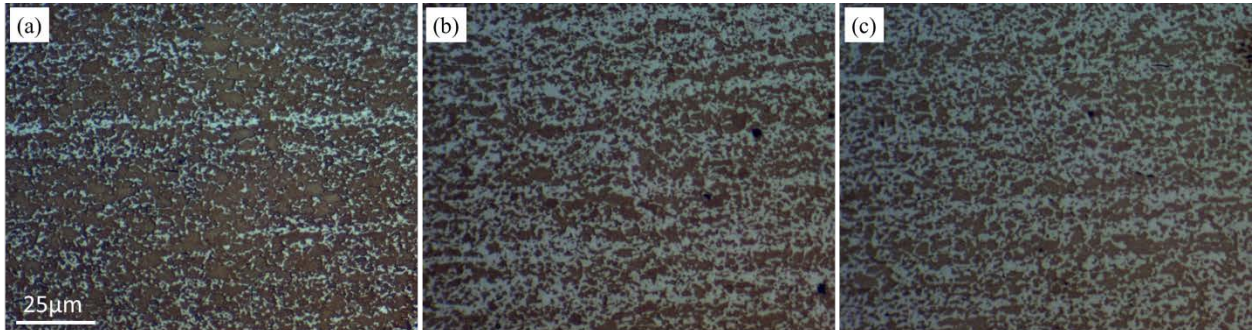


Figure A1. LePera etched microstructures of DPV annealed at 780°C for (a) 1 minute ($18\pm 1\%$ MA), (b) 2 minutes ($37\pm 2\%$ MA), and (c) 5 minutes ($39\pm 3\%$ MA) and then water quenched.

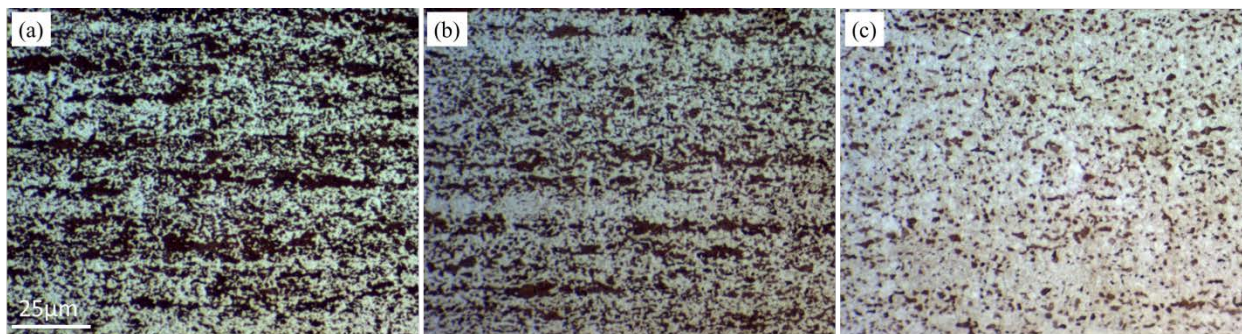


Figure A2. LePera etched microstructures of DPNbV annealed at 780°C for (a) 1 minute ($47\pm 2\%$ MA), (b) 2 minutes ($54\pm 1\%$ MA), and (c) 5 minutes ($85\pm 1\%$ MA) and then water quenched.

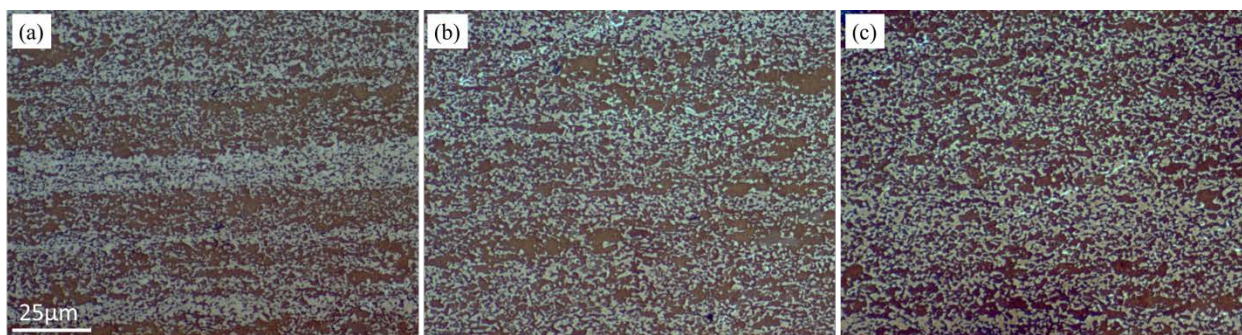


Figure A3. LePera etched microstructures of DPVN annealed at 780°C for (a) 1 minute ($34\pm 2\%$ MA), (b) 2 minutes ($38\pm 2\%$ MA), and (c) 5 minutes ($39\pm 3\%$ MA) and then water quenched.

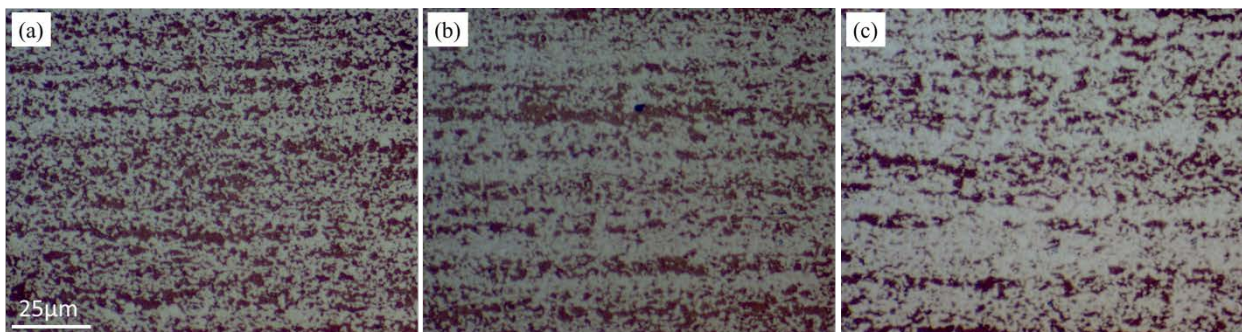


Figure A4. LePera etched microstructures of DPNb annealed at 780°C for (a) 1 minute ($51\pm 2\%$ MA), (b) 2 minutes ($54\pm 3\%$ MA), and (c) 5 minutes ($64\pm 3\%$ MA) and then water quenched.

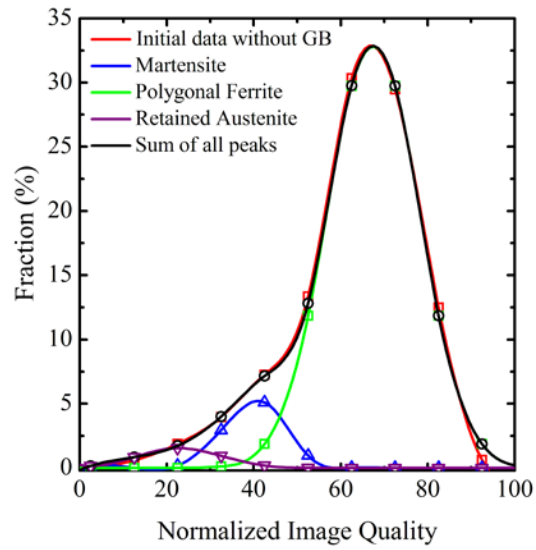
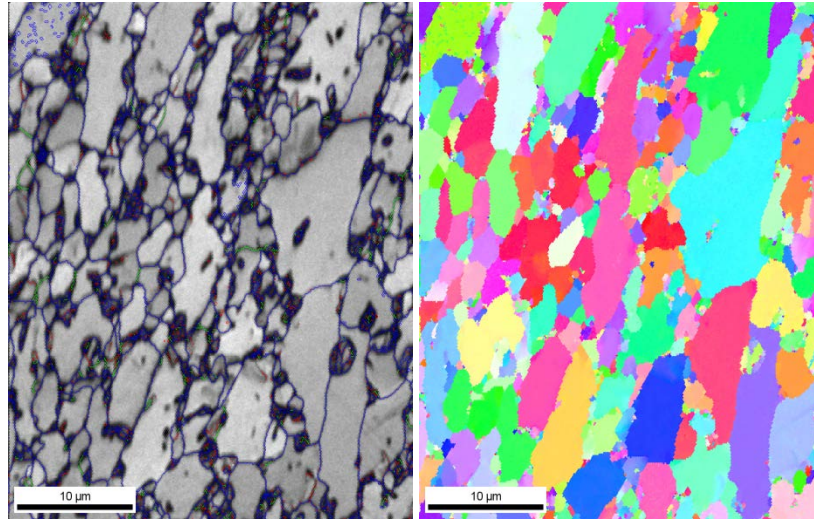


Figure A5. DPV, Gleeble A3 (standard galvanizing processing), IQ image (up left) (red lines 2°-5°, green lines 5°-15°, and blue lines 15°-180°), IPF mapping (up right), and IQ peak fitting curves (below).

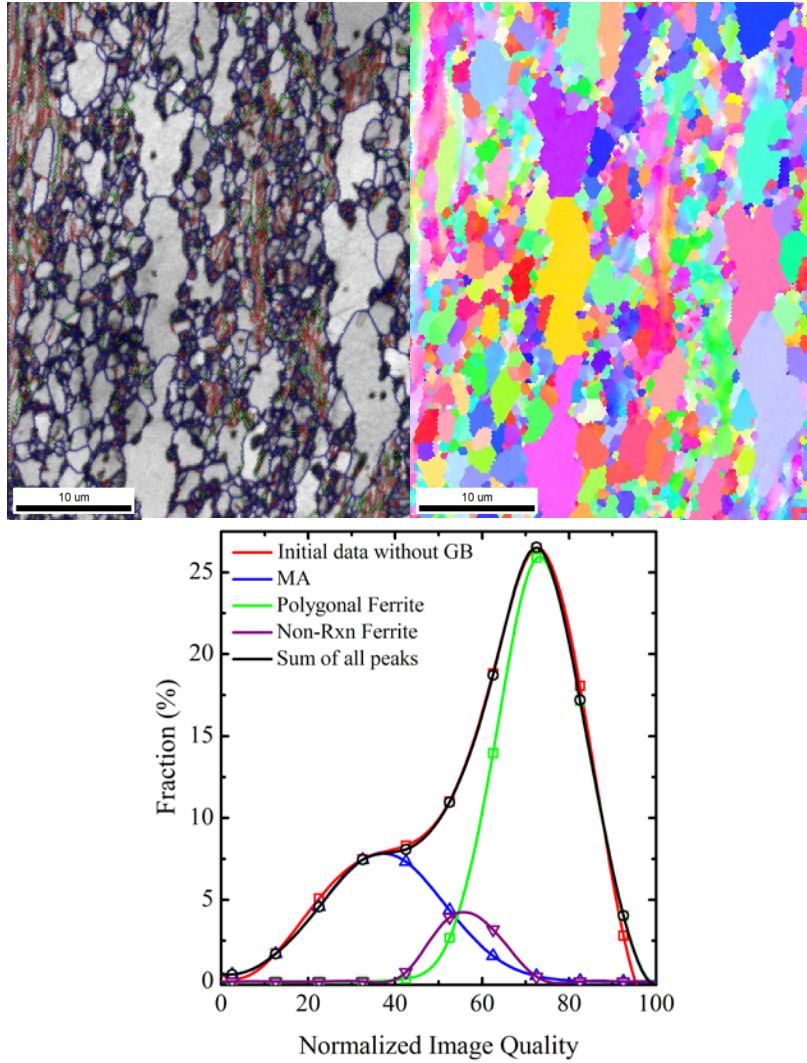


Figure A6. DPNbV, Gleeble A3 (standard galvanizing processing), IQ image (up left) (red lines 2°-5°, green lines 5°-15°, and blue lines 15°-180°), IPF mapping (up right), and IQ peak fitting curves (below).

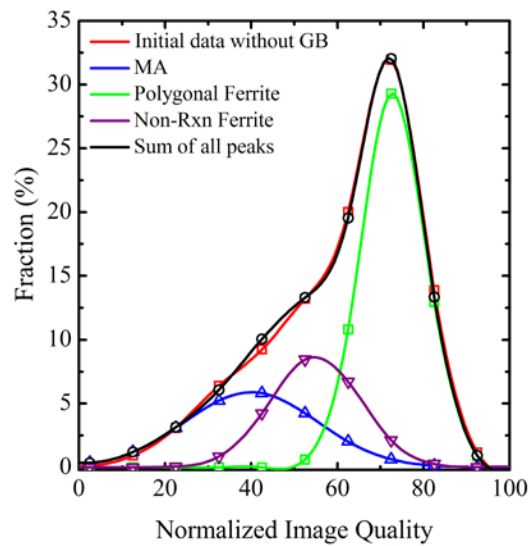
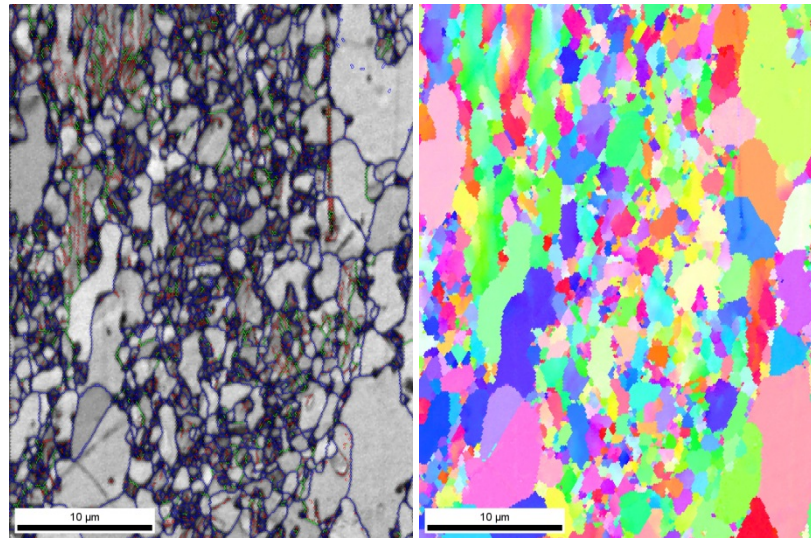


Figure A7. DPVN, Gleeble A3 (standard galvanizing processing), IQ image (up left) (red lines 2°-5°, green lines 5°-15°, and blue lines 15°-180°), IPF mapping (up right), and IQ peak fitting curves (below).

Table A1. Volume fractions of RA, polygonal ferrite and martensite from IQ peak fitting for DPV, GI (A3)

DP_V GI(A3)	Retained Austenite (RA)	Polygonal Ferrite	Martensite
Volume fraction(%)	3.7	87.1	9.2
Peak(IQ)	22.6	67.5	40.4

Table A2. Volume fractions of RA, polygonal ferrite and martensite from IQ peak fitting for DPNbV, GI (A3)

DP_NbV GI(A3)	MA	Polygonal Ferrite	Non-Rxn Ferrite
Volume fraction(%)	28	64	8
Peak(IQ)	37.5	73.7	56.2

Table A3. Volume fractions of RA, polygonal ferrite and martensite from IQ peak fitting for DPVN, GI (A3)

DP_VN GI(A3)	MA	Polygonal Ferrite	Non-Rxn Ferrite
Volume fraction(%)	23	54	23
Peak(IQ)	39.5	73.1	54.7

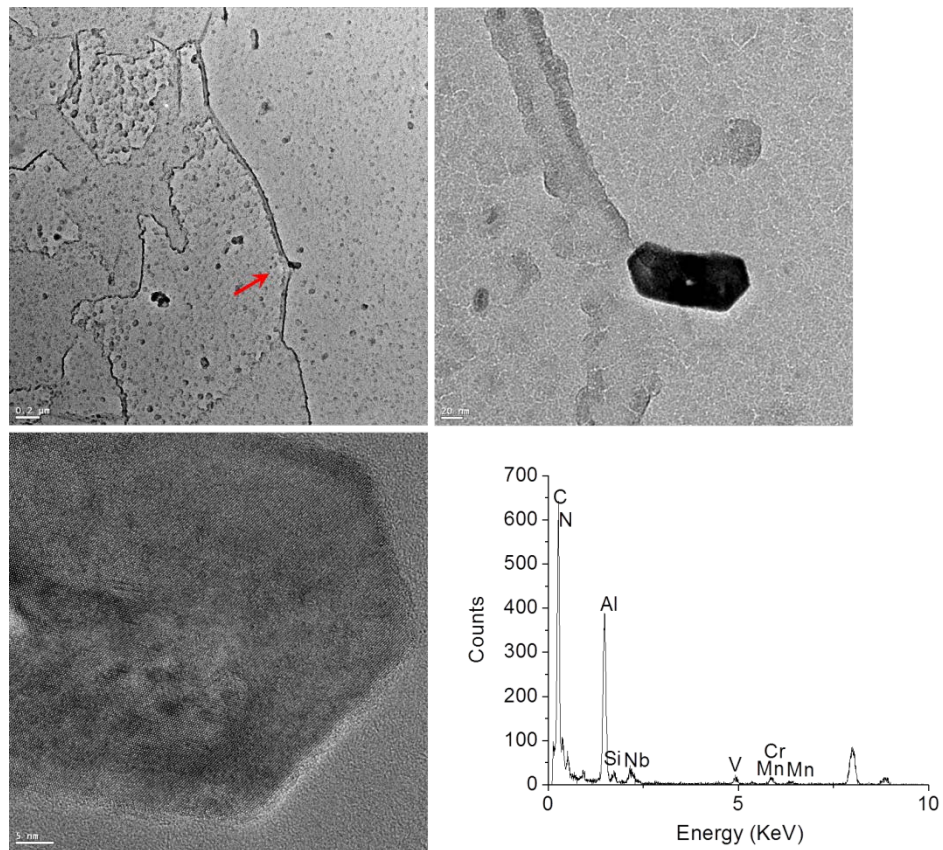


Figure A8. AlN found at the ferrite grain boundary for DP_NbV, GI (A3) standard galvanizing processing, carbon replica sample.

BIBLIOGRAPHY

1. K. Cho, K.V. Redkin, M.Hua, C.I. Garcia, and A.J. DeArdo, Recent development of Nb-containing DP590, DP780, and DP980 steels for production on continuous galvanizing lines, *Advanced Steels 2011*: p. 177-185.
2. Kristian Mathis, Tomas Krajenak, Radomir Kuzel, Jenő Gubicza, Structure and mechanical behaviour of interstitial-free steel processed by equal-channel angular pressing, *Journal of Alloys and Compounds*, 2011. **509**: p. 3522-3525.
3. V. Ballarin, A. Perlade, X. Lemoine, O. Bouaziz, and S. Forest, Mechanisms and modeling of bake-hardening steels: Part II. complex loading paths, *Metallurgical and Materials Transactions A* 2009. **40A**: p. 1375-1382.
4. Zhengyou Tang, Hua Ding, Linxiu Du, and Long Li, Microstructures and mechanical properties of Si-Al-Mn TRIP steel with niobium, *Journal of Materials Science and Technology* 2007. **23**(6): p. 790-794.
5. S.G. Hong, H.J. Jun, K.B. Kang, C.G. Park, Evolution of precipitates in the Nb-Ti-V microalloyed HSLA steels during reheating, *Scripta Materialia*, 2003. **48**: p. 1201-1206.
6. P.C.M. Rodrigues, E.V. Pereloma, D.B. Santos, Mechanical properties of an HSLA bainitic steel subjected to controlled rolling with accelerated cooling, *Materials Science and Engineering*, 2000. **A283**: p. 136-143.
7. Porsche Engineering Services Inc., Materials and Processes #9, ULSAB-AVC-PES Engineering report. Technical report, ULSAB-AVC, 2001 October.
8. J.Becker, E. Hornbogen and F. Wendl, Analysis of Mechanical Properties of A Low-Alloyed Mo-Steel with Different Phosphorus Additions, *Fundamentals of Dual-Phase Steels*, R.A.Kot and B.L.Bramfitt, ed; AIME, New York, N.Y., 1981: p. 383-398.
9. M.S. Rashid, and B.V.N. Rao, Tempering characteristics of a vanadium containing dual phase steel , *Metallurgical Transactions A*, 1982. **13A**: p. 1679-1686.
10. Toshiyuki Kato, Koichi Hashiguchi, Isao Takahashi, Toshio Irie, and Nobuo Ohashi, Development of as-hot-rolled dual-phase steel sheet, *Fundamentals of Dual-Phase Steels*, R.A.Kot and B.L.Bramfitt, ed; AIME, New York, N.Y., 1981: p. 199-220.
11. T. Furukawa and M. Tanino, Structure formation and mechanical properties of intercritically annealed or as-hot-rolled dual-phase steels, *Fundamentals of Dual-Phase Steels*, R.A.Kot and B.L.Bramfitt, ed; AIME, New York, N.Y., 1981: p. 221-248.

12. Pierre Messien, Jean-Claude Herman, Tony Greday, Phase transformation and microstructures of intercritically annealed dual-phase steels, *Fundamentals of Dual-Phase Steels*, R.A.Kot and B.L.Bramfitt, ed; AIME, New York, N.Y., 1981: p. 161-180.
13. A.F. Grawley, M.T. Shehata, N. Pussegoda, C.M. Mitchell, and W.R. Tyson, Processing, properties and modelling of experimental batch-annealed dual-phase steels, *Fundamentals of Dual-Phase Steels*, R.A.Kot and B.L.Bramfitt, ed; AIME, New York, N.Y., 1981: p. 181-197.
14. G.R. Speich, Physical metallurgy of dual-phase steels, *Fundamentals of Dual-Phase Steels*, R.A.Kot and B.L.Bramfitt, ed; AIME, New York, N.Y., 1981: p. 3-45.
15. T.Tanaka, M.Nishida, K.Hashiguchi and T.Kato, Formation and Properties of Ferrite Plus Martensite Dual-Phase Structures, *Structure and Properties of Dual-Phase Steels*, R.A.Kot and J.W.Morris, ed; AIME, New York, N.Y., 1979: p. 221-241.
16. R.G.Davies, The deformation behavior of a vanadium-strengthened dual phase steel, *Metallurgical Transactions A*, 1978. **9A**: p. 41-52.
17. Koh-ichi Sugimoto, Masahiro Misu, Mitsuyuki Kobayashi and Hidenori Shirasawa, Effects of second phase morphology on retained austenite morphology and tensile properties in a TRIP-aided dual-phase steel sheet, *ISIJ International*, 1993. **33**(7): p. 775-782.
18. H.K.D.H.Bhadeshia and D.V.Edmonds, Analysis of mechanical properties and microstructure of high-silicon dual-phase steel, *Metal Science*, 1980. **14**: p. 41-49.
19. N.J.Kim and G.Thomas, Effects of morphology on the mechanical behavior of a dual phase Fe/2Si/0.1C steel, *Metallurgical Transactions A*, 1981. **12A**: p. 483-489.
20. M.Sarwar and R.Priestner , Influence of ferrite-martensite microstructural morphology on tensile properties of dual-phase steel, *Journal of Materials Science* 1996. **31**: p. 2091-2095.
21. R.G.Davies, Influence of martensite composition and content on the properties of dual phase steels, *Metallurgical Transactions A*, 1978. **9A**: p. 671-679.
22. M.H Saleh, R Priestner, Retained austenite in dual-phase silicon steels and its effect on mechanical properties, *Journal of Materials Processing Technology*, 2001. **113**(1-3, 15): p. 587-593.
23. Ali Bayram, Agah Uguz, and Murat Ula, Effects of microstructure and notches on the mechanical properties of dual-phase steels, *Materials Characterization* 1999. **43**: p. 259-269.
24. R.G.Davies, Influence of silicon and phosphorus on the mechanical properties of both ferrite and dual-phase steels, *Metallurgical Transactions A*, 1979. **10A**: p. 113-118.
25. Shoujin Sun, Martin Pugh, Properties of thermomechanically processed dual-phase steels containing fibrous martensite, *Materials Science and Engineering A*, 2002. **335**: p. 298-308.
26. E.Ahmad, T.Manzoor, N.Hussain, Thermomechanical processing in the intercritical region and tensile properties of dual-phase steel, *Materials Science and Engineering A*, 2009. **508**: p. 259-265.

27. Z.Jiang, J.Lian, and J.Chen, Strain hardening behaviour and its relationship to tensile mechanical properties of dual phase steel, *Materials Science and Technology*, 1992. **8**: p. 1075-1081.
28. A.H.Nakagawa and G.Thomas, Microstructure-mechanical property relationships of dual-phase steel wire, *Metallurgical Transactions A*, 1985. **16A**: p. 831-840.
29. Xuan Liang, Jun Li, YingHong Peng, Effect of water quench process on mechanical properties of cold rolled dual phase steel microalloyed with niobium, *Materials Letters*, 2008. **62**: p. 327-329.
30. P.Movahed, S.Kolahgar, S.P.H.Marashi, M.Pouranvari, N.Parvin, The effect of intercritical heat treatment temperature on the tensile properties and work hardening behavior of ferrite-martensite dual phase steel sheets, *Materials Science and Engineering A*, 2009. **518**: p. 1-6.
31. A.K. Jena, M.C. Chaturvedi, On the effect of the volume fraction on martensite on the tensile strength of dual-phase steel, *Materials Science and Engineering*, 1988. **100**: p. 1-6.
32. J. Lis, , A.K. Lis, C. Kolan, Processing and properties of C–Mn steel with dual-phase microstructure, *Journal of Materials Processing Technology*, 2005. **162-163**: p. 350-354.
33. I.A.El-Sesy, Z.M.El-Baradie, Influence carbon and/or iron carbide on the structure and properties of dual-phase steels, *Materials Letters*, 2002. **57**: p. 580-585.
34. J.Y. Koo, M.J. Young, and G. Thomas, On the law of mixtures in dual-phase steels, *Metallurgical Transactions*, 1980. **11A**: p. 852-854.
35. I. Tamura, Y. Tomata, A. Akao, Y. Yamaoha, M. Ozawa, and S. Kanotoni, On the strength and ductility of two-phase iron alloys, *Trans. Iron and Steel Inst. Japan*, 1973. **13**: p. 283-292.
36. G.R. Speich, and R.L. Miller, Mechanical properties of ferrite martensite steels, *Structure and Properties of Dual-Phase Steels*, R.A.Kot and J.W.Morris, ed; AIME, New York, N.Y., 1979: p. 145-182.
37. W.C. Leslie, and R.J. Sober, The strength of ferrite and of martensite as functions of composition, temperature, and strain rate, *Trans. ASM*, 1967. **60**: p. 459-484.
38. J.H. Hollomon, Tensile Deformation, *Am. Inst. Min. Metall. Eng. Trans. Iron Steel Div*, 1945. **162**: p. 268-289.
39. A. Considere, Memoire sur l'emploi du fer et de l'acier dans les constructions, *Ann. Ponts de Chauss* 1885. **9**: p. 574-575.
40. J.M. Rigsbee, J.K. Abraham, A.T. Davenport, J.E. Franklin, and J.W. Pickens, Structure-processing and structure-property relationships in commercially processed dual-phase steels, *Structure and Properties of Dual-Phase Steels*, R.A.Kot and J.W.Morris, ed; AIME, New York, N.Y., 1979: p. 304-329.
41. F.H. Samuel, Effect of strain rate and microstructure on the work hardening of a Cr-Mo-Si steel, *Mater. Sci. Eng.* , 1987. **92**: p. I5-I8.
42. B. Jaoul, Etude de plasticite et application aux meatux, *J. Mech. Phys. Solid.* , 1957. **5**: p. 95-114.

43. C. Crussard, Relationship between exact form of tensile curves of metals and accompanying changes in their structure, *Rev. Metall.* , 1953. **50**: p. 697-710.
44. P. Ludwik, *Elements of technical mechanics*, Springer, Berlin 1909.
45. S.N. Monteiro and R. Reed-Hill, On the double-n behaviour of iron, *Metall. Mater. Trans. B* 1971. **2**: p. 2947-2948.
46. L.F. Ramos, D.K. Matlock, and G. Krauss, On the deformation behavior of dual-phase steels, *Metallurgical Transactions A* 1979. **10**: p. 259-261.
47. Z.H. Jiang, Z.Z. Guan, J.S. Lian, The relationship between ductility and material parameters for dual-phase steel , *J. Mater. Sci.* , 1993. **28**(7): p. 1814-1818.
48. F.H. Samuel, Tensile stress-strain analysis of dual-phase structures in a Mn-Cr-Si steel, *Mater. Sci. Eng.*, 1987. **92**: p. L1-L4.
49. B.K. Jha, R. Avtar, V. Sagar Dwivedi, and V. Ramaswamy, Applicability of modified Crussard-Jaoul analysis on the deformation behaviour of dual-phase steels , *J. Mater. Sci. Lett.* , 1987. **6**: p. 891-893.
50. H.W. Swift, Plastic instability under plane stress, *J. Mech. Phys. Solid.*, 1952. **1**: p. 1-18.
51. M.S. Rashid, Relationship between steel microstructure and formability, *Formable HSLA and Dual-Phase Steels*, R.A. Kot and J.W. Morris, ed. AIME, New York, NY., 1979: p. 1-24.
52. G.R. Speich and R.L. Miller, Tempering of ferrite-martensite steels, *Fundamentals of Dual-Phase Steels*, R.A.Kot and B.L.Bramfitt, ed; AIME, New York, N.Y., 1981: p. 279-304.
53. S.J. Kim, Effects of manganese content and heat treatment condition on mechanical properties and microstructure of fine-grained low-carbon TRIP-aided steels, *Materials Science Forum*, 2010. **638-642**: p. 3313-3318.
54. L.A. Dobrzanski, W. Borek, M. Ondrula, Thermomechanical processing and microstructure evolution of high manganese austenite TRIP-type steels, *Journal of Achievements in Materials and Manufacturing Engineering* 2012. **53**(2): p. 59-66.
55. B. Wietbrock, M. Bambach, S. Seuren, G. Hirt, Homogenization strategy and material characterization of high-manganese TRIP and TWIP steels , *Materials Science Forum* 2010. **638-642**: p. 3134-3139.
56. A. Grajcar, M. Opiela, G. Fojt-Dymara, The influence of hot-working conditions on a structure of high-manganese steel , *Archives of Civil and Mechanical Engineering* 2009. **9**(3): p. 49-58.
57. L.A. Dobrzanski, A. Grajcar, W. Borek, Microstructure evolution of high-manganese steel during the thermomechanical processing, *Archives of Materials Science and Engineering* 2009. **37**(2): p. 69-76.
58. A. Grajcar, E. Kalinowska-Ozgowiez, M. Opiela, B. Grzegorzczuk, K. Golombek, Effects of Mn and Nb on the macro- and Microsegregation in high-Mn high-Al content TRIP steels , *Archives of Materials Science and Engineering*, 2011. **49**(1): p. 5-14.

59. A. Grajcar, S. Lesz, Influence of Nb microaddition on a microstructure of low-alloyed steels with increased manganese content , *Materials Science Forum*, 2012. **706-709**: p. 2124-2129.
60. S. Lee, S.J. Lee, S. Santhosh Kumar, K. Lee, B.C. De Cooman, Localized deformation in multiphase, ultra-fine-grained 6 pct Mn transformation-induced plasticity steel, *Metallurgical and Materials Transactions A*, 2011. **42**: p. 3638-3651.
61. A. Grajcar, R. Kuziak, W. Zalecki, Third generation of AHSS with increased fraction of retained austenite for the automotive industry, *Archives of Civil and Mechanical Engineering*, 2012. **12**: p. 334-341.
62. T.Matsushita, Influence of manganese on the physical properties of carbon steels, *Science Reports, Tohoku University, Sendai, Japan*, 1919. **8**: p. 79.
63. S.I.Hoyt, The metals and common alloys, *Metallography, Part II*, 1921: p. 340.
64. H.M.Howe, The role of manganese, Topical discussion on the role of the general alloying elements in the alloy steels , *A.S.T.M.Proc* 1917. **17**: p. 5.
65. S.J. Lee, S. Lee, B.C. De Cooman, Mn partitioning during intercritical annealing of ultrafine-grained 6% Mn transformation-induced plasticity steel, *Scripta Materialia* 2011. **64**: p. 649-652.
66. A. Grajcar, M. Kaminska, M. Opiela, P. Skrzypczyk, B. Grzegorzczak, E. Kalinowska-Ozgowicz, Segregation of alloying elements in thermomechanically rolled medium-Mn multiphase steels , *Journal of Achievements in Materials and Manufacturing Engineering*, 2012. **55(2)**: p. 256-264.
67. Robert J. Glodowski, A review of vanadium microalloying in hot rolled steel sheet products, *International Seminar 2005 on Application Technologies of Vanadium in Flat-Rolled Steels*, 2005: p. 43-51.
68. Toshio Murakami, Hitoshi Hatano, Goro Miyamoto and Tadashi furuhara, Effects of ferrite growth rate on interphase boundary precipitation in V microalloyed steels, *ISIJ International* 2012. **52(4)**: p. 616-625.
69. K. He and D.V. Edmonds, Formation of acicular ferrite and influence of vanadium alloying, *Materials Science and Technology* 2002. **18**: p. 289-296.
70. C.G.Mateo, C. Capdevila, F.G.Caballero and C.Garcia de Andres, *ISIJ International*, 2008. **48**: p. 1270.
71. H.H.Jin, C. Shin and H.C.Lee, *Solid State Phenom* 2008. **135**: p. 111.
72. J.S. Park, M. Ajmal and R. Priestner, Tensile properties of simulated thin slab cast and direct rolled low-carbon steel microalloyed with Nb, V and Ti, *ISIJ International*, 2000. **40(4)**: p. 380-385.
73. Y. Li, J.A. Wilson, D.N. Crowther, P.S. Mitchell, A.J. Craven and T.N. Baker, The effects of vanadium, Niobium, Titanium and Zirconium on the microstructure and mechanical properties of thin slab cast steels , *ISIJ International*, 2004. **44(6)**: p. 1093-1102.

74. S.K. Mishra, S. Das, S. Ranganathan, Precipitation in high strength low alloy (HSLA) steel: a TEM study, *Materials Science and Engineering*, 2002. **A323**: p. 285-292.
75. E. Courtois, T. Epicier, C. Scott, EELS study of niobium carbo-nitride nano-precipitates in ferrite, *Micron* 2006. **37**: p. 492-502.
76. F. Danoix, E. Bemont, P. Maugis and D. Blavette, Atom probe tomography I. Early stages of precipitation of NbC and NbN in ferritic steels, *Advanced Engineering Materials* 2006. **8**(12): p. 1202-1205.
77. Kelvin Y. Xie, Lan Yao, Chen Zhu, Julie M. Cairney, Chris R. Killmore, Frank J. Barbaro, James G. Williams, and Simon P. Ringer, Effect of Nb microalloying and hot rolling on microstructure and properties of ultrathin cast strip steels produced by the CASTRIP process, *Metallurgical and Materials Transactions A*, 2011. **42A**: p. 2199-2206.
78. M.G. Burke, L.J. Cuddy, J. Piller, M.K. Miller, Combined APFIM-TEM study of Nb(CN) precipitation in HSLA steel, *Materials Science and Technology*, 1988. **4**: p. 113-116.
79. Kelvin Y. Xie, Tianxiao Zheng, Julie M. Cairney, Harold Kaul, James G. Williams, Frank J. Barbaro, Chris R. Killmore, and Simon P. Ringer, Strengthening from Nb-rich clusters in a Nb-microalloyed steel, *Scripta Materialia*, 2012. **66**: p. 710-713.
80. Mohrbacher, H., Advanced metallurgical concepts for DP steels with improved formability and damage resistance. Online paper
81. K. Hashiguchi, T.K., M. Nishida and T. Tanaka, Kawasaki Steel Technical Report No. 1, 1980 September p. 70
82. T. Irie, S.S., K. Hashiguchi, I. Takahashi and O. Hashimoto, Kawasaki Steel Technical Report No. 2 1981: p. 14
83. Davies, R.G., Influence of martensite composition and content on the properties of dual phase steels. *Metall. Trans. A*, 1978. **9**: p. 671-679.
84. Nishizawa, F.T.a.T., *Journal of the Japan Institute of Metals*, 1976. **40(1)**: p. 12
85. S. Lee, D.M.a.C.V.T., *ISIJ International*, 2011. **51**, **No.11** p. 1903
86. V.I.Savran, Y.Vav Leeuwen, D.N.Hanlon, C.Kwakernaak, W.G.Sloof, J.Sietsma, Microstructural features of austenite formation in C35 and C45 alloys, *Metallurgical and Materials Transactions A*, 2007. **38A**: p. 946-955.
87. C.I.Garcia and A.J. Deardo, Formation of austenite in 1.5 Pct Mn steels, *Metallurgical Transactions A* 1981. **12A**: p. 521-530.
88. Speich G.R. and Szirmae, Formation of austenite from ferrite and ferrite-carbide aggregate, *Transactions TMS-AIME*, 1969. **245**: p. 1063-1074.
89. Grozier J.D., Paxton H.W., and Mullins W.W., The growth of austenite into ferrite in the iron-nitrogen system, *Transactions TMS-AIME*, 1965. **233**: p. 130-142.

90. Nehrenberg A.E., The growth of austenite as related to prior structure , Transactions TMS-AIME, 1950. **188**: p. 162-174.
91. Dirnfeld S.F., Korevaar B.M., The transformation to austenite in a fine grained tool steel, Metallurgical Transactions 1974. **5**: p. 1437.
92. Bailey E.F. and Harris W.J., Austenite formation during tempering and its effects on mechanical properties, Journal of Metals 1950: p. 997.
93. N.C. Law and D.V. Edmonds, The formation of austenite in a low-alloy steel, Metallurgical Transactions A 1980. **11A**: p. 33-46.
94. R.R. Judd and H.W. Paxton, Kinetics of austenite formation from a spheroidized ferrite-carbide aggregate, Transactions TMS-AIME, 1968. **242**: p. 206-215.
95. P. Wycliffe, G.R. Purdy and J.D. Embury , Austenite growth in the intercritical annealing of ternary and quaternary dual-phase steels , Fundamentals of Dual-Phase Steels, R.A.Kot and B.L.Bramfitt, ed; AIME, New York, N.Y., 1981: p. 59-83.
96. M.S. Rashid, and B.V.N. Rao, Tempering characteristics of a vanadium containing dual phase steel , Fundamentals of Dual-Phase Steels, R.A.Kot and B.L.Bramfitt, ed; AIME, New York, N.Y., 1981: p. 249-264.
97. R.G.Davies, Tempering of dual-phase steels, Fundamentals of Dual-Phase Steels, R.A.Kot and B.L.Bramfitt, ed; AIME, New York, N.Y., 1981: p. 265-277.
98. G.R. Speich, A.J. Schwoeble, and G.P. Huffman, Tempering of Mn and Mn-Si-V dual-phase steels, Metallurgical Transactions A, 1983. **14A**: p. 1079-1086.
99. A.Anazadeh Sayed, Sh. Kheirandish, Affect of the tempering temperature on the microstructure and mechanical properties of dual phase steels, Materials Science and Engineering A, 2012. **532** p. 21-25.
100. X. Fang, Z.Fan, B.Ralph, P.Evans, R.Underhill, Effects of tempering temperature on tensile and hole expansion properties of a C-Mn steel, Journal of Materials Processing Technology, 2003. **132**: p. 215-218.
101. S.S.M. Tavares, P.D.Pedroza, J.R. Teodosio, and T. Gurova, Mechanical properties of a quenched and tempered dual phase steel, Scripta Materialia 1999. **40**(8): p. 887-892
102. Peng-Heng Chang, Temper-Aging of continuously annealed low carbon dual phase steel, Metallurgical Transactions A 1984. **15A**: p. 73-86.
103. T.Waterschoot, K.Verbeken and B.C.DE Cooman, Tempering kinetics of the martensite phase in DP steel, ISIJ International, 2006. **46**: p. 138-146.
104. V.H.Baltazar, Hernandez, S.S.Nayak, and Y. Zhou, Tempering of martensite in dual-phase steels and its effects on softening behavior, Metallurgical and Materials Transactions A, 2011. **42**(10): p. 3115-3129.

105. A.Kamp, S.Celotto, D.N.Hanlon, Effects of tempering on the mechanical properties of high strength dual-phase steels, *Materials Science and Engineering A*, 2012. **538**: p. 35-41.
106. Suleyman Gunduz, Effects of chemical composition, martensite volume fraction and tempering on tensile behaviour of dual phase steels, *Materials Letters*, 2009. **63**: p. 2381-2383.
107. Han Sang Lee, Byoungchul Hwang, Sunghak Lee, Chang Gil Lee, Sung-Joon Kim, Effects of martensite morphology and tempering on dynamic deformation behavior of dual-phase steels, *Metallurgical and Materials Transactions A*, 2004. **35A**: p. 2371-2382.
108. A.A.Korda, Y.Mutoh, Y.Miyashita, T.Sadasue, and S.L.Manan, In situ observation of fatigue crack retardation in banded ferrite-pearlite microstructure due to crack branching , *Scripta Materialia* 2006. **8**: p. 1835-1840
109. S.W.Thompson and P.R.Howell, Factors influencing ferrite/pearlite banding and origin of large pearlite nodules in a hypoeutectoid plate steel, *Materials Science and Technology*, 1992. **8**: p. 777-784.
110. D.Chae, D.A.Koss, A.L.Wilson and P.R.Howell, Effect of microstructural banding on failure initiation of HT-100 steel, *Metallurgical and Materials Transactions A*, 2000. **31A**: p. 995-1005.
111. H.K.D.H. Bhadeshia, Phase transformations contributing to the properties of modern steels , *Bulletin of the Polish Academy of Sciences* 2010. **58**: p. 255-265.
112. P.G.Bastien, The mechanism of formation of banded structures, *Journal of the Iron and Steel Institute* 1957. **187**: p. 281-291.
113. Benoit Krebs, Lionel Germain, Alain Hazotte, Mohamed Goune, Banded structure in dual phase steels in relation with the austenite-to-ferrite transformation mechanisms, *J Mater Sci* 2011. **46**: p. 7026-7038.
114. C.F.Jatczak, D.J.Girardi, and E.S.Rowland, On banding in steel, *Trans. ASM* 1956. **48**: p. 279-305.
115. J.S.Kirkaldy, J.von Destinon-Forstmann, and R.J.Brigham, Simulation of banding in steels, *Canadian Metallurgical Quarterly* 1962. **59**: p. 59-81.
116. Y.J. Park, A.P. Coldren and J.W. Morrow, Effect of martensite bands and elongated manganese sulfide inclusions on the formability of dual-phase steels, *Fundamentals of Dual-Phase Steels*, R.A.Kot and B.L.Bramfitt, ed; AIME, New York, N.Y., 1981: p. 485-497.
117. J.D. Verhoeven, A review of microsegregation induced banding phenomena in steels, *Journal of materials engineering and performance*, 2000. **9**: p. 286-296.
118. S.E. Offerman, N.H. Van Dijk, M.Th. Rekveldt, J. Sietsma and S. Van der Zwaag, Ferrite/pearlite band formation in hot rolled medium carbon steel, *Materials Science and Technology*, 2002. **18**: p. 297-303.
119. Grossterlinden R, Kawalla R, Lotter U, Pircher H, Formation of pearlitic banded structures in ferritic-pearlitic steels, *Steel Res* 1992. **63**: p. 331.

120. Francisca G. Caballero, Andrea Garcia-Junceda, Carlos Capdevila and Carlos Carcia de Andres, Evolution of microstructural banding during the manufacturing process of dual phase steels, *Materials Transactions* 2006. **47**(9): p. 2269-2276.
121. J.R. Davis (ed.), *Metals Handbook: Desk Edition*. (ASM International, Materials Park), 2006: p. 72.
122. L. Zhao, N.H. van Dijk, E. Bruck, J. Sietsma, S. van der Zwaag, Magnetic and X-ray diffraction measurements for the determination of retained austenite in TRIP steels, *Materials Science and Engineering A*, 2001. **313**: p. 145-152.
123. E. Maurer, K. Schroeter, The determination of austenite contents by the measurement of magnetic saturation values, *Stahl und Eisen*, 1929. **49**: p. 929.
124. S.H.Magner, R.J.De Angelis, W.N.Weins, and J.D.Makinson, A historical review of retained austenite and its measurement by X-ray diffraction, *JCPD-International Centre for Diffraction Data 2002, Advances in X-ray Analysis*, 2002. **45**: p. 92-97.
125. A.J. Wilkinson, D.J.D., Quantitative deformation studies using back scatter patterns. *Acta metal. Mater.*, 1991. **39**(12): p. 3047-3055
126. Choi, S.H.and Jin Y.S., Evaluation of stored energy in cold-rolled steels from EBSD data. *Materials Science and Engineering A*, 2004. **371**: p. 149-159
127. Chao Fang, C. Isaac Garcia, Shi-Hoon Choi, and Anthony J. Deardo, A study of the batch annealing of cold-rolled HSLA steels containing niobium or titanium. *Metallurgical and Materials Transactions A*, 2015. **46A**: p. 3635-3645
128. Humphreys, F.J., Grain and subgrain characterization by electron backscatter diffraction. *Journal of Materials Science*, 2001. **36**(3833-54).
129. W.T. Read, W.Shockley, Dislocation models of crystal grain boundaries. *Phys. Rev.* , 1950. **78**(3): p. 275-289.
130. Choi, S.H., Monte Carlo technique for simulation of recrystallization texture in interstitial free steels. *Materials Science Forum*, 2002. **408-412** p. 469-474
131. Choi, S.H., F. Barlat, and J.H. Chung, Modeling of textures and yield surfaces during recrystallization in IF steel sheets. *Scripta Materialia*, 2001. **45**: p. 1155-62
132. Choi, S.H., Simulation of stored energy and orientation gradients in cold-rolled interstitial free steels. *Acta Materialia*, 2003 **51**: p. 1775-1788
133. Stibitz, G.R., *Phys. Rev.* , 1937 **49** p. 872
134. A. Borbely, J.H.D., and T. Ungar An X-ray method for the determination of stored energies in texture components of deformed metals: application to cold worked ultra high purity iron. *Acta materialia* 2000 **48** p. 2005-2016.
135. Kazeminezhad, M., Relationship between the stored energy and indentation hardness of copper after compression test: models and measurements *J. Mater. Sci.* , 2008 **43** p. 3500-3504

136. Mitra Taheri, Hasso Weiland, and Anthony Rollett A method of measuring stored energy macroscopically using statistically stored dislocations in commercial purity aluminum Metallurgical and Materials Transactions A 2006 **37A** p. 19-25
137. Glodowski, R.J., An empirical prediction model of the incremental strengthening of ferrite/pearlite steels with additions of vanadium and nitrogen, with emphasis on the effective nitrogen level International Journal of Metallurgical Engineering 2013 **2(1)** p. 56-61
138. A. Bag, K.K.Ray, and E.S. Dwarakadasa Influence of martensite content and morphology on tensile and impact properties of high-martensite dual-phase steels Metallurgical and Materials Transactions A, 1999. **30A**: p. 1193-1202
139. Kohei Hasegawa, Kenji Kawamura, Toshiaki Urabe and Yoshihiro Hosoya, Effects of Microstructure on Stretch-flange-formability of 980 MPa Grade Cold-rolled Ultra High Strength Steel Sheets. ISIJ International 2004 **44, No.3** p. 603-609
140. X. Fang, Z. Fan, B. Ralph, P. Evans, R. Underhill Effects of tempering temperature on tensile and hole expansion properties of a C-Mn steel Journal of Materials Processing Technology 2003 **132** p. 215-218
141. D.I. Hyun, S.M. Oak, S.S. Kang, Y.H. Moon Estimation of hole flangeability for high strength steel plates Journal of Materials Processing Technology 2002 **130-131** p. 9-13
142. Kohichi Sugimoto, Jyunya Sakaguchi, Tsutomu Ida, and Takahiro Kashima Stretch-flangeability of a high-strength TRIP type bainitic sheet steel ISIJ International 2000 **40, No.9** p. 920-926
143. X. Gang, Z. Fan, B. Ralph, P. Evans, R. Underhill The relationships between tensile properties and hole expansion property of C-Mn steels. Journal of Materials Science 2003 **38** p. 3877-3882
144. B.S. Levy, M. Gibbs, and C.J. Van Tyne Failure during sheared edge stretching of dual-phase steels Metallurgical and Materials Transactions A 2013 **44A** p. 3635-3648
145. S. Zaefferer, J. Ohlert, W. Bleck, A study of microstructure, transformation mechanisms and correlation between microstructure and mechanical properties of a low alloyed TRIP steel. Acta Materialia, 2004. **52** p. 2765-2778
146. Marco Wendler, Benedikt Reichel, Ralf Eckner, Olga Fabrichnaya, Lutz Kauger, Andreas Weib, and Javad Mola, Effect of vanadium nitride precipitation on the martensitic transformation and mechanical properties of CrMnNi cast austenitic steels. Metallurgical and Materials Transactions A, 2014: p. 1-13
147. Naoya Kamikawa, Kensuke Sato, Goro Miyamoto, Mitsuhiro Murayama, Nobuaki Sekido, Kaneaki Tsuzaki, and Tadashi Furuhashi, Stress-strain behavior of ferrite and bainite with nano-precipitation in low carbon steels. Acta Materialia, 2015 **83**: p. 383-396
148. Y.J. Zhang, G. Miyamoto, K. Shinbo, T.Furuhashi, T. Ohmura, T. Suzuki, and K. Tsuzaki, Effects of transformation temperature on VC interphase precipitation and resultant hardness in low-carbon steels. Acta Materialia, 2015 **84**: p. 375-384

149. G. Miyamoto, R. Hori, B. Poorganji, and T. Furuwara, Interphase precipitation of VC and resultant hardening in V-added medium carbon steels *ISIJ International* 2011 **51, No.10** p. 1733-1739
150. Rune Lagneborg, Bevis Hutchinson, Tadeusz Siwecki, Stanislaw Zajac, Swerea Kimab, The role of vanadium in microalloyed steels. Stockholm, Sweden 2014.
151. P. Movahed, S. Kolahgar, S.P.H. Marashi, M. Pouranvari, N. Parvin, The effect of intercritical heat treatment temperature on the tensile properties and work hardening behavior of ferrite-martensite dual phase steel sheets. *Materials Science and Engineering A*, 2009. **518** p. 1-6
152. Wu, Jinghui, Development of a new technique to identify and quantify complex austenite decomposition products. University of Pittsburgh, Ph.D thesis 2005.